THE UNIVERSITY OF CHICAGO

TRANSPORT PROPERTY ON MERCURY CHALCOGENIDE COLLOIDAL QUANTUM DOT

A DISSERTATION SUBMITTED TO

THE FACULTY OF THE DIVISION OF THE PHYSICAL SCIENCES

IN CANDIDACY FOR THE DEGREE OF

DOCTOR OF PHILOSOPHY

DEPARTMENT OF PHYSICS

BY

MENGLU CHEN

CHICAGO, ILLINOIS

AUGUST 2020

In memory of my grandfather Shicai Chen

Table of Contents

List of Tables

List of Figures

Acknowledgments

First of all, I want to express my deepest gratitude to my adviser Professor Philippe Guyot-Sionnest for his useful guidance, creative ideas, and great support during my Ph.D. I started working in PGS lab with my physics 335 project on carrier transport study of quantum dots, when I was impressed with his ability to simplify a complex problem with a clear physics picture from basic theory, design experiments, and figure out the interesting properties. It helped me to get a good start and gain the initial motivation for my Ph.D. research. Having benefited from his way of thinking and working in scientific research, I can notice the continuous improvement in my knowledge and ability to solve complicated problems in the last few years. I am truly thankful for the opportunity to work with him, which is one of the most important experiences in my life.

I would like to thank all my committee members, Prof. Peter Littlewood, Prof. David Schuster, and Prof. Henry Frisch. The conversations with them always inspired me with a deeper understanding of physics, which helped me a lot in my Ph.D.

I am very thankful to all former and current group members in PGS lab, Dr. Zhiyou Deng, Dr. Guohua Shen, Dr. Xin Tang, Dr. Matt Ackerman, Christopher Melnychuk, Ananth Kamath, and Haozhi Zhang. It was a great experience to work together closely with these creative and diligent people. I would like to express my gratitude to all the collaborators, Prof. Dmitri Talapin, Prof. Xinzheng Lan, Prof. Christophe Delerue, Prof. Yuanyuan Wang, Dr. Margaret Hudson, and Dr. Benjamin Diroll. Without their effort and instructions, the research projects could not go smoothly. I would also like to thank Dr. Qiti Guo, Dr. Justin Jureller, Dr. Yimei Chen for their knowledge and patience in the instrument training sessions.

Finally, I want to thank my family. I cannot imagine how to go through these years without them. My parents, though did not understand my research, always stood behind me. My husband, Qi He, made the cold winter in Chicago warm and sunny. It is so delightful that our ten years' relationship from high school finally resulted in a happy marriage. Last but not least, I would like to thank my adorable son Andrew Chen He, whose arrival let me re-think the meaning of my life.

Chapter 1: Overview

Beginning in the early 1980s and extending to the present, colloidal nanocrystals(NC) have become an important class of materials with great potential for applications ranging from medicine to electronic and optoelectronic devices. Nanocrystals naturally form short-range order solids, limited by their dispersity, solubility, solvent evaporation, particle-substrate interactions, and particle-particle interactions. People work hard on understanding and overcoming those problems to achieve superlattices or superstructure with nanocrystals. Besides, the design of surface ligands has been developed a lot from long hydrocarbon chains to short cross-linking ligands and metal chalcogenide complexes in the last 40 years. Transport in nanocrystal films has also been investigated a lot such as doping, spin-dependent transport, and transport mechanism. Since narrow size distributions, rational shape-engineering, compositional modulation, electronic doping, and tailored surface chemistries are now feasible for a widening range of these materials, the performance of NC-based devices has become competitive to other state-of-the-art materials.

Semiconductor NCs, for example, hold unique promise for near- and mid-infrared technologies, where very few semiconductor materials are available. Mercury chalcogenide colloidal quantum dots(QD) are of interest as solution based materials in the mid-IR spectral range. Aggregated HgTe QDs are typically undoped or lightly p-doped with size-dependent bandgaps and have shown promise as mid-IR detectors, as proved by Keuleyan *et al* in 2011. In contrast to aggregated HgTe, non-aggregated mercury chalcogenide QDs are usually stably n-doped in ambient conditions, which allowed the realizations of QDs intraband photodetectors. These materials have made great progress in mid-IR detection in the last few years including background limited photovoltaic (PV) devices, and are expected to lead to the simplified fabrication of high resolution mid-infrared cameras, Plasmon resonance enhanced PV devices and multi-spectral detectors. The performances

of some NC-based mid-IR devices have already been comparable with the current commercial epitaxial devices. The precise engineering of the electronic interactions and wave functions with nanomaterials is a promising avenue for further improvement, which is the main project of my Ph.D. project. This thesis focuses on a deeper understanding of electrical transport in nanoparticle solids when carriers must travel via the nanocrystal states.

In **chapter 2**, I use electrochemistry to provide the measurement of the Fermi level and the absolute measurements of the filled and empty state energies with the application of a voltage. This work helps to obtain the energy structure and doping level of those mercury chalcogenide QDs. I also build a spectroelectrochemistry set-up to investigate the fine conduction band in the HgTe/Se quantum dot, and apply this method to the CdSe quantum well.

In **chapter 3**, I present the work on HgTe/Se QD films which show high mobility for charges transported through discrete QD states. A hybrid surface passivation process efficiently eliminates surface states, provides tunable air-stable doping, and enables hysteresis-free filling of QD states evidenced by strong conductance modulation. The Hall effect in this experiment may require more thinking although I try to give a reasonable explanation.

In **Chapter 4**, I show the size polydispersity effect on HgSe colloidal quantum dot. The results show mobility quite exponentially dependent on size dispersion, indicating the dispersion causes effect related to the activation energy. This effect could be from the monodispersed quantum dots narrowing the energy difference between sites, which causes the reduction in the barrier height for transport. This is well explained by my simulation. I also discuss the size distribution effect on the intraband and its effect on photoconductor property.

In **chapter 5**, I discuss the magnetic transport properties on HgTe QDs. A positive-quadratic magnetoresistance is observed which can be several 100% at low temperature and scales like x (1-x) where x is the fractional occupation of the 1Se state. There is also a negative magnetoresistance of 1-20% from 300 K to 10 K which is rather independent of the fractional occupation, and which follows a negative exponential dependence with the magnetic field.

In **chapter 6**, I take HgTe QD as an example, showing that the high carrier mobility is generally beneficial for QD device applications.

Chapter 2: Reversible Electrochemistry of Mercury Chalcogenide Quantum Dots Films

In this chapter, I explain how electrochemistry method is used to determine the absolute positions of the energy levels of QDs of Hg (S, Se, Te), which are of interest as mid-infrared materials. The bulk valence bands are then determined to be at -5.85 eV, -5.50 eV, -4.92 eV and -4.77 eV (±0.05 eV) for zinc-blend HgS, HgSe, non-aggregated and aggregated HgTe, respectively and they are in the same order as the anions p-orbital energies. The conduction bands are conversely at -5.20 eV, -5.50 eV, -4.92 eV and -4.77 eV. The stable ambient n-doping of non-aggregated Hg (S, Se, Te) quantum dots arises because the conduction band is sufficiently lower than the measured environment Fermi level of ~ -4.7 eV to allow for n-doping in the QDs even with significant electron confinement. The position of the Fermi level and the quantum dots states are sensitive to different surface treatments, providing an avenue to control doping. At the end of this chapter, electrochemical gating is further used to determine the carrier mobility in the films of the three different systems as a function of QD size. Non-aggregated Hg (S, Se, Te) shows increasing mobility with increasing particle sizes while aggregated HgTe shows a non-monotonous behavior, which is attributed to some degree of aggregation of HgTe QDs.

Spectra-electrochemistry is also used for the more detailed level assignment of nanocrystals and results are compared with photoinduced transient spectroscopy.

This chapter includes the published result from reference [9, 11, 12, 56] as well as some unpublished data.

2.1 Introduction

QDs of zinc-blend mercury chalcogenides, Hg (S, Se, Te)[1], are of interest as solution based materials in the mid-IR spectral range. Aggregated HgTe QDs are typically undoped or weakly p-type with size-dependent bandgaps and have shown promise as mid-IR detectors[2]. Recent advances include background limited photovoltaic devices[3,4], the simplified fabrication of high resolution mid-infrared cameras[5], plasmon resonance enhanced PV devices[6] and multi-spectral detectors[7,8]. In contrast to aggregated HgTe, non-aggregated mercury chalcogenides QDs are stably n-doped in ambient conditions[9-11], which allowed the realizations of QDs intraband photodetectors[10,13,14]. One explanation for the markedly different doping of the mercury chalcogenides has been the relative positions of the environmental Fermi level and the energy levels of the dots[9]. It has also been observed that exposure of the QDs to various conditions could strongly change the doping level as determined by the strength of the intraband transitions[10,13,15]. This has been proposed to arise through a displacement of the QD states with respect to the environment Fermi level[9]. In general, small infrared gaps place strong requirements on the control of the Fermi level around the QDs since this determines the doping which strongly affects the photodetector properties. Therefore, it is important to assess the absolute energy of the states of the QDs, their sensitivity to the surface condition[16,17] and the origin of the Fermi level, to ultimately control doping in these QD films.

Electrochemistry is a powerful technique. It provides the measurement of the Fermi level and reversible electrochemistry allows the absolute measurements of the filled and empty state energies with the application of a voltage[18]. With a bi-potentiostat, it gives the conduction as a function of the density of states of the QD films[19]. Therefore, a single cyclic voltammetry experiment can readily provide information that could otherwise be obtained by the combination of

photoemission[20], inverse photoemission and field effect transistor (FET) gating. While reversible electrochemistry is limited by the chemical stability of the materials, irreversible electrochemistry can also be used to learn about chemical processes and decomposition at QD surfaces[21-23]. Another distinction is that the environment must be an electrolyte, allowing for ionic conduction.

This chapter presents results from an extensive study of the reversible electrochemistry of films of the three mercury chalcogenides QDs. The redox potentials of the QD states, the absolute position of the bulk bands, the doping, the origin of the Fermi level, and the mobility as a function of QD size are determined.

2.2 Typical electrochemistry results

Figure 2-1 shows the picture of the electrochemistry cell and schematic of electrochemistry set-up. There are four electrodes in the setup: two Pt working electrodes, one reference electrode, and one Pt counter electrode. During the measurement, the bipotentiostat (DY2300 series Digi-Ivy) applies a small bias (5mV) to the working electrodes and measures the currents of the two working electrodes (I_1, I_2) as a function of potential. (I_1+I_2) is the charging current of the film while (I_1 - I_2)/2 is the conduction current. The conductance (G) is G= (I_1-I_2)/(2*bias). The scanning rate is 50 mV/s. The bi-potentiostat also records the rest potential (= Fermi level) before and after the cyclic voltammetry. The temperature is monitored by a chromel-alumel thermocouple (HH12B OMEGA). An Ag/AgCl reference electrode is used in the cell. The potential difference between the Ag/AgCl reference electrode and a standard calomel electrode (SCE) is measured before and after the experiment using a voltmeter in an identical solution but at room temperature. Unless stated otherwise, the sample is immersed in an electrochemical cell filled with 0.1M tetrabutylammonium perchlorate in propylene carbonate, under nitrogen bubbling, and cooled in an ethanol/dry ice bath (203 K). As in prior electrochemical studies, cooling is used to minimize the Faradaic current due to the reaction of impurities[24]. We note that no precautions were taken to guarantee an anhydrous electrolyte, and H_2O is the expected dominant contamination.

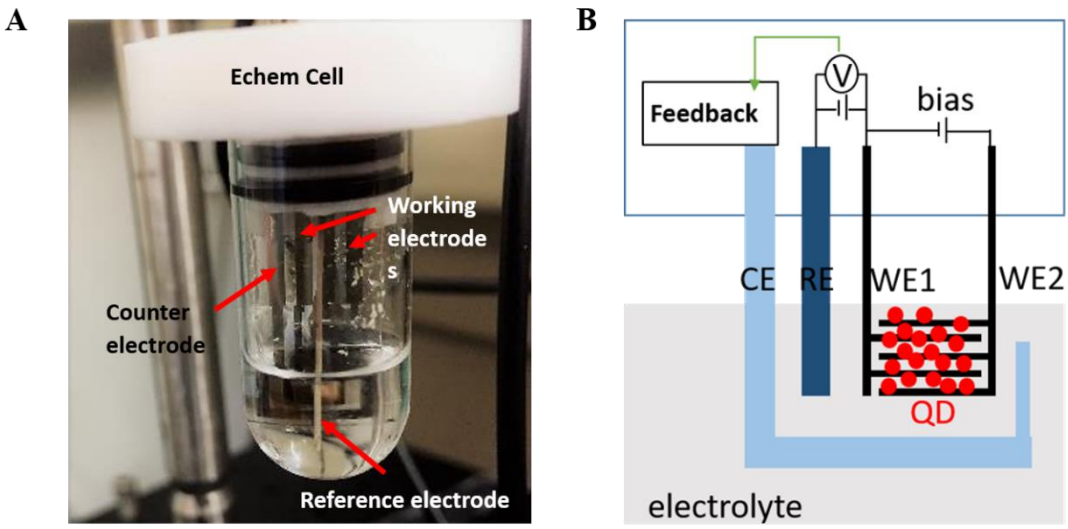

Figure 2-1. Electrochemistry set-up. (A) picture of the electrochemistry cell. **(B)** Schematic of electrochemistry set-up.

Figure 2-2(A~D) shows the typical results from a cyclic voltammetry experiment for CQD films of HgS (average diameter 5 nm), HgSe (average diameter 6.8 nm), aggregated HgTe (average diameter 7.1 nm) and non-aggregated HgTe (average diameter 9.6 nm). HgS[17], HgSe[10], aggregated HgTe[25] and non-aggregated HgTe[11] QDs are prepared following reported methods. For electrochemical measurements, we use thin films of dodecanethiol capped QDs (< 100 nm), drop-cast on interdigitated electrodes. Ligand exchange is done using 2% HCl (v/v) and 2% ethanedithiol (EDT) (v/v) in isopropyl alcohol (IPA) for 30 secs in ambient conditions, rinsing with IPA and drying with N_2 as reported previously[25]. As described later, different film treatments produce different results. For example, when the films are treated with pure IPA in air, the mobilities are much smaller. The redox potentials also differ by up to 0.2V from sample to sample of the same quantum dot sizes and the doping level is variable, which may be caused by the uncontrolled amounts of ligands left as well as the variable extent of oxidation. In this chapter, unless otherwise mentioned, we use the EdT/HCl/IPA treatment in air as it affords repeatable redox positions (within 0.05V) and rest potentials, as well as good film conductance.

The reversibility of the electrochemistry is evident in **Fig.2-2(A~D).** This is consistent with simple charge transfer to an electroactive film[18]. Extending the scan range in the oxidation and reduction directions leads to increasing Faradaic currents as electrons or holes are consumed in irreversible chemical reactions. For reversible electrochemistry involving only charge flowing back and forth into the QD state, the potential must stay in the range of the electrochemical stability, with no reactions. To estimate stability limits, we use $(HgX)_n+2e^-\rightarrow Hg(HgX)_{n-1}+X^{2-}$ for the reduction decomposition potential, $E_{r,dec}$, and $(HgX)_n\rightarrow(HgX)_{n-1}X+Hg^{2+}+2e^-$ for the oxidation decomposition potential $E_{o,dec}$ [26,10]. These can be determined using standard aqueous redox potentials and standard energy of formation $\Delta G^o_{f,HgX}$, such that $E_{r,dec} = E^0_{X/X^{2-}} + \Delta G^o_{f,HgX}/2F$ and $E_{o,dec} = E^0_{Hg^{2+}/Hg} - \Delta G^o_{f,HgX}/2F$ where F is the Faraday constant. The region of stability is [-0.99V, +0.85V] for HgS, [-1.17V, +0.76V] for HgSe and [-1.3V, +0.75V] for HgTe, with potentials referenced to SCE. The oxidation limit in our experiments can therefore be explained by the oxidation decomposition, around +0.8V/SCE for all three systems. However, the reduction limit is experimentally much more positive than -1V/SCE, and this may be due to other reactions not considered above or impurities.

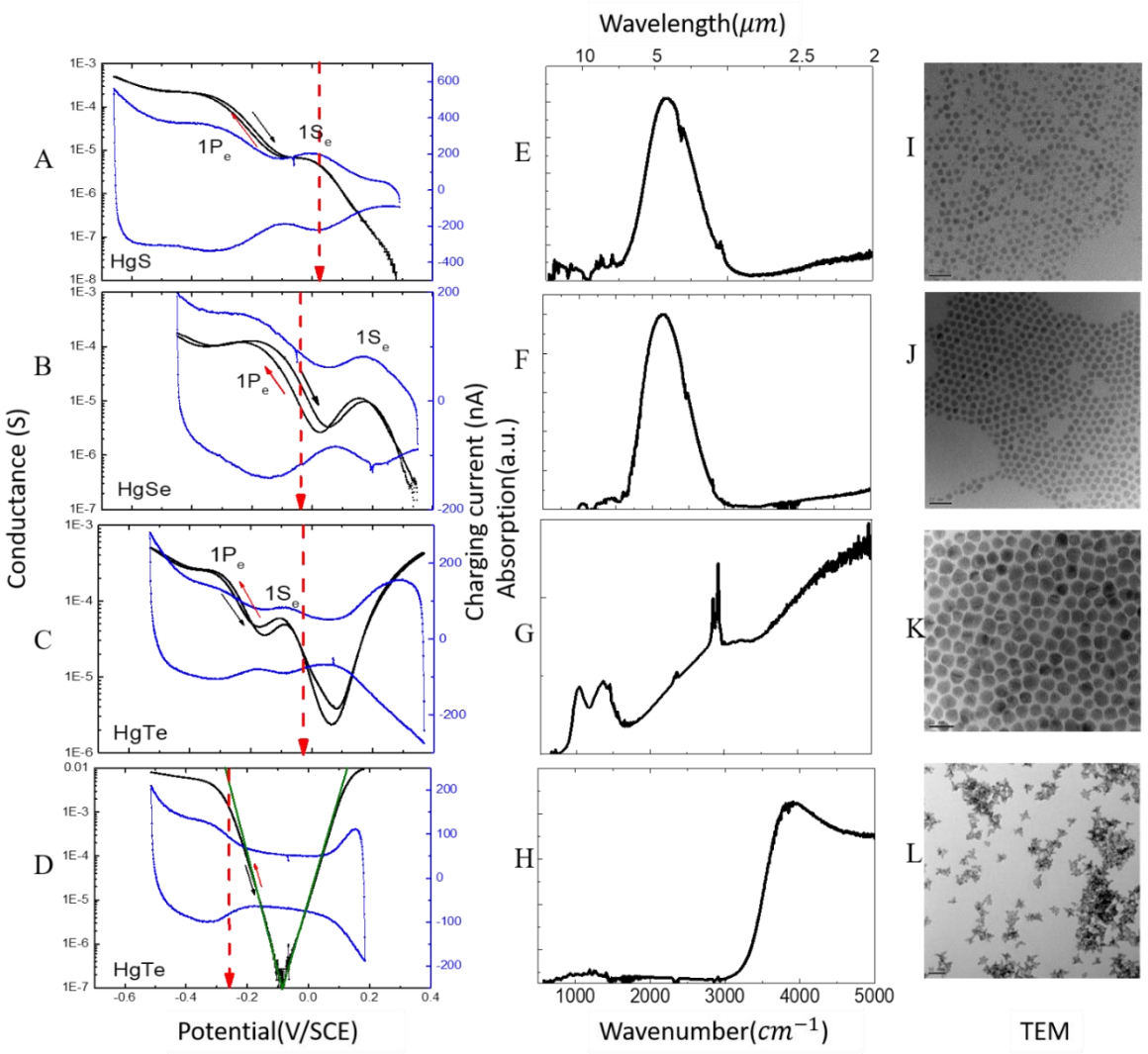

Figure 2-2: Typical electrochemistry results combined with optical absorption and TEM. **(A~D)** Cyclic voltammetry of films of HgS (5 nm), HgSe (6.8 nm), non-aggregated HgTe (9.6 nm), and aggregated HgTe (7.1 nm) QDs, respectively. The blue lines are the charging currents, the black lines are the conductance, and the red arrow indicates the rest potential. Small arrows indicate the scan directions, with the reduction being towards negative potential and oxidation towards positive potentials. **(E~H)** Infrared absorption of films of the same HgS, HgSe, non-aggregated and aggregated HgTe QDs films, respectively. **(I~L)** TEM images of the same colloid dispersions. The scale bars are 20nm and 50nm. HgS has a size distribution of 13%, HgSe ~ 9%, non-aggregated HgTe is ~9% and aggregated HgTe is ~10%. Partial of the plots are adapted from reference 9.

Fig.2-2(A, B) show that both HgS and HgSe show n-type conductivity with reversible charging current waves but no p-type conductivity. At positive potentials, the conductivity remains in the

noise and there is no reversible charging current when the potential scan is reversed. Therefore, if holes are injected, the QDs undergo some irreversible process on the time scale of the cyclic voltammetry and p-type conductivity is not achieved. This is consistent with the position of the valence band determined later, and the oxidation decomposition limit determined above. On the n-side, the two reversible reduction/oxidation waves are assigned to electron injection into the $1S_e$ and $1P_e$ states. The filling of these states is also reflected in large increases in the conductance. The features in the charging and conduction currents can both be used to determine the redox potentials of $1S_e$ and $1P_e$. As previously reported for HgSe QD[10], there is a striking conductance minimum between $1S_e$ and $1P_e$ state shown in **Fig2-2B**, indicative of a small or zero density of states between $1S_e$ and $1P_e$. **Fig2-2(A, C)** now shows a similar feature for HgS and non-aggregated HgTe, respectively. For HgSe, there is also a clear minimum between $1P_e$ and higher states, while there is an inflection point for HgS. We believe that this reflects the broader size distribution of HgS QDs, as judged by the transmission electron microscopy (TEM) pictures of the samples in **Fig2-2(I, J)**.

In contrast to HgS and HgSe, HgTe QD film exhibit both n-type and p-type charging and conductivity, as previously reported[27] and shown in **Fig2-2(C, D)**. The charging current shows an electrochemical gap between a clearly resolved peak on the reduction side assigned to electron injection into $1S_e$, and a wave on the oxidation side assigned to hole injection. The n-type change in non-aggregated HgTe is very similar to HgS and HgSe. Unlike HgS, HgSe, and non-aggregated HgTe, an electrochemical signature of $1P_e$ is not readily observed for aggregated HgTe. This may be due to a smaller energy separation and different level positions in the non-spherical HgTe QDs[25]. For aggregated HgTe, the charging current at positive and negative

potentials is quite reversible. The log of the conductance has a V-shape with potential over 5 orders of magnitude. This can be explained by the Nernst equation with the conductance being proportional to the number of carriers. Considering only two states, $1S_e$ and $1S_h$, each possibly occupied by two electrons, the conductance in the low doping regime is,

$G \sim \frac{2}{V_{nc}} \mu_e \exp\left[-\frac{eV-E_{1Se}}{k_B T}\right] + \frac{2}{V_{nc}} \mu_p \exp[+\frac{eV-E_{1Sh})}{k_B T}]$, where V is the applied potential, k_B is the Boltzmann constant, T is the temperature, μ_e and μ_p are electron and hole mobility, V_{nc} is the volume per nanocrystal. The log scale shows instead a Nernst slope of 42±2 mV/decade, consistent with the temperature of 203 K $\ln(10)\, k_B T/e$= 40 mV/decade. There are also no clear electrochemical features associated with filling of specific hole states for both HgTe QDs, likely because the hole states are much closer to one another due to the high hole mass.

The difference in doping between the four systems is apparent in **Figure 2-2**. The Fermi level of the films is directly determined by electrochemistry by simply measuring the rest potential of the films in the open circuit condition. As shown in **Fig. 2-2(A~D)**, the rest potential is similar for all four films, but the QD states positions vary strongly. For HgS, HgSe, and non-aggregated HgTe QD films, **Fig.2-2(A~C)** shows that the rest potential is more negative than some of the QD states films and therefore the films are n-doped. For the HgSe QDs of 6.8 nm, the Fermi level is in the $1P_e$ wave, and therefore $1S_e$ is filled while $1P_e$ is partially filled. For the HgS QDs of 5 nm and non-aggregated HgTe QDs of 9.6 nm, only $1S_e$ is partially filled.

For the aggregated HgTe CQD film, **Fig.2-2D** shows that the Fermi level is in the electrochemical gap but slightly towards the positive side rather than at the minimum of conductance. he aggregated HgTe film is therefore very weakly p-doped. In **Fig.2-2D**, the conductance at the rest potential is about 10^4 times smaller than at the maximum, and therefore the hole doping is of the

order of 10^{-4} per QD, which is consistent with the lack of evidence of doping in the linear absorption spectrum.

One interesting feature observed in non-aggregated HgTe spectroscopy is the splitting of the intraband (~1300 cm^{-1}) as showed in Fig.2-2G. This is due to the spin-orbital coupling which would be explained in the **Chapter 2.5.1** spectroelectrochemistry section.

2.3 Determination of the energy of the states

2.3.1 Electrochemistry charging energy correction

To determine the $1S_e$ and $1P_e$ states electrochemical potentials, we use the reducing charging current and fit the waves to Gaussians and assign the first peak to $1S_e$ and the second one to $1P_e$. To calculate N(V) from the data, we calculate the total charging charge after subtraction of the capacitive component and normalize to a value of N(V)=1 at the peak of the $1S_e$ state charging. This procedure works well as long as the $1S_e$ state wave is well defined, and it provides N(V) for the whole potential range in **Figure 2-3(A, B)**. The procedure is checked by looking at the second peak in the charging wave, which should be at the half filling of the $1P_e$ state, and it is indeed occurring around 5 electrons per dots, as shown in **Fig. 2-3(A, B)**.

Fig. 2-3(C, D) show the significant discrepancy between the $1S_e$-$1P_e$ energy difference determined by the peaks in the cyclic voltammetry and the $1S_e$-$1P_e$ optical transition energy. However, after correcting the optical data for the exciton binding energy and the electrochemical data for the charging energy, **Fig.2-3(C, D)** show that they match well for all measured sizes of HgS and HgSe QDs.

The charging energy correction increases linearly with charge and it therefore also contributes significantly to the broadening of the redox $1S_e$ and $1P_e$ waves. In **Fig.2-3A**, applying the correction for the charging energy of 5 nm HgS dots reduces the FWHM of the $1S_e$ charging peak from 0.142 eV to 0.078 eV which is closer to the expected Nernstian width of ~$3.8k_BT$ ~0.068 eV (peak $\propto \frac{1}{k_BT}\frac{e^{E/k_BT}}{(1+e^{E/k_BT})^2}$) . Similarly, the width of the 8.7 nm HgSe (**Fig.2-3B**) $1S_e$ charging peak also reduces from 0.131 eV to 0.108 eV. The width of the $1P_e$ charging peak, which is significantly larger than the $1S_e$ state, is also very significantly reduced after the correction due to the charging

energy, from 0.563 eV to 0.212 eV for the 5 nm HgS and from 0.478 eV to 0.188 eV for the 8.7 nm HgSe respectively.

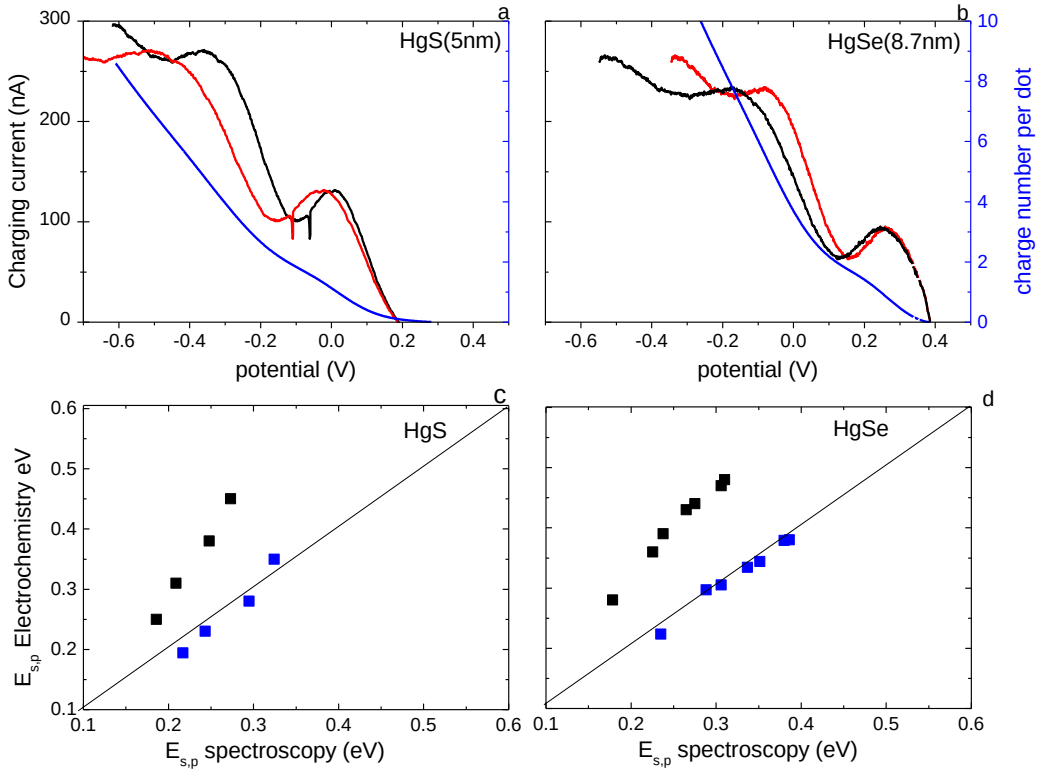

Figure 2-3: Electrochemistry charging energy correction (A, B) charging current as a function of potential before (black curve) and after (red curve) the charging energy correction for 5 nm HgS and 8.7 nm HgSe dots respectively and the number of electrons per dot obtained by integrated the charging current (blue curve).**(C, D)** The experimental value of the energy separation between $1S_e$ and $1P_e$ state determined by electrochemistry as a function of the optical transition energy (back dots), highlighting the significant differences. The electrochemically derived energy separation after the charging energy correction is also shown as a function of the optically derived energy separation after correction for the exciton binding energy (blue dots), bringing the two determinations in good agreement. The figure is adapted from reference 9.

We emphasize that the choices for ε and the simple charging energy of a metallic sphere are simplistic. In contrast to monolayer protected metal colloids in solution in a high electrolyte concentration[28], where the charging energy is well accounted for by the capacitance across the

monolayer and dominated by the Helmholtz layer on the ligand shell, the QDs studied here are in a complicated environment, as a film, surrounded by other QDs, with a thin ligand layer, and in a concentrated electrolyte. Injected charges are screened by the neighboring dots, ions on a portion of their surface as well as the diffuse layer. The charging energy in QD films is therefore difficult to model, including the effects of ions, ligands, particle, and void size, and film structure[29]. Nevertheless, the good agreement between the optical and electrochemical determination of $E_{S,P}$, after corrections for the exciton binding energy and the charging energy, gives some confidence in our procedure.

Other simple approximations could be favored. As one example, instead of the isolated metal sphere in a uniform dielectric constant, we could have chosen the isolated sphere capacitor as the model for the charging energy. The charging energy of a metallic sphere capacitor is $E_c = \frac{N(V)e^2 d}{4\pi\varepsilon\varepsilon_0 r(r+d)}$ where d is the dielectric layer. The bulky tetrabutylammonium ions (ionic radius ~ 0.45 nm), should minimize specific interaction with the dots, such that the Helmholtz layer is away from the surface by the ion radius. With the addition of the ethanedithiol ligand layer (flat dithiol estimated at ~ 0.2 nm), a distance of d ~ 0.65nm can be estimated for the dielectric thickness. A dielectric constant of ~ 2 is estimated based on alkanes. This distance is similar to the Debye length for the diffuse layer is $\lambda_D = \sqrt{\frac{\varepsilon_{PC}\varepsilon_0 k_B T}{2N_A e^2 I}} = 0.7nm$, where N_A is the Avogadro constant and I is the ionic strength of the electrolyte used in this work. With a 0.65nm Helmholtz layer thickness and a dielectric constant of 2 for the intermediate material, a metallic sphere capacitor would have a charging energy of 60mV per electron for a 2.5 nm radius QD. This is twice as large as the value used in the text and likely overestimates the charging energy because the surface available for the electrolyte is only a fraction of the QD surface. In the end, we justify our choice of the charging

energy by the quality of the agreement of two independent measures of energies, electrochemical and optical, in **Fig. 2-3**.

2.3.2 Determination of the energy of the states

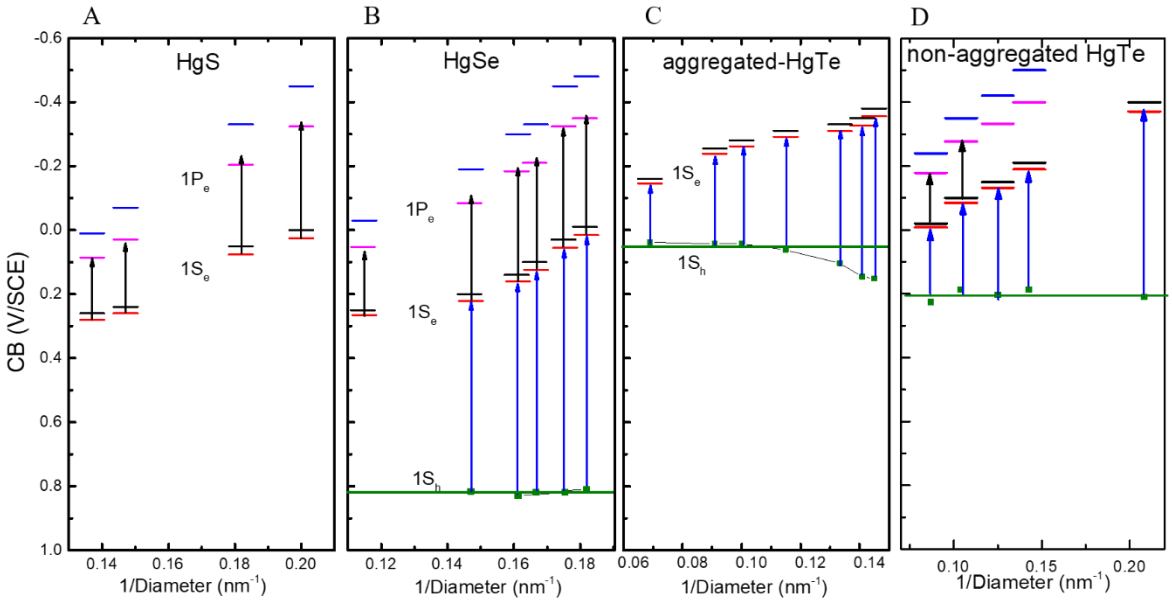

Figure 2-4. Electronic states (A-D) Positions of the electronic states measured by electrochemistry (black for $1S_e$, blue for $1P_e$) and after correction by the charging energy (red for $1S_e$ and pink for $1P_e$) as well as the intraband $1S_e$-$1P_e$ (length of black arrow) and interband $1S_h$-$1S_e$ (length of blue arrow) transition value measured by spectroscopy and corrected for the exciton binding energies. The first three plots are adapted from reference 9.

Figure 2-4 gives the value of the peak of the $1S_e$ reduction waves for HgS, HgSe, and HgTe QDs as a function of size. It is readily apparent that the $1S_e$ states of the HgSe QDs have the most positive potentials and are therefore the easiest to reduce, closely followed by HgS, with both being much more easily reduced than HgTe. In order to relate the reduction potential, E^{echem}, to the state energy, E, one needs to correct for the charging energy, E_c, where $E^{echem} = E + E_c$[20,29]. E_c arises from the polarization of the material created by the electron as well as the electrostatic interaction with other electrons. As discussed in **Chapter 2.3.1**, for E_c, we use the approximation of an isolated metallic sphere in a homogeneous medium with dielectric constant ε, $E_c = \frac{N(V)e^2}{4\pi\varepsilon\varepsilon_0 r}$,

where $N(V)$ is the number of doped electrons already in the sphere at a certain potential *V*. *N(V)*=1 for the first electron in $1S_e$, which is taken as the peak of the Gaussian fitting the $1S_e$ reduction wave. For the environment dielectric constant, we use $\varepsilon = 20$, motivated by the dielectric constant of the chalcogenides, $\varepsilon_{QD} \sim 20$ for HgS, HgSe and HgTe, and between the high dielectric constant of propylene carbonate (PC) $\varepsilon_{PC} = 64$ and the low dielectric constant of ~ 2 for the ligands. This value for ε gives a charging energy per electron in $1S_e$ of E_{c1Se} ~ 30meV for particles of 2.5 nm radius, scaling as $\frac{1}{r}$. The correction due to charging is therefore quite small for $1S_e$. **Fig.2-4** shows the corrected $1S_e$ energies for the four systems as a function of size.

In order to establish consistency between the optical and electrochemical measurements, we show the potential at the peak of the $1P_e$ current wave in **Fig.2-4**. Because this state is highly charged, N(V) =5 at half-filling, the $1P_e$ state energy after the charging energy correction is much more displaced upwards in **Fig.2-4**, As discussed in **Chapter 2.3.1**. This value of N(V) is verified by integrating the charging current and normalizing it to N(V)=1 at the $1S_e$ peak, giving indeed N(V)~ 5 at the $1P_e$ peak. This electrochemical determination of the $1S_e$-$1P_e$ energy difference after charging energy correction, $E_{S,P}$, can then be compared with the independently measured optical $1S_e$-$1P_e$ transition energy. It is also necessary to add to the optical transition energy the exciton binding energy in order to get the optically derived value of $E_{S,P}$. For the Coulomb interaction between a hole in $1S_e$ and an electron in $1P_e$, we use $-1.6 * \frac{e^2}{4\pi\varepsilon_{QD}\varepsilon_0 r}$ for the wave functions in an infinite spherical box.[24] The optically derived value of $E_{S,P}$ is indicated by the length of the black arrow pointing from $1S_e$ to $1P_e$ in **Fig.2-4**. There is a rather good agreement between the corrected electrochemical and optical data and this highlights the importance of the corrections. For HgTe and HgSe, **Fig. 2-4** also provides the measured $1S_e$-$1S_h$ interband transition energies.

The interband energy is corrected by $-1.8 * \frac{e^2}{4\pi\varepsilon_{QD}\varepsilon_0 r}$ to account for the $1S_e$-$1S_h$ exciton binding energy[30]. For n-doped QDs, the interband energy is measured after exposure of the solutions to S^{2-} which has been shown to partially un-dope the QDs[10,17]. Projecting from $1S_e$ gives an estimate of $1S_h$ which could not be determined from the electrochemical data. **Fig.2-4** shows again a rather good agreement between the electrochemically derived energy differences and the optical transitions. For both HgSe and HgTe, **Fig.2-4** shows a rather flat $1S_h$ state energy dependence, which is consistent with the massive hole band. Extrapolating the $1S_h$ energy at infinite size gives valence band positions at 0.05 V/SCE, 0.2 V/SCE and 0.82 V/SCE for aggregated HgTe, non-aggregated HgTe and HgSe, respectively. One could obviously see the reason for different doping of aggregated and non-aggregated HgTe is due to the about 0.15 eV shift of the band position.

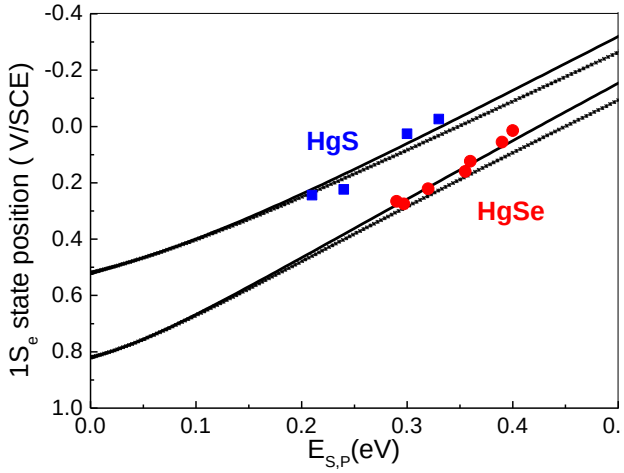

Figure 2-5: **Energy scale comparison between theory and experiment.** Confinement energy of the $1S_e$ state as a function of the energy difference between $1S_e$ and $1P_e$ calculated with the two-band $\boldsymbol{k} \cdot \boldsymbol{p}$ model for two different values for the Kane parameter E_p with 20eV (black line) and 9eV (black dashed line). The experimental $1S_e$ energy derived from electrochemistry and corrected for the charging energy is graphed as a function of $E_{S,\,P}$ obtained by spectroscopy corrected by removing the exciton binding energy. The only free parameter is the bottom of the conduction band, E_{cb} shown on the y-axis for zero $E_{S,\,P}$. The figure is adapted from reference 9.

We also use a simple two-band $\boldsymbol{k} \cdot \boldsymbol{p}$ model as an alternative means of extracting the bulk band position. For the conduction band dispersion as a function of the wave vector k, $\mathbf{k} \cdot \boldsymbol{p}$ gives $E =$

$\frac{1}{2}\left(\frac{\hbar^2k^2}{m_0} - E_g\right) + \sqrt{\frac{\hbar^2k^2}{2m_0}E_p + \frac{E_g^2}{4}}$. We use $k=\pi/R$ for $1S_e$ and $k=4.49/R$ for $1P_e$. For HgS QDs, we choose the energy gap E_g =0.65eV [17]. A previous reference[31] calculated a Kane parameter E_p of 9eV, which is much smaller than ~20eV typical of II-VI and III-V semiconductors[32,17]. The uncertainty on E_p leads to a poor determination of the band energy when trying to directly fit the $1S_e$ energy. However, the ratio of $E_{S,P}$ and $E_{S,cb}$ (energy separation between $1S_e$ state and bottom of the conduction band E_{cb}) is only weakly sensitive to E_p [10], as shown in **Fig.2-5**. Combining the optically derived $E_{S,P}$ and the $1S_e$ state position measured by the electrochemistry and corrected for the charging energy, we then obtain E_{cb} =0.52V±0.03V (SCE) for HgS as shown in **Fig.2-5**. For HgSe, we use E_g=-0.20eV [33] and obtain E_{cb} =0.82V±0.01V (SCE) as shown in **Fig.2-5**, with the errors determined from the fits. This is rather consistent with the position of E_{1Sh} previously evaluated in **Fig.2-4**, as expected for this zero-gap material.

2.3.3 The absolute bulk band positions for Hg (S, Se, Te)

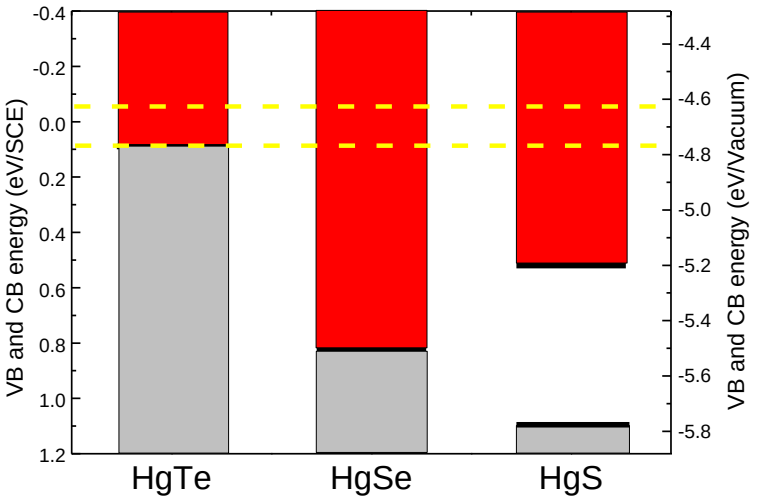

Figure 2-6: The absolute bulk band positions for Hg (S, Se, Te). Energies of the valence band (gray volume) and conduction band (red volume) for aggregated HgTe, HgSe and HgS. The yellow dashed line shows the range of the Fermi level measured by electrochemistry in the experimental conditions described in the text. The figure is adapted from reference 9.

Overall, using E_{SCE}= -4.68±0.02eV /vacuum[34], **Fig.2-6** proposes the experimental values for the absolute bulk band positions for the three mercury chalcogenides (aggregated HgTe value used in the figure). It shows that HgTe/HgSe is strongly Type II, while HgSe/HgS is type I.

The valence band is at E_{vb} = -5.85eV, -5.50eV and -4.77eV for HgS, HgSe and aggregated HgTe, respectively, with an estimated accuracy of ±0.05V. The energies of the valence bands increase in the order S, Se, Te, and this follows the trend of the anion p-orbital energies[35]. The measurements place HgSe 0.35 eV higher than HgS, and aggregated HgTe 1.08 eV higher than HgS. Calculations by Wei and Zunger place HgSe 0.23 eV higher than HgS, and HgTe 0.69 eV higher than HgS[35]. The discrepancies are larger than the experimental error bars and this may reflect surface effects. The valence band of HgTe is calculated to be 0.36 eV higher than CdTe[35] and HgTe/CdTe heterostructures are known to be type I. Our value for aggregated HgTe (-4.77eV) may then be consistent with the value for CdTe (-5.0eV) determined spectro-electrochemically with diamine ligands[36]. However, photoemission measurements in air give the -4.74 eV for CdTe with thiol ligands[20]. The differences may highlight effects of environment and ligands. Therefore, we emphasize that the values reported here are for the specific experimental conditions, after the EdT/HCl/IPA treatment and in the PC electrolyte.

Fig.2-6 also shows that HgS and HgSe have quite oxidizing valence bands and this is in accord with the absence of p-type conductivity, given the oxidation decomposition potential discussed earlier.

2.3.4 Fermi level of the QDs films

It was previously proposed[7,12] that the self-doping of HgS and HgSe QDs doping arises from the relative position of the Fermi level of the environment and the nanocrystal states, similar to a gating effect. However, it may be argued that, as in bulk materials, the doping must be an effect of chemical composition, the result of aliovalent dopants or a stoichiometry imbalance[37]. Such doping mechanism is observed for nanocrystals such as in Cu_xS_{2-2x} [38] and Al:ZnO [39]. The two situations are distinguishable by electrochemistry. In the case of gating, the charging current is minimal and it only transfers charges in the QD states. In the case of chemical doping, the current must be large since it must also neutralize all donors or acceptors.

Fig.2-2 shows that the rest potential is similar (within ~ 0.05 V), for all three mercury chalcogenide QD films in the same electrolyte and after the same EdT/HCl/IPA treatment. Both the QD films and clean Pt or Au electrode show a similar rest potential which indicates that the rest potential is set by the solution. Adding equimolar ferrocenium tetrafluoroborate and ferrocene changes the rest potential to the Ferrocenium/Ferrocene redox potential at ~+0.3V/SCE, as expected. The rest potential was the same in different electrolytes ($LiClO_4$/PC, $LiClO_4$/Formamide, TBAP/Formamide, Tetrabutylammonium Chloride/ Formamide). The fact that different salts do not affect the rest potential indicates that the rest potential is set by a common impurity in the salts or the solvents, which is most likely water. The cyclic voltammetry in **Fig.2-2** also indicates that there is very little charging current besides the one necessary to charge the dots. The impedance around the rest potential, measured by summing forward and backward charging currents and dividing by the voltage, is also large, ~ 10 MΩ. Therefore, there is no evidence for significant redox reaction around the Fermi level, which confirms that the Fermi level of the as-prepared QD films in **Fig.2-2**, is set by the environment[10].

Chemical doping can however arise from a high density of redox active surface sites, typically called traps, on the QD such that the Fermi level is at equilibrium with the dominant surface redox reaction. We tested this by measuring the rest potential as a function of Cl^- for an aqueous electrolyte at room temperature. We found that the rest potential is not affected at low Cl^- concentration, as expected from the previous results since the addition of KCl, does not affect the Fermi level of aqueous solutions. However, at concentrations above 10^{-2} M, the rest potential starts to follow the Nernst equation with 30mV/decade. This is consistent with $Hg^{(0)}/Hg_2Cl_2$ now setting the Fermi level. Cyclic voltammetry around the rest potential at high Cl^- concentrations shows a strong Faradaic current corresponding to a low impedance of ~100 kΩ as shown in **Figure 2-7**. Thus, when the CQDs films are exposed to a high aqueous Cl^- concentration, there is a chemical modification of the dot surface with an equilibrium between $Hg^{(0)}$ and insoluble surface mercury chlorides which then sets the rest potential.

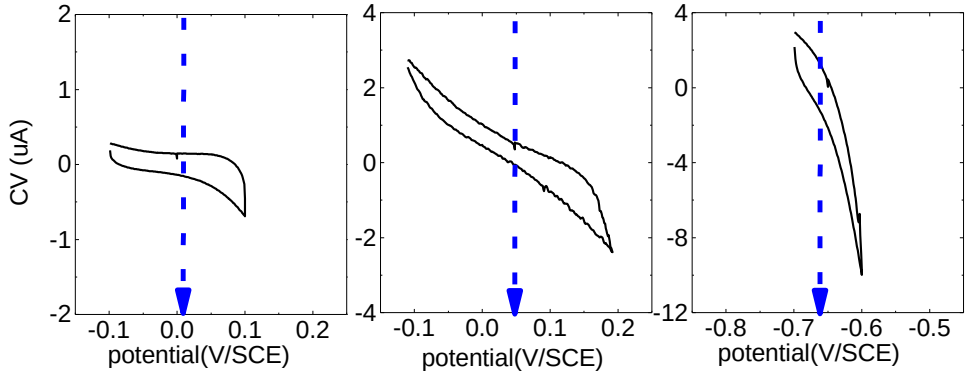

Figure 2-7: Faradaic current around Fermi level for the aggregated HgTe film in different electrolyte. Faradaic current of HgTe film in 0.1M TBAP/PC, 1M KCl/H_2O and 0.5M Na_2S/ H_2O, respectively. Blue arrows show the Fermi level. The impedance at the rest potentials are 10 MΩ, 100 kΩ and 5 kΩ, respectively. The figure is adapted from reference 9.

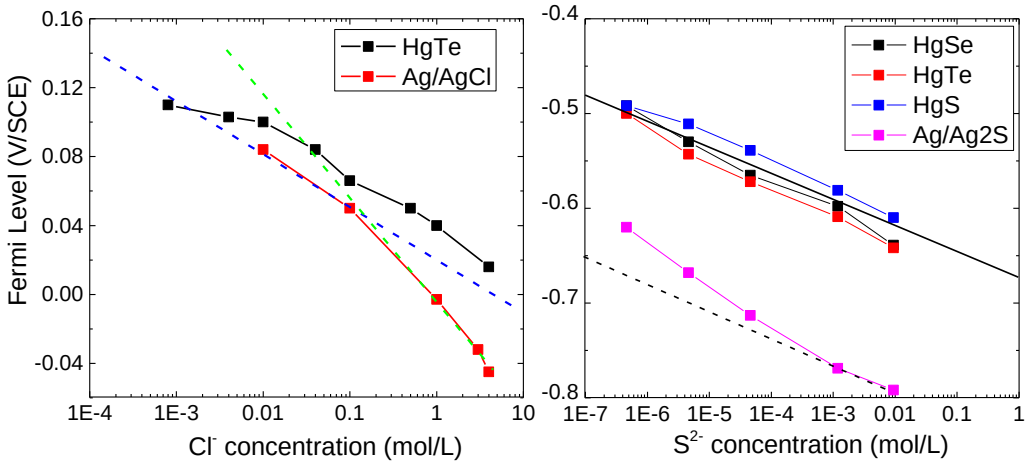

Figure 2-8: Fermi level of QDs in the presence of Cl^- and S^{2-} . (A) Fermi level of aggregated HgTe CQD film (Black square) and Ag/AgCl electrodes (red square) as a function of Cl^- concentration, in an aqueous electrolyte. The blue and green dashed lines are Nernst values for Hg_2Cl_2/Hg and AgCl/Ag[40] electrodes at room temperature respectively. **(B)**Fermi level of HgSe (black), aggregated HgTe(red) and HgS (blue) QD film and Ag_2S/Ag electrode dependence on S^{2-} concentration in electrolyte. Solid black lines and dashed black lines are the Nernst values for HgS/Hg and Ag_2S/Ag[40,41] electrodes at room temperature respectively. The figure is adapted from reference 9.

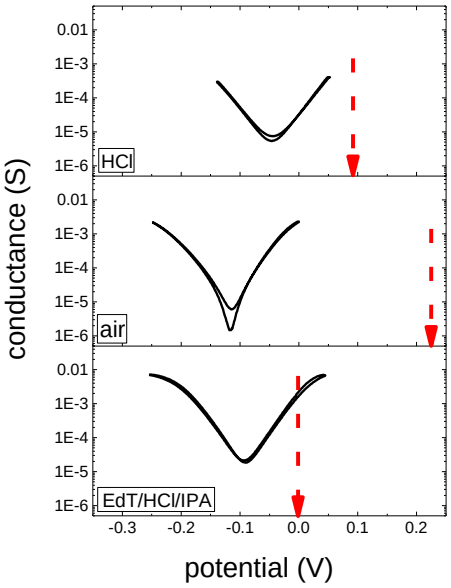

Figure 2-9. Fermi level shift in the aggregated HgTe band. Fermi level (red arrow) shift in electrochemistry with different treatment like EdT/HCl/IPA, the film exposed to air 12hrs and adding HCl after being exposed to air. The figure is adapted from reference 9.

A similar effect is observed in high concentration of S^{2-}, also in aqueous solutions at room temperature. This is done in a glovebox under nitrogen to avoid oxidation of the sulfide. The rest potentials start around 0.1V/SCE at low S^{2-} concentration and for all HgTe, HgSe and HgS QD

films the rest potential decreases with the slope ~ 30mV per decade as showed in **Figure 2-8** as expected for Hg/HgS. The extrapolation to 1M [S^{2-}] is also similar to the reported standard potential for Hg/HgS of -0.672V/SCE[42]. The cyclic voltammetry shows a strong Faradaic current corresponding to a very low impedance of a few kΩ. Therefore, under high sulfide concentration, there is a chemical modification of the dot surface with an equilibrium between $Hg^{(0)}$ and insoluble surface mercury sulfides which sets the rest potential.

A third and practical example of chemical doping is the formation of Hg/HgO after prolonged exposure to air. Films of HgTe QDs in air for a day or longer show gradual increases in the dark conductivity, by several orders of magnitude for small size QDs. Electrochemistry shows that this is accompanied by a positive shift of the rest potential to ~ 0.25V/SCE, as showed in **Figure 2-9**, close to the Hg/HgO redox potential of +0.28V/SCE at pH7 [42]. By scanning the electrochemical potential, we verified a smaller negative shift of the QD states, which shows that the QDs become strongly p-doped after air exposure. Low dark conductivity and mid-gap rest-potential can be partially recovered upon reducing potential under inert (N_2) conditions. Partial recovery is also observed after exposure to the EdT/HCl/IPA solution which dissolves the oxide.

2.3.5 Effect of surface treatment on the doping level

Controlling doping in QDs is of great importance. Prior work[10,17] showed that treating HgSe and HgS QDs solution with S^{2-} could decrease n-doping while Hg^{2+} or Cd^{2+} would increase n-doping. It was suggested, but not verified, that this arises because surface modification shifts the energy of

the QDs with respect to the environment Fermi level. A wider range of chemicals has also been shown to tune the doping level[15]. The effect was also observed in films but to a lesser extent, and it was seen by shifts of the redox potentials[10] as well as variations of the intensity of the intraband transition. **Figure 2-10** show directly that the $1S_e$ state of HgSe QDs shifts negative by ~ 0.1-0.2V when films have been dipped into dilute $(NH_4)_2S$ (dissolved in methanol), followed by rinsing with IPA. The rest potential changes little, being still determined by the environment. From the position of the rest potential and $1S_e$ state, we determine that the S^{2-} treatment changes the $1S_e$ doping from ~ 1 e^- to ~ 0 for 5.7 nm HgSe dots, and from 3 e^- to 2 e^- for 8.7 nm HgSe dots. Dipping the films into a cadmium acetate solution moves the $1S_e$ state back in the positive direction, such that one recovers a good fraction of the starting doping level. This is consistent with spectroscopic observation that the strength of the intraband transition decreases by 70% for 5.7nm HgS film after S^{2-} un-doping and recovers strongly after Cd^{2+} exposure.

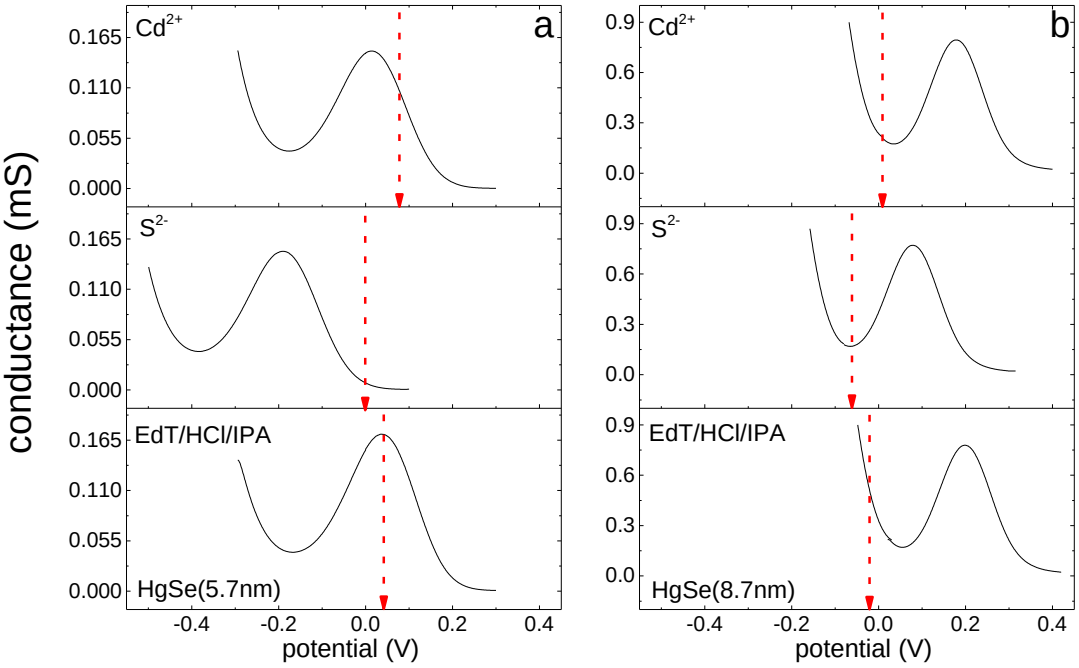

Figure 2-10. band shift with surface treatment on HgSe QDs. (A, B) Conductance and rest potential of films of two sizes of HgSe CQDs with different treatments, sequential from bottom to top. The figure is adapted from reference 9.

We note that the optical measurements are performed dry under nitrogen such that the doping level is likely not the same as in solution. The effects of exposure to S^{2-} and Cd^{2+} have been previously assigned to adsorption of these ions and the dipoles or double layer polarization to counter-ions, and we support this explanation. Similar effects were also reported with CdSe QDs[43]. The zeta potential measurements in non-polar solvents can also report on the relative doping but not the absolute values, as showed in the **Figure 2-11**. Since the Debye length is large in non-polar solvent, we use the Hückel relation for electrophoretic mobility μ_e and zeta potential, $\zeta = \frac{\eta}{\varepsilon_r \varepsilon_0}\mu_e$, where ε_r is the dielectric constant of the dispersion medium (6.4 for BZC at 20 ºC.) and η is dynamic viscosity of the dispersion medium ($1.36*10^{-3}$ Pa·s for BZC at 20 ºC). Considering *N* elementary charges per dot, the electrophoretic mobility is $\mu_e = \frac{Ne}{6\pi\eta a}$ [44] where a is the hydrodynamic radius of the particle. The zeta potential is then proportional to the charge per dot, $\zeta = \frac{Ne}{6\pi\varepsilon_r\varepsilon_0 a}$ when ζ is less than 100mV ~ $4k_BT$ [44]. As shown in **Fig.2-11**, the 8.7 nm HgSe dots in BZC have a distribution of zeta potential centered at -49mV. This is close to the value expected for 2 electrons per dot using the measured 10.5-nm-hydrodynamic diameter. After sulfide-treatment, ζ ~-25mV which is consistent with N=1. Subsequent mercury-treatment gives a distribution of up to four zeta potentials -78mV (N=3), -50mV (N=2), -25mV (N=1) and 0mV(N=0). Over time, this evolves to a single peak at -51mV (N=2). These results follow qualitatively the trend of the electrochemical and optical determination of doping level of the films.

However, we found that HgTe QDs also show negative zeta potentials, therefore uncorrelated with their un-doped character. Non-zero zeta potentials have been observed previously for un-doped QDs[45], because the zeta potential rather reflects the relative electron affinity of the solvent and

solute. Therefore, we propose that the changes of zeta potential in non-polar solvents can report on the relative doping but not the absolute values. We note that the negative charge of the three types of QDs in BZC allows efficient deposition of films on the positive electrode when a dc voltage is applied, as previously demonstrated with other QDs[46].

As previously recognized, the sensitivity of the doping to the surface treatment is an opportunity for future uses of the materials[10,13,15-17].

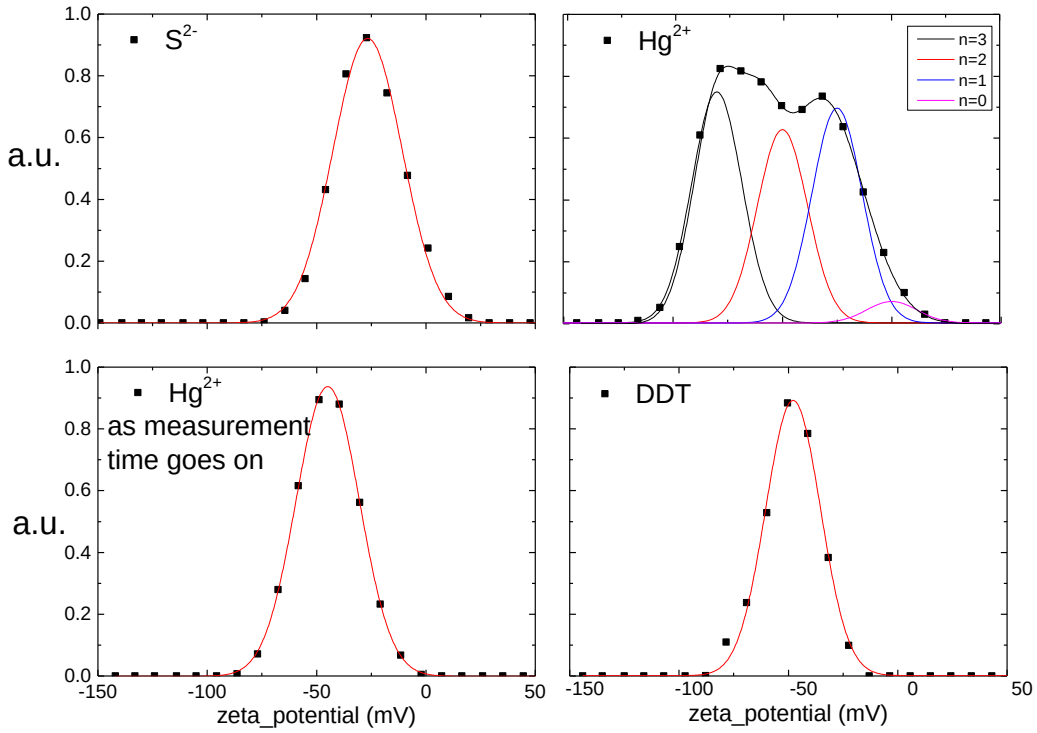

Figure 2-11. Zeta potential of HgSe. Zeta potential of 8.7nm HgSe with different surface treatment. The measured hydrodynamic diameter is ~10.5nm with 1.8nm standard deviation. The figure is adapted from reference 9.

2.4 Electrical Mobility

The electrical mobility is an important parameter in the discussion of materials for photodetectors. Using a bipotentiostat, we extract the mobility. The mobility is given by $\mu = \sigma/ne$, where σ is the conductivity, n is the carrier density and e is the elementary charge. n is directly measured from the charging current after subtracting the double layer charging current, as described in the method. For the interdigitated electrodes of spacing d=5μm and finger width d_0=10μm, we calculate the mobility as $\mu = \frac{G(d+d_0)d}{\int_{t=0}^{t(V)} idt}$. [22] The differential mobility is $\mu^d = \frac{d\sigma}{dn}\frac{1}{e} = \frac{dG}{dV}(d+d_0)d/\frac{d(\int_{t=0}^{t(V)} idt)}{dV}$ where G is the measured conductance, V is the potential. **Figure 2-12** shows the differential mobility of mercury chalcogenide QD films at different potential. The differential mobility typically starts in the noise. It reaches a maximum on the rising edge of the $1S_e$ state filling, becomes zero at the peak of the charging wave, and turns negative as the conductance decreases with further charge injection. For HgSe and HgSe, this pattern repeats for the $1P_e$ state. For HgTe, the electron and hole mobilities are similar.

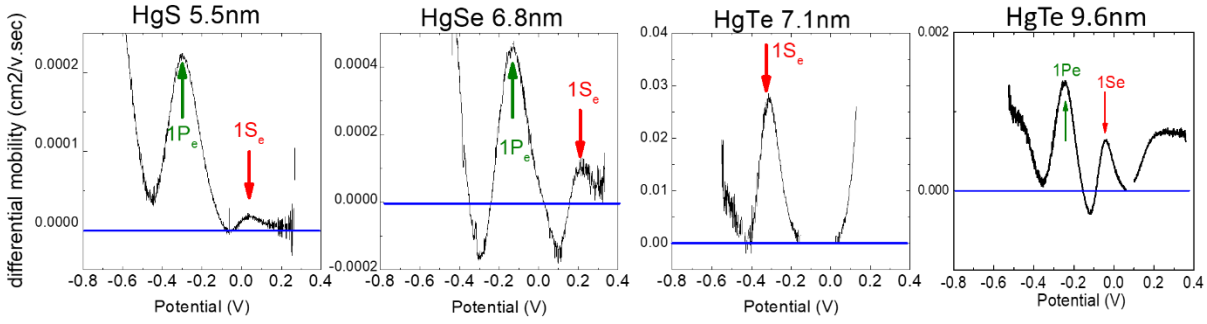

Figure 2-12. Differential mobility. Differential mobility of HgS (5.5 nm), HgSe (6.8 nm), aggregated HgTe (7.1 nm) and non-aggregated HgTe (9.6 nm), respectively. The first maximum of the differential mobility associated with the $1S_e$ states is indicated by a vertical arrow and it appears around 0.5 e^- per dot. HgS and HgSe QD films have similar mobility while the mobility of the aggregated HgTe QDs film is 2 orders larger. The first three plots are adapted from reference 9.

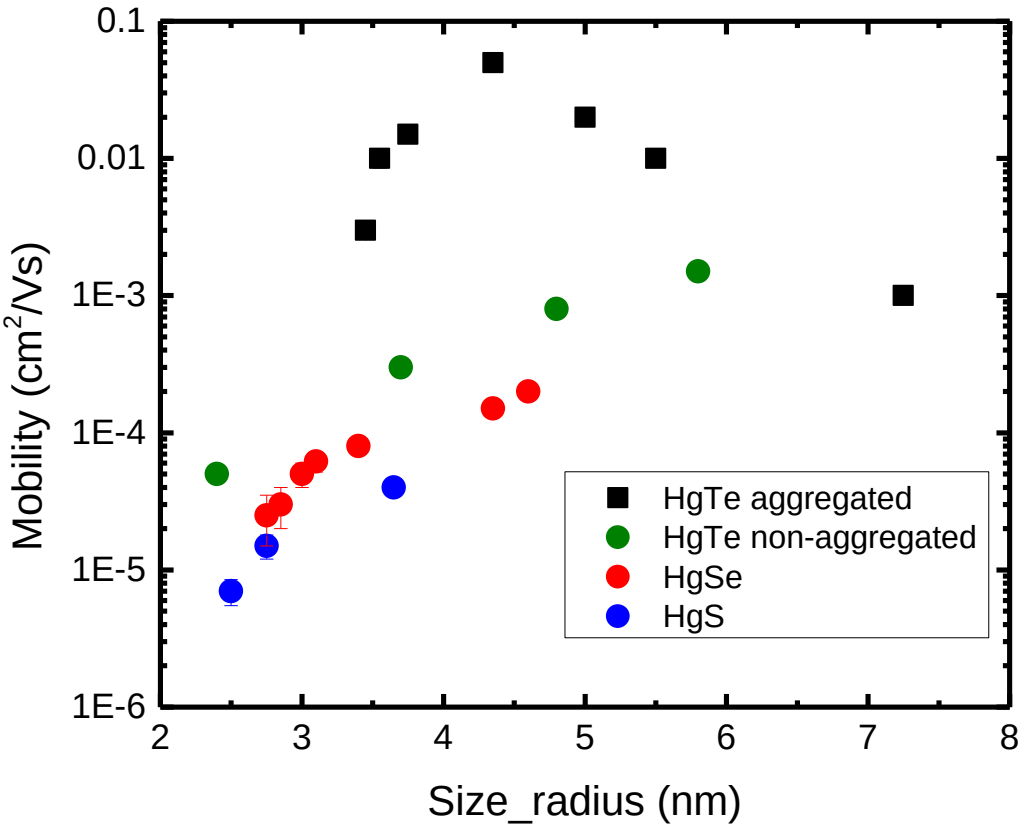

Figure 2-13. Size dependent mobility of mercury chalcogenide QDs. Size dependent differential mobility maximum, measured on the rising edge of the 1Se state filling, for aggregated HgTe (black square), non-aggregated HgTe (green dot), HgSe (blue dot) and HgS (red dot). Partof the figure is adapted from reference 9.

Figure 2-13 shows the size dependent mobility for the three materials. The results for aggregated HgTe and HgSe are consistent with prior reports[27,10], but with a much more extensive range of sizes. The most striking effect is the roughly two orders of magnitude higher mobility of aggregated HgTe QD films compared to non-aggregated HgTe, HgSe and HgS. The electron mobility of the aggregated HgTe films is not monotonous with particle size, with a fortuitous

optimum for dots in the 2-5 μm band gap range with the best photodetector performance so far. We think that this mostly reflects a beneficial role of aggregation, as reported previously in the experiments on mid-IR HgTe QDs detectors[3,4]. As shown in **Fig.2-2(I-L),** the aggregation of the HgTe QDs is seen in TEM images of films made from dilute suspensions, while similar concentration of HgS, HgSe and non-aggregated HgTe shows well-separated dots. In solutions, dynamic light scattering measurements show that the aggregated HgTe QDs form clusters varying from 20nm to 100 nm depending on dots size, while the others show individual particles. We note that future efforts to improve HgTe QDs photodetectors will naturally aim for non-aggregated HgTe QDs but with negative effects on mobilities as discussed in the **Chapter 6**.

The second significant observation is that, for all separated Hg (S, Se, Te) QD films, the mobility increases with increasing size. The mobility for QD solids has been reported to be decreasing[47] or increasing with increasing sizes[48,49]. Assuming a hopping mechanism, which is consistent with the low mobility observed here, the mobility is given by $\mu = ed^2/(6\tau_{hop} k_B T)$, where d is the interdot center to center separation ~ diameter, and τ_{hop} is the hopping time[50]. The measured mobilities for separated Hg (S, Se, Te) QDs increase more strongly than d^2, suggesting that the hopping time shortens for larger particles. The hopping time is itself the inverse of the electron transfer rate, affected exponentially by several factors. Even for fixed interdot distance, there are competing factors. The barrier height should decrease for smaller particles, and this was given as the primary reason why a reverse size dependence was observed for PbS nanoparticles[47,19]. On the other hand, the energetic disorder and the charging energy, which both contribute to the hoping activation energy decreases at larger size[50]. With the higher conduction band for HgS determined earlier, the barrier height should be larger for HgS CDs than for HgSe QDs. This would lead to a higher

mobility for HgS than HgSe, while the opposite is observed. This suggests that the barrier height is not a dominant effect and that the main effect could be the activation energy. We tested this conjecture by comparing the mobility of HgSe dots with similar average radius but different size dispersion. The mobility of 9.0nm$\pm$2.1nm HgSe sample (size dispersion~23% and FWHM of $1S_e$ ~0.17eV) is $5*10^{-6}$ cm^2/Vs while the 9.2$\pm$0.09nm sample (size dispersion~ 10% and FWHM of $1S_e$ ~0.07eV) is $2*10^{-4}$ cm^2/Vs. This result agrees qualitatively with the simulations by Xu *et al* on the effect of size polydispersity on electron mobility[51]. Comparing HgSe and HgS QDs the lower mobility with HgS QDs may then be a reflection of their wider size dispersion. In these systems, we therefore propose that the activation energy dominates the mobility trend, which explains the increase of the mobility with increasing sizes. More detailed discussion on size polydispersity effect on mobility would be discussed in **Chapter 4**.

We note that the discussion above assumes a hopping model. Shabaev *et al* proposed an alternate model[52] based on the opposite starting point of ballistic charge motion with increased scattering induced by disorder. Measurements of the temperature dependent mobility will provide additional information to test models. We would show temperature dependent mobility measurement in the later chapters.

2.5 Spectroelectrochemistry

2.5.1 HgTe system

Fig.2-2G shows that there is a splitting in the intraband of separated HgTe QDs, due to the degenerate of $1P_e$ state caused by the spin-orbital coupling. To understand the observed splitting of the $1P_e$ state in HgTe QDs, the intraband absorbance using a well-established tight-binding model has been modeled by our collaborators, Christophe Delerue and Guy Allan[25,53]. As shown in **Figure 2-14**, for highly symmetric particle shapes, spheres (**Fig. 2-14a**) and octahedra (**Fig. 2-14b**), the intraband absorbance is split into two peaks due to spin-orbit coupling. The effect of lower symmetry confinement potentials accounts for the additional splitting of the higher energy peak. For asymmetric particle shapes, oblate ellipsoids (**Fig. 2-14c**) and truncated cubes (**Fig. 2-14d**) with unequal truncations.

To experimentally see this detailed state structure, spectroelectrochemistry is used. By using spectroelectrochemistry, we can observe changes in the absorbance of a QD sample at a range of controlled doping densities[19,27,54,55]. In this technique, the absorbance of a QD film is measured under a series of potentials applied in an electrochemical cell. Thus, we can manipulate the Fermi level of a QD film and observe the intraband absorbance and excitonic bleach across a range of doping levels.

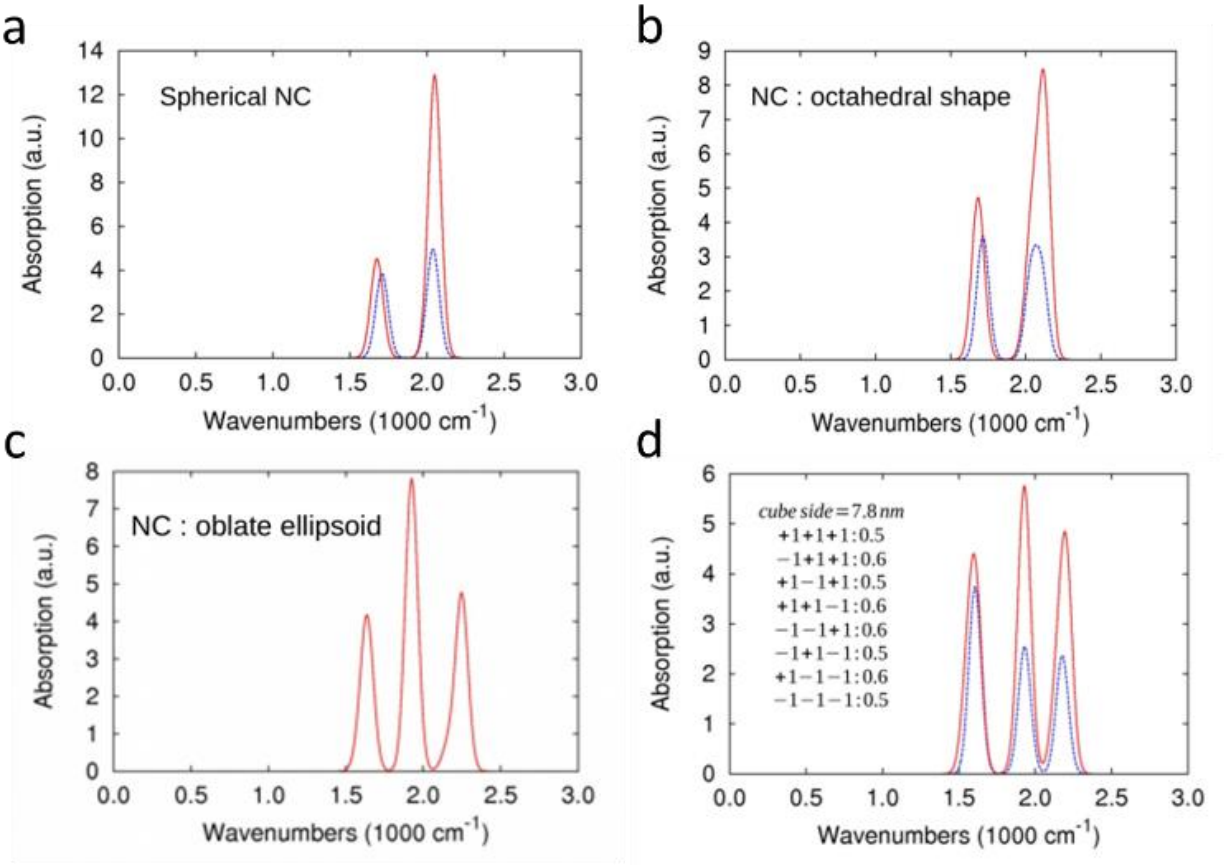

Figure 2-14. $1P_e$ state splitting based on tight-binding model. This figure shows predicted intraband peaks for different shapes of HgTe QDs with the same volume. (a) sphere and (b) octahedron, exhibit two peaks while structures with lower symmetry, (c) oblate ellipsoid and (d) unevenly truncated cube, exhibit three peaks. $1S_e$ state half filled (blue), $1S_e$ state fully filled (red). The figure is adapted from reference 12.

A batch of small HgTe QDs (~ 6 nm in diameter) are used, such that the intraband absorbance fell in the transparency window of the solvent (propylene carbonate, PC) and electrolyte (tetrabutylammonium perchlorate, TBAP). A film was prepared by drop-casting a concentrated QD solution onto a glass substrate with interdigitated gold electrodes. To make the sample sufficiently conductive, the QDs were cross-linked with ethanedithiol through an on-film ligand exchange.[20] The resulting QD film was placed in a cell with electrolyte solution (PC/TBAP) and pressed against a KBr window to minimize solvent absorbance. A bias was applied to the film

using a bipotentiostat with electrochemical potentials monitored with a Ag/AgCl wire pseudoreference. This cell was placed in an FTIR spectrometer, and the absorbance of the film was measured in reflectance mode across a series of applied biases. The spectrum of the intrinsic HgTe QD film at 0 V was taken as a background, and the change in absorbance at a given bias was measured (**Figure 2-15**).

Several features change in the absorbance of the HgTe QDs under negative bias. In the interband region of the spectrum, two bleach features appear which correspond closely to the position of the first two excitonic features in the absorbance spectrum of the as-synthesized QDs (**Fig.2-15c**). Additionally, an induced absorbance appears below the first excitonic bleach. At lower energies, we see an induced absorbance with three closely-spaced peaks that matches the intraband absorbance seen in chemically doped QDs. The peak spacing and relative oscillator strength of the three peaks do not change with increasing bias. This suggests that under our experimental conditions we only observe the effects of doping up to two electrons per QD because additional intraband absorbance features should emerge at high bias upon doping of the $1P_e$ level[27]. This further confirms that the three intraband transitions observed in HgTe QDs occur from the first conduction band state ($1S_e$) to a series of closely-spaced excited states. Moreover, the consistent intraband lineshape across the applied bias indicates that electron-electron interactions in QDs doped with two electrons do not have a significant effect on the state energies or transition probability.

As the bias becomes more negative and the electron doping increases, the magnitude of the excitonic bleach and intraband absorbance increases and then plateaus when the $1S_e$ state is filled

with two electrons. The change in absorbance as a function of bias can be modeled to determine the QD band positions. When the Fermi level is aligned with the $1S_e$ state, the state has a 50% probability of being filled with electrons according to Fermi-Dirac statistics. Assuming that the induced absorbance or bleach is directly proportional to the electron occupation, the point at which the Fermi level aligns with the state should be at the midpoint of intensity increase for the peak in question. Here, the midpoint for each of the observed transitions is approximately -0.4 V, and the point at which the absorbance plateaus, corresponding to full occupation of the $1S_e$ state, is between -0.6 V (**Fig. 2-15d**) and -0.65 V (**Fig. 2-15e**). Using cyclic voltammetry, we confirmed that the $1S_e$ state contains one electron at approximately -0.4 V and two electrons at approximately -0.65 V.

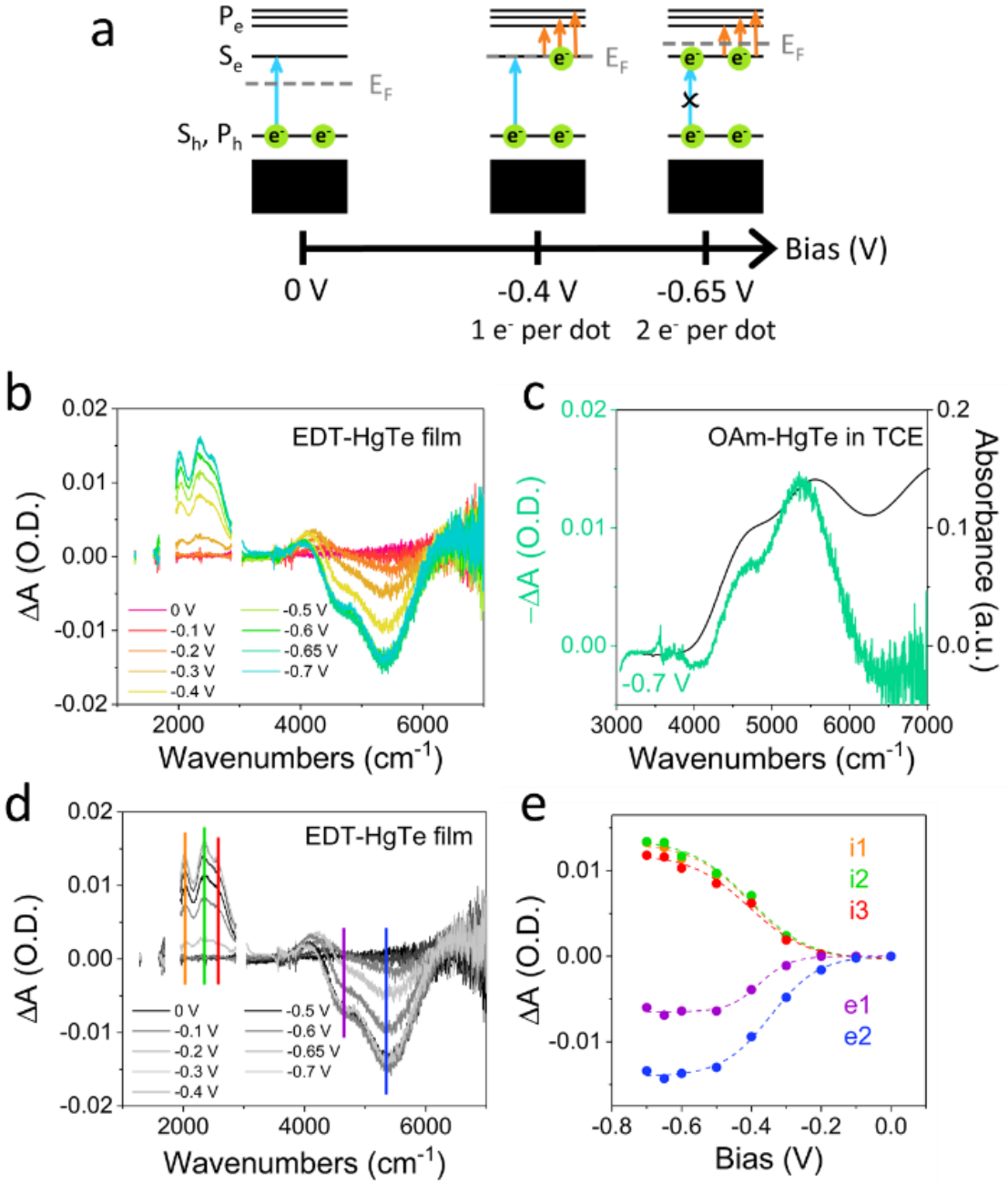

Figure 2-15. 6 nm HgTe QDs spectroelectrochemistry. (a) Illustration of the change in the Fermi level (E_F) with applied negative bias and its effect on interband absorbance (blue arrow) and intraband absorbance (orange arrows) of a QD film. **(b)** Difference spectra for a film of EDT-crosslinked HgTe QDs under a series of biases. As a negative bias is applied, an intraband absorbance appears and the first two excitonic features are bleached. **(c)** The bleach in spectroelectrochemistry matches the energy of the first two excitonic features in a solution absorbance measurement of the as-synthesized HgTe QDs. **(e)** The change in absorbance for 3 intraband transitions (i1-i3) and two excitonic bleaches (e1, e2) as a function of applied bias and their corresponding sigmoidal fits, with the position of each transition marked in **(d)** with the corresponding color. The figure is adapted from reference 12.

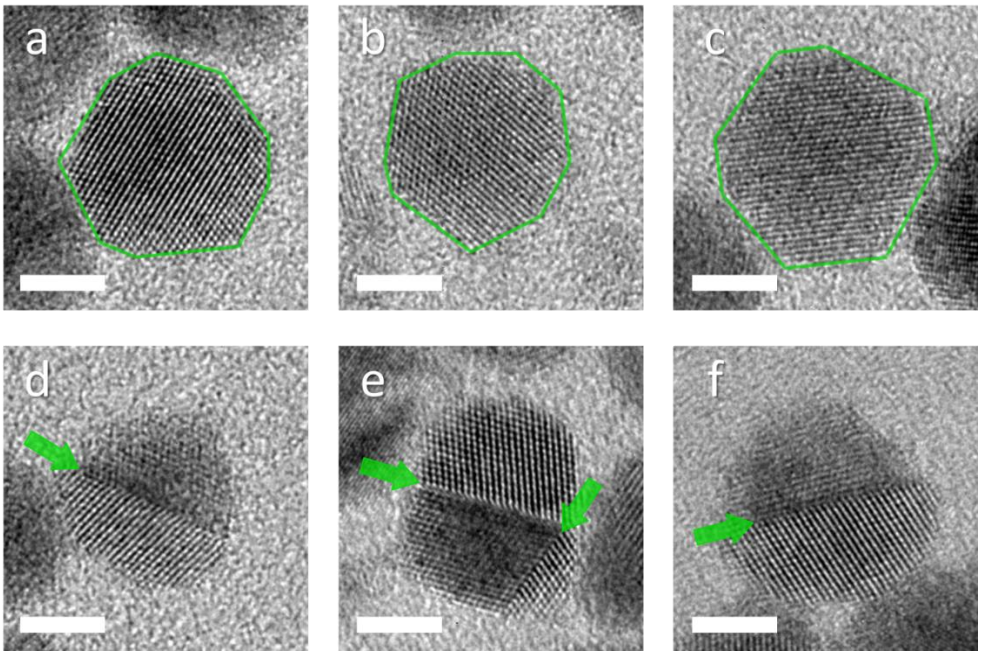

Figure 2-16. High resolution TEM images of HgTe QDs. **(a-c)** Green outline indicates edges, highlighting non-uniform shapes. **(d-e)** Green arrows indicate plane defects. (All scale bars: 5 nm) The figure is adapted from reference 12.

The prediction of the intraband absorbance splitting into three peaks closely mimics experimental results. Thus, the $1P_e$ level is split primarily by strong spin-orbit coupling and additionally split by asymmetry that breaks the degeneracy of the x, y, and z axes. Based on close examination of high resolution TEM images performed by our collaborator Dr. Margaret H Hudson, HgTe QDs are reasonably modeled as a low-symmetry near-sphere like a truncated cube (**Figure 2-16**). The TEM images also reveal planar defects which could account for the reduction of symmetry in the confinement potential.

2.5.2 HgSe system

Since the splitting in the HgTe QD $1P_e$ is caused primarily by strong spin-orbit coupling, one could predict HgSe QD would have the similar splitting but much smaller energy difference due to the Se lighter than Te.

We again use the spectroelectrochemistry to explore the detailed band structure of HgSe QD. HgSe QD (~6nm in diameter) solid was prepared on Au interdigitated electrodes (IDE), and cross-linked with a 2%(v/v) solution of EDT//IPA, then rinsed with IPA. The IDE is on glass with spacing d = 20μm and finger width d_0 = 10 μm. The spectroelectrochemical cell is assembled and filled with 0.1M anhydrous tetrabutylammonium perchlorate/ propylene carbonate in glovebox. The sample electrode is pressed lightly against the KBr window of the cell to minimize the infrared absorption from the electrolyte. Then the cell is put in the Fourier transform infrared spectrometer (Thermo Nicolet iS50 Advanced FTIR with near-, far-, and mid-IR). Spectra are measured in reflectance. We first characterize the cyclic voltammetry and the film conductance by a bi-potentiostat. Then, we set the potential at the conductance dip where the doping is ~2e/dot in the HgSe QDs ($1S_e$ state fully filled). This spectrum is taken as the background.

One could see multi features in the absorption spectra (**Figure 2-17**) with electrochemical gating. With positive potentials (remove electrons in the conduction band) as showed in **Fig.2-17a**, there is one bleached feature ~2600 cm^{-1} from $1S_e$-$1P_e$ transition and an induced feature ~6000 cm^{-1} from $1S_h$-$1S_e$ transition. The obvious asymmetry of the bleached feature ~2600 cm^{-1} at small positive potential, indicate the detailed energy structure in the $1P_e$ state. I assign this to the spin-orbital splitting causing an energy difference of ~500 cm^{-1} between $1P_e^{1/2}$ and $1P_e^{3/2}$ as shown in **Fig.2-17c**. The induced absorption feature in spectra~6000 cm^{-1} also shows multi-peaks. This

could be explained by the heavy hole and light hole energy difference ~0.275 eV at 0 K in the valance band of HgSe bulk material. At room temperature, the gap should naturally be smaller. Here, we find the difference between $1S_h^H$ and $1S_h^L$ is ~0.15 eV.

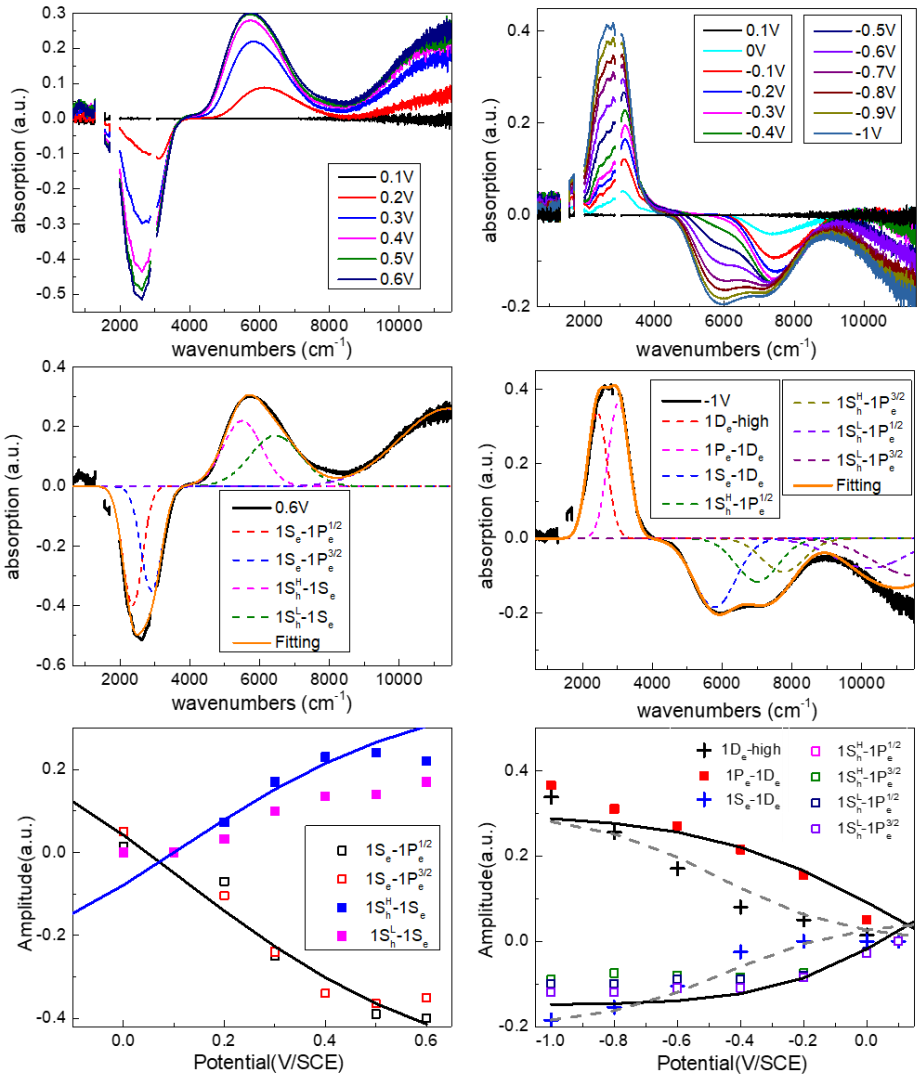

Figure 2-17. Spectroelectrochemistry of 6 nm HgSe. The background spectrum is measured at the potential at the conductance dip (0.1V) where the doping ~2e/dot in the HgSe QDs ($1S_e$ state fully filled). (a) & (b) relative absorption spectra at different potential. (c) & (d) Multi-Gaussian fit of selected spectra at +0.6 V and -1V, respectively. (e) & (f) Amplitude of the Gaussians associated with each transition versus the potential applied. The lines are Nernst functions $\frac{1}{1+\exp[(E-E_0)/\Delta E]}$ guides to the eyes.

The spectra are more complex with more negative potential, inducing more electron to the conduction band, as shown in **Fig.2-17b**. The first bleached feature ~7500 cm^{-1} saturated around -0.4 V where the 1Pe state is almost fully filled which is informed by the conductance curve. This feature includes the $1S_h^H$ to $1P_e^{1/2}$ and $1P_e^{3/2}$ transition. The $1S_h^L$ to $1P_e^{1/2}$ and $1P_e^{3/2}$ transition also appeared at the same time in the bluer range. The second bleached feature ~5800 cm^{-1} appeared with more negative potential while $1D_e$ state start being filled, indicating the bleach of $1S_e$ to $1D_e$ transition. The induced feature shows $1P_e$ to $1D_e$ transition ~3000 cm^{-1} and the 1D to higher states ~2200 cm^{-1}. **Fig.2-17(e, f)** show the amplitudes of each transition change with different potential. The lines are Nernst functions $\frac{1}{1+\exp[(E-E_0)/\Delta E]}$ guides to the eyes. E_0=0.1eV, ΔE=0.3eV for the solid line. E_0=-0.4eV, ΔE=0.2eV for the solid line.

2.5.3 Other nanocrystal system

The spectroelectrochemistry is also very useful in other nanocrystal system, taking CdSe colloidal quantum wells (CQWs) as an example[56]. Typical static absorption spectra of CdSe CQWs are shown in **Fig.2-18a**. CdSe CQWs are transparent in the NIR and show excitonic absorptions at visible wavelengths determined by their two-dimensional electronic structure. The excitonic wavelengths are diagnostic of the CQW thickness, here shown for 3.5 to 6.5 ML samples. Upon absorption of an above-bandgap photon, the CQWs display three bleaching features, shown in **Fig.2-18b**, which represent heavy-hole (HH), light-hole (LH), and spin–orbit (SO) hole transitions to the first electronic shelf (E_1)[57]. At the same time, and displayed in **Fig.2-18c**, spectrally narrow absorption features emerge in the NIR spectral window. The energetic position of the NIR

absorption features depends on the CQW thickness: identical photoinduced absorptions were observed in other CQW samples with the same thickness.

Two additional experiments support that the NIR-photoinduced absorptions arise from intersubband transitions. First, the kinetics of the visible bleaching feature and the NIR-induced absorption were directly compared for the same samples at similar pump fluence. As shown in **Fig.2-18d**, the kinetic traces of these features overlap for each of the samples measured, which provides evidence that the NIR-photoinduced absorption occurs when excitons are present in the nanostructures. The photoinduced spectra were done by Dr Benjamin Diroll. Second, spectroelectrochemical results demonstrate that NIR absorption features are obtained for CQW films when electrochemically charged. Solid thin films of CQWs are prepared by drop-casting followed by soaking for 1 min in a 5 $mg\,mL^{-1}$ methanolic solution of benzoic acid. Similar to earlier reports on electrochromic quantum dots[58], negative applied biases lead to filling of the CdSe CQW conduction band with electrons, which reveals intersubband absorption features of electrons (**Fig.2-18e**). The conductivity of the CQW films also increases as electrons fill the conduction band. As plotted in **Fig.2-18e**, the NIR-induced absorption features observed in spectroelectrochemical experiments are nearly identical in energy to those observed after photoexcitation.

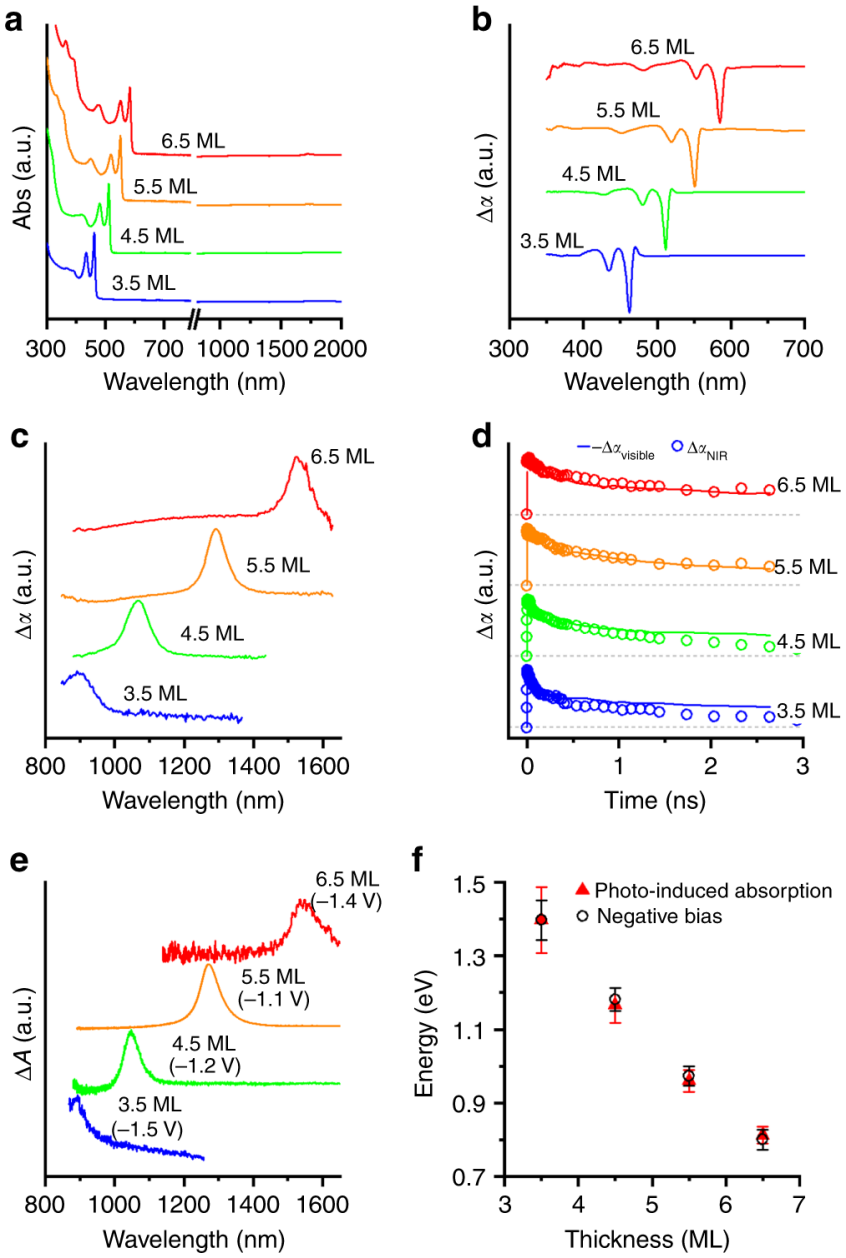

Figure 2-18. Thickness-dependent static and time-resolved optical properties of CdSe CQWs. **(a)** The 295 K static absorption spectra covering visible and NIR energies of CdSe CQW ensembles with atomically defined thicknesses, as labeled in the panel. Data were collected in two separate measurements for the visible and NIR (merged at 800 nm). **(b)** Visible- and **(c)** NIR-probe transient absorption spectra of the same samples with 400 nm excitation at 10 ps delay. **(d)** Transient absorption dynamics of the first excitonic bleach feature (shown as solid lines) and the NIR-induced absorption feature (shown as open circles) for each of the samples at comparable fluence. **(e)** Static change in absorption spectra (ΔA) of electrochemically pumped CQW samples under applied bias (vs. SCE listed on the plot) in an electrolyte. **(f)** Fitted energy of the photoinduced (closed red triangles) and electrochemically induced (open black circles) NIR absorption feature vs. the thickness (in monolayers of CdSe units). The error bars represent the full-width at half-maximum of the features. The figure is adapted from reference 56.

2.6 Conclusion

In summary, this chapter provides the investigation of the absolute energy positions of the three chalcogenide materials, the position of the quantum dot states, and an explanation of their very different doping and mobilities.

This electrochemical study of films of HgS, HgSe, and HgTe QDs focused on reversible conditions and it provided information on the doping level, the redox potential of the QD states as a function of size, the band positions of the bulk materials, and the mobility of carriers in the films. The conduction bands are measured at -5.20 eV for HgS, -5.50eV for HgSe, -4.92eV for non-aggregated HgTe and -4.77 eV for aggregated HgTe. The stable ambient n-doping of Hg (S, Se) QDs and large separated HgTe CQDs arises because the $1S_e$ state is lower than the measured environment Fermi level of ~ -4.7 eV even with significant electron confinement. Taking into account the zero-gap of HgTe and HgSe but the 0.65 eV gap of HgS (zinc blend form), the energies of the valence bands increase in the order S, Se, Te as expected from the order of the anion p-orbital energies. The tuning of the redox potential of the QD states with size is clearly observed and the charging energy is an important contribution to the redox potential, especially for $1P_e$ which is multiply charged.

The origin of the position of the Fermi level is also investigated. In particular, it settles whether it is due to the solution environment or to surface species/stoichiometry effects, with both situations demonstrated in different conditions. For films treated by EdT/HCl/IPA, the Fermi level is set by the environment. However, under high concentrations of Cl^- or Sulfide or after prolonged exposure to ambient air, the films are modified and the Fermi level becomes set by the Hg/Hg_2Cl_2, Hg/HgS and Hg/HgO redox equilibria respectively. Matching the Fermi level with the known redox

potential of surface species provides a perspective on the influence of the surface for QDs. The modification of the surface is also shown to directly shift the energy of the QD states and change doping in qualitative accord with optical observations. For example, brief sulfide exposure or oxidation in the air over long enough exposure (one day), shifts HgTe towards p-doping for HgTe while HgSe and HgS become less n-doped, while brief exposure to hydrochlorides or metal ions reverse the effect. Dynamic light scattering measurements are consistent with TEM images. For the HgSe colloids, the negative zeta potential is consistent with the doping observed, but the negative zeta potential for undoped HgTe is not. Therefore, the zeta-potential is not an indicator of carrier doping even in non-polar solvents.

Electrochemical gating was used to determine the mobilities for all three films over a range of sizes. For non-aggregated Hg (S, Se, Te) the mobility increases with increasing size. After the ethanedithiol ligand exchange, they have small mobility for the $1S_e$ state, around 10^{-3} cm^2/Vs. In contrast, aggregated HgTe QD films have much higher mobility, ~ 10^{-2} cm^2/Vs for mid-IR QDs, with a non-monotonous dependence on the size of the dots, and this is attributed to the partial aggregation of the non-spherical HgTe QDs in solution.

Finally, we use spectroelectrochemistry to investigate the detailed band structure with different states filling. The spectroelectrochemistry helps to figure out the splitting in the $1P_e$ state in HgSe and HgTe QD, and intersubband energy of CdSe CQWs which is comparable with the photoinduced measurement.

2.7 Methods

Colloidal Atomic Layer Deposition: The QDs in solution are exposed to sulfide, by adding 1 mL formamide, 50 μL oleylamine and 150 μL of 0.1 M $(NH_4)_2S$ to 1mL of QD solution in BZC, and stirring the emulsion for 5 min. Then the solution is washed twice with formamide. The CQDs are exposed to mercury, using 1mL mercury precursor solution (prepared by dissolving 0.05mmol $HgCl_2$ in 10ml oleylamine, 10ml trichloroethylene and 0.5ml trioctylphosphine at 120℃) and 1mL of QD solution in BZC, following the same steps as above.

Dynamic light scattering and Zeta-potential measurement: A Malvern Zetasizer Nano ZS is used to measure the QDs size and Zeta-potential in BZC solution at 20 ℃ by dynamic light scattering (DLS).

Film preparation: QD films are made by drop-casting from BZC (or other nonpolar sovlent) solution onto interdigitated electrodes (commercial CHE Instruments 012126 IDA electrode or other homemade electrode based on the measurements) or a ZnSe window for electrochemistry and spectroscopy respectively, and dried in air at ambient temperature. The film thickness is kept below 100 nm, to facilitate a homogenous electrochemical response of the film.

Effect of ions in aqueous electrolyte: Different Cl^- concentrations are prepared by dissolving different amounts of KCl in H_2O. Different S^{2-} concentrations in aqueous medium are prepared in a glovebox under Argon by dissolving different amount of Na_2S in a pH=12.6 buffer and monitoring the pH. The total concentration of sulfide is determined by the amount of Na_2S added according to,

$$[Na_2S] = [S]_{total} = [H_2S] + [HS^-] + [S^{2-}],$$

where $K_1 = 9.12 * 10^{-8}$, $K_2 = 1.2 * 10^{-15}$ are the ionization constant for H_2S [59]. Then the actual S^{2-} concentration is obtained as $[S^{2-}] = [S]_{total}/(1 + \frac{[H^+]}{K_2} + \frac{[H^+]^2}{K_1K_2})$.

Spectroscopy: Infrared spectra are measured in the attenuated total internal reflection (ATR), using a Fourier transform infrared spectrometer (Nicolet Magna IR550). Samples are drop-cast on a double sided polished ZnSe plate with 45° polished beveled edges. The plate dimensions are 36mm x 8mm x 2.5mm.

Spectroelectrochemistry: Nanocrystal films were prepared on Au interdigitated electrodes (IDE), and cross-linked with short ligands to increase the conductivity (usually 2%(v/v) solution of EDT//IPA). The IDE is on glass with spacing d = 20μm and finger width d_0 = 10 μm. The spectroelectrochemical cell is assembled and filled with 0.1M anhydrous tetrabutylammonium perchlorate/ propylene carbonate in glovebox. The sample electrode is pressed lightly against the KBr window of the cell to minimize the infrared absorption from the electrolyte. Then the cell is put in the Fourier transform infrared spectrometer (usually Thermo Nicolet iS50 Advanced FTIR with near-, far-, and mid-IR). Spectra are measured in reflectance. The cyclic voltammetry and the film conductance would be characterized first by a bi-potentiostat. A proper potential would be set, whose spectrum is taken as the background, before measuring the difference spectra.

References

[1] Kershaw, S. V.; Susha, A. S.; Rogach, A. L. Narrow Bandgap Colloidal Metal Chalcogenide Quantum Dots: Synthetic Methods, Heterostructures, Assemblies, Electronic and Infrared Optical Properties. *Chem. Soc. Rev.* **2013**, *42*, 3033-3087.

[2] Keuleyan, S.; Lhuillier, E.; Brajuskovic, V.; Guyot-Sionnest, P. Mid-Infrared HgTe Colloidal Quantum Dot Photodetectors. *Nat. Photonics* **2011**, *5*, 489-493.

[3] Guyot-Sionnest, P.; Roberts, J. A. Background Limited Mid-infrared Photodetection with Photovoltaic HgTe Colloidal Quantum Dots. *Appl. Phys. Lett.* **2015**, *107*, 253104.

[4] Ackerman, M. M.; Tang, X.; Guyot-Sionnest, P. Fast and Sensitive Colloidal Quantum Dot Mid-wave Infrared Photodetectors. *ACS nano* **2018**, 12, 7264-7171.

[5] Buurma, C.; Pimpinella, R.E.; Ciani, A. J.; Feldman, J.S.; Grein, C.H.; Guyot-Sionnest, P. MWIR Imaging with Low Cost Colloidal Quantum Dot Films. *SPIE Nanoscience+ Engineering. International Society for Optics and Photonics*, **2016**, 993303-993303-7.

[6] Tang, X.; Ackerman, M. M.; Guyot-Sionnest, P. Thermal Imaging with Plasmon Resonance Enhanced HgTe Colloidal Quantum Dot Photovoltaic Devices. *ACS nano* **2018**, 12, 7362-7370.

[7] Tang, X.; Tang, X.; Lai, K. W. C. Scalable Fabrication of Infrared Detectors with Multispectral Photoresponse Based on Patterned Colloidal Quantum Dot Films. *ACS Photonics* **2016**, *3*, 2396-2404.

[8] Tang, X.; Ackerman, M. M.; Chen, M.; Guyot-Sionnest, P. Dual-band Infrared Imaging using Stacked Colloidal Quantum Dot Photodiodes. *Nature Photonics* **2019**, 13, 277.

[9] Chen, M.; Guyot-Sionnest, P. Reversible electrochemistry of mercury chalcogenide colloidal quantum dot films. *ACS Nano* **2017**, 11, 4165– 4173.

[10] Deng, Z; Jeong, K.S. ; Guyot-Sionnest, P. Colloidal Quantum Dots Intraband Photodetectors. *ACS Nano* **2014**, *8*, 11707–11714.

[11] Shen, G.; Chen, M.; Guyot-Sionnest, P. Synthesis of Nonaggregating HgTe Colloidal Quantum Dots and the Emergence of Air-stable N-doping. *J. Phys Chem. Lett.* **2017**, 8, 2224-2228.

[12] Hudson, M. H.; Chen, M.; Kamysbayev, V.; Janke, E. M.; Lan, X.; Allan, G.; Delerue, C.; Lee, B.; Guyot-Sionnest, P.; Talapin, D. V. Conduction band fine structure in colloidal HgTe quantum dots. *ACS Nano* **2018**, 12, 9397– 9404.

[13] Lhuillier, E.; Scarafagio, M.; Hease, P.; Nadal, B.; Aubin, H.; Xu, X. Z.; Lequeux, N.; Patriarche, G.; Ithurria, S.; Dubertret, B. Infrared Photodetection Based on Colloidal Quantum-Dot Films with High Mobility and Optical Absorption up to THz. *Nano Lett.* **2016**, *16*, 1282-1286.

[14] Tang, X.; Wu, G. f.; Lai, K. W. C. Plasmon Resonance Enhanced Colloidal HgSe Quantum Dot Filterless Narrowband Photodetectors for Mid-Wave Infrared. *J. Mater. Chem. C* **2017**, 362-369.

[15] Robin, A.; Livache, C.; Ithurria, S.; Lacaze, E.; Dubertret, B.; Lhuillier, E. Surface Control of Doping in Self-Doped Nanocrystals. *ACS Appl. Mater. Interfaces* **2016**, *8*, 27122-27128.

[16] Deng, Z.; Guyot-Sionnest, P. Intraband Luminescence from HgSe/CdS Core/Shell Quantum Dots. *ACS Nano* **2016**, *10*, 2121-2127.

[17] Shen, G.; Guyot-Sionnest, P. HgS and HgS/CdS Colloidal Quantum Dots with Infrared Intraband Transitions and Emergence of a Surface Plasmon. *J. Phys Chem. C* **2016**, *120*, 11744-11753.

[18] Bard, A.J. ; Faulkner, L.R. Electrochemical Methods, Fundamentals and Applications. *JOHN WILEY & SONS, INC.* **2001**; pp1-17.

[19] Yu, D.; Wang, C. J.; Guyot-Sionnest, P. N-Type Conducting CdSe Nanocrystal Solids. *Science* **2003**, *300*, 1277–1280.

[20] Jasieniak, J.; Califano, M.; E.Watkins, S. Size-Dependent Valence and Conduction Band-Edge Energies of Semiconductor Nanocrystals. *ACS Nano* **2011**, *5*, 5888-5902

[21] Amelia, M.; Lincheneau, C.; Silvi, S.; Credi, A. Electrochemical Properties of CdSe and CdTe Quantum Dots. *Chem. Soc. Rev.* **2012**, *41*, 5728-5743.

[22] Osipovich, N. P.; Poznyak, S. K.; Lesnyak, V.; Gaponik, N. Cyclic Voltammetry as A Sensitive Method for *In Situ* Probing of Chemical Transformations in Quantum Dots. *J. Phys. Chem. Chem. Phys.* **2016**, *18*, 10355-10361.

[23] Poznyak, S. K.; Osipovich, N. P.; Shavel, A.; Talapin, D. V.; Gao, M. Y.; Eychmuller, A.; Gaponik, N. Size-Dependent Electrochemical Behavior of Thiol-capped CdTe Nanocrystals in Aqueous Solution. *J, Phys Chem. B* **2005**, *109*, 1094-1100.

[24] Guyot-Sionnest, P.; Wang,C.J. Fast Voltammetric and Electrochromic Response of Semiconductor Nanocrystal Thin Films. *J, Phys Chem. B* **2003**, *107*, 7355-7359.

[25] Keuleyan, S. E.; Guyot-Sionnest, P.; Delerue, C.; Allan, G. Mercury Telluride Colloidal Quantum Dots: Electronic Structure, Size-Dependent Spectra, and Photocurrent Detection up to 12 μm. *ACS Nano* **2014**, *8*, 8676-8682.

[26] Gerischer H, J. on The Stability of Semiconductor Electrodes Against Photodecomposition. *J. Electroanal. Chem* **1977**, *82*, 133-143.

[27] Liu, H.; Keuleyan, S.; Guyot-Sionnest, P. N- and P-Type HgTe Quantum Dot Films. *J. Phys. Chem. C* **2012**, *116*, 1344-1349.

[28] Murray, R. W. Nanoelectrochemistry: Metal Nanoparticles, Nanoelectrodes, and Nanopores. *Chem. Rev.* **2008**, *108,* 2668-2720.

[29] Boehme, S. C.; Vanmaekelbergh, D.; Evers, W. H.; Siebbeles, L. D. A.; Houtepen, A. J. *In Situ* Spectroelectrochemical Determination of Energy Levels and Energy Level Offsets in Quantum-Dot Heterojunctions. *J, Phys Chem. B* **2016**, *120*, 5164-5173.

[30] Brus, L. E. Electron–Electron and Electron-Hole Interactions in Small Semiconductor Crystallites: The Size Dependence of The Lowest Excited Electronic State. *J. Chem. Phys.* **1984**, *80*, 4403-4409.

[31] Svane, A.; Christensen, N. E.; Cardona, M.; Chantis, A. N.; van Schilfgaarde, M.; Kotani, T. Quasiparticle Band Structures of β-HgS, HgSe, and HgTe. *Phys. Rev. B* **2011**, *84*, 205205.

[32] Yu, P.; Cardona, M. Fundamentals of Semiconductors; Springer-Verlag: Berlin, Heidelberg, **2010**, pp 68-71.

[33] Einfeldt, S.; Goschenhofer, F.; Becker, C. R.; Landwehr, G. Optical Properties of HgSe. *Phys. Rev. B* **1995**, *51*, 4915-4925.

[34] Trasatti, S. The Absolute Electrode Potential: an Explanatory Note. *J. Pure Appl. Chem.* **1986**, *58*, 955–966.

[35] Wei, S.H.; Zunger, A. Calculated Natural Band Offsets of all II–VI and III–V Semiconductors: Chemical Trends and The Role of Cation Orbitals. *Appl. Phys. Lett.* **1998**, *72*, 2011-2013.

[36] Boehme, S. C.; Azpiroz, J. M.; Aulin, Y. V.; Grozema, F. C.; Vanmaekelbergh, D.; Siebbeles, L. D.; Infante, I.; Houtepen, A. J. Density of Trap States and Auger-mediated Electron Trapping in CdTe Quantum-Dot Solids. *Nano Lett* **2015**, *15*, 3056-3066.

[37] Stavrinadis, A.; Konstantatos, G. Strategies for the Controlled Electronic Doping of Colloidal Quantum Dot Solids. *Chemphyschem* **2016**, *17*, 632-644.

[38] Zhao, Y. X.; Pan, H. C.; Lou, Y. B.; Qiu, X. F.; Zhu, J. J.; Burda, C. Plasmonic Cu2-xS Nanocrystals: Optical and Structural Properties of Copper-Deficient Copper(I) Sulfides. *J. Am. Chem. Soc.* **2009**, *131*, 4253-4261.

[39] Buonsanti, R.; Llordes, A.; Aloni, S.; Helms, B. A.; Milliron, D. J. Tunable Infrared Absorption and Visible Transparency of Colloidal Aluminum-Doped Zinc Oxide Nanocrystals. *Nano Lett.* **2011**, *11*, 4706-4710.

[40] Dobčnik, D.; Igor G.; Kolar, M. A Silver-Silver Sulphide Selective Electrode Prepared by means of Chemical Treatment of Silver Wire. *Acta Chim. Slovaca.* **1998**, *45*, 209-216.

[41] Inzelt, G.; Lewenstam, A.; Scholz, F. Handbook of Reference Electrodes, Springer-Verlag: Berlin, Heidelberg **2013**, pp 115-116.

[42] Inzelt, György; Lewenstam, Andrzej; Scholz,Fritz, Handbook of Reference Electrodes, Springer-Verlag: Berlin, Heidelberg **2013**, pp 115-116.

[43] Carroll, G. M.; Tsui, E. Y.; Brozek, C. K.; Gamelin, D. R. Spectroelectrochemical Measurement of Surface Electrostatic Contributions to Colloidal CdSe Nanocrystal Redox Potentials. *Chem. Mater.* **2016**, *28*, 7912-7918.

[44] OBrien, R.; White, L.R. Electrophoretic Mobility of a Spherical Colloidal. *J. Chem. Soc., Faraday Trans.* **1978**, *74*, 1607-1626.

[45] Shevchenko, E. V.; Talapin, D. V.; Kotov, N. A.; O'Brien, S.; Murray, C. B. Structural Diversity in Binary Nanoparticle Superlattices. *Nat. Lett.* **2006**, 439, 55-59.

[46] Islam, M. X.; Telesca, D.A.; Steigerwald, M.L.; Herman, I.P. Controlled Electrophoretic Deposition of Smooth and Robust Films of CdSe Nanocrystals. *Chem. Mater.* **2004**, 16, 49-54.

[47] Yazdani, N.; Bozyigit, D.; Yarema, O.; Yarema, M.; Wood, V. Hole Mobility in Nanocrystal Solids as A Function of Constituent Nanocrystal Size. *J. Phys. Chem. Lett.* **2014**, *5*, 3522-3527.

[48] Kang, M. S.; Sahu, A.; Norris, D. J.; Frisbie, C. D. Size-dependent Electrical Transport in CdSe Nanocrystal Thin Films. *Nano Lett.* **2010**, *10*, 3727-3732.

[49] Liu, Y.; Gibbs, M.; Puthussery, J.; Gaik, S.; Ihly, R.; Hillhouse, H. W.; Law, M. Dependence of Carrier Mobility on Nanocrystal Size and Ligand Length in PbSe Nanocrystal Solids. *Nano Lett.* **2010**, *10*, 1960-1969.

[50] Guyot-Sionnest, P. Electrical Transport in Colloidal Quantum Dot Films. *J. Phys. Chem. Lett.* **2012**, *3*, 1169-1175.

[51] Xu, S.; Thian, D.; Wang, S.; Wang, Y.; Prinz, F. B. Effects of Size Polydispersity on Electron Mobility in A Two-dimensional Quantum-dot Superlattice. *Phys. Rev. B* **2014**, *90*.

[52] Shabaev, A.; Efros, A. L.; Efros, A. L. Dark and Photo-Conductivity in Ordered Array of Nanocrystals. *Nano Lett.* **2013**, *13*, 5454-5461.

[53] Allan, G.; Delerue, C., *Physical Review B* **2012**, 86, 165437.

[54] Wehrenberg, B. L.; Guyot-Sionnest, P., *J. Am. Chem. Soc.* **2003**, 125, 7806-7807.

[55] Spittel, D.; Poppe, J.; Meerbach, C.; Ziegler, C.; Hickey, S. G.; Eychmüller, A., *ACS Nano* **2017**, 11, 12174-12184.

[56] Diroll, B.T.; Chen, M.; Coropceanu, I.; Williams, K.R.; Talapin, D.V.; Guyot-Sionnest, P.; Schaller, R.D. Polarized Near-infrared Intersubband Absorptions in CdSe Colloidal Quantum Wells. *Nat. Commun.* **2019**,10, 4511.

[57] Ithurria, S. et al. Colloidal Nanoplatelets with Two-dimensional Electronic Structure. *Nat. Mater.* **2011**, 10, 936–941.

[58] Wang, C.; Shim, M.; Guyot-Sionnest, P. Electrochromic nanocrystal quantum dots. *Science* **2001**, 291, 2390–2392.

[59] Swift, E. H.; Butler, E. A. Quantitative Measurements and Chemical Equilibria; W. H. Freeman and Company: San Francisco, **1972**, 374-379.

Chapter 3: State-Resolved Transport on QDs with High Carrier Mobility

In Chapter 2, I used electrochemistry to measure carrier mobility in HgX (X=S, Se, Te) quantum dot films. This leads naturally to desiring to perform more detailed studies on the carrier transport properties. On the fundamental side, the transport mechanisms in disordered system like QD solids is not well understood. For example, the mobility for QD solids has been reported to be decreasing or increasing with increasing sizes, and this has not been well explained yet. An open fundamental question is whether solids of artificial atoms like the CQDs could become good conductors with effectively ballistic transport at least across several CQDs. On the application side, improving transport should benefit QD technologies, For example, improving charge mobility in quantum dot films would improve the performance of photodetectors, solar cells, and LEDs. However, these applications also require preserving well-defined quantum dot electronic states and optical transitions.

In this chapter, I present HgSe and HgTe QD films which show high charge mobility for carriers transported through discrete QD states. A novel hybrid surface passivation process developed by the collaboration with Prof. Dmitri Talapin's group, efficiently eliminates surface states, provides tunable air-stable n- and p-doping, and enables hysteresis-free filling of QD states evidenced by strong conductance modulation. QD films dried at room temperature without any post treatments exhibit mobility up to μ~8 $cm^2V^{-1}s^{-1}$ at low carrier density with similar drift and Hall mobilities at all temperatures.

This chapter includes the published result from reference 46, 47, 61, as well as some unpublished data.

3.1 HgTe QD system

3.1.1 Introduction

Electron transport in solution-cast QD films ranges from low-mobility values, $\mu < 10^{-3}$ $cm^2V^{-1}s^{-1}$, up to ~ 20 $cm^2V^{-1}s^{-1}$ that is on par with the best organic and other solution-processed semiconductors.[1-3] A negative temperature dependence $\partial\mu/\partial T < 0$, defined as bandlike, has been observed in the high mobility QD films near room temperature.[4-7] The nature of the states involved in high-mobility transport, however, remains uncertain. The highest mobility has been achieved with annealed systems, [4,6,8] but even minor sintering of individual QDs is expected to perturb QD discrete density of electronic states. A high concentration of free carriers also promotes high mobility,[8] but free carriers trigger Auger recombination which is detrimental for QD optoelectronic devices.[9] To date, fully delocalized transport, with finite conductance at zero temperature, has been approached only with highly doped and sintered ZnO nanocrystals.[10] On the other hand, when QD solids showed signatures of state-resolved transport through S and P quantum-confined states,[11,12] the mobility was very low, μ < 0.1 $cm^2V^{-1}s^{-1}$,[13] and transport was purely by activated electron hopping.[14] While coherent transport and the emergence of minibands in ordered coupled QD solids are theoretically possible,[15,16] even the arrays of epitaxially-necked QDs have shown surprisingly low mobility (~0.1 $cm^2V^{-1}s^{-1}$) and the QD density of state was not resolved.[8,17] Therefore, it remains an open challenge to achieve high mobility while retaining QD states.[18] This is also the most interesting direction to improve emerging applications of CQDs for optical detection, emission, lasers and sensing.[1] In this chapter, we describes a system that achieves simultaneously high mobility and bandlike transport through discrete QD states. The transport properties of surface-engineered HgTe QD solids are examined with Field-Effect Transistor (FET), Hall- and Seebeck measurements, and discussed along several possible models.

3.1.2 HgTe CQDs Characterization

Bulk HgTe is a semimetal with zero band gap, such that HgTe QDs provide a solution-processable semiconductor with an optical gap tunable across the entire infrared region.[19,20] HgTe QDs are developed for infrared photodetectors,[2] and their electronic structure has been studied experimentally[19,21] and computationally[22]. **Figure 3-1A** shows ensemble absorption spectra with resolved excitonic transitions for HgTe QDs with diameter 12.5 ± 1.0 nm. We optimized the synthesis,[23] and achieved size distributions less than 10% std. dev. which translates to sub-60 meV full width at half maximum of the first excitonic.

Depending on the surface chemistry, HgTe QDs can be intrinsic or doped. The addition of electrons to the 1Se state (n-type doping) bleaches the interband h-1Se excitonic transitions and causes the appearance of new intraband 1Se-1Pe absorption peaks (**Fig.3-1A**).[21]

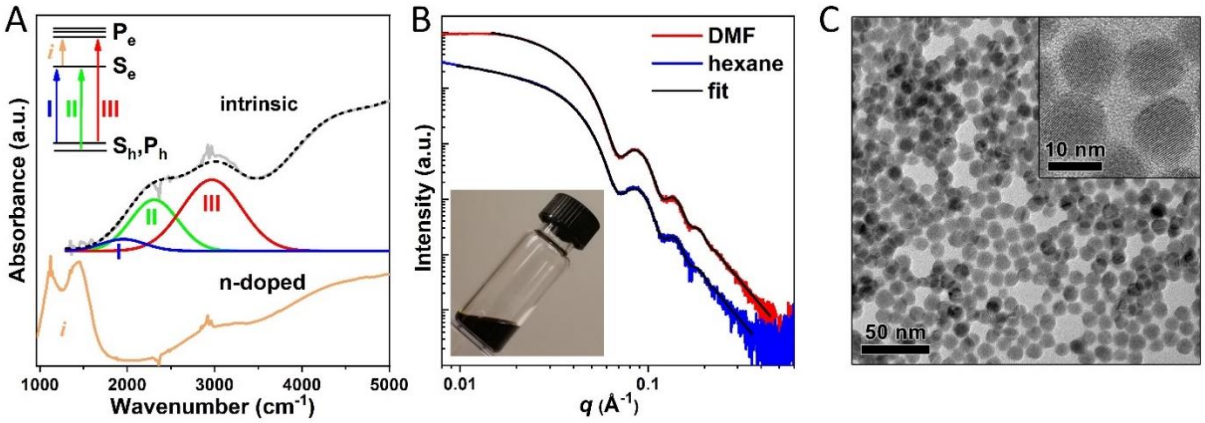

Figure 3-1. HgTe Quantum Dots. (A) Absorption spectra of undoped and n-type doped 12.5 ± 1.0 nm HgTe QDs. The blue, green and red lines are the Gaussian fittings, and the black dashed line a fit to the experimental data shown in grey. The inset shows the electronic structure and optical transitions for HgTe QDs. (B) Small-Angle X-ray Scattering shows similar colloidal stability of oleylamine-capped HgTe QDs in hexane and the same QDs dispersed in DMF after the ligand-exchange. Inset shows a photograph of stable colloidal solution of HgTe QDs dispersed in DMF following the solution ligand exchange process. (C) TEM image of ligand-exchanged 12.5 ± 1.0 nm HgTe QDs used for charge transport studies. The high-resolution TEM image in the inset shows good crystallinity and small separations between ligand-exchanged HgTe QDs. This figure is adapted from ref 47.

A solution-phase ligand exchange was applied, forming stable nanoinks in DMF (**Methods**).[24] Small-Angle X-ray scattering (SAXS, **Fig.3-1B**) and electron microscopy (**Fig.3-1C**) confirmed that the size and shape of HgTe QDs were preserved after the ligand exchange. For transport studies, HgTe QD films were spin-cast at room temperature, with no additional heat treatments. Electron microscopy and Small-Angle X-ray Scattering (SAXS) done by Dr Margaret H Hudson, and Vladislav Kamysbayev showed that the films consist of randomly-packed QDs (**Figure 3-2**) with a high packing density ~68%, including $HgCl_2$ in the ligand shell a very short dot-to-dot separation l = 3-4 Å. The solution and film-deposited QDs also show similar emission spectra (**Figure 3-3**).

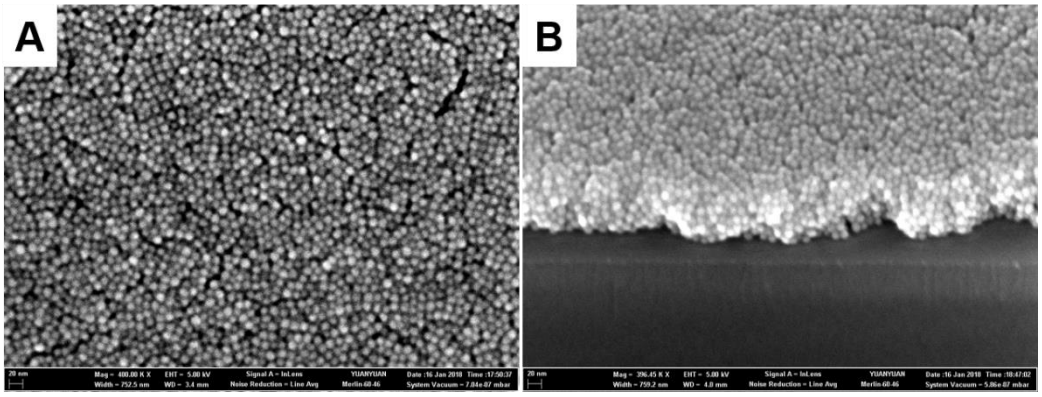

Figure 3-2. SEM images. High-resolution SEM images (top view and view at 45 deg. angle) of a film of ligand-exchanged 13.1 ± 1.1 nm HgTe QDs used for charge transport studies. This figure is adapted from ref 47.

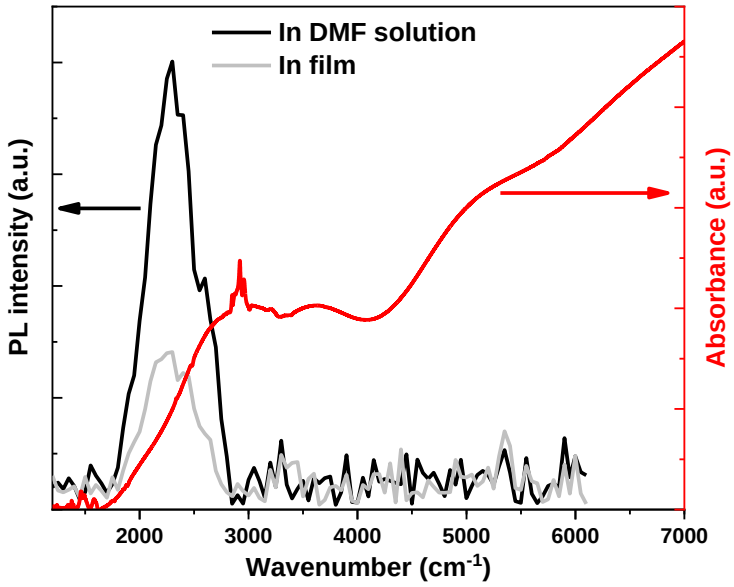

Figure 3-3. Absorption and PL studies of 10.9 ± 1.0 nm HgTe QDs. The red line shows an absorbance spectrum for a solution of oleylamine-capped QDs in tetrachloroethylene, dedoped by treatment with molecular iodine. Photoluminescence spectra were measured for the same QDs after ligand exchange into DMF with $HgCl_2$, 2-Mercaptoethanol, n-butylamine, and n-butylammonium chloride. Solution PL spectra were measured in DMF. For film-PL studies, the DMF-dispersed HgTe QDs were spincast on Si wafer. The photoexcitation was performed by using an 808 nm continuous laser modulated at 100 kHz. This figure is adapted from ref 47.

3.1.3 HgTe QD Transport Property Measurement

To characterize the transport property of HgTe QD solid, several different methods are used, including FET, electrochemistry, Hall effect and Seebeck measurement.

1. Sates Filling Resolved by FET

A bottom-gate geometry (**Figure 3-4**) was applied in thin film FETs (**Methods**). The length of the FET channel was varied from 3 μm to 3 mm without any significant impact on the device performance demonstrating the long-range uniformity of QD layers.

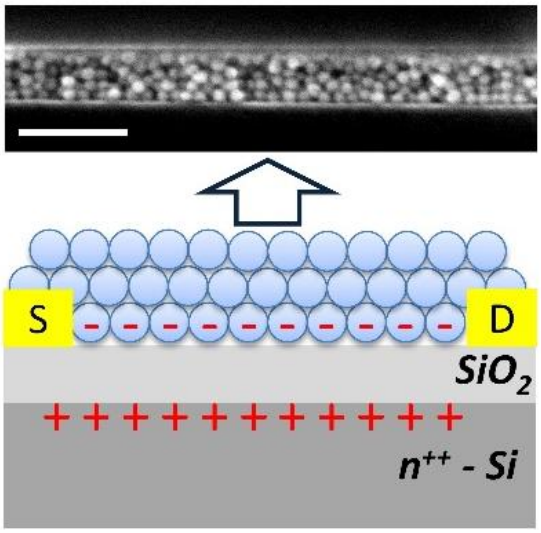

Figure 3-4. Schematic of FET. Schematic of a solid state QD FET and a cross-sectional SEM image of an FET channel showing randomly-packed HgTe QDs. The scale bar is 100 nm.

The well-resolved conductance peaks in the n-type region of the HgTe QD FETs, are observed in a wide temperature range (**Figure 3-5**).[11,12]

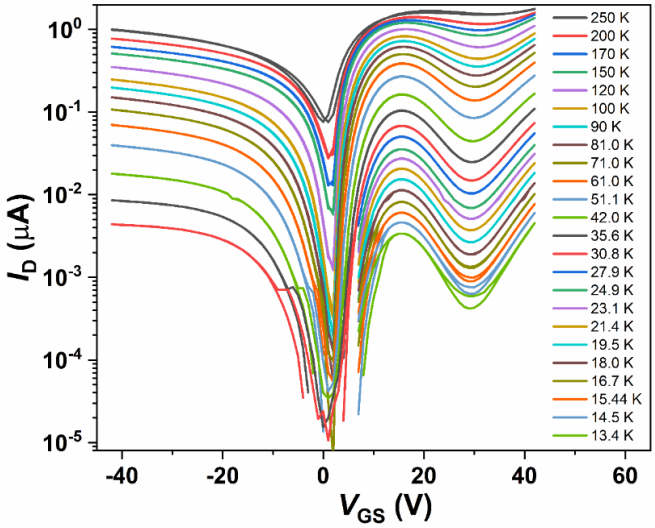

Figure 3-5. Temperature-dependent transfer characteristics for a HgTe QD transistor. Plots of I_{DS} versus V_{GS} at V_{DS} = 0.1 V for an ambipolar FET assembled from 10.0 ± 1.1 nm HgTe QDs (L = 10 μm, W = 400 μm). At low temperatures, there is large noise close to the intrinsic states. Consequently, the currents were not presented, for V_{GS} less than 7 V, at temperatures below 30 K. This figure is adapted from ref 47.

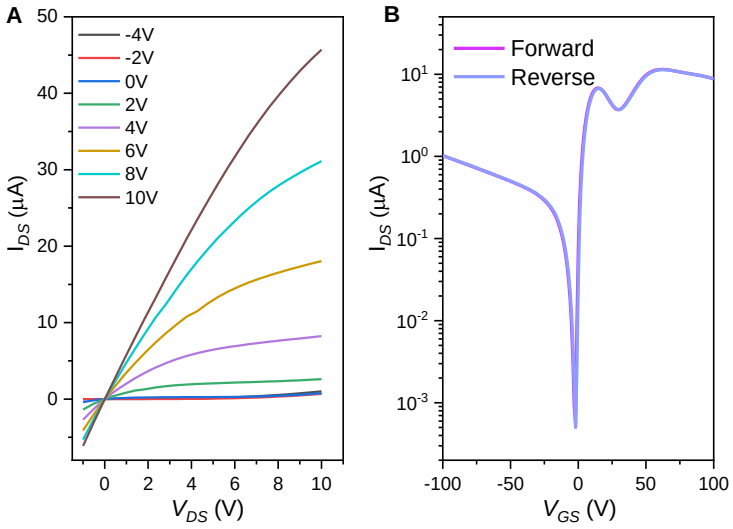

Figure 3-6. The output and transfer characteristics of HgTe QD FETs. (A) Output and (B) transfer characteristics at V_{DS} = 0.2 V for an ambipolar FET assembled from 10 ± 1.1 nm HgTe QDs (L = 10 μm, W = 400 μm). This figure is adapted from ref 47.

The output and transfer characteristics of HgTe QD FETs show efficient current modulation (**Figure 3-6**). The hysteresis-free transfer characteristics imply a highly reversible QD charging/discharging process where no noticeable surface states are involved in charge injection and transport.

We also verified that in all measurements FET channel current exceeded the gate leakage current by several orders of magnitude as shown in **Figure 3-7**, the transfer curve for a FET device with ~60 nm-thick film of 13.8 ± 1.1 nm HgTe QDs, measured at 79 K. The first conductance peak is attributed to the half-filling of the 1Se electronic state.

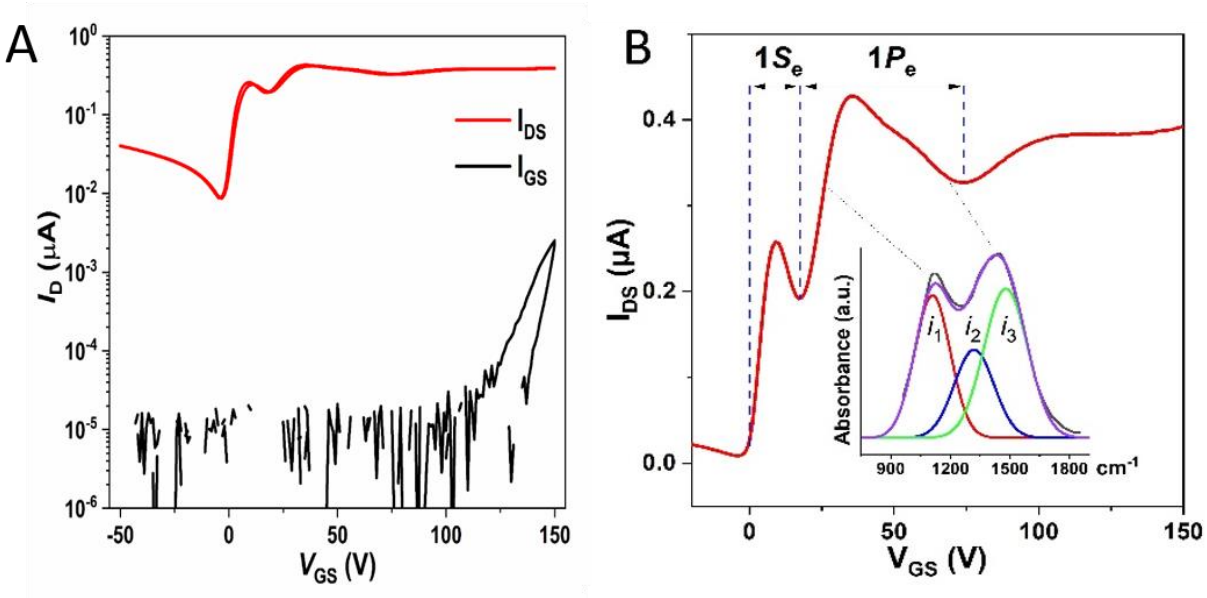

Figure 3-7. The transfer characteristic of a solid-state FET using 13.8 ± 1.1 nm HgTe QDs. (A) Drain current (I_{DS}-V_{GS}) and gate current (I_{GS}-V_{GS}) vs gate voltage characteristics of FET device with ~60 nm-thick film of 13.8 ± 1.1 nm HgTe QDs, measured at 79 K. Both forward and reverse scans were presented. The hysteresis-free I_{DS}-V_{GS} curve, together with 3-4 orders of magnitude lower I_{GS}, compared to I_{DS}, supports a highly reversible charging/discharging process during the measurements. (B) The transfer characteristic (recorded at 79 K) of a solid-state FET using 13.8 ± 1.1 nm HgTe QDs, demonstrating sequential filling of *s*- and *p*-orbitals of HgTe QDs. The splitting of the *p*-orbital results in an unsymmetrical p-state filling curve, in agreement with the intra-band optical absorption spectrum shown in the inset. This figure is adapted from ref 47.

Using the FET gate dielectric capacitance and dense two-dimensional QD packing, we estimate V_{GS} required to add one electron per QD in the FET channel, $V^e = 8.4$ V. We assumed that all injected carriers were accumulated within the first layer of the QD film. This QD array can be regarded as a 2-dimensional (2-D) lattice system. In the case of 2-D packing, the packing density η is assumed to be ~90.6% corresponding to hexagonal packing). The equation for estimated V^e for every electron:

$$V^e = V_G - V_{th} = \frac{Q}{C} = \frac{\mathrm{S}\times\eta\times\mathrm{e}/(\pi\times\mathrm{R}^2)}{\varepsilon_{SiO_2}\times\varepsilon_0\times S/d} \qquad (3\text{-}1)$$

Where V_G is the gate bias, V_{th} is the threshold voltage, R is the radius of the HgTe QDs, e is the elementary charge $1.6 \times 10^{-19}\ C$, ε_{SiO_2}= 3.9 is the dielectric constant of SiO_2, ε_0 is the vacuum permittivity $8.85 \times 10^{-12}\ F/m$, S is the area of the device and d the thickness of the SiO_2 dielectric layer (300 nm). For HgTe QDs with a diameter of 13.8 nm, by applying the above equation, the calculated V^e is calculated to be 8.4 V. If we take into account the size distribution, i.e., 13.8 ± 1.1 nm, V^e is in the range of 7.2~9.9 V. This is in good agreement with the measured 17 V range of the 1Se peak corresponding to 2 electrons per QD. The next peak spans a 57 V range, which is consistent with 6 electrons needed to fill the 1Pe states. The 1Pe peak is structured and this matches the fine structure of the intraband absorption of HgTe QDs (**Figure 3-7B, inset**), a result of the lifted degeneracy of the 1Pe-states of HgTe QDs due to strong spin-orbit coupling.[21] The relation of the conduction peaks and valleys to the filling of QD states is supported by the expected scaling $V^e \propto d^{-2}$ – higher gate bias is required to achieve the same charge/dot in FETs made of smaller HgTe QDs (**Figures 3-8 and 3-9**).

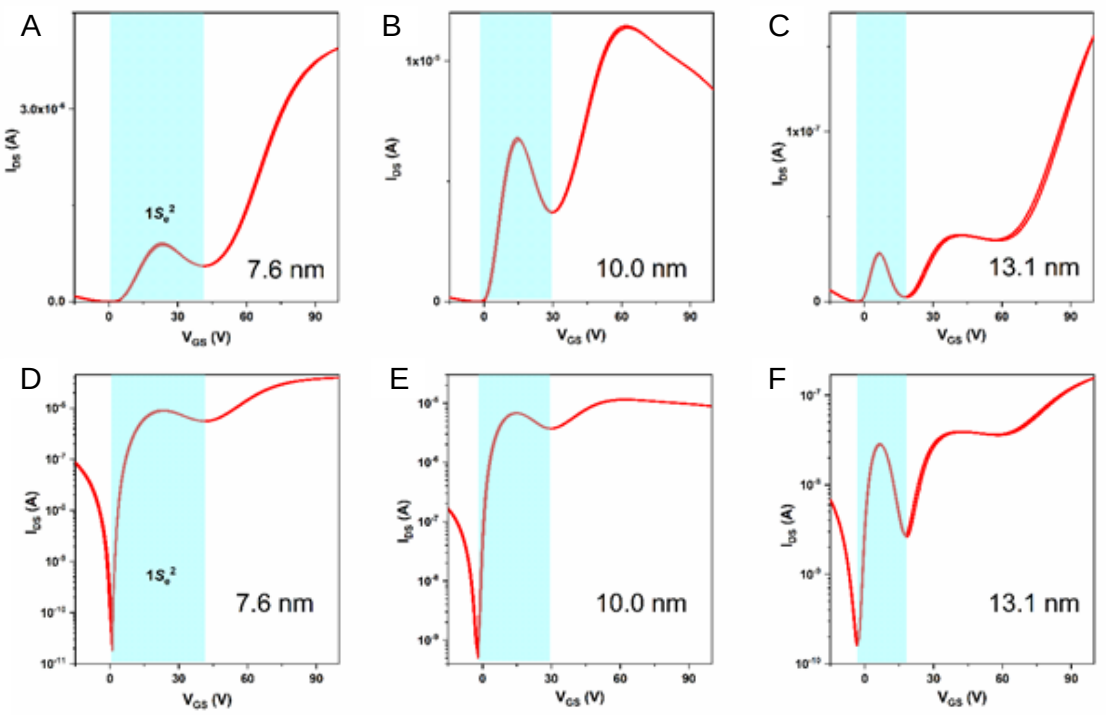

Figure 3-8. The transfer characteristics of FETs made of HgTe QDs of different sizes. (A-C) linear and (D-F) logarithmic scales to better show the conductivity modulation related to quantum state filling. This figure is adapted from ref 47.

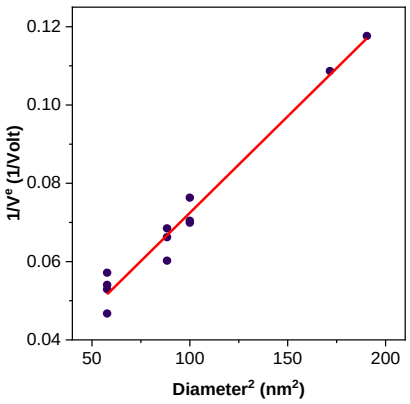

Figure 3-9. Plot of $1/V^e$ as a function of the diameter of the HgTe QDs. V^e defines the effective gate bias required to fill one electron per QD. V^e is then estimated using the equation $V^e = (V_{valley} - V_{th})/2$, where V_{valley} corresponds to V_{GS} at the conductance valley between S- and P-state current in the transfer curves and V_{th} the threshold voltage extracted from the transfer curves. The linear relationship for $1/V^e$ vs. Diameter^2 suggests that indeed it is the two-dimensional packing density of the QDs that defines the gate bias required to populate each electron of the QDs. This figure is adapted from ref 47.

The assignment of the FET conductance peak to 1Se is further confirmed by spectroelectrochemistry[21] (**Figure 3-10**).

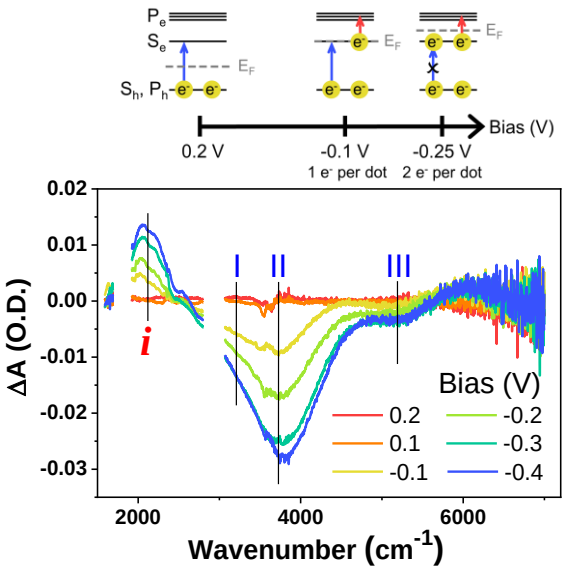

Figure 3-10. Spectroelectrochemistry. Top: The change of the Fermi level (E_F) with applied negative bias and its effect on the intensity of the interband (I, II, III) and intraband (*i*) optical transitions are shown in Figure 3-1A. Bottom: The absorption difference spectra for a film of electrochemically biased ligand-exchanged 7.6 ± 0.8 nm HgTe QDs *vs.* reference Ag/AgCl electrode at 203 K. When a negative (reducing) bias is applied, the intraband absorbance (*i*) appears and the excitonic transitions (I, II, III) are bleached. This figure is adapted from ref 47.

We think that a combination of high monodispersity of QDs, low state degeneracy, favorable surface chemistry with no intervening surface states, Ohmic contacts between QDs and Au electrodes, and QD sizes large enough to confine most gate-injected charges to the first monolayer of QDs, are the reasons why the conductance peaks are well resolved in our QD films. In a solid-state FET, the gate field extends into the semiconductor channel for the depth defined by the Thomas-Fermi screening length, which is comparable to QD diameter. In FETs made of larger QDs, major charges are distributed within a single QD layer adjacent to the gate dielectric,

resulting in sharp conduction minima. At lower temperatures, the FET features sharpen (**Figure 3-11**) pointing to a low density of electronic states between 1Se- and 1Pe-orbitals of HgTe QDs.

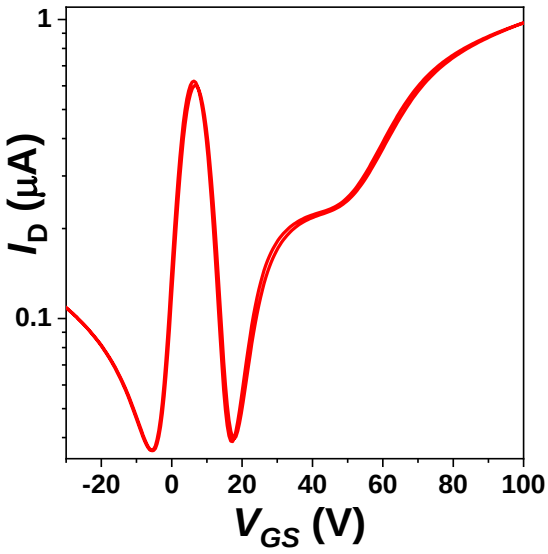

Figure 3-11. State filling studies of HgTe QDs with 15.1 ± 1.3 nm size using about a monolayer-thick QD film as the FET channel. The FET transfer curve measured at 78K shows a well-resolved gap between 1Se and 1Pe quantum states. In contrast to optical absorption spectra which typically experience difficulty with resolving sharp excitonic features for large QDs, the solid-state FETs show more pronounced separation between 1Se and 1Pe states in large QDs for which the gate field does not penetrate beyond single QD layer. The FET devices with channel thickness close to one QD layer show 1Se-1Pe and h1-1Se gaps equally sharp. This figure is adapted from ref 47.

The clear appearance of 1Se and 1Pe QD states in the conductivity data indicate that electrons move through a network of well-defined quantum-confined states. We rule out even mild sintering because bulk HgTe is a semimetal, and QD sintering would lead to a large broadening of the state distribution and loss of optical, electrochemical, and FET characteristics. To further strengthen this point, $\sigma(T)$ at the intrinsic doping point follows an Arrhenius activation energy which matches

half the optical band gap of individual QDs corrected by the exciton binding energy (**Figures 3-12**).

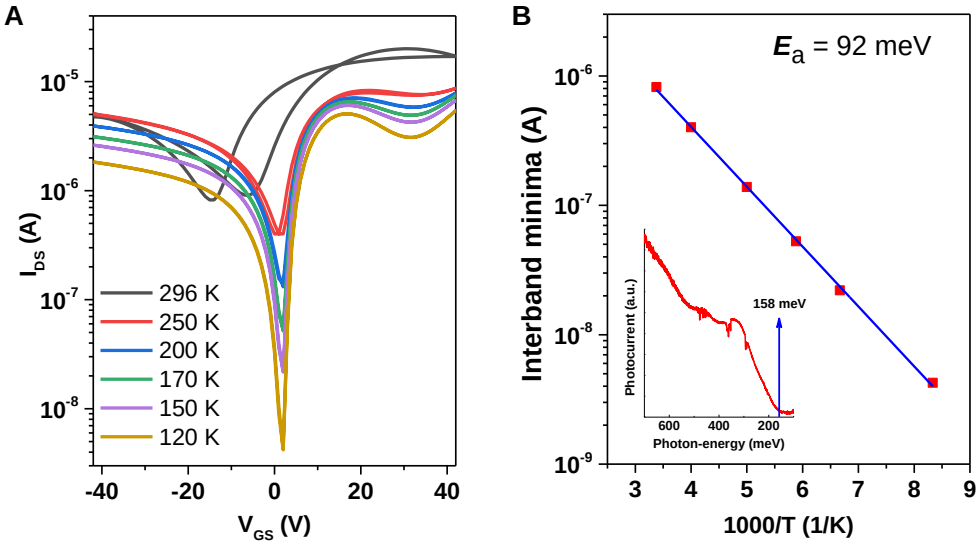

Figure 3-12. Bandgap calculation from the temperature-dependent transfer curves. (A) Plots of I_D versus V_{GS} at V_{DS} = 1 V for the device with 10 nm HgTe QD solid. Note that V_{DS} was applied at 1 V instead of 0.1 V such that the interband minima current can be extracted reliably at lower temperatures. (B) The interband minima currents as a function as temperature show an Arrhenius activation energy ~92 meV, suggesting an electronic bandgap ~184 meV. When corrected by an exciton binding energy of 26 meV using the equation $E_b = -1.8\, e^2/(4\pi\varepsilon\varepsilon_0 r)$, an optical bandgap ~158 meV is achieved, which is in good agreement with the photocurrent onset from a photoconductor, shown in the inset based on the same batch of HgTe QDs. This figure is adapted from ref 47.

2. FET Drift Mobility

The other observation is the two orders magnitude improvement in electron mobility compared to any previous reports for QD devices showing state-resolved transport. FET mobility (μ_{FET}), extracted in the linear regime, was calculated by fitting the experimental data to the following equation:

$$\mu_{\mathrm{FET}} = \frac{L}{WC_iV_D}\frac{dI_D}{dV_G}, \qquad (3\text{-}2)$$

where L, W, C_i, V_D, I_D, and V_G are the channel length, channel width, capacitance per unit area, drain voltage, drain current, and gate voltage, respectively. For thin films (~20-30 nm), the sharp increase in conductance at low charge injection levels (for both electron and hole) suggests an electronically clean bandgap, i.e., free of in-gap states. Interestingly, the use of thicker QD films (~60-80 nm) improves further the electron mobility. We understand that the improvement might come from improved continuity of the film and the more favorable dielectric environment in a thicker film. Note that there is a large hysteresis at room temperature, which decreases as the temperature decreases. At temperatures below 250 K, the hysteresis is negligible (**Figure 3-5**).

Figure 3-13 shows the electron FET mobility (μ_e^{FET}) measured for a film of 13.1 ± 1.1 nm HgTe QDs at a doping level of ~0.5 *e*/QD (~$3.3\cdot10^{16}$ cm^{-3}) from 5 K to 250 K. For these dots, the mobility peaks at 8 $cm^2V^{-1}s^{-1}$ at 77 K. At higher temperatures, there is a "bandlike" behavior with $\partial\mu_e^{FET}/\partial T < 0$. At lower temperatures, the mobility decreases with no apparent plateau, but it is still larger than 1 $cm^2V^{-1}s^{-1}$ at 9 K. Dividing the film conductivity (σ) at n ~ 1 *e*/QD by the surface charge density provides mobility which is very similar to μ_e^{FET} at n ~ 0.5 *e*/QD (**Figure 3-13**).

We also noted that in FET at low temperatures electrons move more efficiently through 1Se states, while the transport through 1Pe-type states gets suppressed, which becomes particularly obvious at low temperatures. This effect is counter-intuitive for the hopping conduction because 1Pe-states have higher degeneracy compared to 1Se-states. Besides, electrons moving through 1Pe states should experience lower activation barriers compared to 1Se electrons. Electrochemically-gated films show higher conductance for 1Pe but that is at a higher temperature. One possible explanation for the reduced conductivity of Pe states at lower temperatures compared to 1Se is the greater

energy disorder (reduced degeneracy) for 1Pe compared to 1Se as evidenced by the breadth of the intraband absorption. Another possible explanation is that the wavefunction of the lower energy 1Se state has a greater weight near the dot surface due to the inverted band structure of HgTe.[22] We may also speculate that in high-mobility HgTe QD samples electron delocalization extends over multiple QDs and spherically-symmetric 1Se states can form coherent domains even in disordered glassy QD films, while the angular components of 1Pe orbitals are much more sensitive to a positional disorder of individual QDs. Such an effect has been previously observed in indium-gallium-zinc oxide and some other amorphous semiconductors.[23] Relatively weak coupling of the 1Pe- and 1De- type orbitals may also explain why no mobility edge was observed in heavily-doped QD solids.

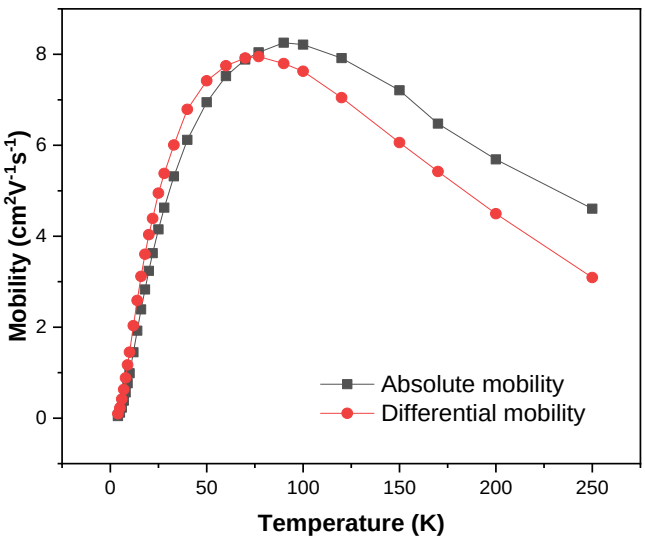

Figure 3-13. Comparison between the FET differential mobility and the mobility extracted from film conductivity and carrier density. The absolute mobility is extracted using the equation $\mu = \sigma/(ne)$, where σ, n, e are the conductivity, the carrier density, and the elementary charge $1.6 \times 10^{-19} C$, respectively. The carrier density is extracted from the 3-D packing density (~68%) and the doping level of the HgTe QDs derived from the transfer curves at 77 K. An electron doping density of 0.55 e/dot is used based on the relationship between the gate bias and the size of HgTe

QDs. The doping level is assumed to be constant during the temperature range as investigated. This figure is adapted from ref 47.

We studied several samples with different QD sizes, from 7.6 to 13.8 nm, that showed qualitatively similar behavior. The peak mobility generally increased and shifted to lower temperatures with increasing HgTe QD size (**Figure 3-14**). For the 7.6 ± 0.8 nm sample, there was no bandlike region and the mobility was below 1 $cm^2V^{-1}s^{-1}$ in the measured temperature range.

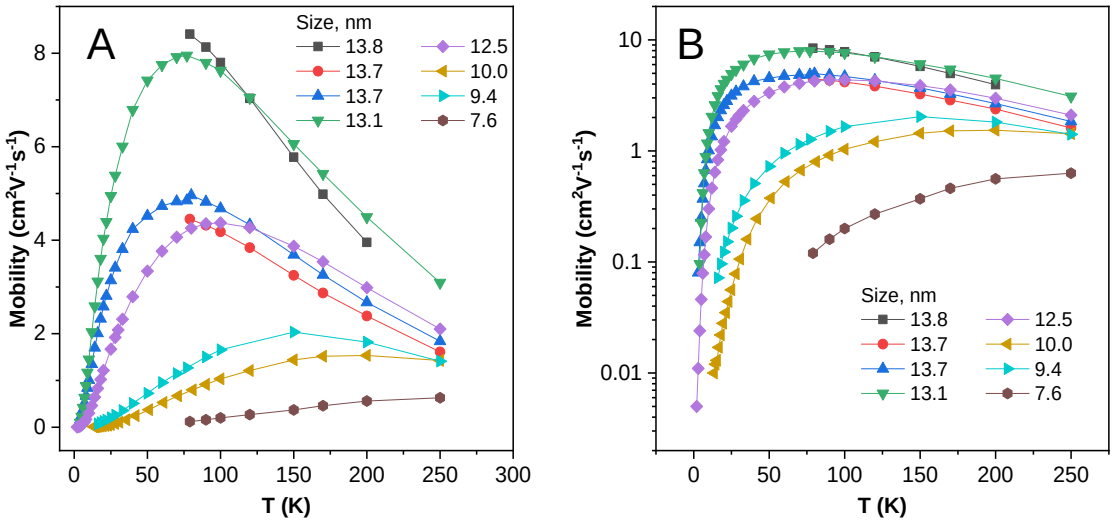

Figure 3-14. Temperature-dependent FET electron mobility for the films of HgTe QDs of different sizes and same surface ligands. (A) Linear scale and (B) Log scale. This figure is adapted from ref 47.

3. Mobility Measurement by Electrochemistry

The high electron mobility of HgTe QD films is also observed by electrolyte-gating (**Figure 3-15**). More detailed electrochemistry measurements on high mobility HgTe QD solid are discussed in **Chapter 4**.

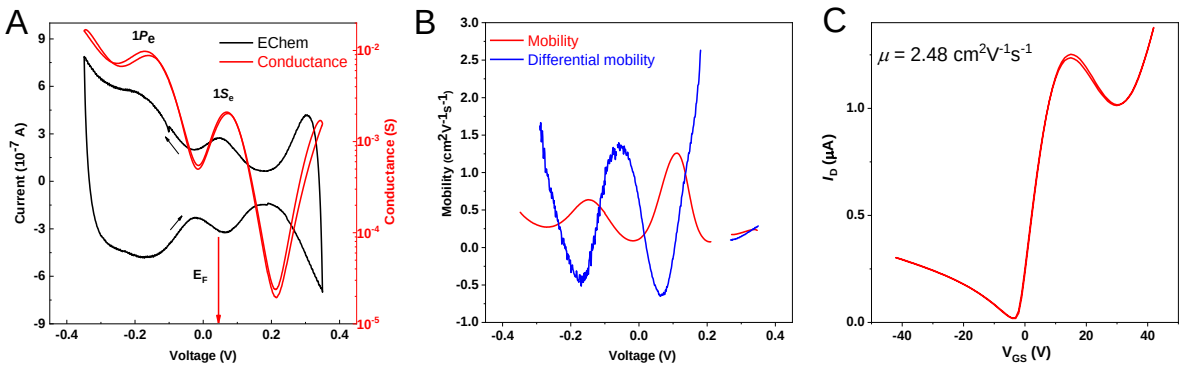

Figure 3-15. Mobility analysis from electrochemical studies. (A) Cyclic voltammetry current and conductance at 203 K. The voltage dependence of the conductance across the gap between the hole states and the 1Se state is consistent with the Nernst equation. A Nernst slope of 23.0 ± 0.8 V^{-1} is achieved, which is consistent with the temperature of 203 K ($\frac{e}{\ln(10)*k_BT}$= 24.8 V^{-1}). The red arrow indicates the Fermi level of the quantum dots in this environment. The black arrows indicate the scan direction. (B) The mobility analysis of 10.0 ± 1.0 nm HgTe QDs from electrochemistry experiments. The maximum mobility—achieved below 1e/QD doping level—is ~1.3 $cm^2V^{-1}s^{-1}$ at 203 K. (C) Transfer curve for a solid-state HgTe QD FET prepared from the same batch of HgTe QDs. Plots of I_D versus V_{GS} at V_{DS} = 0.1 V for an ambipolar FET assembled from 10.0 ± 1.1 nm HgTe QDs (L = 10 μm, W = 400 μm) measured at 200 K. The linear regime electron mobility is calculated to be 2.48 $cm^2V^{-1}s^{-1}$, in good agreement with the electrochemistry analysis. This figure is adapted from ref 47.

The narrow bandgap of HgTe QDs is aligned with the effective Fermi level of the environment (~ -4.5 eV relative to vacuum). This allows for air stable n- and p-type doping, which is unique among semiconductor QDs. By varying the amount of added $HgCl_2$ during the ligand exchange (**Methods**), we can prepare n-type, p-type, and nearly intrinsic QD solids (details are discussed in **Chapter 4**). The hybrid surface treatment enables not only excellent electron mobility but also high hole mobility μ_h^{FET} ~ 1.3 $cm^2V^{-1}s^{-1}$ **(Figure 3-16)**. However, the transfer characteristics of p-type QD FETs did not show discrete hole states, possibly because of the denser hole states due to the much larger hole effective mass.[22] As judged by FET threshold voltages, the doping of HgTe QDs does not change appreciably upon cooling from 250 K down to 4 K, showing no sign of carrier freeze-out.

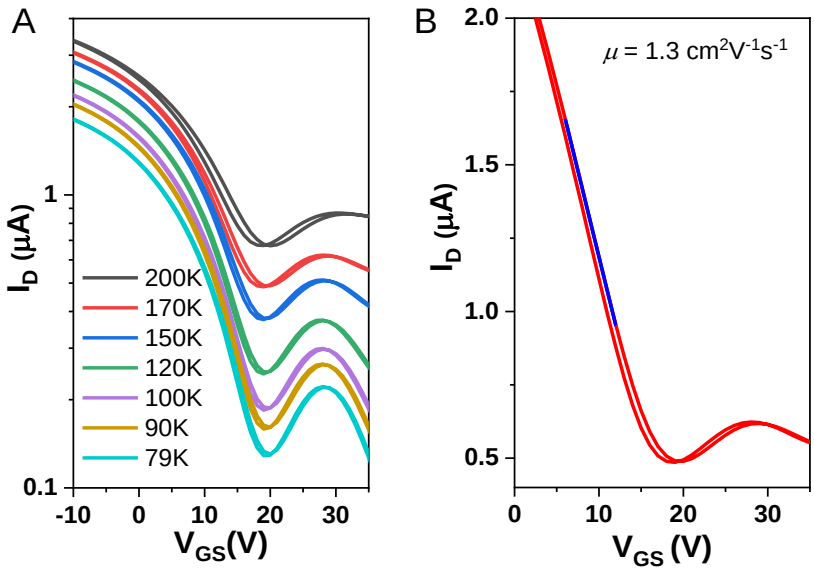

Figure 3-16. Transfer curve for a p-type transistor based on ~11 nm HgTe QDs. (A) Plots of I_{DS} versus V_{GS} at V_{DS} = 0.2 V for an ambipolar HgTe QD FET. (B)demonstrating hole mobility beyond 1 $cm^2V^{-1}s^{-1}$ at a temperature of 170 K. This figure is adapted from ref 47.

4. Hall Mobility

To provide complementary insights into the transport, we performed Hall measurements on HgTe QD solids. A Hall bar geometry with a 3 mm long conduction channel allowed measuring both Hall and FET mobility on the same QD film. The devices were measured in a Physical Property Measurement System (PPMS) setup. For the films in the Hall effect study, both solution ligand exchange and the deposition of the films were performed in an N_2 filled glove box. The films were kept in a high vacuum at ~10^{-6} torr for ~12 hrs to mimic as much as possible the conditions for regular FET devices. The thickness is measured to be ~65 nm determined by SEM. The corresponding transfer curves at different temperatures are shown in **Figure 3-17**. The modest on/off ratios can be attributed to the multiple-layer stacking that compromises the effective gating effect through the whole thickness. The sample shows drift electron mobilities that peak at 2.69 $cm^2V^{-1}s^{-1}$ at 100 K before dropping to 0.31 $cm^2V^{-1}s^{-1}$ at 10 K. The Hall mobilities were measured

without applying gate bias. Electrical noise prevented Hall measurements when the drift mobility was smaller than ~ 0.1 $cm^2V^{-1}s^{-1}$.

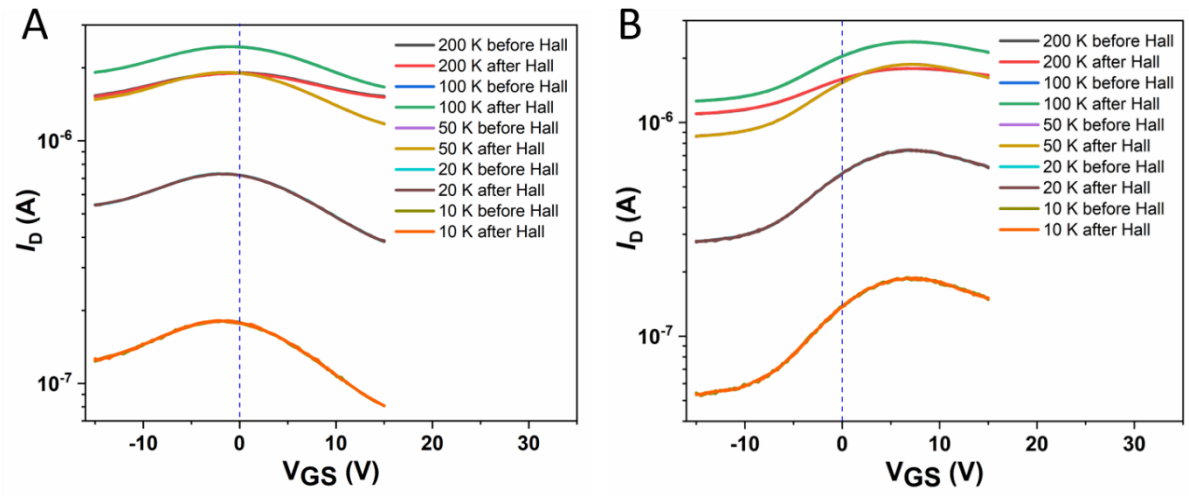

Figure 3-17. Transfer curves for a 13.1 ± 1.1 nm HgTe QD Hall bar device. (A) ~1 e/QD doping (B) ~0.5 e/QD doping at the temperature range from 10 to 200 K. Transfer curves for a HgTe QD Hall bar device with both forward and reverse scans are included. The hysteresis-free transfer curves support a highly reversible charging/discharging process. In the meantime, the transfer curves, before and after Hall measurements, overlap with each other, further verifying that there was no change of the HgTe QD active layer during the Hall measurements. This figure is adapted from ref 47.

The Hall mobilities agree well with FET mobilities in a temperature range from 100 to 10 K (**Figures 3-18B**). Further cooling down induces larger device resistance that limits the constant currents that can be used and no reliable Hall mobility could be measured. It is worth noting that, for a doping level ~1e/dot shown in **Figure 3-17A**, the FET mobilities are extracted in the linear region that is below the 1e/dot doping level while the Hall mobilities are measured close to 1e/dot condition. FET mobilities and Hall mobilities were therefore measured under different doping levels. We addressed this concern by purposely oxidizing the same Hall bar device, i.e., exposing the device to air. This lowers the n-type doping, as shown in **Figure 3-17B**, close to 0.5 e/dot condition. Importantly, this means that the Hall mobilities are measured in the linear mobility

region where FET mobilities are extracted. **Figure 3-17A** shows the scan of the magnetic field applied to a 13.1 ± 1.1 nm HgTe QD film, and the Hall voltages recorded at different temperatures. **Figure 3-17B** compares μ_e^{Hall} and μ_e^{FET}, both measured at ~0.5e/QD doping. The measurements show that the μ_e^{Hall}/μ_e^{FET} the ratio is within 50% of unity across all temperatures. Interestingly, the air exposure also improves the FET mobilities while the trend was well maintained, i.e., peak mobility of 4.84 $cm^2V^{-1}s^{-1}$ was achieved at 100 K. The mobility remained 0.60 $cm^2V^{-1}s^{-1}$ at 10 K. The FET mobilities, once again, agree well with Hall mobilities (**Figure 3-18B**). This further verifies that, indeed, for HgTe QD films, the Hall mobilities are comparable to FET mobilities.

Hall mobility (μ_H) and concentration (n_H) were calculated from the following equations by fitting experimental data:

$$\mu_H = \frac{h\sigma}{BI}|V_H|, \quad n_H = \frac{BI}{eh}\frac{1}{|V_H|}, \quad (3\text{-}3)$$

where *I*, *B*, σ, and *h* are the applied current, magnetic field, conductivity, and film thickness, respectively. The V_H values, measured from four different contact configurations, were averaged to calculate μ_H and n_H. Note that, for the Hall bar geometries used in this work, the ratio of channel width to channel length is small. For the comparison between FET- and Hall mobilities, the channel width was corrected by measuring the channel width for every device using an optical microscope.

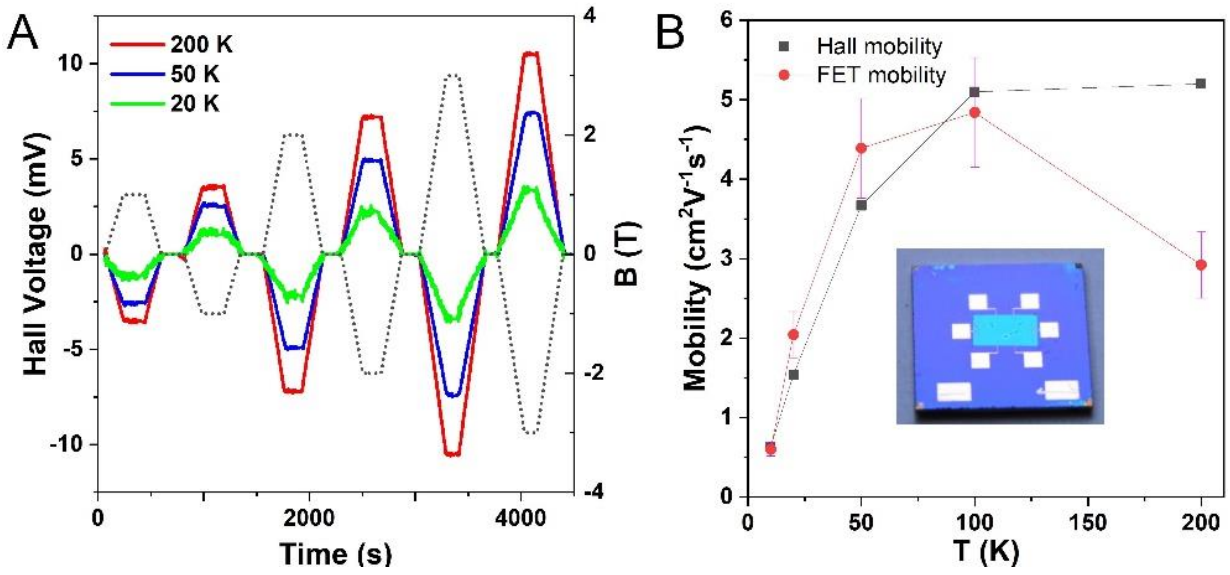

Figure 3-18. **Hall effect on HgTe QD films.** (A) The magnetic field (dashed line) applied to a film of 13.1 ± 1.1 nm HgTe QDs with ~0.5 e/QD doping and the Hall voltage (solid lines) recorded at different temperatures from 20 to 200 K. (B) The comparison of the Hall and FET mobilities measured for the same HgTe QD film. The error bars associated with the FET mobilities originate from the deviation of the channel widths, where the real channel width, as defined by the HgTe QD film, set the lower limit and the photolithographically-defined source/drain-electrode-length the upper limit. The FET mobilities were averaged between the upper and lower limits. The major error bars associated with the Hall mobilities originate from the determination of the hall bar resistance measured by the Van der Paul method (relative error ~5 % estimated following the NIST guideline) The inset shows the Hall bar capacitively coupled to a silicon back gate. This figure is adapted from ref 47.

5. Seebeck Effect Measurements

For Seebeck coefficient measurements, a home-made substrate holder (**Figure 3-20A**) was used such that the measurements could be performed by a Physical Property Measurement System (PPMS, Quantum Design). Two parallel Au bars were patterned on a fused silica wafer with a separation of 3 mm. HgTe QDs were deposited on the substrate such that the two Au bars were well connected both mechanically and electrically and shown in **Figure 3-20B**. The films were

left inside the glovebox overnight, which was then pumped inside a thermal evaporation chamber overnight to get rid of residual solvents. For the temperature-dependent Seebeck coefficient measurements, the temperatures were controlled by PPMS. At a fixed temperature, a small constant current was applied by Keithley 2400 to one of the hotplates, resulting in a temperature difference between the two Au bars. An Agilent 34410A Digital Multimeter was used to measure the thermal voltages and to read the temperatures from the two thermocouples. Thermal voltages (ΔV) between the two Au bars were recorded by monitoring the voltage differences between the two Cu legs of both thermocouples. The temperature differences (ΔT) could be derived from the voltage differences associated with the two T-type thermal couples. Seebeck coefficients of HgTe QD film relative to Cu were then calculated using the equation $S = -\Delta V/\Delta T$. At the same time, the resistances of the devices at different temperatures were also recorded by the Multimeter.

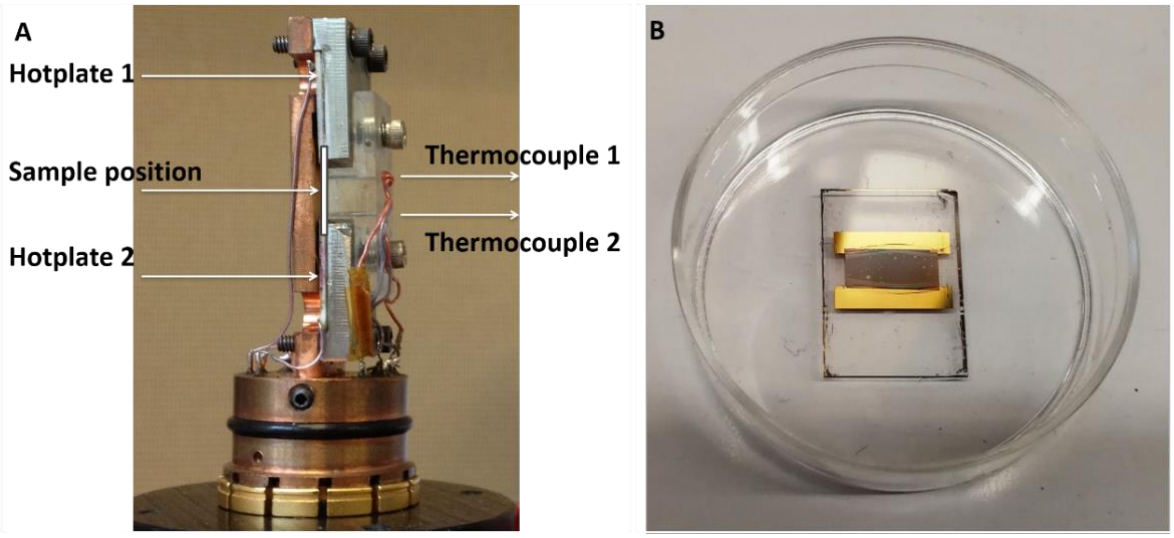

Figure 3-19. Seebeck setup. (A) Sample holder for Seebeck coefficient measurements and (B) the picture of a device used for thermopower measurements. This figure is adapted from ref 47.

The temperature-dependence of Seebeck coefficient (S), $S = -\Delta V/\Delta T$, is presented in **Figure 3-20** for 13.1 ± 1.1 nm HgTe QD film with a ~ 0.5e/dot doping level. The data show a negative S, consistent with the electron being the charge carrier and linear scaling with temperature with a magnitude of 31 μV/K at 200 K.

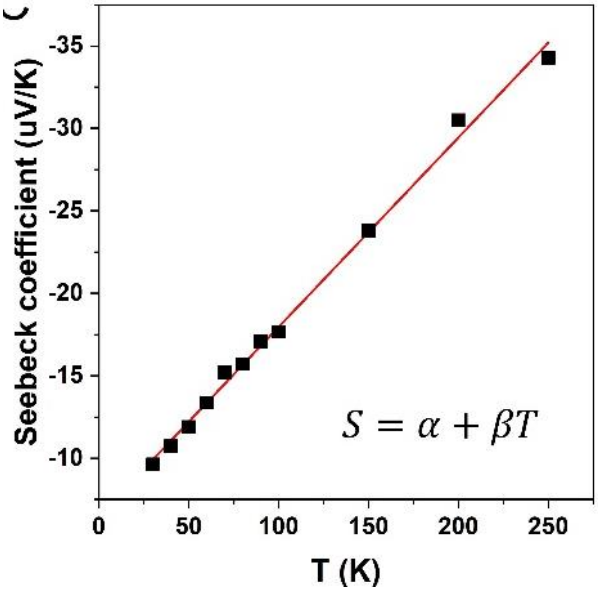

Figure 3-20. The temperature-dependent Seebeck coefficient. Seebeck coefficient measured for a 13.1 ± 1.1 nm HgTe QD solid across a temperature range from 30 to 250 K. The film was made on a glass substrate in the same conditions as the film with doping level is expected to be ~ 0.5e/dot. This figure is adapted from ref 47.

3.1.4 HgTe QD Transport Mechanism Discussion

The fully reversible and state-resolved transport with $\mu_e^{FET} \approx \mu_e^{Hall} > 1$ $cm^2V^{-1}s^{-1}$ properties, makes HgTe QD system convenient to discuss transport mechanisms in QD solids. In the low-mobility samples, electrons move by thermally activated hops.[14] It remains an open question of what mechanisms can account for high mobility QD films, with a spread of viewpoints on the ability to achieve delocalized transport through QD states.[7,8,17,18] In crystalline and disordered semiconductors, an insulator-to-metal transition, evidenced by a finite conductance at zero temperature, can be observed at sufficiently high doping.[25] In our case, the mobility drop at low temperatures does not support the metallic behavior at zero temperature. However, it is transported at finite temperature and low doping levels that are relevant for practical applications of QDs in photodetectors and LEDs.

The bandlike regime is suggestive of some delocalization.[22] Yet since the same behavior can be mimicked by hopping we are compelled to discuss various models.[18]

1. The Marcus model for non-adiabatic hopping

A hopping model is the small-polaron Marcus electron transfer model given by[26,27]

$$\mu(T) = \frac{e(d+l)^2}{\hbar}\frac{2\pi}{6}\frac{J^2}{\sqrt{4\pi\lambda(k_BT)^3}}exp\left(\frac{-(\lambda+\Delta G)^2}{4\lambda k_BT}\right), \quad (3\text{-}4)$$

where J is the electronic transfer integral, λ is the reorganization energy, and ΔG is the energy disorder. “Band-like” behavior was observed for QDs larger than 7.6 nm as shown in **Figure3-21**. The fits use calculated reorganization energy λ discussed below, to extract the two parameters of

disorder energy ΔG and the coupling energy J. There are therefore only two adjustable parameters used for fitting experimental data.

Table 3-1 gives the fitting parameters. As the reorganization energy λ decreases with increasing QD size, the disorder energy ΔG also decreases with size, as expected, and the magnitudes are smaller than the values estimated in Supplementary Discussion 1, but generally within the same order of magnitude. The coupling energy is relatively constant at J ~ 1 meV. The magnitude is reasonable, consistent with small shifts of the optical spectra in film and solutions. The lack of significant size effect on J may be a compensation between two effects: as particles become smaller, the 1Se energy increases, lowering the barrier for tunneling and increasing coupling, while the tunneling should also scale like an area of contact and therefore decrease.

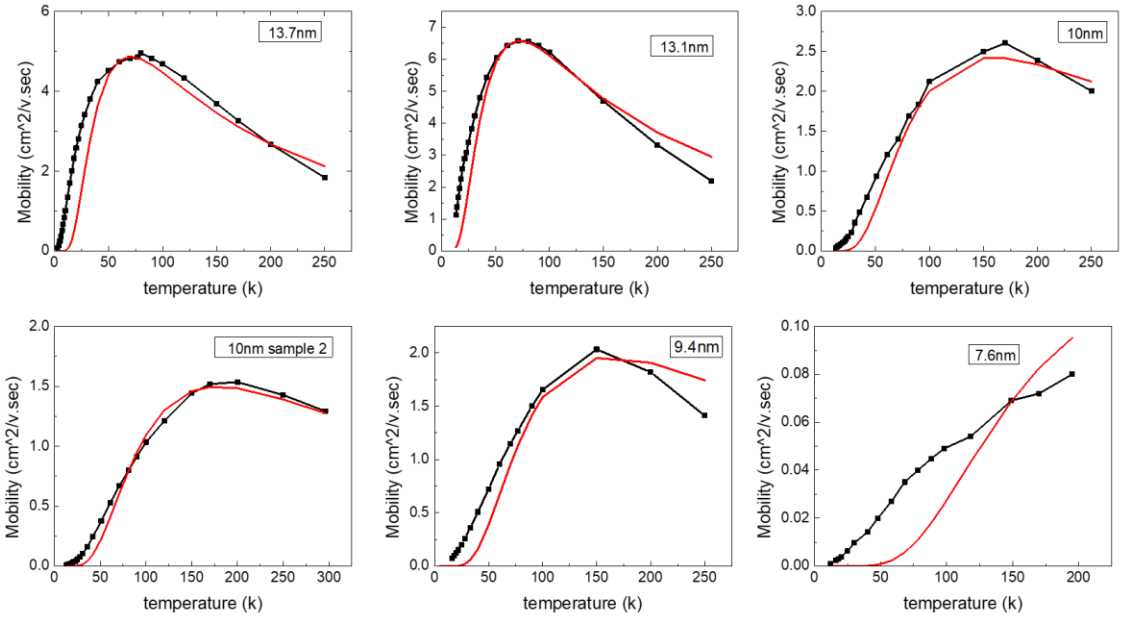

Figure 3-21. Marcus theory fitting for μ_e^{FET} in the films of HgTe QDs with different sizes.

Table 3-1. Parameters used in the Marcus theory fitting.

QD size	Calculated λ	ΔG	J
13.7 nm	5mV	8.5mV	1mV
13.1 nm	6.3mV	9mV	1.3mV
10 nm	7mV	17mV	1.6mV
10 nm (sample2)	7mV	18.5mV	1.5mV
9.4 nm	8mV	18mV	1.8mV
7.6nm	17mV	35mV	1.1mV

Estimation of QD reorganization energy: The reorganization energy is due to the polarization of the material. An estimate, as provided by Prodanovic et al,[27] is

$$\lambda = \frac{e}{4\pi\varepsilon_0}\left(\frac{1}{r} - \frac{1}{2(r+l)}\right)\left(\frac{1}{\varepsilon_M} - \frac{1}{\varepsilon_{st}}\right) \quad (3\text{-}5)$$

where e is the elementary charge $1.6 \times 10^{-19}\ C$, $\varepsilon_M = 7.3$ is the optical dielectric constant of the matrix surrounding QDs, ε_{st} is its static dielectric constant. For an approximation of ε_{st}, the static dielectric constant for bulk HgTe is 21 while the optical dielectric constant of HgTe is 15.2. We scale ε_{st} with the same factor as bulk HgTe. ε_0 is the vacuum permittivity $8.85 \times 10^{-12}\ F/m$, l is the interdot separation and r the radius of the QDs. With a dot separation of $l = 0.5\ nm$ and a dot radius of $r = 6.5\ nm$, the reorganization energy is then $\lambda \sim 5$ meV. Smaller values result if the matrix is more polarizable.

Estimation of QD Charging energy: another estimate for λ is to use the electron-electron repulsion[18], E_c, using the equation:

$$E_c = \frac{e}{4\pi\varepsilon_M\varepsilon_0 r} \times \frac{l}{r+l} \qquad (3\text{-}6)$$

where e is the elementary charge $1.6 \times 10^{-19}\ C$, ε_M is the dielectric constant of the matrix surrounding QDs, ε_0 is the vacuum permittivity $8.85 \times 10^{-12}\ F/m$, l is the interdot separation and r the radius of the QDs. With a dot separation of $l = 0.5\ nm$ and a dot radius of $r = 6.5\ nm$, the charging energy is calculated to be 2.3 meV.

Taking HgTe QDs with d = 13.1 nm as an example, with interdot spacing l = 0.4 nm, and assuming reorganization energy of λ ~5 meV, the Marcus model gives ΔG = 9 meV, and J = 1.3 meV. Results on smaller sizes show increasing activation energy consistent with larger disorder and reorganization energy, and the disappearance of the bandlike regime. Therefore, the Marcus model provides a plausible model for mobility magnitude and dependence on size and temperature. However, it seriously underestimates the mobility at low temperature. As shown in **Figure 3-22B**, there is very low activation energy from 50 K to 5 K, of the order of 1.7 meV. It, therefore, seems that the electrons easily find paths with low energy barriers. At the lowest temperatures, there is also an increasing deviation from the Arrhenius behavior. This is expected for a system with a range of activation energies.

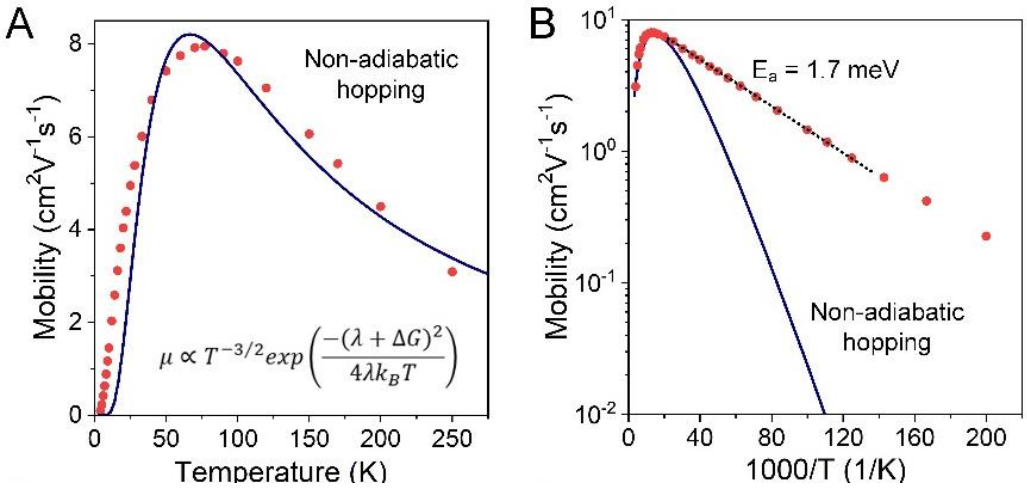

Figure 3-22. Charge transport studies of 13.1 ± 1.1 nm HgTe QD solids. (A) Temperature-dependent FET mobility (μ) compared to the Marcus theory for non-adiabatic hopping. (B) The mobility follows Arrhenius behavior at the temperature range from 5 to 50 K with activation energy (E_a) under 2 meV, while the Marcus theory shows large deviations from the experiment. This figure is adapted from ref 47.

2. Efros-Shklovskii Variable-Range Hopping

Electron-electron interactions are also expected to lead to the Efros-Shklovskii Variable-Range Hopping (ES-VRH)[14,25] with

$$\mu(T) \sim \exp\left[-(T_{ES}/T)^{1/2}\right] \qquad (3\text{-}7)$$

Since VRH is a scaling argument, it is accurate in the limit of weak coupling, where the mobility drops by several orders of magnitude with temperature. Therefore, there is limited validity to fit the data to the VRH model here. Besides, there is no prescription for the pre-exponential factor. Nevertheless, since the Einstein relation suggests a T^{-1} preexponential factor,[18] we applied Eq. (3.7) to the mobility data of 13.1 ± 1.1 nm HgTe QD solids and obtained $T_{ES} \approx 350\ K$ (**Figure 3-23**).

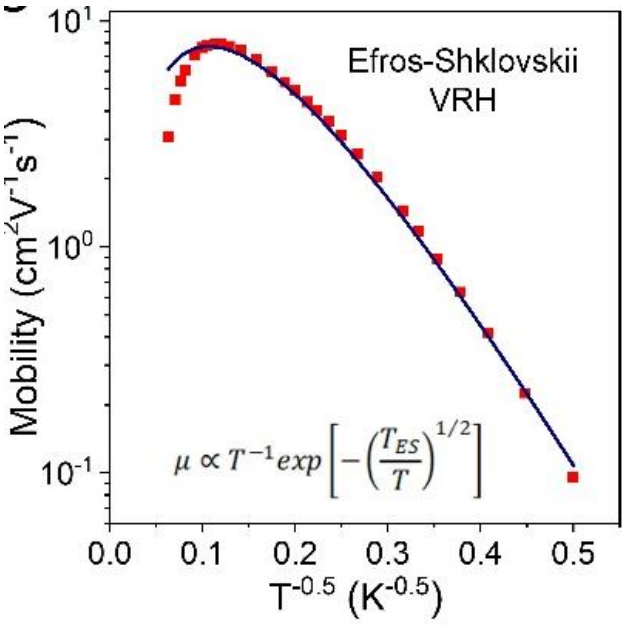

Figure 3-23. Efros-Shklovskii Variable-Range Hopping. Best fit for the temperature-dependent mobility of 13.1 ± 1.1 nm HgTe QD using the Efros-Shklovskii variable range hopping with T^{-1} preexponential factor obtained from the Einstein relation. This figure is adapted from ref 47.

The electron localization length is given by $\xi = \beta e^2/(4\pi\varepsilon\varepsilon_0 k_B T_{ES})$, where ε is a macroscopic dielectric constant, β is a numerical constant (β_{3D}~2.8 for 3D transport and β_{2D}~6.1 for 2D transport).[25] Since in a QD FET major charge transport occurs through one layer of QDs adjacent to the gate dielectric,[28] the 2D case is more relevant. This analysis, using $\varepsilon = 7.3$ estimated by the optical dielectric constant of HgTe QD films, which is also in agreement with the Maxwell-Garnett theory, gives $\xi_{2D} = 39\,nm$ that exceeds the diameter of individual HgTe QDs, suggesting delocalization of electrons over multiple QDs. One should be careful with taking this number as a quantitative measure for the degree of delocalization because a larger value of ε is possible, as it is the static dielectric constant of QD films that should be used (ε=20.9 for bulk HgTe would be an upper limit), and the localization length would then be proportionally smaller. At the same time, the recent studies suggest using β~9.6 for doped semiconductor nanocrystals,[8] which would

proportionally increase the localization length. It has been argued that $\xi > d$ manifests an approach to the metal-insulator transition in highly doped nanocrystalline materials.[8,10]

3. Other Model

Recent theoretical studies of the insulator-to-metal transition in organic and granular semiconductors point to the importance of the domain-localization regime.[29-32] An alternative to a hopping model may be a heterogeneous system with delocalized transport within locally coherent domains of multiple QDs, separated by insulating barriers with hopping conduction. At high T, σ is controlled by delocalized transport within such domains, while at low T slow inter-domain hops create transport bottlenecks.

Careful inspection of high-resolution SEM images (**Figure 3-2**) shows small cracks and variations in local packing density of QDs, similar to sketch in **Figure 3-24**. Conduction in such systems should take into account sample heterogeneity. Such models have been developed for conducting polymers approaching the insulator-to-metal transition.[16,17] There, the conductivity of regions with ordered polymer chains is high, while the total resistance is also affected by the disordered regions along the current path.

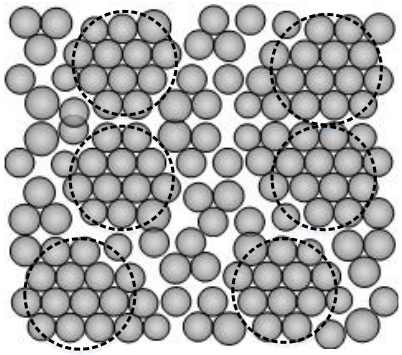

Figure 3-24. A sketch showing local variations in the packing density of individual QDs. This may result in formation of strongly-coupled domains of finite size separated by barriers with weaker coupling between QDs.

Assuming that the conduction paths consist of combinations of higher- and lower-conductivity regions, tour collaborator Prof. Dmitri Talapin fits experimental conductance data to a simple model of series resistances for islands with dispersive band transport and conductivity σ_M, separated by regions with hopping conductivity σ_{hop}, with a temperature dependence identical to ES-VRH or hopping conductivity in granular metals:[17,18]

$$\sigma_M(T) = \sigma_M^*(T/T^*)^{-3/2} \qquad (3\text{-}8)$$

$$\sigma_{hop}(T) = \sigma_{hop}^* exp\left[-(T_0/T)^{1/2}\right] \qquad (3\text{-}9)$$

A phenomenological form

$$\sigma(T)^{-1} = AT^{3/2} + Bexp\left[\left(\frac{T_0}{T}\right)^{1/2}\right] \qquad (3\text{-}10)$$

has been proposed for highly doped organic conductors, where metallic regions are separated by insulating barriers with hopping conduction.[32] This is conceptually similar to the models used for organic conductors, where good agreement with experimental data was observed for highly-doped polyaniline, polypyrrole and some other materials near the insulator to metal transitions.[17]

Figure 3-25 shows that the three-parameter fit with **Eq. (3.10)** is in excellent agreement with the experimental conductivity data for 13.1 nm HgTe QDs. If we take T_0 =121 K as an approximation for T_{ES} in ES-VRH scaling, we can estimate the localization length $\xi = \beta e^2/(4\pi\varepsilon\varepsilon_0 k_B T_{ES})$. Using parameters discussed before, $\xi_{3D} = 64\ nm$, which can be related to the size of domains with metallic conductivity. Excellent fits are also obtained for the other sizes as shown in **Figure 3-26**. **Table 3-2** shows the parameters extracted from the fits.

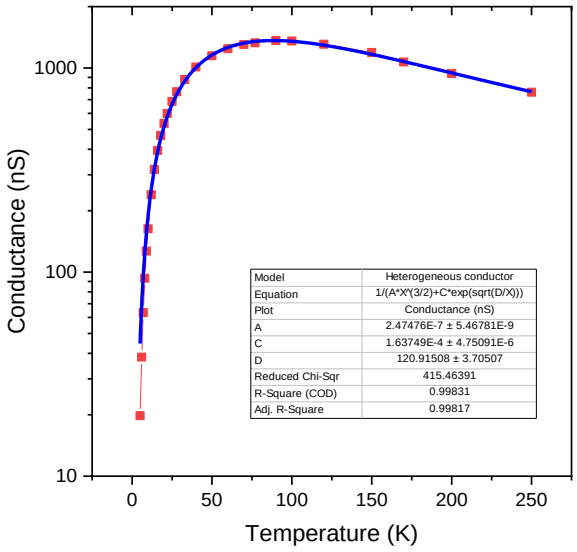

Figure 3-25. Temperature-dependent conductance of ungated 13.1 ± 1.1 nm HgTe QD film with ~0.55 e/QD doping level. Blue line shows the fit to a model used for heterogeneous conductors with metallic regions separated by insulating barriers. This figure is adapted from ref 47.

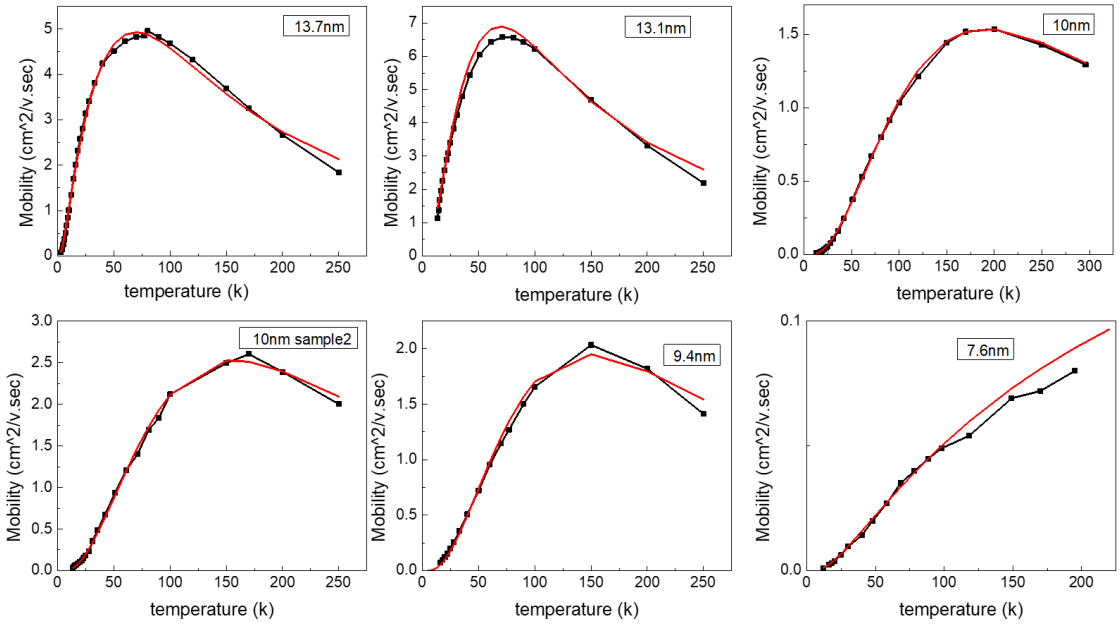

Figure 3-26. Fits of the mobility for all samples using the heterogeneous conductor model.

Table 3-2. Parameters used in the heterogeneous conductor model fits in **Figure 3-26**

QD size	$\boldsymbol{A}$	**B**	$\boldsymbol{T_0}$
13.7nm	0.97×10^{-4}	0.047	90K
13.1nm	0.86×10^{-4}	0.02	169K
10nm	1.0×10^{-4}	0.049	815K
10nm (sample2)	0.82×10^{-4}	0.031	642K
9.4nm	1.16×10^{-4}	0.04	608K
7.6nm	0.58×10^{-4}	2.62	404K

It is also not clear how spatial heterogeneity can coexist with nearly ideal Hall effect observed in HgTe QD solids. In the organic conductor literature, a value close to unity for μ^{Hall}/μ^{FET} is supporting evidence for delocalization.[33-37] This is because highly doped crystalline semiconductors always show a ratio close to unity, as opposed to disordered hopping semiconductors which show anomalously low Hall mobility. However, delocalization is not a strict requirement since a ratio close to unity can be observed for ions in electrolytes.[38] Hopping also causes a conceptual problem since there is no velocity, therefore no Lorentz force and no Hall effect. Holstein proposed that the magnetic field modifies the interferences for the different pathways between several sites, such that hopping can still lead to a Hall effect albeit not necessarily ideal.[39,40] One experimental study for crystalline Ge in the impurity hopping regime showed no measurable Hall effect and therefore did not support Holstein's predictions.[41] However, an ideal Hall mobility may still be obtained in a particular case of hopping. A proposed proof is to consider a random walker of charge q, with a single hopping time, τ, between neighboring sites

separated by a distance d. The diffusion coefficient is $D = \frac{d^2}{6\tau}$, and the drift mobility is $\mu_D = \frac{qD}{kT}$. When an electric field, E_x, is applied in the longitudinal direction, the charge distribution spreads and also drifts at a velocity $v_x = \mu_D E_x$. In a reference frame that moves at the drift velocity, the charge distribution only spreads. Now, one adds a magnetic field B_z in the z direction. In the fixed frame, the assumption that hopping produces no Lorentz force leads to no Hall voltage along the y direction. However, the Lorentz force is also specific of the reference frame. In the moving frame, the magnetic field gives rise to an electric field $E_y = -v_x B_z$. The force on the diffusing charge cloud is now electrostatic and identical to the Lorentz force. Therefore, the compensating voltage is consistent with an ideal Hall voltage and mobility. Since the physical result must not depend on the reference frame, the assumption of zero Hall voltage for hopping must be incorrect. If this is true for a unique time τ, it will also be true if the hopping time has a distribution but all carriers explore the same range of time distribution. Then, all carriers have the same average mobility, and Hall mobility should still be ideal. However, if some carriers have different paths, for example, due to their energies, then the Hall mobility can be far from ideal. This situation is seen in weakly doped amorphous semiconductors. An illustrative example is a two-carriers model, where the average drift mobility is $\mu_D = \frac{n_1\mu_1 + n_2\mu_2}{n_1 + n_2}$ while the average Hall mobility is $\mu_H = \frac{n_1{\mu_1}^2 + n_2{\mu_2}^2}{n_1\mu_1 + n_2\mu_2}$, such that the two values can be very different. In the QD solids discussed here, we then propose that the nearly ideal Hall mobility can still be interpreted in the context of hopping on the condition that all carriers follow similar paths.

For the Seebeck effect, in organic conductors, the linear $S\ vs.\ T$ scaling is taken as indicative of delocalization. For example, the transition from $S \propto T^{1/2}$ to $S \propto T$ has been observed in doped

polyaniline and polypyrrole samples as they approached the insulator-to-metal transition.[42] In contrast, for materials conducting by hopping between localized sites, it was predicted that Mott VRH yields $S(T) \propto T^{1/3}$ for 2D and $S \propto T^{1/2}$ for 3D transport, while ES-VRH is characterized with temperature-independent *S*.[43,44] However, a classical charge motion can also lead to a linear $S\ vs.\ T$ scaling, and caution that the Seebeck measurement may be not an unambiguous proof of delocalization as the following detailed discussion by Prof. Philippe Guyot-Sionnest.

For a single moving charge type such as an electrolyte, the particle current is given by $J = -\frac{L}{k_B T}\left[\nabla\tilde{\mu} + \frac{Q}{T}\nabla T\right]$ where $\tilde{\mu}$ is the electrochemical potential, Q is the heat carried by the moving charge, and L is the Onsager coefficient.[45] The electrochemical potential is given by the Fermi level which depends on temperature and particle density n, and the electric potential as $\tilde{\mu} = \mu + qV$.

$$J = -\frac{L}{k_B T}\left[\left(\frac{\partial \mu}{\partial n}\right)_T \nabla n + \left(\frac{\partial \mu}{\partial T}\right)_n \nabla T + q\nabla V + \frac{Q}{T}\nabla T\right]$$

this includes the contribution of the particle current from the diffusion coefficient definition $-D\nabla n$, and the contribution from the conductivity $-\frac{\sigma}{q}\nabla V$. Identification of the terms leads to the relation $\sigma = \frac{Dq^2}{\left(\frac{\partial \mu}{\partial n}\right)_T}$.

For a classical non-interacting gas, $\mu = k_B T \ln n$ so that $\sigma = nq\frac{qD}{k_B T} = nq\mu_q$ where μ_q is the electric mobility and this recovers the Einstein relation. The particle current must be zero at equilibrium and the Seebeck coefficient is defined as $S = -\frac{\nabla V}{\nabla T}$. We take $\nabla n = 0$ because of charge

neutrality. Then $S = -\frac{\frac{\partial \mu}{\partial T}\Big)_n + \frac{Q}{T}}{q}$. We further neglect the heat carried by the charge assuming it to be a small contribution and get the simpler expression

$$S = -\frac{1}{q}\frac{\partial \mu}{\partial T}\Big)_n$$

This expression contains no implicit dependence on conductivity. Since n is constant, we write

$$S = -\frac{1}{q}\frac{\partial n}{\partial T}\Big)_\mu \Big/ \frac{\partial n}{\partial \mu}\Big)_T$$

For $n(\mu, T)$ we use a density of state for 1Se such that

$$n(\mu, T) = \int D(E)\frac{1}{e^{\frac{(E-\mu)}{k_B T}} - 1}dE$$

If the density of state is large around the Fermi level, one can use the Sommerfeld expansion to get $n(\mu, T) \sim \int_{-\infty}^{\mu} D(E)\,dE + {k_B}^2 T^2 \frac{\pi^2}{6} D'(\mu)$

Then we get

$$S = -\frac{{k_B}^2}{q}\frac{\pi^2}{3}\frac{D'(\mu)}{D(\mu)}T \quad (3\text{-}11)$$

This is still the Mott formula but there is nothing specific about the nature of the transport. The only requirement is that there are states that are thermally accessible at the Fermi level so that the Sommerfeld expansion is appropriate. It is therefore proposed that the linearity of the Seebeck coefficient with temperature cannot obviously be used to argue for delocalization.

Aside from the transport mechanism, the high electron and hole mobilities are generally beneficial for QD device applications. We demonstrate this point by comparing the characteristics of two mid-IR photodetectors made of the same batch of 9.0 nm HgTe QDs with our new hybrid mercaptoethanol-$HgCl_2$ (ME-$HgCl_2$) ligands and with traditionally used[2] 1,2-ethanedithiol (EDT) surface treatment, which would be discussed in **Chapter 6**. Whether it is hopping or band transport, the mobility improvement should be similarly advantageous for many other QD devices.[1]

3.1.5 Conclusion

Overall, this work demonstrates that QD solids can achieve high electron mobility without compromising the discrete nature of electronic states. Optimized surface chemistry for HgTe QDs enables about 100-fold mobility improvement compared with any previous QD solids showing state-resolved transport. The band-like temperature dependence suggests some degree of carrier delocalization, but this is also captured by the Marcus hopping model. The nearly ideal Hall effect is also typically accepted as evidence of delocalization but consistent description of transport in high-mobility QD solids still poses a challenge and it remains uncertain whether the mobility arises from hopping or band transport. The benefits of the mobility improvement for QD devices are discussed further in Chapter 6.

3.1.6 Method

1. Materials

$HgCl_2$ (≥98%), iodine (99.99%), 1,2-ethanedithiol (≥98.0% (GC)), HCl (ACS reagent, 37%), 2-Mercaptoethanol (≥99.0%), butylamine (99.5%), isopropanol (≥99.7%, FG), tetrabutylammonium perchlorate (for electrochemical analysis, ≥99.0%) and anhydrous solvents (hexane, toluene, tetrachloroethylene, propylene carbonate, and methanol) were purchased from Sigma Aldrich and used as received. Anhydrous N,N-Dimethylformamide (DMF, 99.8%) and $HgCl_2$ (98+%) were purchased from Alfa Aesar and used as received. Note that the $HgCl_2$ from Alfa Aesar was solely used for solution-phase ligand exchange. Oleylamine was purified following our reported procedures. Bis(trimethylsilyl)telluride (98%) was purchased from Acros and stored inside the freezer in a nitrogen glovebox. N-type Si wafers (Res. ≤0.005 ohm.cm) with 300-nm-thick thermal

oxide were purchased from WaferPro. Ultra-thin Si (25.4 mm in diamter, 73.5 μm in thickness) wafers were purchased from University Wafer.

2. Synthesis of n-butylammonium chloride

N-butylammonium chloride was prepared by using the reaction between HCl and butylamine with a 1:1 molar ratio. The reaction was performed in an ice bath. The product was first dried by using a rotary evaporator, which was further dried in a vacuum oven at 60 ℃ before use.

3. QD synthesis and ligand exchange

HgTe quantum dots (QDs) were synthesized based on a previously reported method.[1,2] For the solution-phase ligand exchange, in a typical process, 0.5 mmol butylammonium chloride, 0.5 mmol mercury(II) chloride, 140 μL 2-Mercaptoethanol and 400 μL n-butylamine were dissolved in 5 mL DMF, forming the hybrid ligand solution. 400 μL HgTe QDs in hexane was then added into the hybrid ligand solution. Slight shaking resulted in the transfer of HgTe QDs from hexane to DMF phase. A one-minute vortexing process was applied to promote the solution-phase ligand exchange. HgTe QDs were precipitated by adding toluene as the anti-solvent, followed by centrifugation at 4,000 r.p.m. for 30 s. After discarding the supernatant, 40 μL DMF was used to dissolve the HgTe QD solids, yielding colloidally-stable HgTe QDs in DMF that were ready for film deposition. The doping of HgTe QDs can be readily tuned by changing the amount of $HgCl_2$. The narrow size distribution has been verified by Small- Angle X-ray Scattering (**Figure 3-27**), with corresponding absorption spectra shown in **Figure 3-28**. The ligand-exchanged HgTe QDs showed negative ζ-potential (**Figure 3-29**).

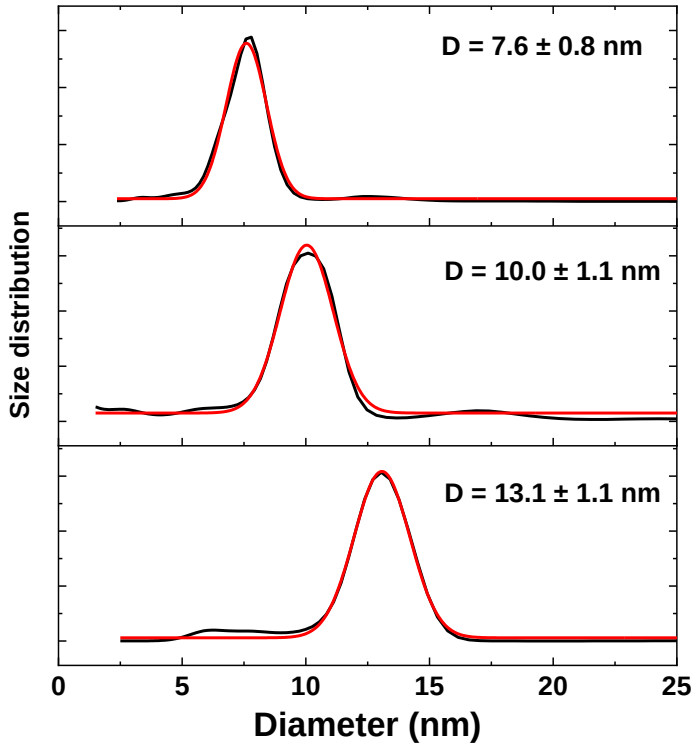

Figure 3-27. Size distribution analysis of ligand-exchanged HgTe QDs with different sizes used for state filling and transport studies. This figure is adapted from ref 47.

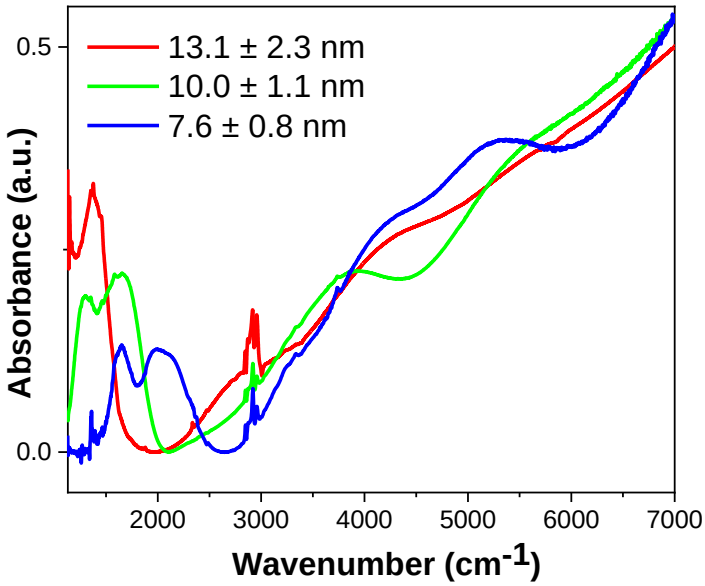

Figure 3-28. Solution absorption spectra of HgTe QDs dispersed in tetrachloroethylene with different sizes used for state filling and transport studies. The sharp peaks near 3000 cm^{-1}

correspond to the oleylamine ligands. Redshifts in the interband and intraband absorption were observed as the size increases, in agreement with a decrease of quantum confinement. This figure is adapted from ref 47.

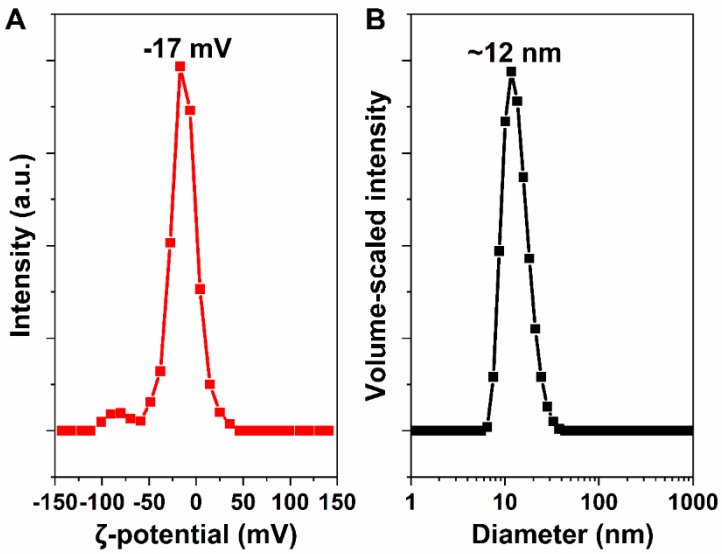

Figure 3-29. (A) ζ-potential and (B) Dynamic Light Scattering analysis of DMF-dispersed HgTe QDs. A negative potential of -17 mV is observed, suggesting the electrostatic contribution to colloidal stabilization. DLS data suggest that the size of HgTe QDs is ~12 nm, in a good agreement with SAXS data (13.1 ± 1.1 nm). This figure is adapted from ref 47.

4. Electrode fabrication process

The substrates (either Silica wafers or fused silica wafers) were cleaned by piranha solution at 270 ℃ for 45 minutes before use. After DI-water rinsing, the substrates were dried by N_2 blow. A layer of hexamethyldisilazane (HMDS) was first deposited by spincoating at 3,000 r.p.m for 45 s followed by mild baking at 115 ℃ for 3 minutes. LOR3A lift-off resists (MicroChem) were then deposited at 3,000 r.p.m for 45 s followed by mild baking at 185 ℃ for 5 minutes. Finally, S1813 photoresist (MicroChem) was deposited at 3,000 r.p.m for 45 s followed by a mild bake at 115 ℃ for 2 minutes. The patterns were then defined by using Heidelberg MLA150 Direct Write

Lithographer. The substrates were then developed in Microposit MF CD-26 Developer. The electrode deposition was performed by using an AJA ATC-Orion 8E e-beam evaporation system. 5-nm Ti adhesion layer was first deposited followed by 100-nm Au. Lift-off was finally performed in Remover PG (MicroChem). The substrates were then thoroughly washed by acetone, 2-propanol, and DI-water, sequentially. N_2 blow was used to dry the substrates. The substrates were finally cut into desired small chips, depending on the targets, by using Disco DAD3240 Automatic Dicing Saw.

5. Solid-state FET fabrication and measurements

Silicon wafers with dry thermal oxide (n^{++} Si/300 nm SiO_2, WaferPro LLC) were used as the substrates. Source and drain electrodes were defined by a photolithography process as discussed above. The deposition of HgTe films was performed inside the glovebox. Before the deposition, the FET substrates were cleaned by O_2 plasma for 10 mins. In a typical spin-casting process, 10 µL DMF-dispersed HgTe QD solution was first dropped on the substrates and uniform films were achieved by spincasting at 2,000 r.p.m for 1 min. The films were kept inside the glovebox overnight to facilitate a slow drying process before any measurements. The devices were then loaded in a Janis cryogenic probe station coupled with a semiconductor analyzer (B1500A, Agilent), followed by ~12 hrs vacuum pumping (~10^{-6} Torr) before the measurements. It is observed that the pumping process leads to improved mobility. We understand that the vacuum pumping process helps to get rid of the residual solvents and volatile ligands, which leads to much denser films and finally delivers improved transport properties.

6. Electrochemically-gated FETs and mobility analysis

The high electron mobility of HgTe CQD films is confirmed by the electrolyte-gating approach. The electrochemistry experiments were performed using a bipotentiostat system (DY2300 series Digi-Ivy), following previous report [3]. The QD films are prepared by spin coating from DMF solution on the Au interdigitated electrode in a manner identical to the samples above. To minimize the Faradaic currents from solution impurities, the cell is cooled to 203 K using an alcohol/dry ice bath. Figure S13A shows the conduction and charging current for the sample, with well resolved peaks for the 1Se state and the 1Pe state, together with evidence for conduction from holes. The voltage dependence of the conductance across the gap between the hole states and the 1Se state is consistent with the Nernst equation. A Nernst slope of 23.0 ± 0.8 V^{-1} is achieved, which is consistent with the temperature of 203 K ($\frac{e}{\ln(10)*k_B T}$= 24.8 V^{-1}). The sample in this measurement was n-doped as determined by the open-circuit potential, indicating between 1 and 2 electrons in the 1Se state. . The maximum mobility—achieved below 1e/dot doping level—is around 1.3 $cm^2V^{-1}s^{-1}$ at 203 K, which is close to FET analysis based on the same batch of HgTe QDs in a similar temperature range. The similarity between the mobility measured by FET and liquid gating is comforting, and at the same time indicates that, for QD solids, the electrolyte does not introduce major scattering of the electrons.

7. Spectroelectrochemical studies

Spectroelectrochemistry experiments were performed by using a bipotentiostat system (DY2300 series Digi-Ivy) coupled with a Fourier-transform infrared spectroscopy (FTIR) setup. The

undoped spectrum, at an applied bias of 0.2 V, is taken as the background. Spectra at more negative potentials (i.e., at different charging levels) are taken with respect to the undoped case.

8. Low-temperature FET measurements

Some low temperature-dependent measurements were carried out using a micro-probe station. Special care was taken to validate the actual sample temperature. Varnish (VGE-7031, Lake Shore) was used to facilitate good thermal contact between the devices and the substrate holder. The devices were further tightened by a few screws. The temperatures were verified by using a calibrated silicon diode (DT-670-SD, Lake Shore Cryotronics Inc.) that was loaded in the same manner with the FET devices. The lowest trusted temperature was verified to be ~13 K. For the low temperature FET and Hall effect measurements, we also used a physical property measurement system (PPMS, Quantum Design) under He-filled inert atmosphere. Hall and Van der Pauw resistivity measurements were performed using a Keithley multimeter (Keithley 2636) controlled by a LabVIEW interface. FET measurements were performed using a semiconductor analyzer (B1500A, Agilent). For devices measured using Physical Property Measurement System (PPMS, Quantum Design), the vacuum pumping processes were performed before the measurements. Due to the improved thermal contact in the He-filled atmosphere, the lowest sample temperature that could be trusted is 4 K.

9. Hall effect measurements and data analysis

The Hall mobilities were measured using a hall bar device architecture. This allows us to probe Hall- and FET mobilities simultaneously. The devices were measured in a Physical Property

Measurement System (PPMS) setup. For the films in the Hall effect study, both solution ligand exchange and the deposition of the films were performed in a N_2 filled glove box. The films were kept in high vacuum at ~10^{-6} torr for ~12 hrs to mimic as much as possible the conditions for regular FET devices.

10. Seebeck effect measurements

For Seebeck coefficient measurements, a home-made substrate holder was used such that the measurements could be performed by a Physical Property Measurement System (PPMS, Quantum Design). Two parallel Au bars were patterned on a fused silica wafer with a separation of 3 mm. HgTe QDs were deposited on the substrate such that the two Au bars were well connected both mechanically and electrically. The films were left inside the glovebox overnight, which was then pumped inside a thermal evaporation chamber overnight to get rid of residual solvents. For the temperature-dependent Seebeck coefficient measurements, the temperatures were controlled by PPMS. At a fixed temperature, a small constant current was applied by Keithley 2400 to one of the hotplates, resulting in a temperature difference between the two Au bars. An Agilent 34410A Digital Multimeter was used to measure the thermal voltages and to read the temperatures from the two thermocouples. Thermal voltages (ΔV) between the two Au bars were recorded by monitoring the voltage differences between the two Cu legs of both thermocouples. The temperature differences (ΔT) could be derived from the voltage differences associated with the two T-type thermal couples. Seebeck coefficients of HgTe QD film relative to Cu were then calculated using the equation $S = -\Delta V/\Delta T$. At the same time, the resistances of the devices at different temperatures were also recorded by the Multimeter. The temperature-dependent conductance was derived from the measured resistance.

11. Photodetection measurement

The photoconduction devices were made of 4 pairs of interdigitated evaporated gold fingers of width 20 microns, gap 20 microns, and length 300 microns, and cover an area of 0.3mm by 0.16mm. As the substrates, we used glass microscope slides or heavily doped Si wafer with 300nm thermally grown SiO_2 layer, for FET measurements on the same device. HgTe QD films were spin coated on the interdigitated electrodes. When measuring the responsivity, the devices faced the 600 °C blackbody source with a 200 Hz chopper. The bias was applied with a 1.5V battery, the current across the sample was amplified by a Femto DLPCA-200 current amplifier and a SR570 voltage amplifier. The noise was measured using a SR760 spectrum analyzer.

Photocurrent spectrum was measured by A Nicolet 550 FTIR spectrometer. The internal glow bar light source was directed to the outer port and imaged on the sample with a 5 cm focal parabolic mirror. Scanning speed of ~0.9 cm/s was typically used (corresponding to ~0.1 msec for the interferogram peak).

12. Ellipsometry measurement

For the ellipsometry measurement, we used the Gaertner Waferskan Ellipsometer Model L116S. Several HgTe/hybrid ligand films with thickness varying from ~80 nm to 260nm were prepared on the Si chips (area: 0.5 inch *0.5 inch, thickness: 1mm).

During the measurement, the HeNe 6328 Angstrom Laser provided less than 1 mW output on sample with 1mm beam diameter at 70° incidence angle. The detector and analyzer then received the reflection and characterized the change of polarization parameters like amplitude ratio and the

phase difference. The optical index was calculated from the polarization parameters. The imaginary part of the refraction index was usually quite small, so we estimated the permittivity of high mobility HgTe as ~n^2 (n is the real part of refraction index).

3.1.7 Appendix

1. Estimation of inhomogeneous broadening and state disorder

QD polydispersity provides a major contribution to disorder of the energy states involved in charge transport (static disorder ΔG, for example). We used several methods to estimate the disorder for the band gap, 1Se and 1Sh states.

The polydispersity results in broadening of the excitonic transitions in the optical absorption spectra. **Figure 3-30** shows the absorption spectra for samples of HgTe QDs with different size used for transport studies fit using a sum of Gaussians and a parabolic background, and **Table 3-3** summarizes full width at half maxima of the excitonic transitions. The width of the excitonic peaks includes both homogeneous and inhomogeneous broadening, and can therefore provide only a rough upper limit for the size-related distribution of the band gap energies. Moreover, the relative intensity of the first excitonic peak decreases with increasing QD size. The small contribution of this peak to the fits for larger QDs complicates the extraction of accurate peak width.

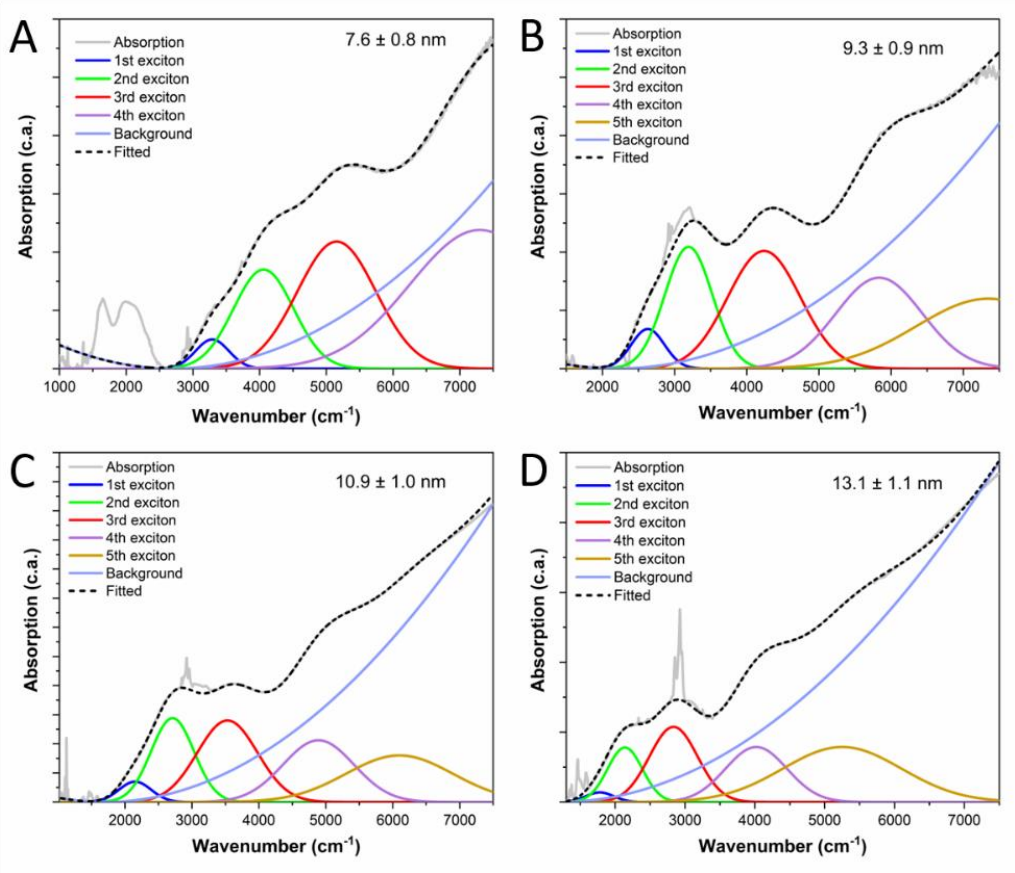

Figure 3-30. Solution absorbance spectra of different sizes of HgTe QDs and fits corresponding to a sum of Gaussians and a parabolic background. This figure is adapted from ref 47.

Table 3-3. Analysis of the excitonic features in the absorption spectra of colloidal HgTe QD samples used for transport studies.

QD diameter ± std. dev. (nm)	1st exciton energy	1st exciton FWHM	2nd exciton energy	2nd exciton FWHM	3rd exciton energy	3rd exciton FWHM
	Transition I		Transition II		Transition III	
13.1 ± 1.1 (*)	1780cm^{-1} 0.221 eV	470cm^{-1} 58 meV	2140cm^{-1} 0.265 eV	590cm^{-1} 73 meV	2835cm^{-1} 0.352 eV	812cm^{-1} 101 meV
12.5 ± 1.0	1950cm^{-1} 0.242 eV	590cm^{-1} 73 meV	2305cm^{-1} 0.286 eV	636cm^{-1} 79 meV	2964cm^{-1} 0.368 eV	800cm^{-1} 99 meV
10.9 ± 1.0	2150cm^{-1} 0.267 eV	565cm^{-1} 70 meV	2710cm^{-1} 0.336 eV	754cm^{-1} 93 meV	3530cm^{-1} 0.438 eV	1060cm^{-1} 131 meV
9.3 ± 0.9	2630cm^{-1} 0.326 eV	542 cm^{-1} 67 meV	3195cm^{-1} 0.396 eV	780 cm^{-1} 97 meV	4240cm^{-1} 0.526 eV	1190 cm^{-1} 148 meV
7.6 ± 0.8	3290cm^{-1} 0.408 eV	590 cm^{-1} 73 meV	4060cm^{-1} 0.503 eV	1060 cm^{-1} 131 meV	5155cm^{-1} 0.639 eV	1390 cm^{-1} 172 meV

The energy difference between 1Sh and 1Se states can be obtained from the optical band gap by using corrections for the 1Se-1Sh exciton binding energy $E_b = -1.78\frac{e^2}{4\pi\varepsilon_{QD}\varepsilon_0 r}$, and polarization energy $E_p = -\frac{e^2}{4\pi\varepsilon_0 r}(\frac{1}{\varepsilon_M}-\frac{1}{\varepsilon_{QD}})$: $E_{1Sh\text{-}1Se} = E_g$ (optical) + $1.78\frac{e^2}{4\pi\varepsilon_0\varepsilon_{QD} r}+\frac{e^2}{4\pi\varepsilon_0 r}(\frac{1}{\varepsilon_M}-\frac{1}{\varepsilon_{QD}})$, where ε_{QD} is the optical dielectric constant of HgTe (ε_{QD} =15.2) and ε_M is optical dielectric constant of the matrix ((the average dielectric constant of the medium around each NC, can be estimated as the volume-weighted average of dielectric constants for the organic spacer (~2) and for the HgTe NC(~ 15.2) using Maxwell Garnett equation, giving ε_M~7, similar to the measured HgTe QDs film optical dielectic constant 7.3). **Table 3-4** summarized these corrections applied to studied HgTe QD samples.

Table 3-4. Corrections used to relate the optical band gap to the energy gap between1Sh and 1Se states for HgTe QDs.

Size (SAXS)	**E_g (optical)**	**Binding energy**	**Polarization**	**$E_{1Sh-1Se}$**
7.6 nm	0.408eV	44.3 meV	29.4 meV	0.482 eV
9.3 nm	0.326eV	36.2 meV	24.0 meV	0.386 eV
10.9 nm	0.267eV	30.9 meV	20.5 meV	0.319 eV
12.5 nm	0.242eV	27.0 meV	17.8meV	0.288 eV
13.1 nm	0.221eV	25.7 meV	17.1meV	0.264 eV

To resolve inhomogeneous effects from the homogeneous contributions to spectral broadening, we estimated inhomogeneous broadening using the size distribution derived from Small-Angle X-ray Scattering (SAXS) measurements. The standard deviation of the QD diameter was converted to full width at half-maximum. The minimum and maximum diameters for the calculation were computed as: $d_{min} = d_{average}$ - (fwhm/2) and $d_{max} = d_{average}$ + (fwhm/2). These values were plugged into an empirical sizing curve to calculate the peak energies corresponding to d_{min} and d_{max}, and the difference between the resulting E_{min} and E_{max} yields the broadening of the excitonic peak that can be attributed to nanocrystal polydispersity. We used empirical sizing curves for the first three excitonic transitions of HgTe quantum dots. Next, the distribution of optical bandgaps was corrected to account for the exciton binding energy and polarization as described above. The results are summarized in **Table 3-5**.

These data can be compared to the electronic structure of HgTe QDs calculated using a two-band k • p model with the Kane parameter E_p=15.5eV and E_g = -0.32eV.[5] The HgTe band structure close to the Γ-point, calculated within this model, showed an excellent agreement with the results obtained by more elaborate tight-binding and eight-band k • p calculations.[6] Based on size and size

deviation measured form SAXS, and taking $k = {}^{2\pi}/_{d}$ for the S-type state, one can calculate the energy gap between 1Sh and 1Se states and the spread of energies associated with the QD size distribution as shown in **Figure 3-3**2 and summarized in **Table 3-5**. There is a good agreement between the numbers obtained using the experimental sizing curve and the k • p model. For large QDs, the agreement between theory and experiment is nearly perfect while for sub-10nm QDs, the k • p model somewhat overestimates the confinement energy, likely because of not accounting for the final height of the confinement potentials, the complex structure of the valence band and spin-orbit coupling effects.

Table 3-5. Measured and calculated band gap energies of HgTe QDs of different size. The disorder of band gap energies was calculated for sample size distributions derived from Small-Angle X-ray Scattering (SAXS) data.

QD size ± std. dev. (SAXS)	**$E_{1Sh-1Se}$ (optical, corrected)**	**ΔE_g optical (FWHM)**	**$\Delta E_{1Sh-1Se}$ (FWHM)**	**$E_{1Sh-1Se}$ (k • p)**	**$\Delta E_{1Sh-1Se}$ (calculated, FWHM)**
7.6±0.8 nm	0.491 eV	0.128 eV	149 meV	0.571eV	195 meV
9.3±0.9 nm	0.393 eV	0.082 eV	103 meV	0.432eV	131 meV
10.9 ±1.0 nm	0.325 eV	0.069 eV	79 meV	0.346eV	107 meV
12.5±1.0 nm	0.292 eV	0.049 eV	59 meV	0.284eV	79 meV
13.1±1.1nm	0.269 eV	0.049 eV	58 meV	0.265eV	77 meV

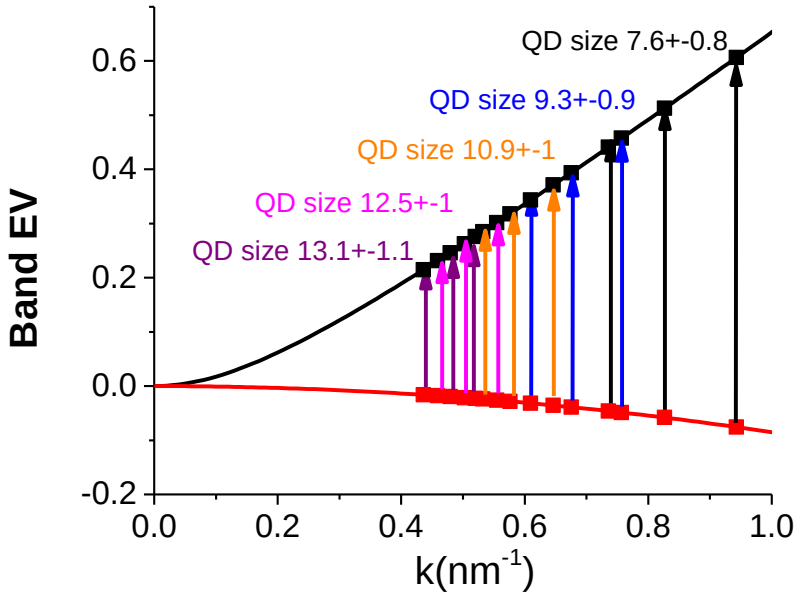

Figure 3-31. The band structure of HgTe near the Γ-point, calculated using two-band k • p model. The points represent energies corresponding to QDs with sized in the middle of size distribution, $d_{min} = d_{average}$- (fwhm/2) and $d_{max} = d_{average}$ + (fwhm/2). The width of QD size distribution was measured by SAXS. This figure is adapted from ref 47.

Due to a large difference in the effective masses of the electron and hole, the electron wavefunction experiences much stronger quantum confinement compared to the hole wavefunction and is, therefore, more sensitive to QD size dispersion. **Figure 3-31** shows the band structure of HgTe close to the Γ-point, with energies corresponding to the average QD size, $d_{min} = d_{average}$- (fwhm/2) and $d_{max} = d_{average}$ + (fwhm/2). These data allow us to separately estimate the disorder of 1Se and 1Sh states introduced by QD size distribution. We summarized the static disorder of 1Se and 1Sh states in Table SD1-4. The disorder of the1Se state is almost an order of magnitude larger than the disorder of the 1Sh states. One can also note that the state energy disorder significantly increases with decreasing QD size.

For the 13.1 ± 1.1 nm HgTe QD sample, our analysis suggests that the energy disorder of 1Se states participating in the charge transport is 70 meV. Taking into account that the two-band k • p model overestimated the disorder of 13.1 nm QDs by about 25% compared to experimental result (**Table 3-5**), the corresponding 1Se state disorder may is likely to be similarly overestimated, which gives ~50 meV (fwhm) as a reasonable lower estimate for the disorder of 1Se states in a film of 13.1 ± 1.1 nm HgTe QDs. This value is smaller than the previously reported energy disorder in high-quality CdSe samples.[7]

Table 3-6. Energy disorder in HgTe QD solids caused by size polydispersity.

QD diameter (nm)	**$\Delta E(1S_e)$ (meV)**	**$\Delta E(1S_h)$ (meV)**
13.1 ± 1.1	70	8
12.5 ± 1.0	70	9
10.9 ± 1.0	94	13
9.3 ± 0.9	114	17
7.6 ± 0.8	165	30

3.2 HgSe QD System

The hybrid ligand exchange discussed in section 3.2 allowed to raise the mobility ~ 100-fold for HgTe CQD films reaching a new regime of conductivity in CQD solids where high mobility and state-resolved conductivity are simultaneously achieved. I ask myself whether it is only a coincident success in HgTe QD films or if I could apply this method to a different QD system with similar improvement. I therefore investigated HgSe QDs. HgSe bulk is a zero-gap semimetal with reversed Γ_6 and Γ_8 band[48] similar to HgTe. However, in contrast to HgTe[49], colloidal quantum dots (CQD) of HgSe are naturally n-doped and display an intense mid-infrared absorption between the lowest electron state labeled 1Se and the next level 1Pe[50-52]. Ag_2Se CQDs also display an intense mid-infrared absorption[53] assigned to an intraband transition and they are attractive for their lower toxicity[54], but the photoconduction properties have been poorer[55]. The HgSe CQDs offer therefore the more promising system for intraband CQD devices and this justifies further studies of the transport properties.

In this section, I apply the hybrid ligands exchange procedure to HgSe CQDs and also get 2 orders improvement in mobility compared to the solid state ligand exchange method which was discussed in chapter 2. I also compare carrier density and mobility values obtained by temperature dependent FET and Hall effect measurements to inform on the transport mechanism.

3.2.1 HgSe QD Characterization

The CQD synthesis follows the former method[50] with oleylamine(OAM) as ligand and $HgCl_2$ and selenourea as reagents. After the reaction, the CQDs are precipitated and redispersed in hexane. HgSe CQDs are drop cast or spin-cast directly from that solution and then cross-linked using ethanedithiol, to make the HgSe/EDT films. Alternatively, the CQDs are transferred to DMF using a hybrid ligand solution of amine/halogen and thiols[46, 47]. After precipitation and redispersion, the DMF CQD ink is used to make the HgSe/hybrid films using room temperature drying. **Fig.3-32** shows 7.5 ±0.5 nm diameter HgSe QDs with oleylamine ligands and dried from hexane as well as after the hybrid ligand exchange and cast from DMF. As with the prior work on HgTe CQD[46, 47], the HgSe/hybrid ligand CQD size remains the same but the spacing is reduced while the TEM shows no obvious sintering or oriented attachment. The absorption spectra in **Fig.3-32B** shows that the n-doping is preserved with different surface ligands. The $1S_e$-$1P_e$ intraband absorption after phase transfer retains a strong peak at ~2000 cm^{-1} showing that quantum confinement is preserved. The absorption peak of HgSe/hybrid ligands and HgSe/EDT is red shifted by ~200 and 120 cm^{-1} compared to HgSe/OAM while the $1S_h$-$1S_e$ interband absorption increases in strength above 5000cm^{-1}. Some of the redshift is therefore assigned to a smaller n-doping. **Fig.3-32B** also shows the smallest C-H stretch absorption around 2900 cm^{-1} for HgSe/ hybrid ligands indicating the removal of the organic ligands in the solid.

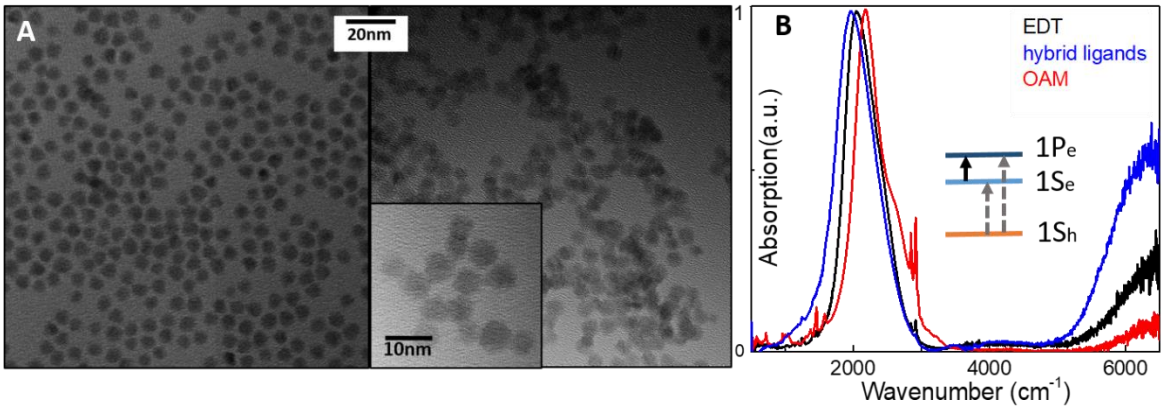

Figure 3-32. Characterization of HgSe QDs. (A) TEM analysis of ~7.5 ±0.5 nm diameter HgSe QDs before (left) and after solution phase ligand exchange (right). **(B)** Absorption spectra of HgSe/OAM, HgSe/EDT and HgSe/hybrid films. This figure is adapted from ref 61.

3.2.2 Transport on HgSe QD Solids

Electrochemical gating and FET measurements of HgSe/hybrid and HgSe/EDT QD films are shown in **Figure 3-35**. **Fig.3-35A** and **Fig.3-35B** show the schematic of the electrochemical set-up and the FET set-up respectively. **Fig.3-35C** shows the cyclic voltammetry (CV) for a HgSe/hybrid film taken at 203K while **Fig.3-35D** shows the FET data at 80K. The CV current peaks in **Fig.3-35C** correspond to the half filling of $1S_e$ (0.18V) and $1P_e$ (-0.12V) with respect to the SCE reference. The rest potential (red arrow) gives the Fermi level at ~ 0V/SCE (SCE, -4.68 eV/Vacuum). The Fermi level corresponds to an estimated doping density at ~2.5 e^-/dot. **Fig.3-35C** shows the film conductivity on the log scale. The peak of the conductance curve matches the half-filling of the 1Se state [3] while the dip is at the filled 1Se-state ($2e^-$/dot). Mobility of ~0.40 cm^2/Vs is obtained at half-filling of the 1Se state. **Fig.3-35D** shows the FET source drain conductivity on a linear and log scale. The FET curves are shown for both scan direction and are essentially hysteresis free. The curves are hysteresis free and resolve the 1Se state half-filling and

the 1Se-1Pe dip within the range of applied gate voltages. The lower magnitude of the conductivity compared to the electrochemical data is due to the lower temperature. The FET differential mobility gives $\mu_F^S = -0.3\ cm^2/Vs$ and $\mu_F^p = 0.7\ cm^2/Vs$ for the $1S_e$ and $1P_e$ states in the linear region. In **Fig.3-35E**, the gate voltage difference between the dip and the 1Se peak is 39 V and this corresponds to a change of doping of 1e/dot using the surface density of the dots and the 300nm SiO_2 dielectric. From the gate voltage at the dip (2e/dot and -17.5 V), we then get the doping density ~2.45 e/dot at zero gate voltage. Along with the HgTe CQD films, these HgSe films are now the second CQD system exhibiting CQD state-resolved FET modulation along with mobility around 1 cm^2/Vs. Measurements for the HgSe/ EDT QDs are shown in **Fig.3-35E and 3-35F.** The electrochemical data are similar except with a slightly larger hysteresis, a 50meV positive shift of $1S_e$ and $1P_e$ indicating a smaller n-doping, and a slightly more pronounced conductance dip, and a much lower overall conductivity. The FET data in **Fig.3-35F** are also very similar but with much lower mobility $\mu_F^S = -0.002\ cm^2/Vs$ and $\mu_F^p = 0.009\ cm^2/Vs$ for the $1S_e$ and $1P_e$ states in the linear region, taken from the linear regions highlighted in red. The higher mobility of the $1P_e$ state compared to $1S_e$ in both systems is similar to prior observations with CdSe CQDs[12] and also tentatively attributed to the larger density of states for $1P_e$.

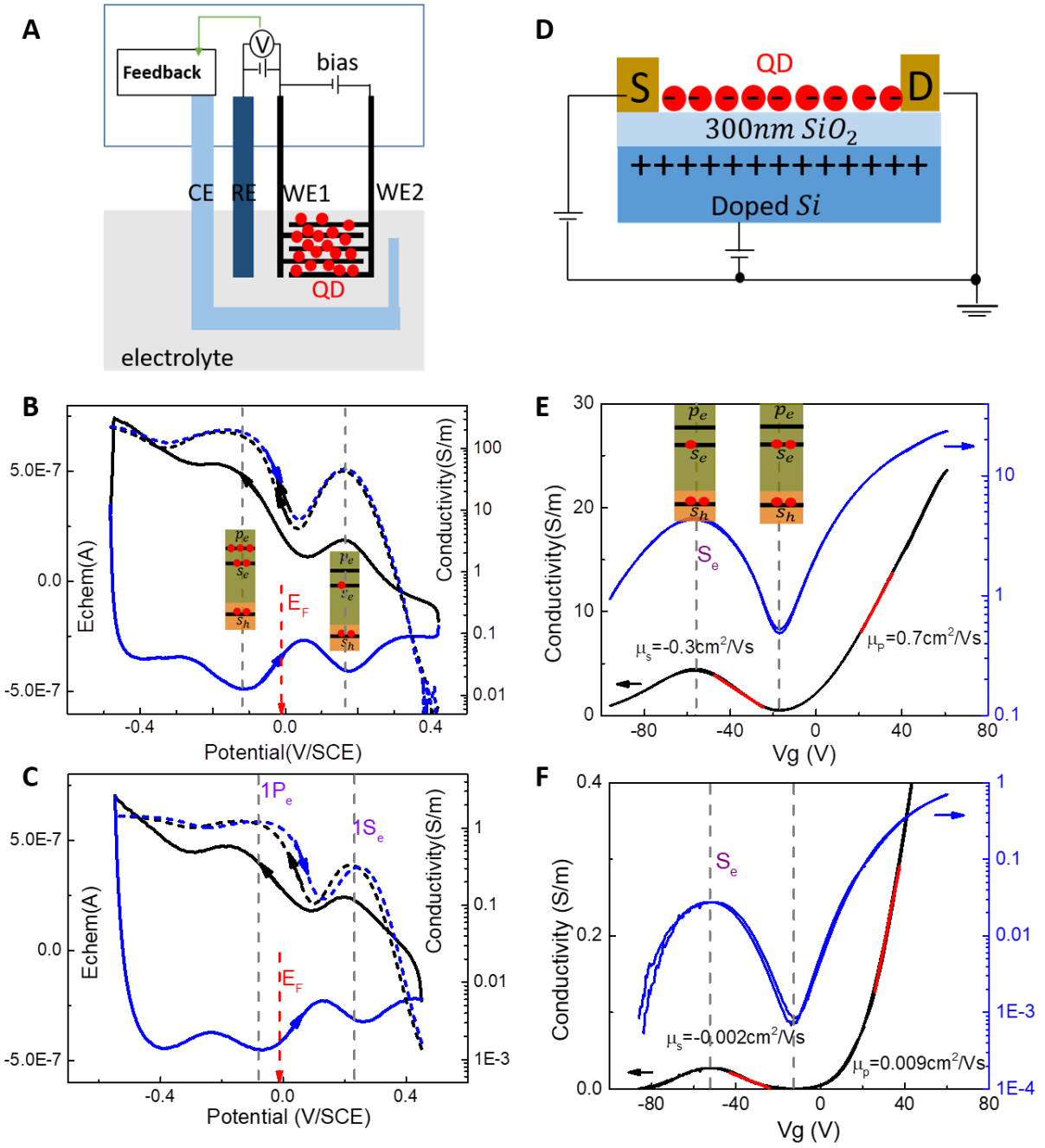

Figure 3-33. Transport study on HgSe CQD. **(A)** Schematic of the electrochemical set-up. **(B)** Cyclic voltammetry curve (solid line) and conductivity (dash line) at 203 K for HgSe/Hybrid. The solid arrow indicates the scan direction, the red dash arrow indicates the Fermi level. The inserts indicate the states filling. **(C)** Cyclic voltammetry curve (solid line) and conductance (dash line) curve at 203 K for HgSe/EDT. **(D)** Schematic of bottom-gate FET **(E)** FET Source-Drain current for HgSe/Hybrid at 80 K **(F)** FET Source-Drain current for HgSe/EDT at 80 K. Films for electrochemistry are ~100 ±10 nm thick, while the FET films are ~35 ± 5 nm, as determined by AFM. This figure is adapted from ref 61.

Further insight in the transport mechanism is obtained by measuring the temperature dependence of the mobility by FET. **Figure 3-36** shows the FET mobilities of HgSe/hybrid and HgSe/EDT QD films from 5 K to 300 K. As shown in **Fig.3-36A**, the mobility peaks at ~1 cm^2/Vs at 170 K for HgSe/hybrid QD films while the HgSe/EDT peaks at 0.0095 cm^2/Vs at room temperature.

For the HgSe/hybrid there is a weak "bandlike' trend, where bandlike is defined as $\frac{d\mu}{dT} < 0$ down to 170K below which the mobility decreases. Such behavior can be understood with the Marcus theory of charge hopping where the mobility is expressed as[26, 27] $\mu = \frac{ed^2}{\hbar}\frac{\sqrt{\pi}}{6}\frac{V^2}{\sqrt{\lambda(kT)^3}} exp\left(\frac{-(\lambda+\Delta G)^2}{4\lambda kT}\right)$ (3-4) where V is the coupling matrix element between the separate quantum dots attributed to their wavefunction overlap, λ is the reorganization energy attributed to polarization, ΔG is the energy difference attributed to disorder and size dispersion, and d is the nearest neighbor distance taken as the center to center distance of the nanocrystals.

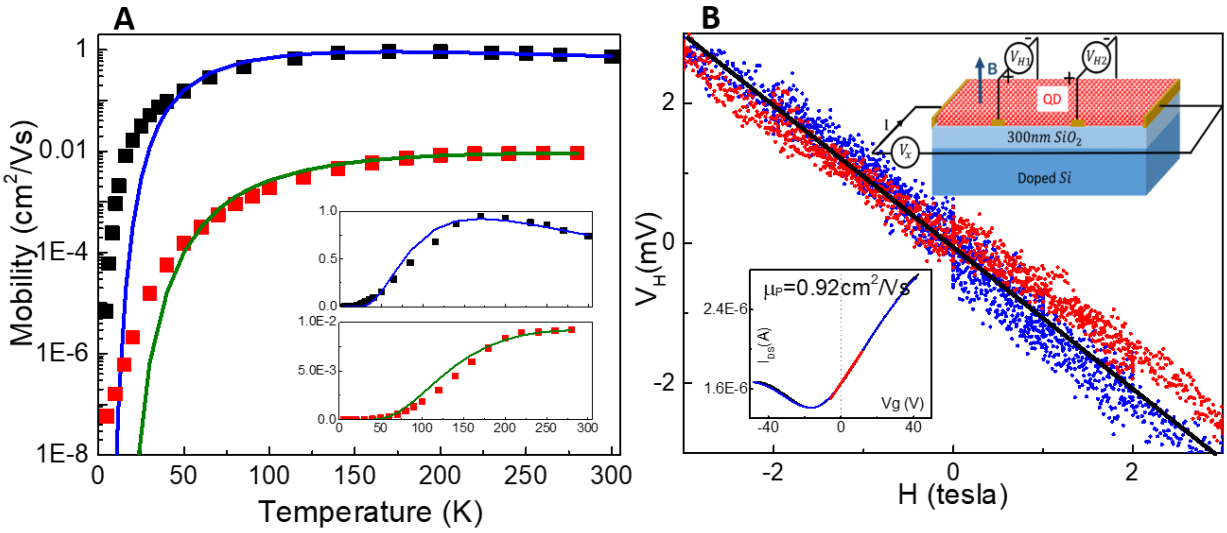

Figure 3-34. FET mobility and Hall voltage. (A) FET Mobility of HgSe/hybrid(black) and HgSe/EDT(red) as a function of temperature as well as Marcus theory fitting. **(B)** Hall voltage measured at 200K of 7.5 ±0.5 nm diameter HgSe/Hybrid QD film with thickness~35 ± 5 nm. The left insert graph shows the FET transport curve measured on the same device while the right insert graph shows the schematic of Hall device with FET structure. This figure is adapted from ref 61.

The reorganization energy is attributed to the polarization of the material and it is estimated as $\lambda = \frac{e}{4\pi\varepsilon_0}\left(\frac{1}{r}-\frac{1}{2(r+l)}\right)\left(\frac{1}{\varepsilon_{opt}}-\frac{1}{\varepsilon_{st}}\right)$ where e is the elementary charge $1.6\times10^{-19}\,C$, ε_{opt} the optical dielectric constant of matrix surrounding QDs, ε_{st} its static dielectric constant, ε_0 the vacuum permittivity $8.85\times10^{-12}\,F/m$, l the interdot separation, and r the radius of the QDs.

For the HgSe/hybrid QD film, we measured an optical dielectric constant of $\varepsilon_{opt}^{hybrid} = 8.2$ by ellipsometry. To estimate the static dielectric constant, we scale it by the same factor as for bulk HgSe where the static and optical dielectric constant are 25.6 and 15.9[58], respectively, giving $\varepsilon_{st}^{hybrid} = 13.2$. With a dot separation $l = 0.5\,nm$ and a dot radius $r = 3.7\,nm$, we get a reorganization energy λ^{hybrid}~11 meV while $d = 2r + l = 7.9nm$. **Fig.3-34A** shows the Marcus theory fit with G^{hybrid} ~20 meV and V^{hybrid} ~ 1.3 meV. All these values are very comparable to recently reported results with HgTe/hybrid CQDs[47] of similar size. Source-Drain current of HgSe/Hybrid measured by FET at different temperatures are shown in **Figure 3-35.**

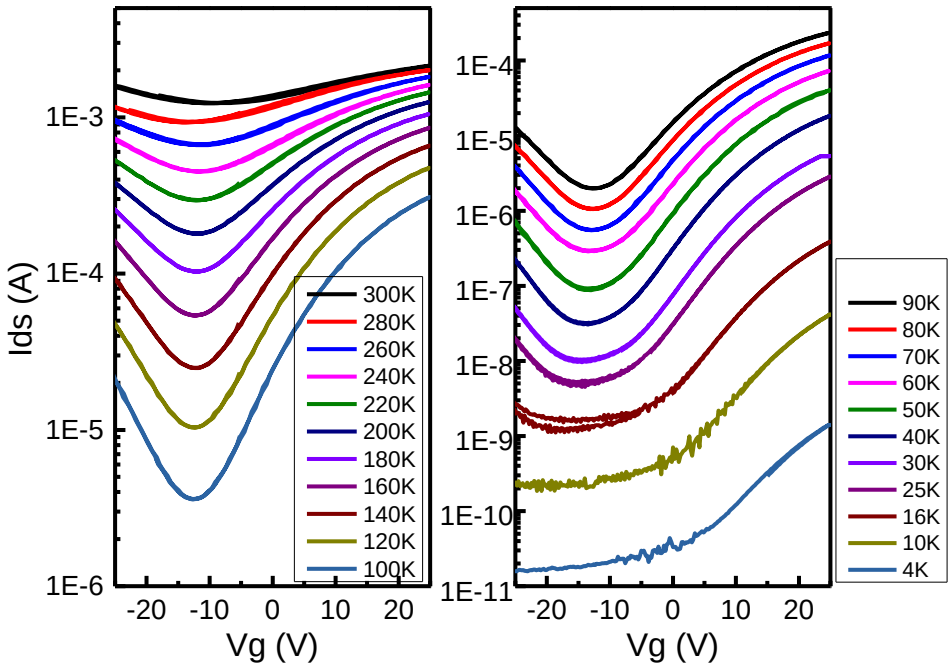

Figure 3-35. FET curves of 7.5nm diameter HgTe/hybrid QD solid as a function of temperature.

For HgSe/EDT QD film, ellipsometry gives $\varepsilon_{opt}^{EDT} = 6.8$, with the lower values assigned to a lower packing fraction of the CQDs. With the same argument as above, we deduce $\varepsilon_{st}^{EDT} = 10.9$. Taking a dot separation of $l = 1\ nm$ and a dot radius of $r = 3.7\ nm$, the calculated reorganization energy is λ^{EDT}~12.5 meV, and the Marcus theory fit gives G^{EDT} ~28 meV and V^{EDT} ~ 0.2 meV. The disorder energy is therefore slightly larger than for HgSe/hybrid but the coupling energy is 6.5 times smaller. This could naturally occur from the interdot separation being larger.

As in the prior work with HgTe CQDs, the Marcus hopping model captures well the mobility magnitude and temperature dependence above 50 K for both HgSe/hybrids and HgSe/EDT, but it underestimates strongly the low temperature mobility, as shown in **Fig.3-34A**. This could be

assigned to a gradually decreasing activation energy from 50 K to 5 K. Since the deviation is similar for strong and weak coupling, it is unlikely to be due to qualitative changes of the transport mechanism. It can also not be explained by variable range hopping, where higher order coupling allows tunneling beyond nearest neighbors, leading to a very steep temperature dependence. Instead, we think that this lower activation energy at lower temperature might be more simply explained by the disorder allowing carriers to find paths with lower and lower energy barriers at lower temperature.

With the higher mobility HgSe/hybrid films, I could independently measure carrier concentration and mobility with the Hall effect, noting that Hall measurements could not be carried out at the lower temperatures due to the reduced mobility. Based on earlier work by Holstein on the small polaron hopping model [27], a similar Hall and drift mobility is often taken as supporting evidence of delocalization for organic conductors[33]. Following the prior work on HgTe/hybrid CQD solids[47],I therefore performed Hall measurements under He-filled inert atmosphere. The insert graph in **Fig. 3-34B** shows the schematic of Hall bar with 1 pair of electrodes to apply a constant current and 2 pairs of electrodes to monitor the Hall voltage (V_{H1}, V_{H2}), with the sample being perpendicular to the magnetic field. The electrodes are prepared on a 300 nm SiO_2/n-doped Si substrate also used as FET substrates. For the Hall measurement, the FET gate needs to be grounded to minimize the noise. Therefore, although the FET mobility is measured on the same samples, we can only compare the two measurements for the ungated sample. The Hall device is measured with an constant applied current $I = 16\ \mu A$, and the resistance is then determined as $R_s = 3.52 \pm 0.18\ M\Omega$ by the Van der Pauw method. When using the Van der Pauw method to determine the resistance, the contacts size and sample thickness must be much smaller than the

distance between the contacts. Following the NIST guidelines[59], we estimate the relative errors caused by the ratio of the contact size to the distance between the contacts, to be ~ 5%. As shown in **Fig.3-34B**, the Hall voltage from the two channels give similar signal $V_H \sim -0.92 \pm 0.08\ mV/tesla$ at 200K. The definition of the sign of V_H is shown in Fig 3A and it indicates that electrons are the majority carriers. Then the Hall Mobility is $\mu_H = \frac{V_H}{BIR_s} = 0.42 \pm 0.06\ cm^2/Vs$.

The insert **in Fig.3-34B** (left) shows the FET transport curve measured on the same device at 200 K, with the channel width *W*=1 mm and channel length *L*= 3 mm and V_{ds}= 6 V, and this results in a differential mobility $\mu_F = 0.92\ cm^2/Vs$ at zero gate voltage. The Hall Mobility therefore is about half of the FET differential drift mobility. One could also estimate the absolute mobility at zero gate. From the FET measurement, the zero gate voltage is at ~0.45 e/dot in the $1P_e$ state. From the conductance and the packing fraction, $\mu_F^{abs} = \frac{\sigma}{ne} = \frac{G \times L}{W \times D} \times \frac{\pi d^3}{6\eta e} = 1.2 \pm 0.5\ cm^2/Vs$ where d is the diameter of HgSe QD and η is the packing density. The packing fraction is estimated as random close-packed $\eta \sim 53\%$ which is consistent with the measured dielectric constant and the Bruggeman effective medium approximation[60]. Therefore, there is a 50% discrepancy where the FET mobility is larger than the Hall mobility. This is a similar but opposite discrepancy than for HgTe CQD films at the same temperature[47] and it may reflect limitations of the measurements. Based on earlier work by Holstein on the small polaron hopping model[39], a similar Hall and drift mobility is often taken as supporting evidence of delocalization for organic conductors[33]. However, it has been proposed to still be compatible with hopping if hoping rates are rather uniform[47].Theoretical investigations might be motivated by this second example of state to state transport with a temperature dependence that can be explained by hopping and yet similar Hall and drift mobility.

The packing fraction can be estimated by the effective medium approximation[60]

$$\delta i \frac{\varepsilon_i - \varepsilon_{eff}}{\varepsilon_i + 2\varepsilon_{eff}} + (1 - \delta i) \frac{\varepsilon_m - \varepsilon_{eff}}{\varepsilon_m + 2\varepsilon_{eff}} = 0$$

where ε_{eff}, ε_m, ε_i are effective dielectric constant of CQDs, dielectric constant of medium, and dielectric constant of the inclusions, and δ_i is the volume fraction of the inclusion. For HgSe/hybrid solid the effective dielectric constant is estimated by the measured index of refraction of 2.85 ± 0.1. The dielectric constant of bulk HgSe is ~15.9[58]. The medium surrounding CQDs includes organic ligands and air and we estimate dielectric constant of medium to be 2.5. The calculated volume fraction (packing fraction) of CQDs is 0.53±0.05.

Therefore, there appears to be a 50% discrepancy between the two mobility measurements, where FET is larger than Hall. We can also compare the carrier densities. From the Hall measurement, the Hall carrier density $n_H = \frac{IB}{eV_H D} = 1.7 \pm 0.4 \times 10^{24}\ m^{-3} \sim 0.29 \pm 0.07\ e/dot$, using a film thickness D ~ 35±5 nm as determined by AFM. FET indicates an average charge of 2.45 $\pm$0.1 electrons/dot after assigning the 1Se peak and gap dip to 1 and 2 electrons respectively. Therefore, the FET indicates 0.45 $\pm$0.1 electrons in the 1Pe state and the two measurements are in agreement. Overall, there is a rather good agreement between FET and Hall effect measurement for the HgSe/hybrid, and this work confirms many of the results obtained with HgTe/hybrid CQDs[47].

3.2.3 Conclusion

In this section, we compared the transport properties of HgSe CQD films made directly from a polar ink after solution transfer with hybrid ligands, or using the traditional casting from nonpolar

solvent followed by solid state ligand exchange with ethanedithiol. The transport properties were investigated by electrochemistry, FET and Hall effect. Both types of films show similar doping and state-resolved conductivity with a conductivity peak at half filling of the $1S_e$ state and a conductivity dip between $1S_e$ and $1P_e$. The mobility with the hybrid ligand is ~100 -fold larger than with ethanedithiol. A peak mobility of ~ 1 cm^2/Vs is obtained at 160K for 7.5 nm HgSe/hybrid. The HgSe/hybrid also show also a weak bandlike range above 160K while Hall and FET mobility are in agreement within a factor of 2. Yet, a Marcus hopping model fits well the temperature dependent mobility for both systems above 50K. The higher mobility of the hybrid arises from an order of magnitude stronger coupling, attributed to the smaller spacing between the CQDs. For both systems, there is a strong deviation from the hopping model at low temperature and this is tentatively attributed to carriers finding paths with lower and lower energy barriers at lower temperature. Overall, the transport properties are very similar to the prior results with HgTe CQDs, and HgSe provides another quantum dot solid where state resolved mobility of 1 cm^2/Vs is observed.

3.2.4 Method

1. Materials

The synthesis of the HgSe CQD follows ref [3]. 0.13 mmol $HgCl_2$ powder (Sigma-Aldrich, 99.5%) is dissolved in 4 mL oleylamine (Sigma-Aldrich, 70%) in a 20 ml vial heated at 95°C for one hour in the N_2 glovebox. 0.2 mmol of selenourea (Aldrich, 98%) is dissolved in 1 mL of oleylamine (Aldrich, 70%) by heating at 140 °C for 2 h under nitrogen in the glovebox, yielding a clear, light orange solution. 0.5mL of that solution is added to the $HgCl_2$/olyelamin solution and reacted for 16 min, then quenched with 10mL hexane. The final product is precipitated with 10mL ethanol,

then dispersed in 2 mL hexane.

For the hybrid ligand exchange, 0.25 mmol butylammonium chloride, 100μL 2-Mercaptoethanol and 200 μL n-butylamine are dissolved in 5 mL DMF following former reference [13], forming the hybrid ligand solution. 0.5 mL HgSe QDs in hexane was then added into the hybrid ligand solution. The QDs quickly transfer from hexane to DMF phase. Then the QDs are precipitated by adding 5mL toluene and centrifuged, then re-dissolved in 100 μL of DMF. Then the films are made by spin-coating and drying at room temperature.

2. FET

The FET differential mobility is given by $\mu_F = \frac{dI_{DS}}{dV_g}\frac{1}{V_{DS}}\frac{1}{C_i}\frac{L}{W}$, where V_{ds}=1 V is the drain-source bias, C_i the capacitance of 300 nm SiO_2. For normal FET measurement, the CQD film is prepared on 4 pairs of interdigitated evaporated gold fingers with gap .L=20 μm, and length 300 microns giving W=2.4 mm for the total channel width. For the Hall device, the channel width is 1mm and the length is 3 mm.

3. Electrochemistry

The bi-potentiostat (DY2300 series Digi-Ivy) applies a small bias (5 mV) to the working electrodes and measures the currents of the two working electrodes. The scanning rate is 50 mV/s. An Ag/AgCl reference electrode is used. The electrolyte is 0.1 M tetrabutylammonium perchlorate in propylene carbonate, under nitrogen bubbling, and cooled in an ethanol/dry ice mixture cooling bath (~203K) with the temperature monitored by a thermocouple.[9] From the conductance G and the non-capacitive current i, the mobility is calculated as $\mu_E = \frac{G*d*(d+d_0)}{\int_{t=0}^{t(v)} i dt}$, where d = 80 μm is the

interdigitated electrode spacing, d_0 = 10 μm is the finger width.

4. Hall effect measurement.

To perform Hall measurements and to compare to the FET mobility, we used a 7 electrode device. The channel width is 1 mm while the electrode gap is 3mm with the Hall probe electrodes placed on the tripartite point. This allows to probe Hall- and FET mobilities simultaneously. The samples are inserted into a Physical Property Measurement System (PPMS-9, quantum design) under a Helium inert atmosphere.

5. Ellipsometry measurement

For the ellipsometry measurement, we use the Gaertner Waferskan Ellipsometer Model L116S. Several HgSe/hybrid and HgSe/EDT films with thickness ~170nm are prepared on the Si chips (area: 0.5 inch *0.5 inch. The imaginary part of the refraction index is much smaller than the real part, so we estimate the permittivity of HgSe ~n^2 (n is the real part of refraction index).

3.2.5 Appendix

FET simulation

In the QD FET simulation, we would simplify the QD film to several layers and each layer with a thickness of the QD diameter. The dimension of FET film area is ~1 mm^2 while the thickness(~10^1nm). Therefore, we could treat every layer of QD as an infinity tablet. We could determine the initial doping density from the non-gate fermi level. When the gate voltage is applied,

it first causes the potential change of the first layer and tune the doping, then we could use Poisson's equation $\nabla^2\varphi = -\frac{\rho}{\varepsilon}$ (φ the electric potential, ρ the charge density, ε permittivity of the medium) to determine the local electric potential and calculate the potential on the second layer. However, the difficulty in applying this idea in simulation is the indetermination of the potential at the first layer and the boundary condition.

Here, we simulate in the opposite direction. We give a guess of the potential φ_n (usually is a very small value) of the last layer which exposes to vacuum with potential zero(noted as $\varphi_{N+1} = 0$). One could calculate the electron numbers in $1S_e$ and $1P_e$ states $n_S(N) = \frac{n_S}{(\exp\frac{(\varphi_N - \mathrm{Ef+Es})}{k_B T}+1)}$, $n_p(N) = \frac{n_p}{\left(\exp\frac{(\varphi_N - \mathrm{Ef+Ep})}{k_B T}+1\right)}$ as well as ρ_n of the n^{th} layer ($n_s = 2, n_p = 6$). By Poisson's equation $\nabla^2\varphi \sim \frac{\varphi_{N+1}+\varphi_{N-1}-2\varphi_N}{d^2} = -\frac{\rho_N}{\varepsilon}$, we calculated the potential of the next layer φ_{N-1}. After a few iterations, we then get the potential distribution of all the layers and could calculate the total electron number change in the film. Then we could calculate the gate voltage $\mathrm{Vg} = \frac{\sum_{i=s,p}^{j=1,2\ldots N}\Delta n_i(j)e}{C_i * d^2}$ depending on the capacity of the SiO_2 layer.

Figure 3-36 shows one example of the potential and electron distribution change with a certain gate and the conductance dependence on gate voltage with the assumption of constant mobility. In the simulation we assume 7.5 nm diameter HgSe QDs with initial doping ~2.35 e/dot. The FET film is ~35 nm thick around 5 layers. **Fig.3-38A&B** shows the doping and the electric potential change of every layer with V_g=-17 V and V_g=-57 V applied at 200 K (layer 1 is the QD layer connect to the SiO_2.

If we use one monolayer HgSe QDs served as channel, then considering the packing density in 2D

We get gate voltage needed for every electron:

$$\Delta V_g = \frac{Q}{C} = \frac{Ne}{\varepsilon_{SiO_2} * 300nm} = \frac{1/((7.5nm)^2)e}{3.9 * 8.85 * \frac{10^{-12}}{300 * 10^{-9}} F/m^2} = 24.5V$$

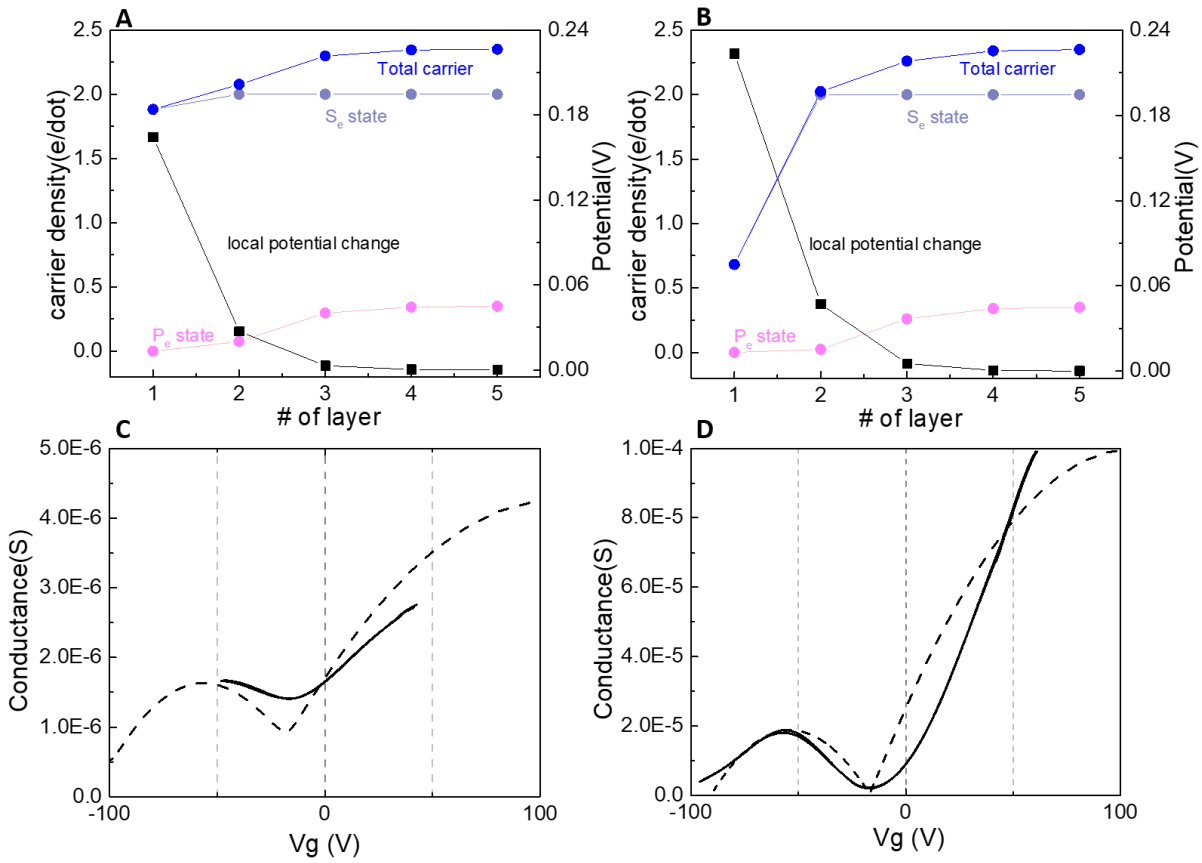

Figure 3-36. FET simulation. (A)&(B) simulation of doping level and the electric potential change of every layer with V_g=-17 V applied and V_g=-57 V at 200 K. **(C)&(D)** Real conductance curve (solid line) and simulated conductance curve (dash line) of ~35 nm thickness film at 200 K and 80 K, respectively.

This value is smaller compared to the experimental data~40V per electron. If the FET gating is efficiently tuning all doping of all the quantum dots, then for this ~35nm film, one would need 115V to tune 1e per dot. From the simulated result, we understand that all the layers are not evenly

gated because of the screening. Here, we could see that with Vg=-17 V applied, the first layer doping change from 2.35 e/dot to 1.88e/dot, second layer doping change from 2.35e/dot to 2.07e/dot, the third layer change from 2.35e/dot to 2.29e/dot. There is a gradual decay in the gating effect. This effect would result in the error in the estimation of the doping level from the FET measurement.

For the conductance calculation, we simply assume electron only hop within the layer with constant mobility μ in all the states.

$$\mathrm{G(E)} \propto n(E)\mathrm{e}\otimes\big[\big(1-\mathrm{f(E)}\big)\mathrm{f(E)}\big]\mu \propto \sum_{i=s,p}^{j=1,2\ldots N} n_i(j)[n_i - n_i(j)]\,\mu$$

where f(E) is the Fermi-Dirac distribution $\mathrm{f(E)} = \frac{1}{1+e^{(E-E_f)/kT}}$, $n(E)$ is the carrier density.

Fig.3-36C&D show simulated conductance compared to experimental result at 200 K and 80 K, respectively. The simulated conductance dip and peak positions fit the real data well. However, the simulation shows more sharp features than the real case due to the disorder effect. For example, the electrons could hop to the neighboring layers, the electron-hole could recombine and there is size distribution of QDs in the real case.

References

[1]. Kagan, C. R., Lifshitz, E., Sargent, E. H. & Talapin, D. V. Building devices from colloidal quantum dots. *Science* **353**, aac5523 (2016).

[2]. Tang, X., Ackerman, M. M., Chen, M. & Guyot-Sionnest, P. Dual-band infrared imaging using stacked colloidal quantum dot photodiodes. *Nat. Photon.* **13**, 277-282 (2019).

[3]. Li, X. *et al.* Bright colloidal quantum dot light-emitting diodes enabled by efficient chlorination. *Nat. Photon.* **12**, 159-164 (2018).

[4]. Lee, J.-S., Kovalenko, M. V., Huang, J., Chung, D. S. & Talapin, D. V. *Nat. Nanotechnol.* **6**, 348-352 (2011).

[5]. Talgorn, E. *et al.* Unity quantum yield of photogenerated charges and band-like transport in quantum-dot solids. *Nat. Nanotechnol.* **6**, 733-739 (2011).

[6]. Choi, J.-H. *et al.* Bandlike Transport in Strongly Coupled and Doped Quantum Dot Solids: A Route to High-Performance Thin-Film Electronics. *Nano Lett.* **12**, 2631-2638 (2012).

[7]. Kagan, C. R. & Murray, C. B. *Nat. Nanotechnol.* **10**, 1013 (2015).

[8]. Chen, T. *et al.* Metal–insulator transition in films of doped semiconductor nanocrystals. *Nat. Mater.* **15**, 299 (2015).

[9]. Klimov, V. I. Optical Nonlinearities and Ultrafast Carrier Dynamics in Semiconductor Nanocrystals. *J. Phys. Chem. B* **104**, 6112-6123 (2000).

[10]. Greenberg, B. L. *et al.* ZnO Nanocrystal Networks Near the Insulator–Metal Transition: Tuning Contact Radius and Electron Density with Intense Pulsed Light. *Nano Lett.* **17**, 4634-4642 (2017).

[11]. Roest, A. L., Kelly, J. J., Vanmaekelbergh, D. & Meulenkamp, E. A. Staircase in the Electron Mobility of a ZnO Quantum Dot Assembly due to Shell Filling. *Phys. Rev. Lett.* **89**, 036801 (2002).

[12]. Yu, D., Wang, C. & Guyot-Sionnest, P. *n*-Type Conducting CdSe Nanocrystal Solids. *Science* **300**, 1277-1280 (2003).

[13]. Chen, M. & Guyot-Sionnest, P. *ACS Nano* **11**, 4165-4173 (2017).

[14]. Yu, D., Wang, C., Wehrenberg, B. L. & Guyot-Sionnest, P. Variable Range Hopping Conduction in Semiconductor Nanocrystal Solids. *Phys. Rev. Lett.* **92**, 216802 (2004).

[15]. Nika, D. L., Pokatilov, E. P., Shao, Q. & Balandin, A. A. Charge-carrier states and light absorption in ordered quantum dot superlattices. *Phys. Rev. B* **76**, 125417 (2007).

[16]. Shabaev, A., Efros, A. L. & Efros, A. L. Dark and Photo-Conductivity in Ordered Array of Nanocrystals. *Nano Lett.* **13**, 5454-5461 (2013).

[17]. Whitham, K. *et al.* Charge transport and localization in atomically coherent quantum dot solids. *Nat. Mater.* **15**, 557 (2016).

[18]. Guyot-Sionnest, P. Electrical Transport in Colloidal Quantum Dot Films. *J. Phys. Chem. Lett.* **3**, 1169-1175 (2012).

[19]. Keuleyan, S. E., Guyot-Sionnest, P., Delerue, C. & Allan, G. *ACS Nano* **8**, 8676-8682 (2014).

[20]. Goubet, N. *et al.* Terahertz HgTe Nanocrystals: Beyond Confinement. *J. Am. Chem. Soc.* **140**, 5033-5036.

[21]. Hudson, M. H. *et al.* Conduction Band Fine Structure in Colloidal HgTe Quantum Dots. *ACS Nano* **12**, 9397-9404 (2018).

[22]. Allan, G. & Delerue, C. *Phys. Rev. B* **86**, 165437 (2012).

[23]. Shen, G., Chen, M. & Guyot-Sionnest, P. *J. Phys. Chem. Lett.* **8**, 2224-2228 (2017).

[24]. Nomura, K. et al. Nature 432, 488-492 (2004).

[25]. Shklovskiĭ, B. I. & Efros, A. L. *Electronic Properties of Doped Semiconductors* (Springer, Berlin, 1984).

[26]. Chu, I.-H., Radulaski, M., Vukmirovic, N., Cheng, H.-P. & Wang, L.-W. Charge Transport in a Quantum Dot Supercrystal. *J. Phys. Chem. C* **115**, 21409-21415 (2011).

[27]. Prodanović, N., Vukmirović, N., Ikonić, Z., Harrison, P. & Indjin, D. Importance of Polaronic Effects for Charge Transport in CdSe Quantum Dot Solids. *J. Phys. Chem. Lett.* **5**, 1335-1340 (2014).

[28]. Reich, K. V., Chen, T. & Shklovskii, B. I. Theory of a field-effect transistor based on a semiconductor nanocrystal array. *Phys. Rev. B* **89**, 235303 (2014).

[29]. Beverly, K. C. *et al.* Quantum dot artificial solids: Understanding the static and dynamic role of size and packing disorder. *Proc. Natl. Acad. Sci.* **99**, 6456-6459 (2002).

[30]. Fratini, S., Mayou, D. & Ciuchi, S. The Transient Localization Scenario for Charge Transport in Crystalline Organic Materials. *Adv. Funct. Mater.* **26**, 2292-2315 (2016).

[31]. Kang, S. D. & Snyder, G. J. Charge-transport model for conducting polymers. *Nat. Mater.* **16**, 252-257 (2016)

[32]. Kaiser, A. B. Electronic transport properties of conducting polymers and carbon nanotubes. *Rep. Prog. Phys.* **64**, 1-49 (2000).

[33]. Sirringhaus, H., Sakanoue, T. & Chang, J.-F. Charge-transport physics of high-mobility molecular semiconductors. *Phys. Status Solidi B* **249**, 1655-1676 (2012).

[34]. Uemura, T. *et al. Phys. Rev. B* **85**, 035313 (2012).

[35]. Yi, H. T., Gartstein, Y. N. & Podzorov, V. Charge carrier coherence and Hall effect in organic semiconductors. *Sci. Rep.* **6**, 23650 (2016).

[36]. Chang, J.-F. *et al*. *Phys. Rev. Lett.* **107**, 066601 (2011).

[37]. Wang, S., Ha, M., Manno, M., Daniel Frisbie, C. & Leighton, C. *Nat. Commun.* **3**, 1210 (2012).

[38]. Meton, M. & Gerard, P. Hall effect in dilute electrolytes. *Chem. Phys. Lett.* **44**, 582-585 (1976).

[39]. Holstein, T. Hall Effect in Impurity Conduction. *Phys. Rev.* **124**, 1329-1347 (1961).

[40]. Chien, C. L. & Westgate, C. R. e. *The Hall effect and its applications* (Plenum, New York, 1980).

[41]. Klein, R. S. Investigation of the Hall effect in impurity-hopping conduction. *Phys. Rev. B* **31**, 2014-2021 (1985).

[42]. Kang, S. D., Dylla, M. & Snyder, G. J. *Phys. Rev. B* **97**, 235201 (2018).

[43]. Kaiser, A. B. *Phys. Rev. B* **40**, 2806-2813 (1989).

[44]. Burns, M. J. & Chaikin, P. M. *J. Phys. C: Solid State Phys.* **18**, L743-L749 (1985).

[45]. Bonetti, M., Nakamae, S., Roger, M. & Guenoun, P. Huge. *J. Chem. Phys* 134, 114513 (2011).

[46]. Chen, M. *et al.* High Carrier Mobility in HgTe Quantum Dot Solids Improves Mid-IR Photodetectors *ACS Photonics*, 6, 2358 (2019).

[47]. Lan, X. *et al.* Quantum dot solids showing state-resolved band-like transport Nature Materials, 19, 323-329 (2020).

[48]. Madelung, O.; Von der Osten, W.; Rössler, U. Intrinsic Properties of Group IV Elements and III-V, II-VI and I-VII Compounds. Springer Science & Business Media 1986, pp218.

[49]. Keuleyan, S.; Lhuillier, E.; Brajuskovic, V.; Guyot-Sionnest, P. Nature Photonics 2011, 5, 489–493

[50]. Deng, Z.; Jeong, K. S.; Guyot-Sionnest, P. ACS Nano 2014, 8, 11707-11714.

[51]. Lhuillier, E.; Scarafagio, M.; Hease, P.; Nadal, B.; Aubin, H.; Xu, X. Z.; Lequeux, N.; Patriarche, G.; Ithurria, S.; Dubertret, B. Nano Lett. 2016, 16, 1282-1286.

[52]. Tang, X.; Wu, G. F.; Lai, K. W. C. J. Mater. Chem. C 2017, 5, 362-369.

[53]. Sahu, A.; Khare, A.; Deng, D. D.; Norris, D. J. Chem. Commun. 2012, 48, 5458-5460.

[54]. Park, M.; Choi, D.; Choi, Y.; Shin, K.; Jeong, K. S. ACS Photonics 2018, 5, 1907-1911.

[55]. Qu, J.; Goubet, N.; Livache, C.; Martinez, B.; Amelot, D.; Gréboval, C.; Chu, A.; Ramade, J.; Cruguel, H.; Ithurria, S.; Silly, M. G.; Lhuillier, E. J. Phys. Chem. C 2018, 122, 18161-18167.

[56]. Kovalenko, M. V.; Scheele, M.; Talapin, D. V. Science 2009, 324, 1417-1420.

[57]. Talapin, D. V.; Murray, C. B. Science 2005, 310, 86–89.

[58]. Berger, L. I. Semiconductor Materials. CRC Press, 1996, pp210.

[59]. "Test Methods for Measuring Resistivity and Hall Coefficient and Determining Hall Mobility in Single-Crystal Semiconductors," ASTM Designation F76, Annual Book of ASTM Standards, 2011, Vol. 10.04

[60]. Choy, T. C. Effective Medium Theory: Principles and Applications. Oxford University Press, 2015, pp165.

[61]. M. Chen, G. Shen, P. Guyot-Sionnest J. Phy. Chem. Lett. 2020, 11, 6, 2303-2307

Chapter 4: Size Distribution Effects on Mobility and Intraband Gap

Table 3-1 in **Chapter 3** shows that the disorder energy ΔG in Marcus theory~10meV, at least one order smaller than the standard deviation (~several hundreds of meV) in the absorption spectra. Does this mean that the Marcus theory is a wrong explanation? To answer this question, it is better to discuss how QD polydispersity provides a major contribution to the disorder of the energy states involved in charge transport.

I choose HgSe CQD as a model system, because it has a rather unique air-stable n-doped property as discussed in **Chapter 2&3** and it has allowed the demonstration of CQD intraband photodetectors in the mid-infrared spectral range. The intraband transition of doped CQD should afford a greater flexibility in designing infrared CQDs by allowing wide bandgap semiconductors, compared to infrared CQDs based on interband transitions which are restricted to the few semiconductors with zero or very narrow bandgap. However, the detector sensitivity of HgSe CQD photoconductors has been about an order of magnitude worse than with HgTe CQD photoconductors at the same wavelength.

There are could be a number of possible reasons for this lower performance, such as insufficient mobility, excessive dark current due to imperfect doping, and ultrafast intraband relaxation. **Chapter 3** shows that a solution ligand exchange procedure successfully improve the mobility by 2 orders over a solid state ligand exchange using ethanedithiol, achieving 1 cm^2/Vs. Yet, this increased mobility did not significantly improve the photoconductivity. Therefore, the lower performance of HgSe CQD is unlikely to be due to the lower mobility.

Regarding the dark current, HgSe CQD films do also exhibit a larger dark current and this could be due to excess doping. There is a difficulty in controlling and locking the doping at exactly 2 electrons per dot, which have to be done when testing multiple samples. Yet, even in this condition,

the dark current is larger than for HgTe of similar wavelength and therefore the excess dark current is unlikely to be due to the imprescise doping.

It is also often believed that intraband relaxation is ultrafast, and a fast non-radiative relaxation proportionally increases the dark current due to generation/recombination by detailed balance argument. However, the photoluminescence efficiency of HgSe CQDs films, although quite low, is not so far from that of HgTe CQD films and the intraband relaxation is actually in the 100ps to ns timescale, not so dissimilar from HgTe CQDs at the same wavelength.

Besides the lower performance, a notable observation with HgSe CQDs is that cooling is far less effective at decreasing the dark current compared to the interband HgTe CQD with the same wavelength. In low mobility CQD systems, the dark current typically decreases with temperature due to the combined effects of a reduced mobility and a decreased thermal population of carriers across the conductivity gap. Although this was not discussed in the previous transport data by FET and electrochemistry, it is apparent that the conductivity gap is significantly shallower for the intraband HgSe compared to interband HgTe with the same optical gap. A possible explanation might be the existence of states in the 1Se-1Pe gaps but these have not been observed in absorption spectroscopy or electrochemistry. The other possible reason discussed here is that the interband and intraband conductivity gap are affected quite differently by size distribution.

In this chapter I present the effect of size distribution on the mobility, the conductivity gap, and the intraband photoresponse of the HgSe CQD system. The experimental results are discussed with simple attempts to include the effect on disorder on transport activation energy and with a

simulation. The effect of the size distribution on the conductivity gap is explored and its influence on the photoconductor property is discussed.

This chapter includes the published result from reference 9 as well as some unpublished data.

4.1 Effect of the size distribution on the mobility

As is well known, increasing the size distribution leads to an obvious broadening of the optical absorption. **Fig.4-1A** shows the optical absorption spectra for HgSe CQD films treated with ethanedithiol (EDT), with a size distribution varying from 6.7% to 18.5% (ratio of the standard diveation of the distribution to the mean size) for a similar average energy of the $1S_e$-$1P_e$ transition around 2000 cm^{-1} at room temperature. Representative TEM pictures of drop cast solutions on TEM grids, without cross linking, are shown in **Fig.4-1B**. Lattice ordering is apparent as the dots become more monodispersed. **Fig.4-1C** shows the full width of half maximum (FWHM) of the 1Se-1Pe transition as a function of size distribution Σ The solid line is a fit of the form $a\sqrt{1+b\Sigma^2}$, with $a = 400\ cm^{-1}$, $b = 0.03$, which suggests the linewidth saturating to a homogenenous width of $400\ cm^{-1}$ at room temperature. The dashed line assumes FWHM $\propto$ size distribution.

With the same samples of varying size distribution, we measured the mobilities at 203K using electrochemistry. The samples are cross linked with EDT and **Fig.4-1D** shows the maximum differential mobility. I use electrochemistry rather than field effect transistor (FET) in the mobility determination because, as discussed in a previous work, the FET mobility depends too strongly on the native doping to provide a reliable measure when comparing different CQD samples, which would be discussed in **Chapter 6**. This effect has been assigned to the vertical doping inhomogeneity inherent to the FET geometry. **Fig.4-1D** shows that the mobility dependence on size distribution is well described by an exponential relation such as $\alpha e^{-\beta\Sigma}$. I explored two different synthetic protocols. With Hg:Se=1:1 (mol/mol) as the ratio of reagents in the synthesis, α=0.005 cm^2/Vs, β=2.1. With Hg:Se=1.3:1 (mol/mol) in synthesis α=0.082 cm^2/Vs and β=2.8. This suggests that a slight excess of Hg is beneficial to the mobility, and I presume that it is because

of the capping by oleylamine/$HgCl_2$ complexes. These complexes might serve as a protection layer from oxidation which are still easily be replaced by the EDT ligands in the cross-linking step. Further increasing Hg: Se ratio does not improve the mobility. The value of α may be taken to indicate the best mobility that one could get for a narrow size with the EDT ligands at 203K.

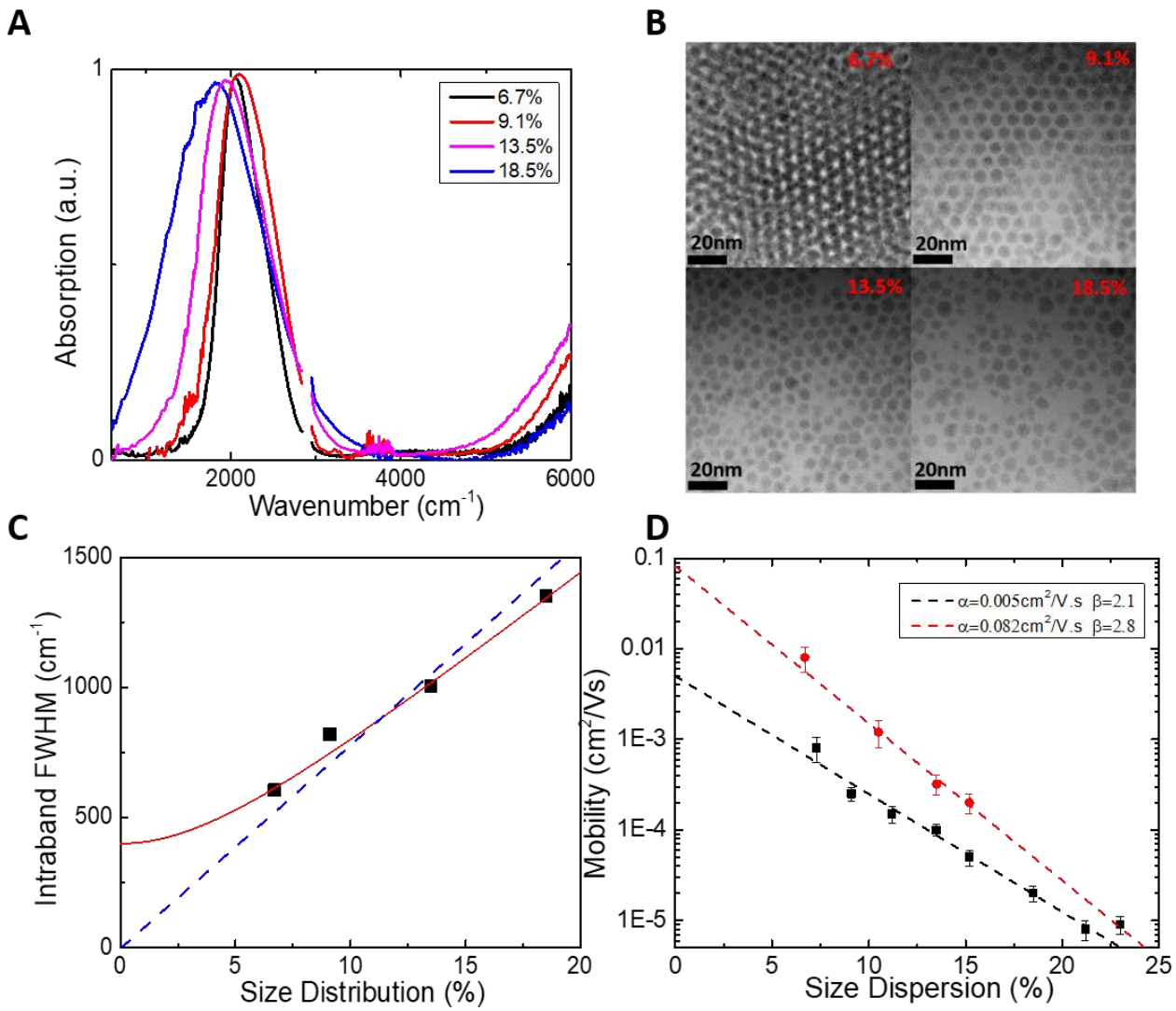

Figure 4-1. Size distribution effect on HgSe. (A) The $1S_e$-$1P_e$ exciton spectra of HgSe with different size distribution. **(B)** TEM of different size distribution HgSe CQDs with $1S_e$-$1P_e$ exciton feature peaked around 2000 cm^{-1}, respectively. **(C)** FWHM of the 1Se-1Pe transition as a function of size distribution. The solid line is a fit of the form $a\sqrt{1+b\Sigma^2}$. The dashed line assumes FWHM $\propto$ size distribution. **(D)** Mobility measured at 203 K by Echem for HgSe/EDT CQD with different

size dispersion. Black dot are mobility of HgSe/EDT with Hg:Se=1:1 (mol/mol) in synthesis while red dot with Hg:Se=1.3:1(mol/mol) in synthesis. The solid lines are fits with $\alpha e^{-\beta \Delta E/E}$ as described in the main text. The figure is adapted from reference 9.

This influence of size distribution of the mobility is intuirively expected. The exponential dependence may be further justified by the expectation that the mobility is limited by an activation energy, which arises in part from the energy disorder energy in CQD. Here I propose a simple model to relate the activation energy to the energetic disorder. If a CQD is surrounded by *n* nearest neighbors, the barrier height for transport, ΔG, is the lowest energy hop to the neighbors. One would then expect that the average barrier height would decrease with the number of nearest neighbors, even though the energy distribution is fixed. Taking the energy distribution to be Gaussian with variance σ , $g(E) = \frac{1}{\sqrt{2\pi\sigma^2}} e^{E^2/2\sigma^2}$ we calculate $\overline{\Delta G} = \int_0^\infty \Delta G \int n g(E_1 + \Delta G) \left[\int_{E_1+\Delta G}^\infty g(E_2) dE_2 \right]^{n-1} dE_1 d\Delta$. The terms in the integral account for the probability of finding n-1 dots with an energy barrier greater than ΔG and one dot with an energy barrier of ΔG. Increasing n dramatically lowers the average energy barrier for a given energy distribution. With 1 nearest neighbor, the average barrier height is 60% σ, while, with 6 nearest neighbors, the average barrier height reduces to 7.5% σ. Such effect may, therefore, explain why the energy disorder ΔG ~20 meV fitted by the Marcus theory (The question at the beginning of this chapter) is much smaller than the FWHM of the optical exciton feature of the narrowest, 6.7%, size distribution sample ~75 meV. It also explains how a broader size distribution increases the energy variance as well as the average barrier height. For a given nearest neighbor number, the average barrier height $\overline{\Delta G}$ is proportional to the standard deviation σ in the size distribution, and this explains the exponential dependence seen in **Fig.4-1D**. A weakness of the model is however in the assumption of a constant number of nearest neighbors.

In addition to the numerical calculation above, we therefore performed a Monte Carlo simulation that specifically includes the effect of disorder on the number of nearest neighbors. The simulation results are shown in **Figure 4-2**. For the average barrier height simulation, we first build a dense packing QD system in 1, 2, 3-dimension as shown in **Fig.4-2A**, respectively. The packing follows a relaxation process.

1. Generate spherical particle size based on the certain distribution (we use Gaussian distribution here, and the energy E depending on the particle size based on the optical measurement.)
2. Random initial position generation for all spheres (dots) in the free space.
3. Overlap relaxation base on the Relaxation Algorithm.
4. Packing space expansion.

Relaxation Algorithm

$\overrightarrow{R_i}$ noted as the i^{th} sphere center vector.

r_i noted as the i^{th} sphere radius.

d_{ij} noted as the distance between the i^{th} sphere center to the j^{th} sphere center.

$\overrightarrow{R_{ij}}$ noted as the repulsion from sphere *i* to sphere *j*. $\overrightarrow{R_{ij}} = \overrightarrow{R_i} + (\overrightarrow{R_j} - \overrightarrow{R_i})\frac{r_i + r_j}{d_{ij}}$

$\overrightarrow{R_i}'$ noted as the total repulsion to sphere *i*. $\overrightarrow{R_i}' = \frac{1}{n_i}\sum_{j=1}^{n_i} \overrightarrow{R_{ij}}$

n_i noted as the total surrounding sphere numbers around the sphere i. (To search the surrounding sphere, only consider the $3\bar{r} \times 3\bar{r} \times 3\bar{r}$ area around the sphere i. If there is no overlap between sphere i and others, move sphere i until it touches the closest neighbor.)

After the packing is densified, we count the average neighbor number of all the spheres. Here, we use the condition that sphere i and sphere j are neighbors if $\frac{d_{ij}-r_i-r_j}{r_i+r_j} < 2\%$, where r_i noted as the i^{th} sphere radius and d_{ij} noted as the distance between the i^{th} sphere center to the j^{th} sphere center. Then, we use the Monte Carlo method to determine the barrier height. First, we randomly generate the initial position of one electron in the i^{th} sphere of the densely packed sphere system. Then, we calculate the hopping rate ω_{ij} from the i^{th} sphere to its neighbor j with $\omega_{ij} = \exp(-\frac{2(d_{ij}-r_i-r_j)}{\alpha} + \frac{E_j-E_i}{2k_BT} + \left|\frac{E_j-E_i}{2k_BT}\right| + \frac{\vec{E}\cdot(\overrightarrow{R_j}-\overrightarrow{R_i})}{2k_BT})$ where α is the localization length and $\vec{E}$ is the applied electric field. Then, we choose the maximum rate $\omega_i = \max(\omega_{ij})$, j=1…n_i. and generate a random number $r_{random} \in [0,1]$. If $\omega_i > r_{random}$, the electron successfully hops and we record the energy difference between the initial and final spheres. We calculated the average barrier height of the 1, 2, 3-dimension systems with 10^4 hops, and the results are shown in **Fig.4-2B.**

The simulation shows a similar trend as the simple Gaussian distribution calculation. As the number of nearest neighbor increases, the average barrier height quickly decreases. The simulated results are slightly higher than the theoretical calculation, which may reflect the limitation of the calculation assuming a single number of nearest neighbors.

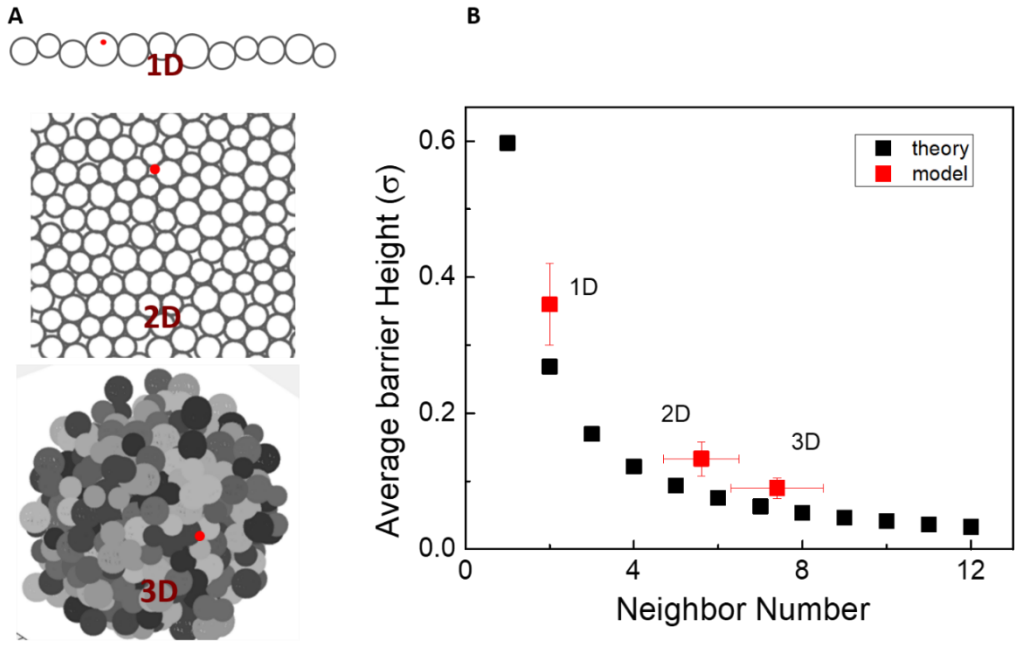

Figure 4-2. Simulation on average barrier height for transport. (A) simulation of QD dense packing in 1, 2, 3-dimension systems. **(B)** Average barrier height calculated by both ideal theoretical Gaussian distribution case and simulated case as described by the text. The figure is adapted from reference 9.

Tin the simulation, it is apparent that with broader size distributions, dense packing becomes increasingly difficult, and this leads to the loss of a clear trend between size distribution and nearest neighbor numbers in the simulation. Furthermore, experimentally, it is typical to see the self-assembly of colloidal nanoparticles in ordered small size-selcted domains[1]. Particle packing procedure does not consider these effects.

Overall, the calculated average barrier height is nicely proportional to the assumed energy distribution, and this is consistent with the experimental mobility activation energy following the experimental size distribution. The reduction of the measured activation energy compared to the width of the energy distribution is also rather satisfyingly explained.

4.2 Size inhomogeneity and intraband gap

In a photoconductor, the dark current limits the sensitivity by being a source of shot noise and 1/f noise[10]. Tuning the system to the minimal dark current is therefore optimal. However, I show here that the interband and intraband CQD differ significantly by the lowest dark current that can be achieved for a given optical gap and size distribution. **Fig.4-3A&B** shows a simple calculation of the conductivity at 80K as a function of the Fermi energy. The lines are given by $G_{interband} \propto \int g(r)\left[f(1S_h)\left(1-f(1S_h)\right)+f(1S_e)\left(1-f(1S_e)\right)\right]dr$ and $G_{intraband} \propto \int g(r)\left[f(1S_e)\left(1-f(1S_e)\right)+3f(1P_e)\left(1-f(1P_e)\right)\right]dr$ where $g(r)$ is a Gaussian distribution, and f is the Fermi function at 80K. In this calculation, $1S_h$ has no dispersion and this is based on the fact that the state originates from the heavy hole band. $1S_e$ and $1P_e$ have a strong dispersion calculated with a simple k.p model. Although simplistic, the calculations illustrate the much stronger effect of disorder on the intraband gap. The experimental results in **Fig.4-3C** show the strong effect of the size distribution on the conductivity gap. The 6.7 % size distribution HgSe/EDT solid show a conductivity modulation of ~30-fold at 80K while the 9.1 % one has less than a 10-fold difference. This is in fair agreement with the model calculation in **Fig.4-3B**. In contrast, HgTe CQD films with similar energy for the $1S_h$-$1S_e$ gap show up to 10^4 modulations,[2,3] agreeing with the simulation in **Fig. 4-3A.** **Fig.4-3B** also shows that the size distribution of ~ 3% would be needed to provide performances comparable to interband. The size distribution of 3% has been achieved with PbSe[4,5] and it is therefore likely that the HgSe intraband photodetection will be improved with better synthetic control.

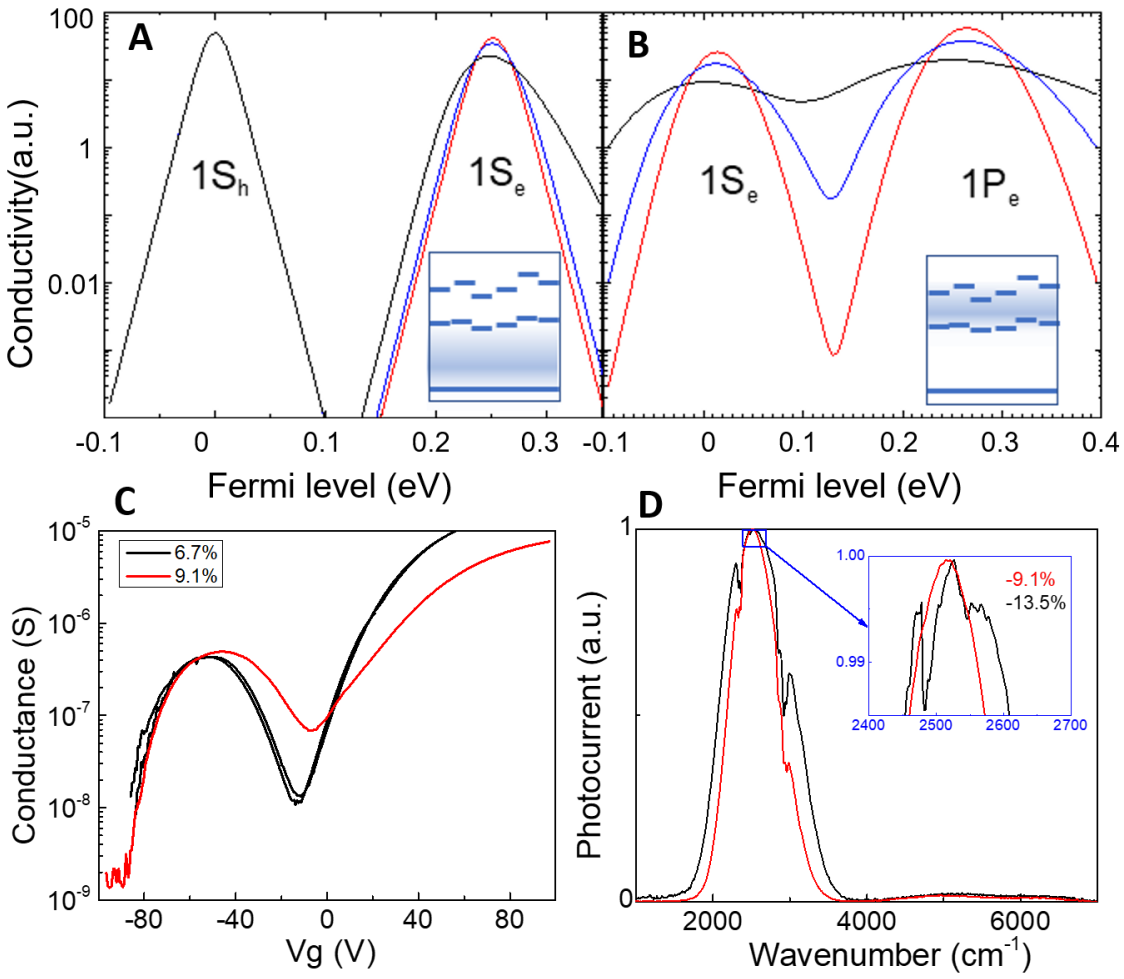

Figure 4-3. Size distribution effect on 0.25eV interband and intraband gaps at 80K. (A) The $1S_h$-$1S_e$ gap interband conductance shows more than 10^6 modulations with the Fermi level in the gap for all three size distributions. **(B)** In contrast, the 1Se-1Pe intraband conductance is rapidly increasing in the gap with increasing size dispersion. The standard deviations of the Gaussian size distribution are 10% (black lines), 5% (blue lines) and 3% (red lines). Insets: schematic effect of size disorder. **(C)** FET transport curve of 6.7% (black) and 9.1% (red) size distribution HgSe/EDT film with similar thickness and doping level at 80 K. **(D)** Photocurrent spectra of 13.5% (black) and 9.1% (red) size distribution HgSe/EDT film with near 2 electrons per dot doping level at 80 K. The ~ 10-fold improved signal to noise of the narrower size distribution film is highlighted by the inset near the peak of the photocurrent spectrum. The figure is adapted from reference 9.

Fig.4-3D shows the Photocurrent spectra of 13.5% (black) and 9.1% (red) size distribution HgSe/EDT films. The photocurrent spectra are measured at 80K, by A Nicolet 550 FTIR spectrometer, with a FTIR scanning at 0.9cm/s and the central interferogram peak is about 100 microseconds. The internal glow bar light source was directed to the outer port and imaged on the sample with a 5 cm focal parabolic mirror. Since small variations in preparation can easily and uncontrollably shift the doping by 0.1 electron per dot, multiple films were tested and the results are given for the films with the lowest dark current and maximum signal to noise for each samples. With 12 V bias, the 13.5% size distribution HgSe/EDT gave a photocurrent of 5.6 nA. The illumination source is a blackbody source at the 600 °C of 21 mm diameter placed 150mm away and chopped at 200Hz. The light is arriving on the detector through a ZnSe window and the silicon wafer and is partially screen by the interdigitated electrodes. The effective sample area is 0.5mm$^{2.}$ and the calculated responsivity is therefore calculated to be 0.13mA/W.The dark current was 545 nA, the measured noise density 1pAHz$^{1/2}$ a factor of 2.5 larger than shot noise $\sqrt{2eI} = 0.4pAHz^{1/2}$, and the specific detectivity is calculated to be 2.6×10^7 Jones at 5μm wavelength. Improving the size distribution readily improved the performance where the 9.1% size distribution HgSe/EDT gave a better photocurrent of 12 nA, a smaller dark current 50 nA, and a corresponding smaller noise density 0.16 pAHz$^{1/2}$ resulting in a specific detectivity 3×10^8 Jones. The more monodispersed sample therefore shows a better responsivity consistent with the improved mobility, and a lower dark current consistent with the deeper conductivity gap, and therefore overall better detectivity. At this stage, we could not get good photodetection with the 6.7% size distribution HgSe/EDTbecause the slightly different synthesis preparation prevented us from adjusting the doping close enough to 2 electrons/dots and this reflects the general difficulty that improved performance with photoconductors requires all things being perfect[6-9].

4.3 Conclusion

In summary, this work investigated the effect of size distribution on transport and photodetection with intraband HgSe CQD films. Experiments shows that improving the size distribution of HgSe QDs exponentially benefits the mobility, and the mobility temperature dependence shows that this is due to a lower activation energy. The lower activation energy is then attributed to the lowering of the average barrier height, and this is observed to be in proportion to the energy distribution resulting from the size distribution. In response to the opening question in this chapter, the average barrier height is proportional to the energy distribution variance, but it is argued that the average barrier height is strongly function of the number of nearest neighbors, becoming as small as 10-5% of the energy variance in 3D solids. It is also proposed that the size distribution has a particularly detrimental effect on the intraband photodetector because both ground and excited states are strongly size-dispersed. As a results the density of states shows a much reduced conductivity gap compared to the case of interband transition where the lowest state is weakly dispersive. Reducing the size distribution will be beneficial to lower the dark current by deepening the conductivity gap. While developing a method for precise and stable doping is a shared challenge for all small gap CQD device application, the synthesis of more monodispersed HgSe CQDs, down to 3% standard deviation is identified as particularly critical for intraband operation.

4.4 Method

1. **HgSe QD synthesis.**

   The 6.7% size distribution HgSe using substituted selenourea[4]. In the glove box, weighed 6 mmol selenium powder (Sigma-Aldrich, 100 mesh, 99.99%) in a 20 ml glass vial. Added

4.8 mL toluene (Sigma-Aldrich, anhydrous, 99.8%), 0.6 mL piperidine (Sigma-Aldrich, 99.5%), and 0.62 mL butyl-isocyanide (Sigma-Aldrich, 97%) to the same vial. Put the vial on a hot plate. Set the hot plate temperature at 115 °C and stirred for 1.5 h. Weighed 0.13 mmol $HgCl_2$ powder (Sigma-Aldrich, 99.5%) along with 4 mL Oleylamine (OAm) (Sigma-Aldrich, 70%) in a 20 ml vial heated at 95°C for one hour in the N_2 glove box. Diluted 0.1 mL of substituted selenourea in 3 mL of OAm, then quickly injected into the Hg precursor and react for 2 hours. Then the mixture was quenched by 8mL toluene. The QDs were precipitated by an excess of ethanol then re-dissolved in 2mL hexane.

The 9.1% size distribution HgSe QDs using 1.3 mmol $HgCl_2$ was dissolved in 4ml OAM at 95°C, then mixed with 0.5mL 0.2M selenourea/OAM for 20min under nitrogen in the glovebox following reference[2]. Then the mixture was quenched by 8mL toluene. The QDs were precipitated by an excess of ethanol then re-dissolved in 2mL hexane.

The 13.5% size distribution HgSe QDs follow the same method as the 9.1% size distribution HgSe QDs synthesis without quench solution.

The 18.5% size distribution HgSe QDs follow the same method as the 9.1% size distribution HgSe QDs synthesis without quench solution and magnetic bar.

2. **FET measurement**.

The voltage is applied by the National Instrument USB-6218 Multifunction I/O Device with a voltage gain. The source-drain current is pre-amplified by the Stanford research system model SR570 then collected by a LabVIEW program. For normal FET

measurement, the CQD film is prepared on 4 pairs of interdigitated evaporated gold fingers of width 20 microns, gap 20 microns, and length 300 microns.

3. **Echem measurement**.

   A 4-electrode system is used in electrochemistry. During the measurement, the bipotentiostat (DY2300 series Digi-Ivy) applies a small bias (5 mV) to the working electrodes and measures the currents of the two working electrodes. The scanning rate is 50 mV/s. An Ag/AgCl reference electrode is used in the cell. the sample is immersed in an electrochemical cell filled with 0.1 M tetrabutylammonium perchlorate in propylene carbonate, under nitrogen bubbling, and cooled in an ethanol/dry ice mixture cooling bath (~203K) with the temperature monitored by a chromel−alumel thermocouple (HH12B OMEGA). As in prior electrochemical studies, cooling is used to minimize the Faradaic current due to the reaction of impurities.

Reference

[1] Ohara, P. C.; Leff, D.V.; Heath, J.R.; Gelbart W.M. Crystallization of Opals from Polydisperse Nanoparticles, Phys. Rev. Lett. 1995, 75, 3466

[2] Lan, X.; Chen, M.; Hudson, M. H.; Kamysbayev, V.; Wang, Y.; Guyot-Sionnest, P.; Talapin, D. V. Quantum Dot Solids Showing State-Resolved Bandlike Transport, Nature Materials. 2020, 19, 323-329.

[3] Chen, M.; Shen, G; Guyot-Sionnest, P. State-Resolved Mobility of 1 cm^2/Vs with HgSe Quantum Dot Films, The Journal of Physical Chemistry Letters 11, 2303-2307.

[4] Kovalenko, M. V.; Talapin, D. V.; Loi, M. A.; Cordella, F.; Hesser, G.; Bodnarchuk, M.I.; Heiss, W. Quasi-seeded Growth of Ligand-tailored PbSe Nanocrystals through Cation-exchange-mediated Nucleation, Angew. Chem., Int. Ed. Engl. 2008, 47, 3029-3033.

[5] Campos, M.; Hendricks, M.P.; Beecher, A.N.; Walravens, W.; Swain, R.A.; Cleveland, G. T.; Hens, Z.; Sfeir, M.Y.; Owen, J.S.; A Tunable Library of Selenourea Precursors to PbSe Nanocrystals with Size Distributions Near that Homogeneous Limit. J. Am. Chem. Soc. 2017, 139, 2296–2305.

[6] Phillips, J. Evaluation of the Fundamental Properties of Quantum Dot Infrared Detectors J. Appl. Phys. 2002, 91, 4590– 4594

[7] Norris, D. J.; Efros, A. L.; Erwin, S. C. Doped Nanocrystals Science 2008, 319, 1776– 1779

[8] Sahu, A.; Kang, M. S.; Kompch, A.; Notthoff, C.; Wills, A. W.; Deng, D.; Winterer, M.; Frisbie, C. D.; Norris, D. J. Electronic Impurity Doping in CdSe Nanocrystals Nano Lett. **2012**, 12, 2587– 2594.

[8] Mocatta, D.; Cohen, G.; Schattner, J.; Millo; Rabani, E.; Banin, U. Heavily Doped Semiconductor Nanocrystal Quantum Dots Science 2011, 332, 77– 81.

[9] Chen, M.; Shen, G; Guyot-Sionnest, P. Size Distribution Effects on Mobility and Intraband Gap of HgSe Quantum Dots(submitted).

Chapter 5: Magnetoresistance on HgTe CQDs

This chapter shows my work on the magnetoresistance of HgTe quantum dot films. Based on ligands exchange procedure described in Chapter 3, the HgTe QD films exhibit a well-defined 1Se state charging, a relatively high mobility (1-10 cm^2/Vs), and similar drift and Hall mobility. However, the delocalization was still uncertain in this system. This motivated this more detailed study of the magnetoresistance in these systems. The magnetoresistance is measured as a function of temperature down to 10K and fractional occupation of the first electronic state. I find a positive-quadratic magnetoresistance which can be several 100% at low temperature and scales like x(1- x) where x is the filling fraction of the state. This positive magnetoresistance is orders of magnitude larger than the effect estimated from mobile carriers. There is also a negative magnetoresistance of 1-20% from 300 K to 10 K which is rather independent of the fractional occupation, and which follows a negative exponential dependence with the magnetic field. It can be empirically fit with an effective g-factor of ~ 100.

This chapter includes the published result from reference 29 as well as some unpublished data.

5.1 Introduction

The magnetoresistive response of a material can open a window into the dispersion and dynamics of the charge carriers, and in opportune cases can be exploited for technological use. In metals, magnetoresistance measurements provide a measure of the electronic coherence length[1].

In magnetic impurity doped semiconductors[2] magnetic polaron can emerge and are investigated experimentally[3,4] and theoretically[5,6].

Quantum dots present the opportunity to tailor the energy levels and take advantage of the Zeeman effect[7]. With small colloidal quantum dots doped with magnetic impurities, very large effective g-factor can be achieved[8] raising the possibility of creating magnetic polarons[9,10] that have been observed optically[11] and which could lead to novel and enhanced magnetoresistance in CQD films.

Prior studies of magnetotransport in CQD films were in a regime of rather low mobility with hoping times in the >1 ns range[12,13,14] much slower than any possible electron coherence or spin reorientation time. Such systems exhibited strong MR attributed to increased confinement under large magnetic fields. They also showed sharp positive MR that was attributed to spin-blockade, mediated by relaxation through the hyperfine interaction[13], similar to reports for weakly conductive organic films[15]. MR effects in Mn:CdSe, as well as Mn:HgS have been tentatively attributed to the polaron formation[16]. With recent progress in the processing of CQDs in polar solvents, much shorter CQD distance can be obtained leading to improved mobility[17]. As such, HgTe CQD films have recently been shown to exhibit excellent retention of the quantum confinement along with mobility in excess of 1 cm^2/Vs[18,19]. Hopping times are estimated to be in the 1-10 ps range[20], which is 1000 times shorter than in previous studies[16]. It is therefore interesting to explore the MR in these new systems. In addition, the occupation of the lowest

electronic level, 1Se, of the CQD can be tuned by a gate with a field effect transistor (FET). This is used here to continuously tune the doping of the HgTe CQD films and explore the MR as a function of the occupation of the 1Se state.

5.2 Experimental Result

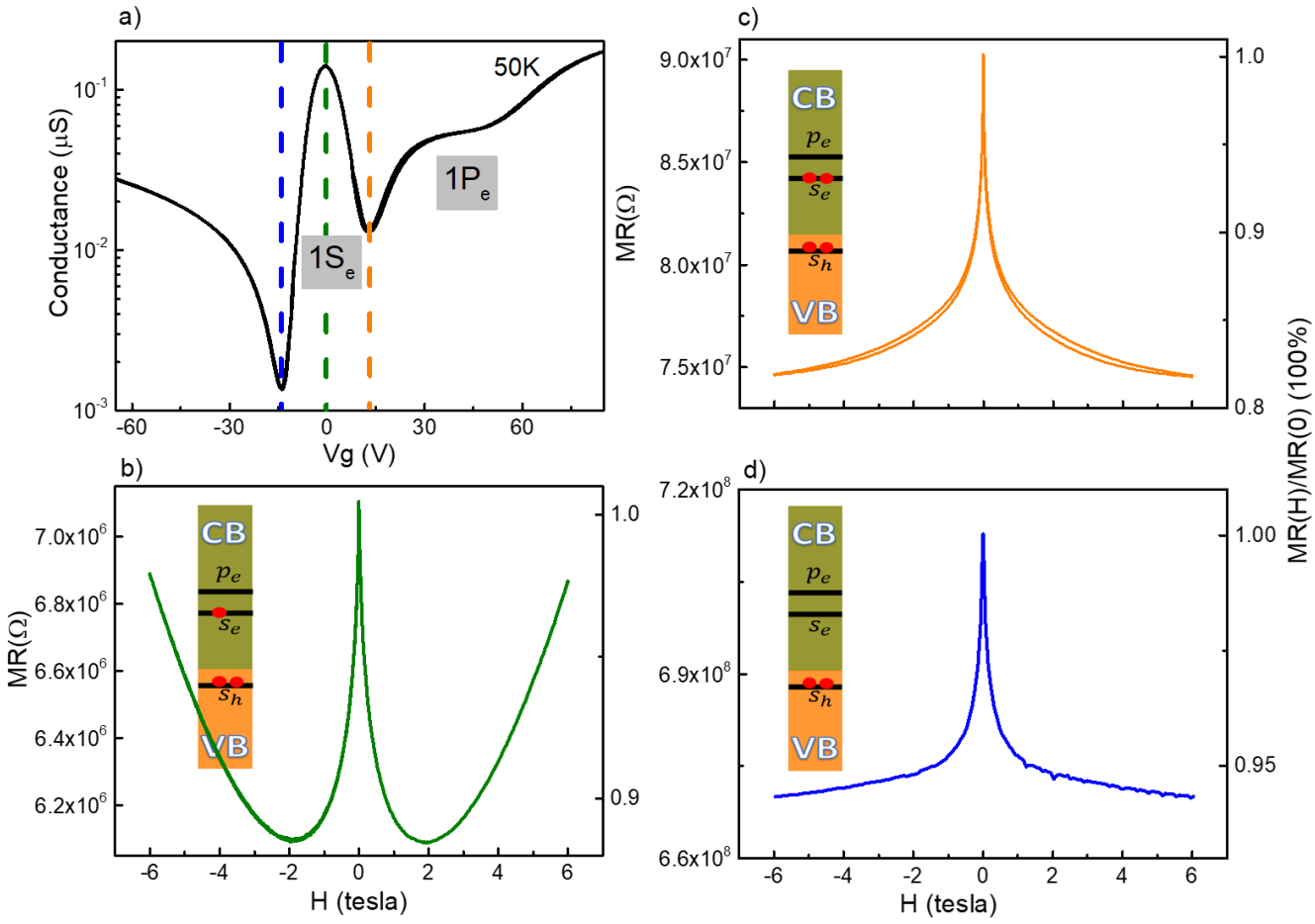

Figure 5-1. Magnetoresistance (MR) of FET-gated 11.5 nm diameter HgTe CQD solid. (a) FET source-drain conductance curve modulated by the gate potential. (b, c, d) MR with the $1S_e$ filling ~2 e/dot, ~1 e/dot and ~0 e/dot with doping indicated by the inserts. All measurements are done at 50K. The figure is adapted from reference 29.

The HgTe quantum dots are synthesized following[21,22] using the long chain oleylamine as a surfactant for steric stabilization. Average sizes from 8 nm to 15 nm diameter are studied (TEM shown in **Figure 5-5a-c**). The CQD films are made following a method reported before[18]. The thin films are spin-coated on a 300 nm SiO_2/Si FET substrate that allows to further tune the doping by up to several electrons in the layer adjacent to the gate. The film thickness is kept to a few monolayers (film cross-section SEM shown in **Figure 5-5d**) in order to have a significant effect of gating but complete device coverage and the films are simply dried at room temperature. The device properties are stable in air such that the samples can then be loaded in a physical property measurement system for electrical characterization.

Figure 5-1a shows a typical source-drain transfer curve as a function of the gate voltage at 50 K with high linear mobility 2.8±0.5 cm^2/Vs at $1S_e$ state. As previously reported, the $1S_e$ state shows as a well-defined peak in the transconductance at all temperatures. The next peak on the n-side is attributed to the 1Pe electrons state. The estimate of the doping from the capacitance and size of the CQDs agrees quantitatively with the filling of the 1Se states, consistent with its two-fold degeneracy [18]. As reported before, [19], the Hg^{2+} amount during the solvent transfer can be used to control the doping at 1 electron on average in $1S_e$ corresponding to a filling fraction x =1/2. This is verified by the conductance peak around 0 V gate potential as showed in Figure 1a. The 50K MR at V_g=0V is shown in **Figure 5-1b**. MR is defined as $\frac{R(H)-R(H=0)}{R(H=0)}$ where H is the applied magnetic field. The MR initially goes quickly negative by ~ 7 % and then grows positive in a parabolic fashion.

The MR is then measured at varying occupation of the 1Se state. **Figure 5-1c & 1d** show the MR at V_g=+14 V for a filled $1S_e$ state (x =1) and at V_g=-15 V for an empty $1S_e$ state. In both cases, the parabolic growth almost disappears while the negative MR is little changed. We verified that

the application of the gate does not introduce artificial MR by comparing samples that start with different doping. By measuring the MR with no gate or different gate voltage but for the same value of x, the measurement results show no obvious difference between these samples as showed in **Figure 5-2**.

Figure 5-2a shows FET transconductance curve with films having about ~1e/dot or without ~0.2e/dot at Vg=0. **Figure 5-2b** shows the MR at 50K for 15 nm diameter HgTe with x=1/2 in the 1Se state achieved at Vg=0 (black) and for another less doped sample with x=1/2 in the 1Se state achieved at Vg=10V (grey). The source/drain bias does not affect the MR of CQD films when the gate is left floating which is why we strived to achieve x=1/2 with the Hg^{2+} control. However, in MR measurement with FET gating, one needs to limit the source/drain bias since it can induce carrier number difference between source and drain. This is apparent in **Figure 5-2c** which shows that small source/drain bias lead to no obvious positive or negative effects on MR while large bias cause artificial effects. In the FET measurement with magnetic field, only a small source/drain bias of ~0.1V is used.

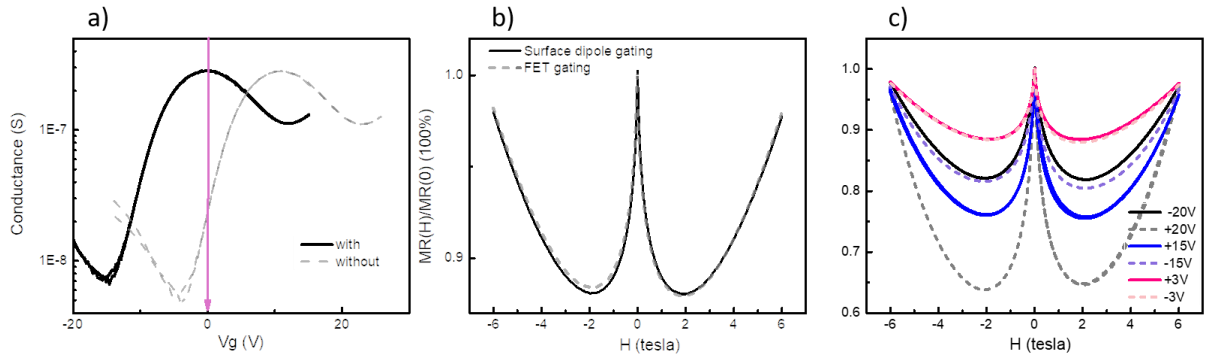

Figure 5-2. **Measurement method effect.** a) comparison between the FET gating of film samples that are prepared with 1 e-/dot (dark) (called "surface dipole gating" due to the presence of the surface dipole from Hg^{2+}) and ~0.2e-/dot (grey) of 15nm diameter HgTe at 50K. b) MR curves

showing nearly identical properties c) Effect of bias on MR for FET gated sample, showing little effect up to 3 V. The figure is adapted from reference 29.

We further investigate the MR at x =1/2, for different temperatures and two diameters (15 nm and 11.5 nm) of HgTe QDs as shown in **Figure 5-3**.

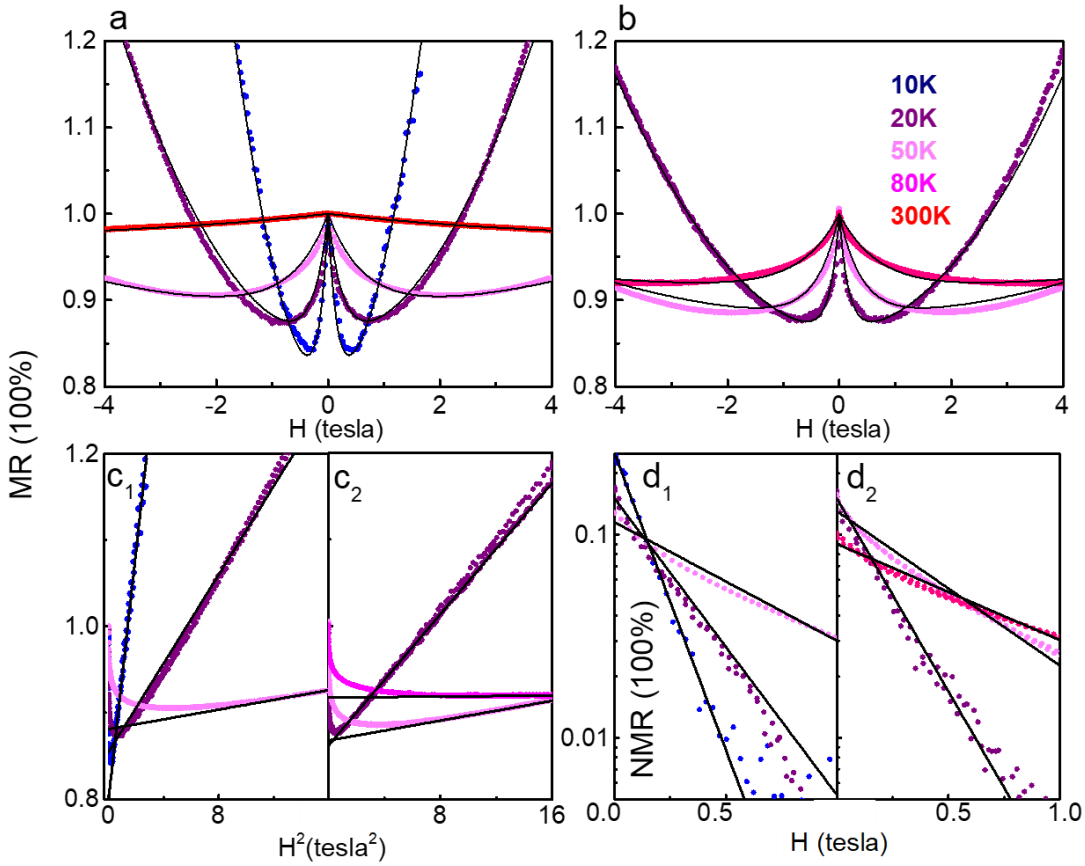

Figure 5-3. Magnetoresistance of x=1/2 doped HgTe CQD films at different temperatures. (a, b) normalized MR for 15 nm and 11.5 nm diameter HgTe CQD, respectively. The temperatures are indicated by color and the lines are fits as described in the text. (c_1, c_2) parabolic fit of the positive MR of 15 nm and 11.5 nm diameter HgTe CQD, respectively. (d_1, d_2) exponential fit of the negative MR for 15 nm and 11.5 nm diameter HgTe CQD, respectively. The figure is adapted from reference 29.

To analyze the MR, we separate the MR into a negative MR (NMR) $\rho(H)^-$and a positive MR (PMR) $\rho(H)^+$, such that the normalized MR is expressed as

$$\frac{R(H)}{R(H=0)} = \frac{1+\rho(H)^+ + \rho(H)^-}{1+\rho(H=0)^+ + \rho(H=0)^-}$$

As shown in **Fig. 5-3c**, at all temperatures, the PMR resembles a quadratic form $\rho(H)^+ = a_+H^2$. a_+ is a parameter with a unit that is a squared mobility (m^4/V^2s^2). The NMR is then obtained by subtracting this parabolic fit to the PMR. As shown in **Fig. 5-3d**, the temperature dependent NMR part resembles a decaying exponential, $\rho(H)^- = a_-e^{-\frac{g\mu_B H}{k_B T}}$ where g is an effective g-factor and a_- is unitless. From these data sets, we find that a_- varies mildly with temperature and fractional occupation as further discussed below, while $g = 110 \pm 8$ for 15 nm dots, $g = 126 \pm 5$ for 11.5nm dot, and g ~70 for 8 nm dot.(**Figure 5-6**) As shown in **Fig. 5-3a and 3b**, the addition of these two components then reproduces rather well the overall MR.

Exploring a wider range of filling fraction is then conveniently done by varying the gate potential at fixed magnetic field and temperature. The source-drain current curves at different magnetic fields for 15nm and 11.5nm diameter HgTe CQDs at 20 K and 50 K are shown in **Figure 5-4**.

These curves show a well resolved $1S_e$ source-drain current peak with clear MR response. However, when charging in the $1P_e$ state at higher gate potential, there is no systematic MR behavior. As previously reported[19], the conductivity in the $1P_e$ state is also strikingly lower than in the $1S_e$ state, at least at the temperatures shown in **Figure 5-4**. This was assigned to several

possible effects[19], including the splitting of the P_e states[22] which effectively lowers the density of states, and the directional frustrations for transport along P-orbitals.

The following discussion therefore only addresses the MR with $1S_e$. Again, the PMR is maximum at x =1/2. At 20 K, the x variation of a_+ could be well fitted by $a_+ \sim a_{+o} x(1-x)$ as shown in **Fig. 5-4e**. At 50K, a_+ could still be well fitted to the same form when $x \lessapprox ¾$, after which it does deviate, possibly due to the effect of thermally populated 1Pe states, Overall, a_+ increases with size, and, as shown in **Fig. 5-4e**, a_+ strongly decreases with increasing temperature. PMR was not observed at room temperature, but we measured the PMR at the fixed x=1/2, from 10K to 100K. As shown in **Fig. 5-4f**, $a_+ \sim T^{-3}$.

The analysis of the NMR shows that a_- is overall less sensitive, increasing less with increasing size, increasing much less with decreasing temperature (**Figure 5-3**) and showing only a weak although monotonous increase with filling fraction (**Figure 5-1**). The different signs and temperature and size effects suggest different origins of the positive and negative MR.

We made a number of tests to verify that the MR was not an artifact of the device shape or material (**Figure 5-7**). For the same CQD film preparation, we observed similar MR on a glass substrate as on the Si/SiO_2 substrate at zero gate. We verified that the MR was not affected by the choice of gold or platinum for the electrodes and also not by the size of the device. Since this study was motivated by the high mobility achieved, we measured the MR of the same HgTe CQDs cross-linked with Ethanedithiol. Such films are more resistive with a two orders of magnitude lower mobility, however they showed similar PMR and NMR (**Figure 5-8**).

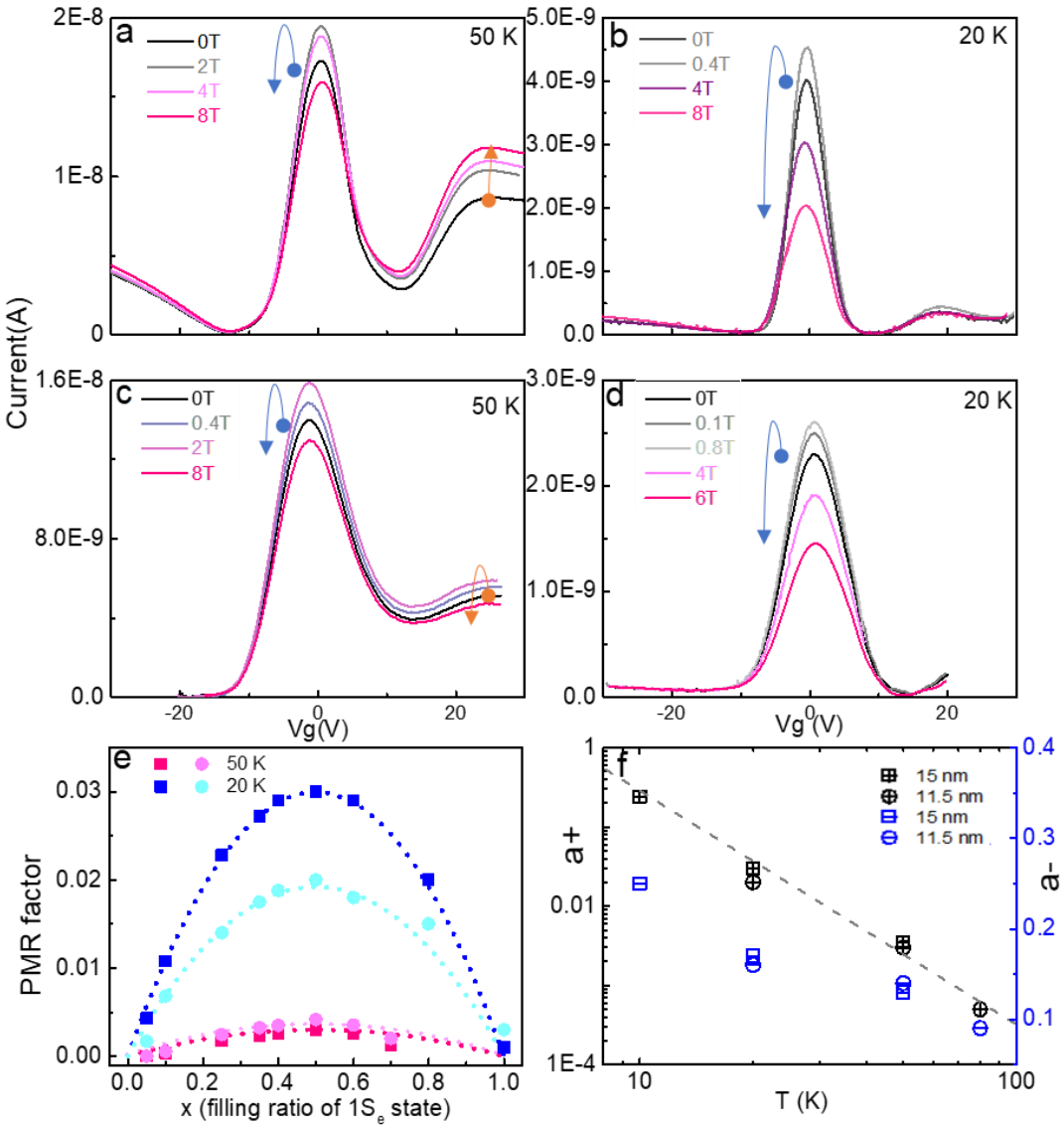

Figure 5-4. PMR factor. (a &b) Source-drain current curve of 15 nm diameter HgTe CQD by FET with 0.1 V bias at fixed magnetic field at 50 K and 20 K, respectively. (c &d) Source-drain current curve of 11.5 nm diameter HgTe CQD by FET with 0.1 V bias at fixed magnetic field at 50 K and 20 K, respectively. The arrows indicate the conductance change in S_e (blue) ans P_e (orange) state corresponding to the increased magnetic field. e) PMR factor a_+ of 15 nm(square) and 11.5 nm(circle) HgTe CQD films at 20 K and 50 K, respectively, fitting by (1- x) x times a constant. f) PMR parameter a_+ (black) and NMR parameter a_-(blue) of 15 nm (square) and 11.5 nm (circle) diameter HgTe CQD solid as a function of temperature. The figure is adapted from reference 29.

5.3 Discussion

While the similarity of the MR with films of low mobility suggests that the MR arises from local effects acting on individual CQDs or pairs of CQDs rather than from extended interactions, we analyze possible mechanisms for the positive and negative MR.

PMR: Explanation 1. (all equation in SI unit) A quadratic PMR naturally arises within the classical picture of a ballistic carrier with a single relaxation time τ. As the Lorentz force causes the electron to deviate from the linear travel direction along the electric field, it travels a shorter distance in the direction of the electric field, and the resistance increase is quadratic for small H. The generalization of this effect is called Kohler's rule [23] and leads to

$$\frac{\Delta\rho}{\rho} = (\frac{ne^2\tau}{m}\frac{1}{ne}H)^2 = (\frac{R_H}{\rho})^2H^2 \sim (\frac{H}{\rho})^2 = (\sigma H)^2$$

Here $R_H = \frac{1}{ne}$ is the Hall parameter, n is the carrier density, τ is the relaxation time, e is the elementary electron charge, and $\sigma = \frac{ne^2\tau}{m}$ is the conductivity.

In a system with a single mobile carrier, the Hall effect compensates for the deviation such that the MR disappears. With two carriers, there is a net positive magnetoresistance that is quadratic for low enough field.

$$\sigma = \frac{(\frac{\sigma_1}{1+{\mu_1}^2H^2} + \frac{\sigma_2}{1+{\mu_2}^2H^2})^2 + (\frac{\mu_1H\sigma_1}{1+{\mu_1}^2H^2} + \frac{\mu_2H\sigma_2}{1+{\mu_2}^2H^2})^2}{\frac{\sigma_1}{1+{\mu_1}^2H^2} + \frac{\sigma_2}{1+{\mu_2}^2H^2}}$$

$$\frac{\Delta\rho(H)^+}{\rho(H=0)} = \frac{\sigma_1\sigma_2(\mu_1-\mu_2)^2H^2}{(\sigma_1+\sigma_2)^2 + (\mu_1\sigma_1+\mu_2\sigma_2)^2H^2}$$

In the CQD films, one might imagine the motion of carriers in a miniband made of the 1Se states. In this case, the "electron" carrier (doping in the $1S_e$ state), and the "hole" carrier (vacancy in the $1S_e$ state) can be considered to have the same relaxation time, such that $(\mu_1 - \mu_2) \sim 2\mu$. We can also assume that $\mu^2 H^2 \ll 1$ since $\mu \sim 10^{-4}$ m^2/Vs . Therefore, considering only the $1S_e$ state, the expression simplifies to $\frac{\Delta\rho(H)^+}{\rho(H=0)} = (1-x)x\,\mu^2 H^2 = a_+ H^2$ over the range of magnetic field accessible in the experiment. This expression captures the experimental quadratic MR and the *x*-dependence. However, it predicts a strong effect of the mobility which is not supported by the experiments. Furthermore, the magnitude is much too large for the measured mobility of ~1 cm^2/Vs. Indeed, the model predicts $a_+ \sim 10^{-8}$ m^4/V^2s^2 at half filling compared to the observed value of 10^{-1} at 10K. We also note that the model of a miniband with partial filling predicts that the mobility should switch sign on either sides of the $1S_e$ conductance peak, while this is inconsistent with the measured Hall mobility[18] which is rather independent of the fractional occupation. The absence of miniband behavior may suggest a mean free path shorter than the dot spacing, and therefore a hopping conduction in these glassy structure CQD films. On the other hand, it must also be that any miniband effect is masked by the much stronger effect observed here.

Explanation 2. Magnetic confinement. In the CQD films at cryogenic temperatures, the mobility decreases with decreasing temperature with an activated behavior. A possible source of the PMR is therefore an increase of the hopping activation energy that could come from the magnetic confinement. This magnetic freeze-out was observed in narrow gap bulk semiconductors with light effective mass such as HgCdTe[24] and InSb[25]. For these narrow gap materials, the electrons hop in the impurity band and the increased impurity binding energy with magnetic field can lead to dramatic increase of the resistance. The magnetic confinement arises from the squared potential

vector term in the Hamiltonian such that $V(r) = \frac{e^2H^2r^2}{8m^*}$ and is quadratic in the magnetic field. Therefore, for small MR, we propose $a_+ \sim \frac{e^2r^2}{8kTm^*}$. For a 15 nm diameter CQD, the effective mass at the $1S_e$ state energy is $0.025m_e$, as estimated by a K•P model of the energy dispersion, and the confinement potential is then $\frac{e^2H^2r^2}{8m^*} \sim 1.25$ meV at 5 T. Such local mechanism would explain why similar PMR is observed for low and high mobility films. The magnitude is about right since $\frac{e^2r^2}{8kTm^*} \sim 0.028$ m^2/V^2s^2 for $r = 7.5$ nm and T= 20K compared to a value of 0.03 in Fig.3e. However, this magnetic confinement model predicts a T^{-1} temperature dependence of the PMR compared to the observed T^{-3}. It also no clear why the PMR scales as $(1-x)x$, unless the conductance at these points becomes dominated by other channels.

NMR: The NMR observed for HgTe CQDs films is rather independent of the doping level, it appears to be associated with a rather large effective g-factor, and it depends weakly or not at all on the mobility. The weak effect of the mobility allows to rule out a negative MR that involves coherent back scattering that leads to weak localization[26]. We also rule out spin blockade effects. The NMR is indeed opposite in sign and quite different to the case of weakly conductive organic films[15] of weakly coupled CdSe CQD[8] films which show an even narrower PMR, also in the 10% range, but with a fixed and very small magnetic field range of ~ 50mT and independent of temperature. That effect is assigned to a spin-blockade where the electron spins need to process around the random hyperfine field, reaching the favorable spin orientation before tunneling. When the magnetic field overcomes the hyperfine field, the electron spin orientations becomes defined, up or down, blocking tunneling depending on the relative spin orientations. The spin-blockade effect is possible when the exchange interaction is smaller than the hyperfine interaction and this

requires a very weak coupling. This was used to explain why the CdSe CQD films do not show the spin-blockade when nearest neighbor hopping is favored. Such explanation for the absence of spin blockade may apply here in the higher mobility HgTe CQD films since nearest neighbor hopping is the dominant situation at the investigated temperatures.

Explanation 1: magnetization. In transition metals, the conduction electrons can be affected by scattering due to the random spin orientation of d-shell electrons. Applying a magnetic field may partially order the spins and reduce the scattering. Fisher and Langer[27] predicted, with only short range spin fluctuation, that the decrease in the resistance would be proportional to M^2. The magnetic field dependence of the magnetization of the $1S_e$ state electrons of g-factor g, is given by the Brillouin function $B(x) = \frac{e^{2z}-1}{e^{2z}+1}$ where $Z=J\ g\mu_B H/k_B T$ and *J=1/2*. Then $\rho(H)^- \sim (M)^2 \sim (\frac{1}{(e^{-z}+e^{z})^4})^2 \sim e^{-4z}$ and NMR $\sim e^{-\frac{2g\mu_B H}{k_B T}}$.

The model does not provide an estimate for the prefactor a_- as this would depend on the interaction between $1S_e$ electrons with some other electron spins. It should also depend on the number of spins as they are the source of scattering. The mechanism should also disappear for full or empty 1Se states and give a strong dependence of x, which is not seen. It is also not likely to be applicable to a hopping conduction regime, where the scattering is already strong enough to localize the carriers on single sites.

Explanation 2: An alternative explanation in the hopping regime is that the Zeeman effect on the $1S_e$ state under a magnetic can reduce the energy barriers. Indeed, if two neighboring dots have an energy difference E, the Zeeman effect can increase the lower state energy by $g\mu_B H$ and

decrease the higher state energy by the same amount. Assuming that spin is not conserved upon tunneling, the barrier becomes smaller by $2g\mu_B H$. This would then lead to an NMR that is simply NMR$= e^{-\frac{2g\mu_B H}{k_B T}}$, with the coefficient $a_- = 1$. This is clearly larger than the experiment which indicates $a_- \sim 0.1$. One possible reason is the assumption of the spin being flipped while only a fraction of the hops may benefit from spin flipping. One also needs to justify the value of the g-factor. The data gives $g = \frac{110 \pm 8}{2} = 55 \pm 4$ and $g = \frac{126 \pm 3}{2} = 63 \pm 1.5$ for 15nm and 11.5nm dot, respectively. This is~ 3-fold larger than the theoretical prediction for the electron g-factor in HgTe quantum dots of the investigated size range. [28] In preliminary experiments, we looked for but did not find optical evidence for such a g-factor. (**Figure 5-9**). This explanation would also imply a saturation of the NMR but it is possible that this is masked by the stronger PMR since 1 tesla magnetic field could give energy shift~5 meV while the site barrier[18] is 10^1-10^2 meV.

5.4 Conclusion

In this work, we measured the MR of an interesting new system consisting of a glassy disordered film of rather monodisperse HgTe quantum dots. With an FET structure, we measured the MR as a function of doping in rather high mobility films (1-10 cm^2/Vs), as a function of temperature down to 10K and fractional occupation of the $1S_e$ electronic state. We observed a positive-quadratic magnetoresistance which can be several 100% at low temperature and scales like x (1- x) where x is the fractional occupation of the $1S_e$ state. This positive magnetoresistance is seven orders of magnitude larger than the effect that could arise from ballistic carriers within the relaxation time approximation. Instead, it is tentatively attributed to the increased confinement induced by the

magnetic field and the increased hopping activation energy. There is also a negative magnetoresistance of 1-20% from 300 K to 10 K which is rather independent of the fractional occupation, and which follows a negative exponential dependence with the magnetic field. It can be empirically fit with an effective g-factor of ~ 100 and it is tentatively attributed to the reduction of barrier heights by the Zeeman splitting of the $1S_e$ state. However, this requires a $1S_e$ electron g-factor for the HgTe QD that is about 3 times larger than predicted. Although these results are not fully understood, they indicate that most of the magnetic effects are rather local in nature. The quality of the materials and the ease of controlling the charge occupation will allow to extend these studies to magnetically doped quantum dots which may have further interesting properties.

5.5 Methods

Monodisperse HgTe CQDs were prepared following reference[22]. A two-phase ligand exchange process was applied to transfer the HgTe QDs from hexane to polar dimethylformamide (DMF) where $HgCl_2$, 2-Mercaptoethanol, butylamine, and butylammonium chloride co-serve as the hybrid ligands[18]. Several different sizes HgTe dots were investigated.

Film preparation: The HgTe QD films were prepared by spin-coating on patterned Au electrode on 300nm SiO_2/Si substrate. Area between the electrodes was 1mm*3mm. The absorption spectra were measured for films made with the same procedure on ZnSe windows.

MR measurement: The CQD solids were inserted into a Physical Property Measurement System (PPMS-9, quantum design) under a helium inert atmosphere. The applied magnetic field was

perpendicular to the films. The resistance was measured by a Keithley 2636A Dual Channel Source meter with the Four-point sensing.

5.6 Appendix

1. TEM of different size HgTe CQD

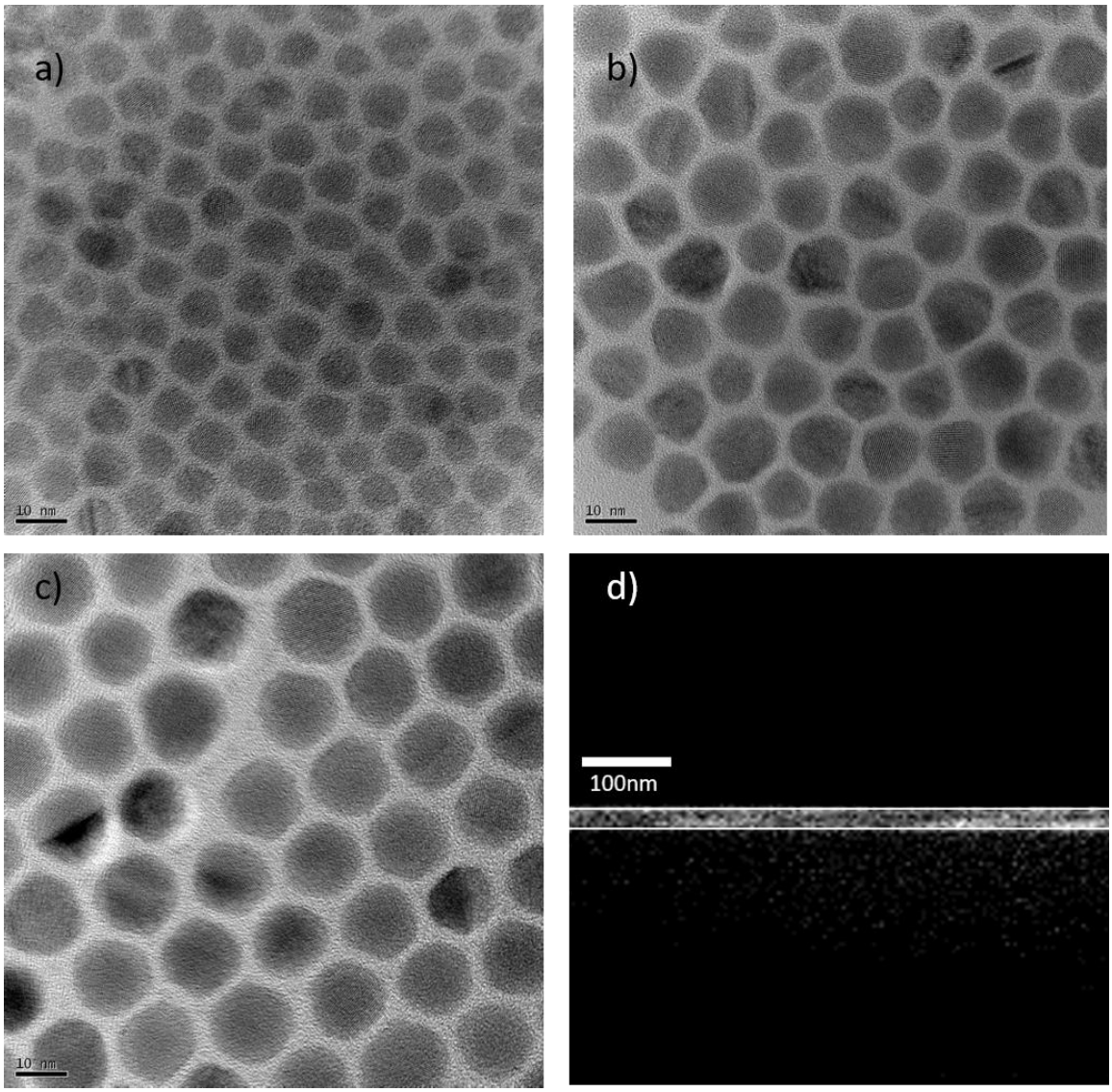

Figure 5-5. **TEM of different size HgTe CQD** a)b)c)TEM of 8nm, 11.5nm and 15nm diameter HgTe CQD, respectively. d) SEM. Cross section of 11.5nm diameter HgTe CQD film of ~2 layers used in the measurements.

2. 8nm diameter HgTe CQD solid MR

Figure 5-6 shows the MR of 8nm diameter HgTe CQD solid at 100K and 20K. The film Thickness ~60nm (around 8 layers quantum dots). The MR could also be fitted nicely by the equation mentioned in before with $g \sim 70$.

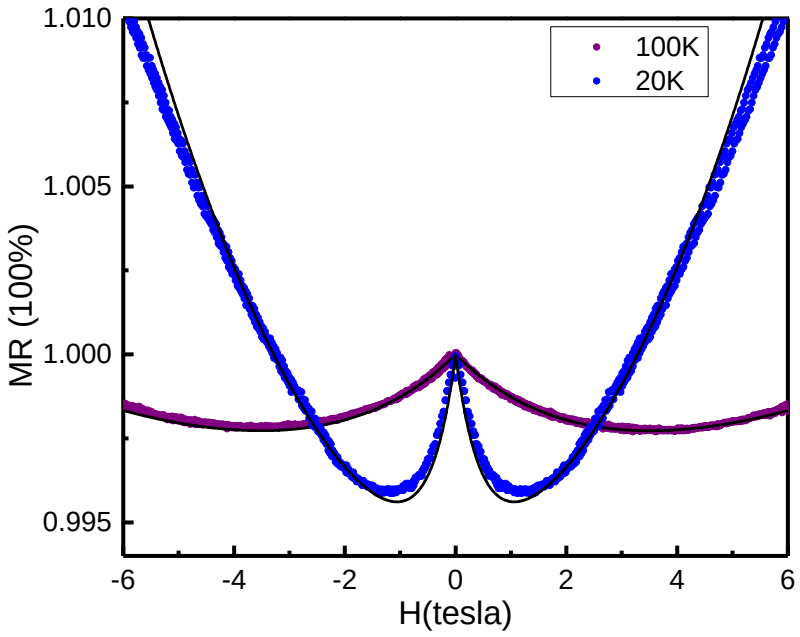

Figure 5-6. MR on 8nm diameter HgTe CQD solid.

3. Substrate and electrode effect on MR.

Substrate and electrode material have no obvious effect on MR. **Figure 5-7** shows the MR curve measured with two different substrate and electrode. The MR curves almost overlap, indicating that the resistance change does not come from the substrates or electrodes and the MR is very

repeatable. Changing the film area from 3mmx1mm to 3mmx5μm also shows no obvious effect on MR.

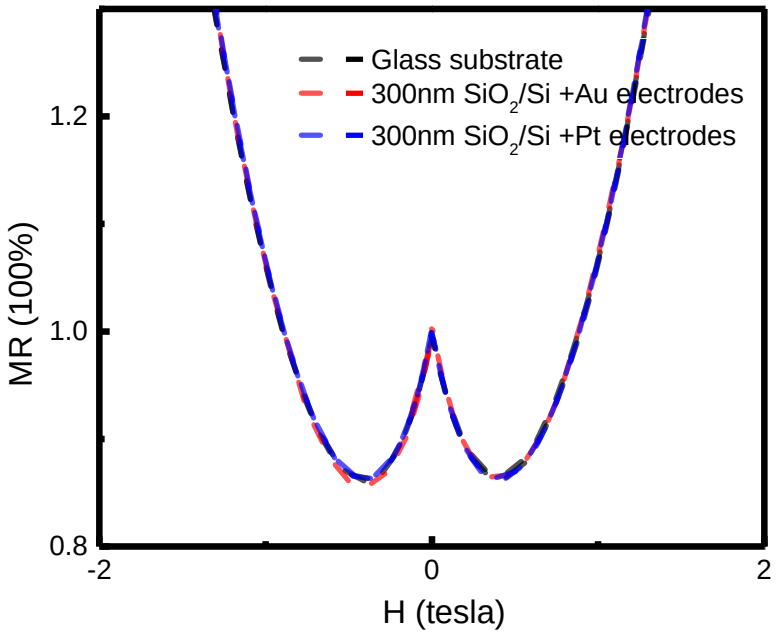

Figure 5-7. MR of 15nm diameter HgTe CQD at 10K with two different substrates and electrodes.

4. Low mobility HgTe MR

EDT treated HgTe quantum dots films have 2 order smaller mobility compared to the polar ligands exchanged HgTe films. The MR, however, has a similar behavior. **Figure 5-8** shows the MR at 50K of low mobility and high mobility 11.5nm HgTe CQD film with similar thickness.

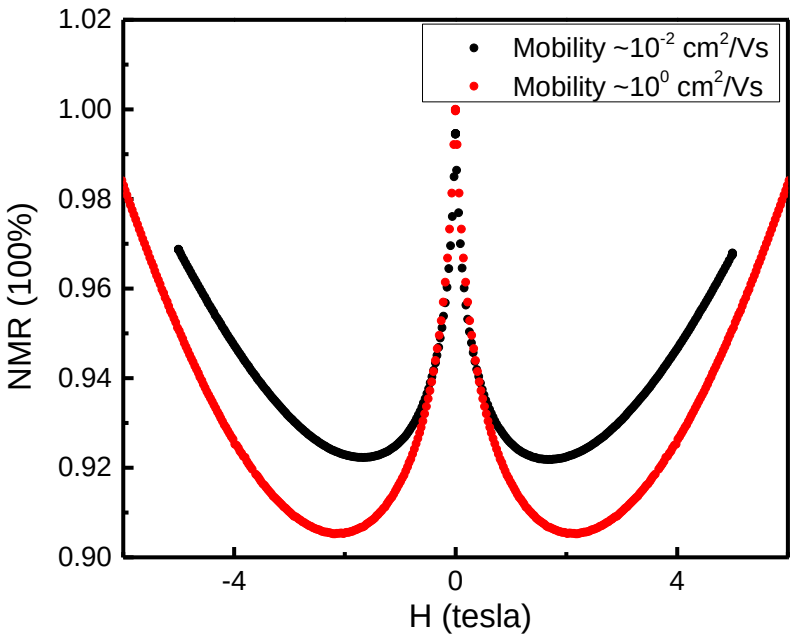

Figure 5-8. MR on low mobility (Black curve) and high mobility (red curve) 11.5 nm diameter HgTe CQD films at 50K.

5. Optical measurement.

Independent measurement of g would be helpful to provide a clue to understand the NMR. If g is the total angular momentum (Landé) g-factor, when g~100, with 0.5 tesla magnetic field, one should see the intraband absorption peak blue (red) shift by ~10cm^{-1} for the $S_{1/2}$ to $P_{3/2}$ ($P_{1/2}$) transition. However, the real situation could be more complex. First, considering all the possible transition for the S-P state as shown in **Figure 5-9a**, the average peak position should not change but the S-P transition should become broader. Second, since we measure an absorption of the QD film, one should consider the convolution (Voigt) of homogenous broadening (Lorentzian) and inhomogeneous broadening (Gaussian). **Figure 5-9b** shows one simulation example of Voigt spectra before and after the homogenous broadening and adding 10cm^{-1}. The insert graph shows

that the effect would be more obvious at the bottom of the peak. However, this is difficult to measure by optical absorption because of the noise level. **Figure 5-9c** shows the intraband absorption with/without external magnetic field (0.5tesla) of 11.5nm HgTe CQD. Although it is a nicely resolved intraband spectrum by recent literature standards[22], it is not possible to ascertain any spectral changes.

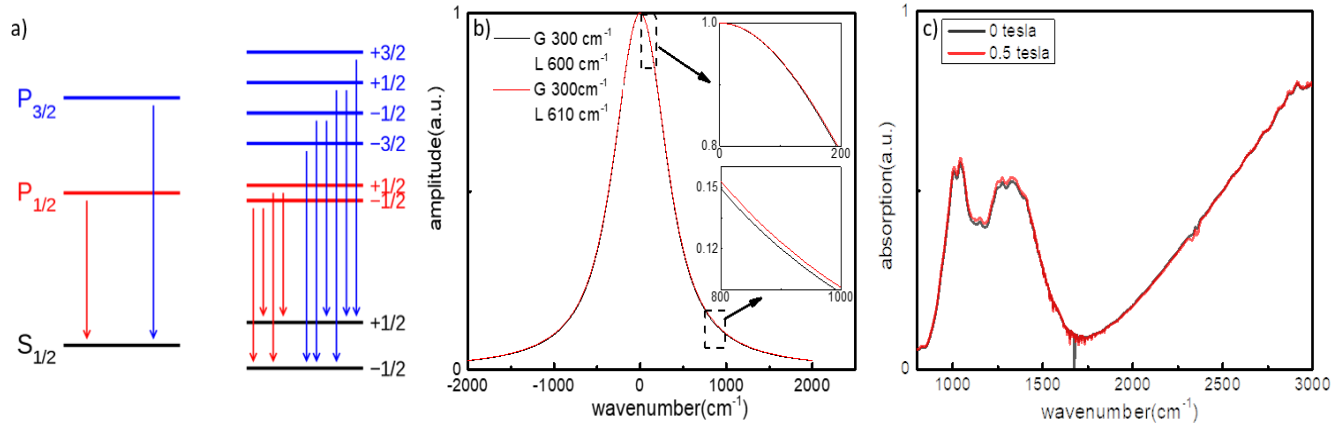

Figure 5-9. Spectra with magnetic field. a) Possible transition for S-P state. b) simulation of Voigt spectra before and after the homogenous broadening adding 10cm^{-1}. The FWHM value are indicated in the graph. c) Intraband absorption with/without external magnetic field of 11.5nm HgTe CQD.

References

[1] N. W. Ashcroft, N.D. Mermin, Solid State Physics. Saunders College, Philadelphia (1976), pp672

[2] J. K. Furdyna, Diluted Magnetic Semiconductors. J. Appl. Phys. 64, R29−R64 (1988).

[3] L. Halbo, R.J. Sladek, Magnetoresistance of Undoped n-Type Gallium Arsenide at Low Temperatures, Physical Review, 173 794-802 (1968).

[4]H. Y. Hwang, S.W. Cheong, P. G. Radaelli, M. Marezio, B. Batlogg, Lattice effects on the magnetoresistance in doped LaMnO3, Phys Rev Lett, 75, 914-917 (1995).

[5] M.R. Boon, Negative Magnetoresistance in Doped Semiconductors, Physical Review B, 7, 761-762 (1973).

[6] P. Majumdar, P. B. Littlewood, Dependence of magnetoresistivity on charge carrier density in metallic ferromagnets and doped magneticsemiconductors, Nature, 395, 479-481 (1998).

[7] R. Rinaldi, P. V. Giugno, R. Cingolani, H. Lipsanen, M. Sopanen, J. Tulkki, and J. Ahopelto, Zeeman Effect in Parabolic Quantum Dots, Phys. Rev. Lett. 77, 342 (1996).

[8] D. J. Norris, N. Yao, F. T. Charnock, T. A. Kennedy, High-Quality Manganese-Doped ZnSe Nanocrystals, Nano letter, 1 3-7 (2000).

[9] R. Beaulac, P. I. Archer, S. T. Ochsenbein, D. R. Gamelin, Mn2+-Doped CdSe Quantum Dots: New Inorganic Materials for Spin-Electronics and Spin-Photonics. Adv. Funct. Mater. 18, 3873−3891 (2008).

[10] S. T. Ochsenbein, Y. Feng, K. M. Whitaker, E. Badaeva, W. K. Liu, X. Li, D. R. Gamelin, Charge-Controlled Magnetism in Colloidal Doped Semiconductor Nanocrystals. Nat. Nanotechnol. 4, 681−687 (2009).

[11] V.A. Vlaskin, R.Beaulac, D. R. Gamelin,, Dopant-Carrier Magnetic Exchange Coupling in Colloidal Inverted Core/Shell Semiconductor Nanocrystals, Nano letter, 9, 4376-4382 (2009).

[12] D. Yu, B. L. Wehrenberg, I. Yang, W. Kang, and P. Guyot-Sionnest, Magnetoresistance of n-type quantum dot solids. Appl. Phys. Lett. 88, 072504 (2006).

[13] P. Guyot-Sionnest, D. Yu, P.H. Jiang, W. Kang, Spin blockade in the conduction of colloidal CdSe nanocrystal films, The Journal of chemical physics, 127 014702 (2007).

[14] A. Pourret, A. Ramirez, P. Guyot-Sionnest, Magnetoresistance of CdSe/CdS Quantum Dot Films. Appl. Phys. Lett. 95, 142105−142108 (2009).

[15] Y. Sheng, T.D. Nguyen, G. Veeraraghavan, Ö. Mermer, M. Wohlgenannt, S. Qiu, U. Scherf, Hyperfine interaction and magnetoresistance in organic semiconductors, Physical Review B, 74 (2006).

[16] H. Liu, P. Guyot-Sionnest, Magnetoresistance of Manganese-Doped Colloidal Quantum Dot Films, The Journal of Physical Chemistry C, 119, 14797-14804 (2015).

[17] M. V. Kovalenko, M. Scheele, D. V. Talapin, Colloidal Nanocrystals with Molecular Metal Chalcogenide Surface Ligands, Science, 12, 324, 1417 (2009).

[18] Lan, X.; Chen, M.; Hudson, M. H.; Kamysbayev, V.; Wang, Y.; Guyot-Sionnest, P.; Talapin, D. V. Quantum Dot Solids Showing State-Resolved Bandlike Transport, Nature Materials 2020.

[19] Chen, M.; Lan, X.; Tang, X.; Wang, Y.; Hudson, M. H.; Talapin, D. V.; Guyot-Sionnest, P. High Carrier Mobility in HgTe Quantum Dot Solids Improves Mid-IR Photodetectors. ACS Photonics 2019, 6, 2358-2365

[20]P. Guyot-Sionnest, Electrical transport in colloidal quantum dot films, The Journal of Physical Chemistry Letters, 3, 1169-1175 (2012).

[21] G. Shen, M. Chen, P. Guyot-Sionnest, Synthesis of Nonaggregating HgTe Colloidal Quantum Dots and the Emergence of Air-Stable n-Doping, The Journal of Physical Chemistry Letters, 8, 2224-2228 (2017).

[22]M. H. Hudson, M. Chen, V. Kamysbayev, E.M. Janke, X. Lan, G. Allan, C. Delerue, B. Lee, P. Guyot-Sionnest, D. V. Talapin, Conduction band fine structure in colloidal HgTe quantum dots, ACS nano, 12, 9397-9404 (2018).

[23] J.M. Ziman, Electrons and Phonons, Oxford University press (1960) pp490

[24] G. De Vos, F. Herlach ,H. W. Myron, Magnetotransport properties of Hg1-xCdxTe in high magnetic fields, Journal of Physics C: Solid State Physics, 19, 2509 (1986)

[25] R. Mansfield, L. Kusztelan, Magnetoresistance and Hall effect in n-type indium antimonide in the magnetic freeze-out region, Journal of Physics C: Solid State Physics, 11, 4157 (1978)

[26] G.Bergmann, Weak localization in thin films: a time-of-flight experiment with conduction electrons. Physics Reports, 107, 1-58 (1984)

[27] M.E. Fisher, J.S. Langer, Resistive Anomalies at Magnetic Critical Points, Physical Review Letters, 20, 665-668 (1968).

[28] X.W. Zhang, J.B. Xia, Electronic structure and electrongfactors of HgTe quantum dots, Journal of Physics D: Applied Physics, 39, 1815-1820 (2006).

[29] M. Chen, X. Lan, M. H. Hudson, G. Shen, P. B. Littlewood, D. V. Talapin, P. Guyot-Sionnest. Magnetoresistance of HgTe Quantum Dot Films (in preparation)

Chapter 6: High Carrier Mobility HgTe QD Mid-IR Photodetectors

To understand the transport mechanism in QD system, and then control it, will also benefit applications. This chapter shows our work on improved mid-infrared photoconductors based on colloidal HgTe quantum dots which are modified using the hybrid ligand exchange and polar phase transfer mentioned in **Chapter 3**. The doping can also be controlled n and p by adjusting the $HgCl_2$ concentration in the ligand exchange process. Photoconductive properties of the high mobility HgTe QD device is compared with the one using prior "solid-state ligand exchange" by ethanedithiol. The new process affords ~ 100-fold increase of the electron and hole mobility, ~100-fold increase in responsivity and ~10-fold increase in detectivity. These photodetector improvements are primarily attributed to the increase in mobility (μ) because the optical properties are mostly unchanged. The noise analysis gives the specific detectivity (D^*) of a photoconductive device is expected to scale as $\sqrt{\mu}$. The application potential is further verified by long-term device stability.

This chapter includes the published result from reference 27 as well as some unpublished data.

6.1 Introduction

The mid-wave (3-5 microns) and long-wave infrared (8-12 microns) are of particular interest for thermal imaging because they match the atmospheric windows. The dominant photon detectors in these ranges are single crystal InSb and HgCdTe, while alternatives based on epitaxial quantum dot infrared photodetectors (QDIP), quantum well (QWIP), and type-II superlattices of III-V semiconductors are receiving increasing attention.[1] However, the cost of single crystal epitaxial growth remains high while interfacing to silicon read-out chips is also complex. Colloidal quantum dots (CQDs) have tunable optical transitions[2] through manipulation of nanocrystal size, shape, and surface. CQDs are therefore being widely investigated for photodetectors from the visible[3,4] to the near-infrared[5-7] and mid-infrared.[8-10] The exciting promise of CQD is the facile fabrication of photodetectors.[6,9] For example, PbS CQDs have been extensively studied for the near-infrared photodetectors,[4-7,9,11-13] and used for the first demonstration of CQD near-infrared imaging sensors.[11] HgTe CQDs allow a broader coverage of the infrared, from near- to far-IR, and are also extensively investigated.[8,10,14,15] Previously reported mid-infrared video imaging devices were also made by simply drop-casting HgTe CQDs on a silicon read-out circuit[16] and using the "solid-state ligand exchange" with ethanedithiol.[4,6-9] The images had a noise-equivalent temperature difference (NETD) of 100mK corresponding to a detectivity of 10^{10} Jones for these photoconductive (PC) device.[16] This is one order of magnitude below InSb commercial cameras operated at the same cryogenic temperatures and significant improvements are therefore needed to bring these devices towards practical relevance.

One clear direction to improve performance is higher mobility since it should help collect photogenerated charges except when the carrier diffusion length is limited by trapping sites.[17, 18] However, the "solid-state ligand exchange" affords mobilities of only ~ 10^{-1} cm^2/Vs.[19] Likely

because of the partially aggregated nature of the CQDs in the solution, success at improving further the mobility of these HgTe CQDs has remained limited.[20] Furthermore, the replacement of bulky surface ligands with small molecules during the solid-state ligand exchange causes significant volume contraction, cracks and voids in CQD films. A general strategy for higher mobility is to use phase transfer in polar solvents[21] and very short or ionic ligands.[22,23] Using a HgTe CQD synthesis that affords spherical and non-aggregated HgTe CQDs,[24,25] we therefore explored several protocols using phase transfer on these HgTe CQDs. A room temperature process was then developed that greatly boosted the mobility above 1 cm^2/Vs while faithfully preserving the optical properties and photoluminescence of the CQDs [26] and also allowing to fine-tune both n- and p-type doping. This chapter reports photodetector performances afforded by this process[27]. The doping and mobility of films are measured using both electrochemical and solid-state field-effect transistor (FET) methods. The responsivity, noise, and detectivity are measured from 300 K to 80 K. The properties are compared with those of lower mobility films prepared from identical HgTe CQDs by the solid-state ligand exchange using ethanedithiol. Since the long-term doping stability of polar phase-transfer-ligand-exchanged CQD films is affected by air exposure, we evaluate the stabilization of the performance using a simple polymer coating.

6.2 Characterization of Mid-IR HgTe CQDs

For the HgTe CQD phase transfer, we start from well dispersed oleylamine capped HgTe CQDs in hexane.[24,25] The CQDs are transferred to dimethyformamide (DMF) using mercaptoethanol, $HgCl_2$, butylamine and butylammonium chloride. This strategy is termed a hybrid ligand exchange because of the use of both organic and inorganic ligands. In this work, clean solutions of the HgTe/hybrid ligands CQDs are then made by precipitation using toluene and redispersion in

dimethyformamide. Films, referred to as HgTe/hybrid, are prepared by spin-coating or drop-casting the polar solution. In order to assess the effects of increased mobility, we compare the properties with films prepared directly from the same oleylamine-capped HgTe CQD followed by solid state ligand exchange using ethanedithiol (EDT), referred as HgTe/EDT. Both types of films have similar appearance, black, smooth, and reflective and their absorption spectra show no noticeable shift of the mid-infrared band-edge absorption. (**Figure 5-1**) However, they differ markedly in their optoelectronic properties.

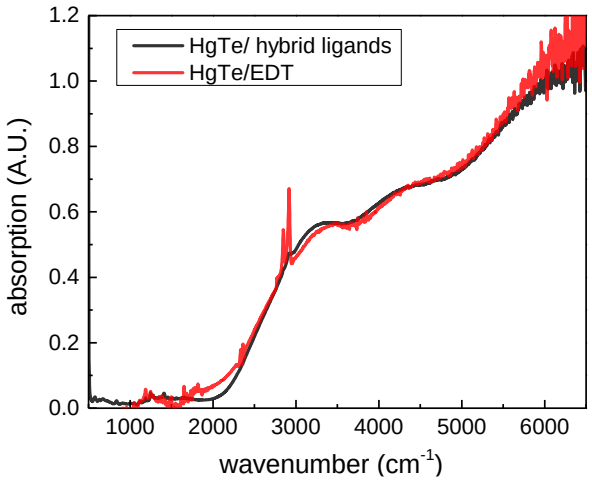

Figure 6-1: Absorption spectra of HgTe/hybrid and HgTe/EDT films. Room temperature absorption spectra of HgTe/hybrid ligands(black), HgTe/EDT(red). This figure is adapted from Ref 27.

The electronic properties are characterized by electrochemical[28] and FET measurements.[29] Cyclic voltammetry(CV) and conductance measurements of the films are used to determine the energy level position and the Fermi level with respect to a reference potential, as well as the mobility.[19] **Figure 6-2** shows the CV and conductance for films of 9 nm diameter HgTe CQDs at 203 K. As shown in **Fig.6-2**, decreasing the concentration of $HgCl_2$ used in the exchange solution leads to a clean rigid shift of the cyclic voltammetry, which is due to shifting the Fermi level from n- to p-

type. Assigning the 1Se state peak area in the CV to 2 electrons/dot, the doping switches from ~1 hole/dot without any $HgCl_2$ in the exchange solution, to ~1 electron/dot with the higher concentration of $HgCl_2$. The n-doping effect of added mercury ions was reported previously for HgS and HgSe CQDs.[30] The sensitivity of the doping to Hg^{2+} was assigned to a shift of the state energies with respect to the environment Fermi level, and this was attributed to surface dipole shifting the electrostatic potential of the CQDs. A surface dipole pointing inward (positive end on the surface) raises the electric potential inside, stabilizing the electron. The n-type direction and the shift of the energy levels with Hg^{2+} are consistent with this assignment.

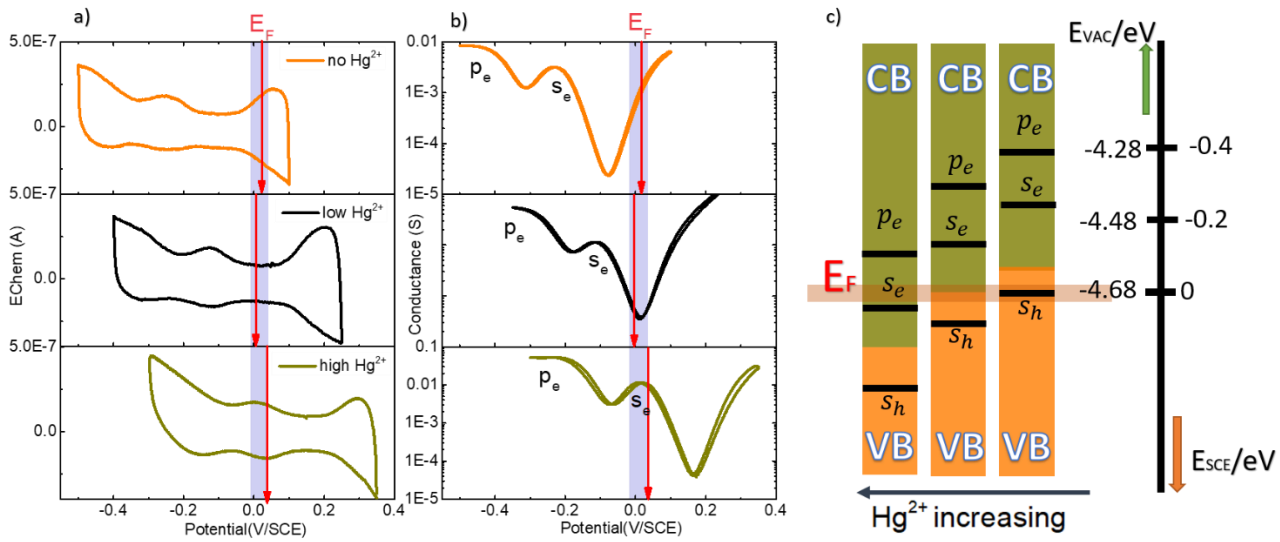

Figure 6-2. Electrochemistry of mid-IR HgTe with different doping. (a,b) Cyclic voltammetry and conductance of films of 9nm diameter HgTe CQD made after phase-transfer without $HgCl_2$(orange), 0.025 mM $HgCl_2$ /0.04 mM HgTe (black) and 0.5 mM $HgCl_2$ /0.04 mM HgTe (olivine) at 203 K. Potentials are referenced to the saturated calomel electrode (SCE). The Fermi level is given by the rest potential (red arrow) and the blue stripe covers the range of rest potentials observed in the electrochemical environment. (c) Energy diagram. This figure is adapted from Ref 27.

The electron and hole mobility obtained by electrochemistry are given in **Table 6-1** for the 9 nm diameter HgTe/hybrid ligands films with different doping. The electron mobility is ~2 cm^2/Vs, similar to the hole mobility of ~1 cm^2/Vs, and both are independent of doping.

Sample doping /mobility	**Electrochemistry**		**Field Effect Transistor**	
	Hole mobility cm^2/Vs	Electron mobility cm^2/Vs	Hole mobility cm^2/Vs	Electron Mobility cm^2/Vs
0.6-1electron/dot	1.3	1.8	0.10	5.9
0.2electron/dot	0.9	1.6	0.30	4.5
Intrinsic	1.2	1.5	0.45	3.4
0.2hole/dot	1.1	2.1	0.62	1.9
1hole/dot	0.9	1.8	0.80	0.18

Table 6-1. Mobility measured by Electrochemical and FET methods. This table is adapted from Ref 27.

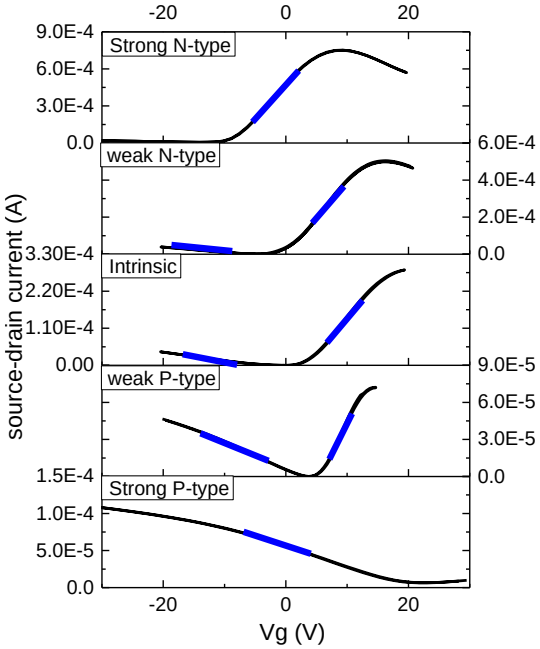

Figure 6-3. FET curve of N-type and P-type HgTe/ hybrid ligands. FET transport curves of different doping level HgTe/hybrid films at ~80K. Strong p-doped (doping ~1h/dot) to strong n-doped (doping ~0.6e/dot).

Complementarily to electrochemistry analysis, FET measurements allow us to obtain the mobility and doping of the dry films, therefore in the same conditions as the photodetector devices. **Figure 6-3** shows the transfer curve of the source-drain current as a function of the gate bias, for ~90 nm thick HgTe/ hybrid films, at 80 K. Varying $HgCl_2$ concentration in the phase transfer step also shifts the FET transfer curves: near-intrinsic doping is achieved with 12mg HgTe processed with 0.025 mM $HgCl_2$, weakly n-doped films with 0.052 mM $HgCl_2$, Strong n-doped films with 0.5mM $HgCl_2$, weakly p-doped films with 0.0125 mM $HgCl_2$ and strong p-doped films with no $HgCl_2$. The doping follows the same trend as in the electrochemical data with respect to the $HgCl_2$ amount. The magnitude of the doping in FET measurements is directly determined from the value of the gate bias at the minimum conductivity, using the estimated CQD surface density and the capacitance for 300nm SiO_2. For these five films the doping is ~0.6 electron/dot, ~0.2 electron/dot, zero, ~0.2 hole/dot and 1 hole/dot, respectively. Achieving a near-intrinsic film is therefore possible with a precise control of the $HgCl_2$ concentration in the ligand exchange step.

The linear regime FET mobility in Table 1 is determined using the slopes of the FET transfer characteristics (blue lines in **Fig.4-3**), calculated as $\mu = \frac{dI_{ds}}{dV_g}\frac{1}{V_{ds}}\frac{1}{C_i}\frac{L}{W}$, where I_{ds} is the drain-source current, V_g is the gate potential, V_{ds} is the drain-source bias, C_i is the capacitance of 300nm SiO_2 gate dielectric, L is the channel length and W is the channel width. **Table 4-1** shows that the electrochemical mobility is independent of doping, while the FET carrier mobility is always maximized for the majority carriers. The effect is quite noticeable and, to our knowledge, such relation between the mobility and doping in CQD FETs has not been reported previously. We propose that it may be due to electron-hole recombination/scattering between the gated layer, which is a monolayer of CQDs next to the gate dielectric,[31] and the more remote region not affected by the gate potential. We also noted that at similar temperatures, the maximum FET electron

mobility is about 3 times larger than the electrochemical mobility, while the maximum FET hole mobility is about the same as the electrochemical mobility. Prior studies on high mobility graphene have shown that the local charges of electrolyte ions introduced additional scattering,[32-34] and further comparative studies will therefore be needed to assess the origin of the differences.

The control HgTe/EDT films made using the same HgTe CQDs are also characterized by electrochemical and FET gating studies. They have an FET mobility of (0.4 ~ 1.6) × 10^{-2} cm^2/Vs (**Figure 6-4**), which is about two orders of magnitude lower.

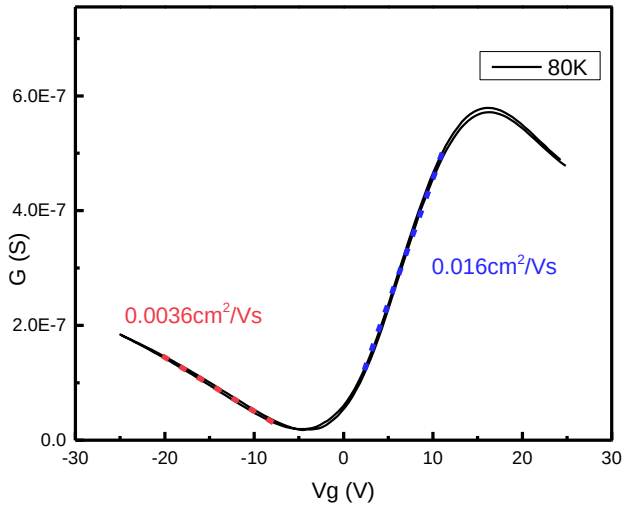

Figure 6-4. FET of HgTe/EDT film at ~80 K. This figure is adapted from Ref 27.

6.3 Photoresponse of Mid-IR HgTe QDs.

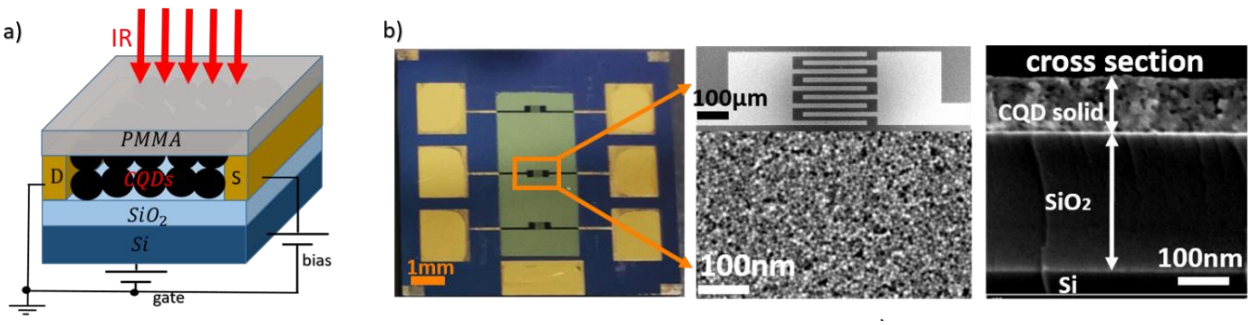

Figure 6-5. Device structure. (a) Schematic of a bottom-gate FET. (b) Photograph and SEM image of 3 FET devices of 0.3mm x 0.16mm. This figure is adapted from Ref 27.

The FET structure (**Figure 6-5**) is to determine doping level of the film, figuring out the nearest intrinsic sample. The transconductance curves are showed in **Figure 6-6**. The inset graphs in **Fig.6-6(a, b, c)** zoomed in regions of FET transfer characteristics near the conductance minima. In contrast to the electrochemical data, the minimum dark current of the doped CQD films is always larger than for undoped samples. This arises because FET gating affects charges mostly in the CQD layer closest to the SiO_2, while electrochemical gating sets the Fermi level over the entire thickness of the CQD film. The insets also show the current under illumination by a 600°C, 21 mm diameter blackbody source placed about 15 cm away. The current under illumination is similar for all three doping levels, but it is the undoped sample that gives the largest relative increase compared to the dark current.

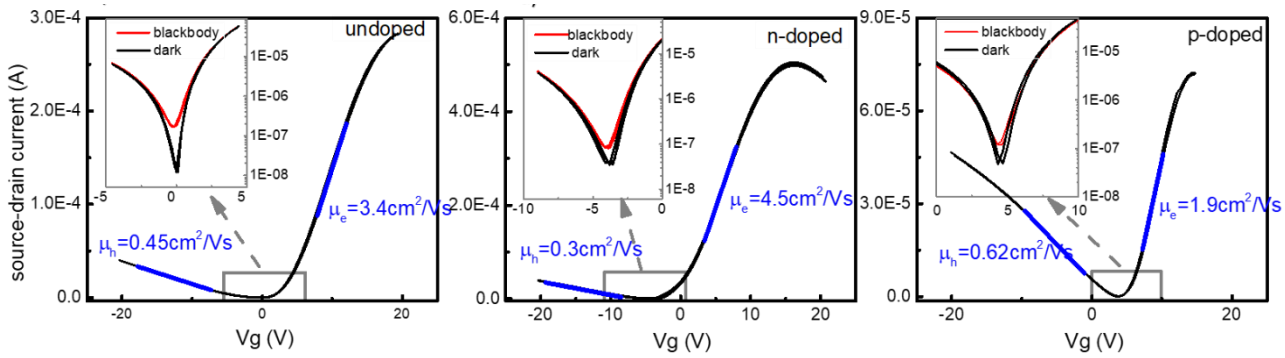

Figure 6-6. Figure out the intrinsic doping device with FET. (a-c) FET transfer characteristics (at 80 K) of near-intrinsic, n-doped and p-doped HgTe/hybrid ligands films, respectively. The insets show zoomed in regions near the conductance minima, showing the photocurrent (red) and dark current (black). The blue lines indicate the slopes used to calculate the hole and electron mobility. This figure is adapted from Ref 27.

The photoresponse spectra of the films are measured with an FTIR in regular scanning mode (**Figure 6-7**). The spectra shown in **Fig.6-7a** are normalized to the response of a DTGS detector, correcting for the effect of the scanning speed as previously reported.[35] HgTe/hybrid and HgTe/EDT have very similar spectra, band edge position, width, and temperature tuning, but with a better signal to noise ratio for HgTe/hybrid and slightly lower hydrocarbon absorption near 3000cm^{-1}. The similar photocurrent spectra confirm the stability of the HgTe CQD during the phase transfer exchange. Between room temperature and 80 K, the cut-off, defined as the half point of the rising detection edge redshifts from 2500 cm^{-1} to 2100 cm^{-1} which is typical for HgTe CQD of that size range. At 80K, the 10%-90% interval of the absorption edge is 750 cm^{-1}. This is significantly wider than the 500cm^{-1} typical with the tetrahedral aggregated HgTe CQDs studied previously.[36] The large width is consistent with the softer absorption edge of the spherical non-aggregated HgTe CQDs and this is an issue that will have to be addressed in the future optimization of the materials.

The dark current of the near-intrinsic films is shown in **Fig.6-7b**. The dark current drops 4 orders of magnitude from room temperature to 80K with a rather simple Arrhenius behavior of activation energy 90 meV. The dark current is proportional to the product of the mobility and carrier concentration $I \sim ne\mu$. Since the films are near-intrinsic, the carrier concentration at the higher temperature is dominated by the thermal carriers such that $n \sim \exp(\frac{-E_g}{2k_BT})$. Assuming that the mobility has a much weaker temperature dependence, the activation energy expected for an intrinsic semiconductor with a 5 microns band edge wavelength should be ~125meV which is larger than observed. Part of the resolution of this discrepancy may be the width of the absorption edge which reduces the effective activation energy. Doped samples show smaller activation energy, and this reflects the movement of the Fermi level within the gap.[37] (**Figure 6-8**) For the same bias, the dark current of the intrinsic HgTe/EDT films is always smaller and this reflects the lower mobility. Normalizing by the thickness and at the same bias, the dark current in **Fig.6-7b** for HgTe/hybrid at 300 K is on average about 55 times larger than for HgTe/EDT, which is less than the expected 100-fold increase from the mobility but of the right order.

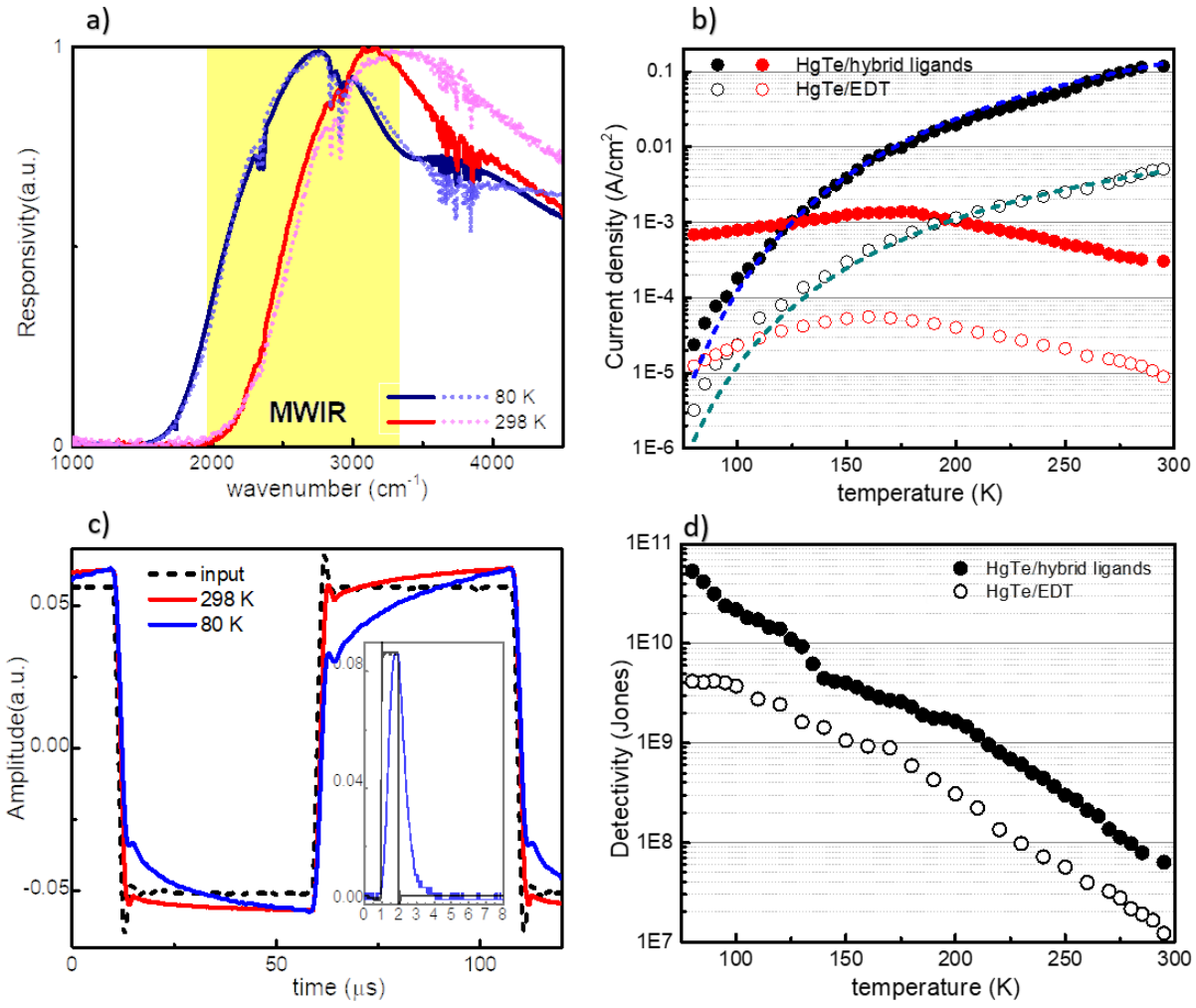

Figure 6-7. Photoconductive property. (a) Photoresponse spectra of HgTe/hybrid (solid lines) and HgTe/EDT (dashed lines) films. (b) Dark current density (black dots) and photocurrent (red dots) as a function of temperature for the two films. The dash lines are Arrhenius fits with activation energy ~90 meV for HgTe/hybrid and 82 meV for HgTe/EDT. The HgTe/hybrid film is 120 nm thick and the HgTe/EDT film is 260 nm thick. (c) Temporal response of the HgTe/hybrid film to a 50 μs light pulse from an 808 nm laser and to a 1μs pulse (inset). (d) Detectivity as a function of temperature for the HgTe/hybrid and HgTe/EDT films. This figure is adapted from Ref 27.

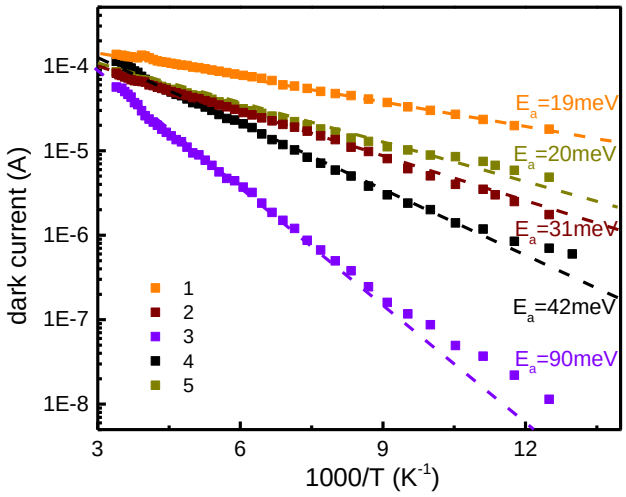

Figure 6-8. **Temperature dependent dark current of films of HgTe/hybrid with different $HgCl_2$ amount**. Dark current of HgTe/hybrid films on the FET devices with different amount of $HgCl_2$, from 0.25mM (sample 1) gradually decreasing to 0mM (sample 5) in the hybrid ligand exchange. This figure is adapted from Ref 27.

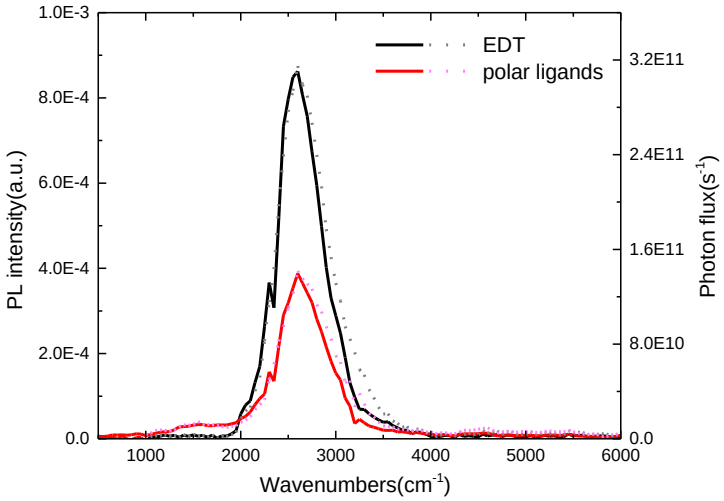

Figure 6-9. Photoluminescence of HgTe/Hybrid and HgTe/EDT. Photoluminescence (solid line) and photon flux (dot line) of HgTe/EDT(black) and HgTe/Hybrid (red) films, respectively. This figure is adapted from Ref 27.

The photocurrent response of the devices to the blackbody source is also shown in **Fig. 6-7b**. The photocurrent is larger for HgTe/hybrid than HgTe/EDT by a similar factor as the dark current. For a photoconductor, the photocurrent is proportional to the product of mobility and carrier lifetime. The ~60-fold larger photocurrent for HgTe/hybrid ligands maybe consistent with the 100-fold higher mobility and a slightly shorter carrier lifetime. The latter statement is supported by photoluminescence (PL) measurements that indicate similar but slightly lower PL quantum yields of $1 \cdot 10^{-4}$ for HgTe/hybrid compared with $1.9 \cdot 10^{-4}$ for HgTe/EDT (**Figure 6-9**). As shown in **Fig.6-7b**, upon cooling from 300 K, the photocurrent initially increases with decreasing temperature, while the dark current decreases. As discussed above, the dark current scales as *n*. On the other hand, the photocurrent is proportional to the lifetime and this scales as 1/ *n* if it is limited by geminate recombination instead of trapping. This explains the mirroring of the dark and photocurrent curves on the log scale in **Fig.6-7b**. Further lowering the temperature below 170K, the photocurrent decreases and this may indicate that the carrier lifetime becomes limited by traps while the mobility and quantum efficiency of charge generation will also decrease.

For the responsivity measurement, we first measure the photocurrent (for example 0.34μA with 1.5V bias on effective area 0.03 cm×0.016 cm at 80 K) from the photoconductor device when illuminated by a 600 °C blackbody source at d=17 cm distance and with a radius r =10.5mm diameter. The blackbody radiation photon number per sec arriving on the sample of area A (cm^2) is $\int_{\tilde{\nu}=1500\,cm^{-1}}^{6000cm^{-1}} \frac{2c\tilde{\nu}^2}{e^{hc\tilde{\nu}/k_BT}-1} abs(\tilde{\nu})\,d\tilde{\nu} \times T(CaF_2) \times \frac{\pi r^2}{d^2} A$, where $\tilde{\nu}$ is the frequency in cm^{-1}, c is the speed of light in cm/s, h is the Planck constant, k_B Boltzmann constant, T is temperature (K). The transmission of the cryostat CaF_2 window is included with $T(CaF_2)$=90%. $abs(\tilde{\nu})$ is taken to be a function from 0 to 1 that mimics the rising photoresponse edge as shown in the figure below. From the mid-point of the absorption edge, we take the photon energy as $2100cm^{-1}$~0.26eV as

the "cut-off" (2100cm^{-1} or λ_c = 4.8 μm at 80 K in **Fig.6-7a**). We then multiply the photon flux by this cut-off photon energy to get a power. This procedure gives the responsivity around the cut-off, since any photon of higher energy will provide the same photocurrent. Then the estimated input power ~30.8μW/mm^2, giving a responsivity 0.23A/W at 80K.

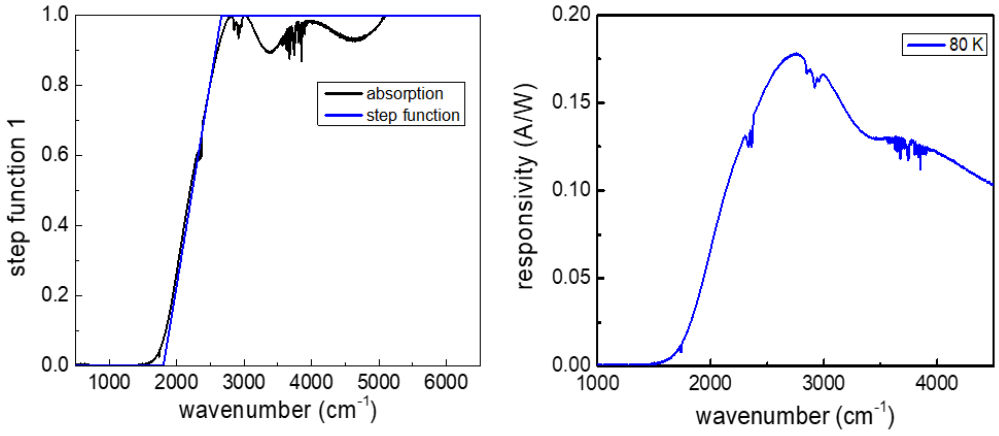

Figure 6-10. Responsivity calculation. (a) step function. (b) Absolute spectral responsivity with the unit A/W of high mobility HgTe QD PC (~90nm thickness, with 1.5V bias) at 80K. This figure is adapted from Ref 27.

The spectral responsivity with the unit A/W in **Figure 6-10**, is obtained by dividing the measured FTIR response spectrum by the spectrum from the DTGS detector corrected by a frequency factor due to the slower speed of the DTGS detector, based on reference[1]. The spectrum is then scaled such that the integral of the spectral responsivity and the blackbody power gives the measured photocurrent. The spectral responsivity in **Fig.6-10b** gives lower value than the integrated responsivity of 0.23A/W stated above, because it scales ~1/$\tilde{\nu}$ and the response edge is soft. The responsivity is found to be linear with bias up to 10 V across the 20 μm gap, resulting in R=0.23 A/W at 1.5 V bias and 1.5 A/W at 10V bias for a film of 120 nm thickness. **Figure 6-11** showed the bias dependence of the responsivity (**Fig.6-11a**), dark current (**Fig.6-11b**), and detectivity (**Fig.6-11c**) for films of three different thicknesses. Average thicknesses are indicated. The

responsivity is proportional to bias, as high as 1.45A/W with 10 V. However, the dark currents increase more at higher bias, resulting in more noise. With 1 to 3V bias, the highest *D** is obtained.

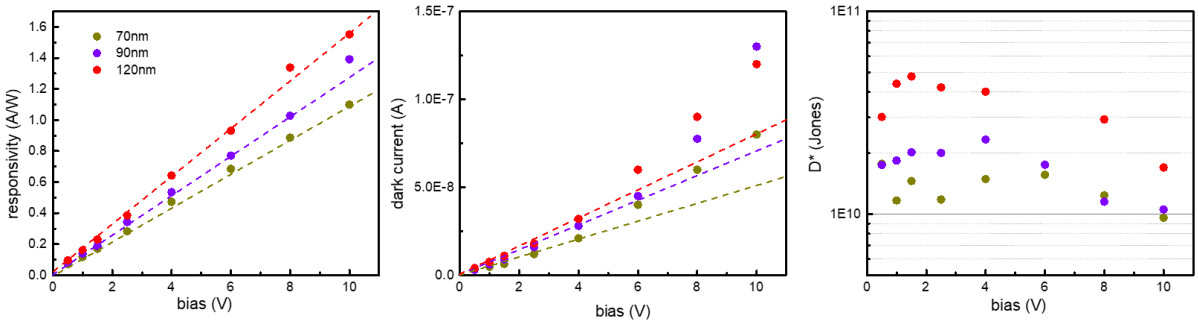

Figure 6-11: Responsivity with different bias on HgTe/hybrid films. (a) responsivity as a function of bias. (b) dark current as a function of bias. (c) detectivity as a function of bias. This figure is adapted from Ref 27.

The external quantum efficiency (EQE) is related to the responsivity as $\frac{R*1.24}{\lambda_{\circ}\ (\mu m)}$ such that EQE ~ 5% with 1.5V bias and ~ 30% at 10V bias. The EQE of a photoconductive device depends on the internal quantum efficiency (IQE) η, the optical absorption A, and the gain g such that $\mathrm{EQE} = g\frac{IQE}{A}$. Therefore, given the small absorption of the thin film (5-10%), $g \times$ IQE reaches or exceeds unity. To evaluate the photoconductive gain, we measured the transient response of the detector, using a pulsed laser source and a current amplifier with a 500 kHz bandwidth. **Figure 6-11c** shows the photo-excited current under 1.5 V bias using an 808nm laser with 50 μs pulses at 298 K (red curve) and 80 K (blue curve) while the insert graph shows the response using a 1 μs pulse close to the 0.7 μs resolution of the amplifier. With the long pulse, there is a dominant component of ~1 μs, and a smaller component of ~12 μs. With the short pulse, at 80 K, the rise time and fall time are 0.9 and 2 μs, without the slow component. The microsecond response time

is then compared to the calculated transit time $\tau_t = \frac{L^2}{\mu V}$ where L is the interdigit distance and V is the bias. Taking a mobility of 2 cm^2/Vs, and a 1.5 V bias across the 20 microns gap, τ_t =1.3 μs. Since the dominant time response is similar to the instrumentation response, while being also similar to the calculated transit time, we conclude the photoconductive gain in the device must be small and that the internal quantum efficiency is of order of magnitude unity limited by the uncertainties of the measurement. **Figure 6-12** shows the diagram of 1/f noise measurement set up and the noise spectra of the 10 kΩ carbon resistor. As a control, the normalized noise shows no dependence on bias.

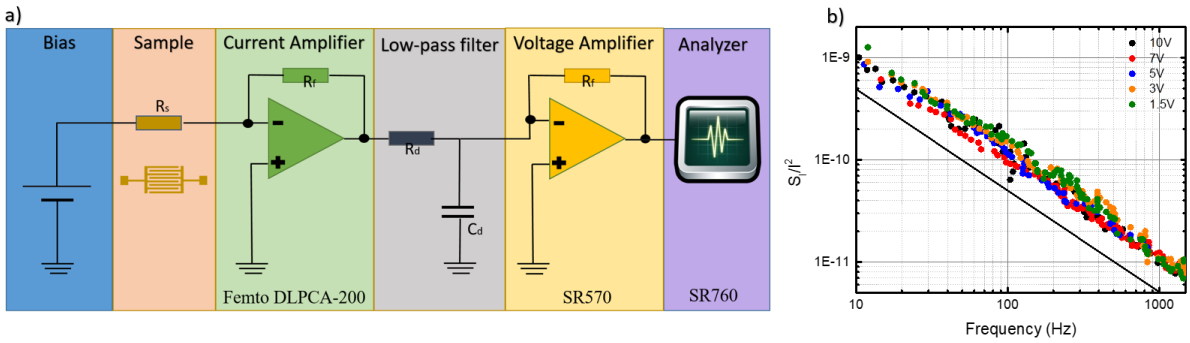

Figure 6-12. 1/f noise measurement set up. (a) 1/f noise set up diagram. (b) Normalized noise spectra of 10 kΩ carbon resistor with different bias (dots) and 1/f noise slope (black line). This figure is adapted from Ref 27.

A photodetector performance is primarily limited by the noise. The specific detectivity is given by $D^* = \frac{R}{i_n}\sqrt{A}$, where i_n is the root mean square(rms) current noise in a 1Hz bandwidth and A is the area of the device. In a biased photoconductor the noise stems from fluctuations of the dark current and it can have significant 1/f components in addition to the shot noise and Johnson noise. Furthermore, while noise from generation/recombination events is multiplied by the gain of the device.[35] Since 1/f noise can be much larger than the shot noise $i_n = \sqrt{2eI}$, the experimentally measured noise spectrum is required to calculate D^*. For commercial detectors, a frequency of

500Hz is often used to measure the noise and quote the detectivity, and this is used here. For the best near-intrinsic HgTe/hybrid device, with a 120nm thickness, at 80 K and at a 1.5 V bias that optimized the detectivity, the detectivity was $D^* = 5.4 \times 10^{10}\ Jones$ at 500 Hz. The dark current was $I_d = 9.6$ nA and the measured noise was $i_n = 100\ fAHz^{-0.5}$ at 500 Hz. The noise was flat above 50 Hz as shown in **Figure 6-13** but 2-fold larger than $\sqrt{2eI} = 55\ fAHz^{-0.5}$. This may reflect a limitation of the electronics. Using the measured responsivity and noise at each temperature, the detectivity from 80K to 300K is shown in **Fig.6-7d**. The 120 nm thick HgTe/hybrid device shows a higher detectivity than the 260 nm thick HgTe/EDT device at all temperatures. Since the responsivity scales as the thickness for thin films and the noise scales as the square root of the thickness, the specific detectivity can be scaled by the square root of the thickness. The detectivity of the HgTe/hybrid ligands material is therefore better than HgTe/EDT by a factor of 10 at 80 K and a factor of 5 at 300 K. As mentioned earlier, a previous realization of infrared imaging camera with HgTe CQD achieved 100mK NEDT, while commercial InSb cameras achieve 10mK, both at cryogenic temperatures. Since detectivity and NEDT are proportional, the order of magnitude improvement realized with the new ligand exchange should allow HgTe CQD photoconductive imagers to approach the performances of existing InSb cameras. The improvement will also benefit HgTe CQD photovoltaic devices[35,36] since the higher mobility, in the geminate recombination regime, will allow longer carrier diffusion lengths and higher operation temperature.

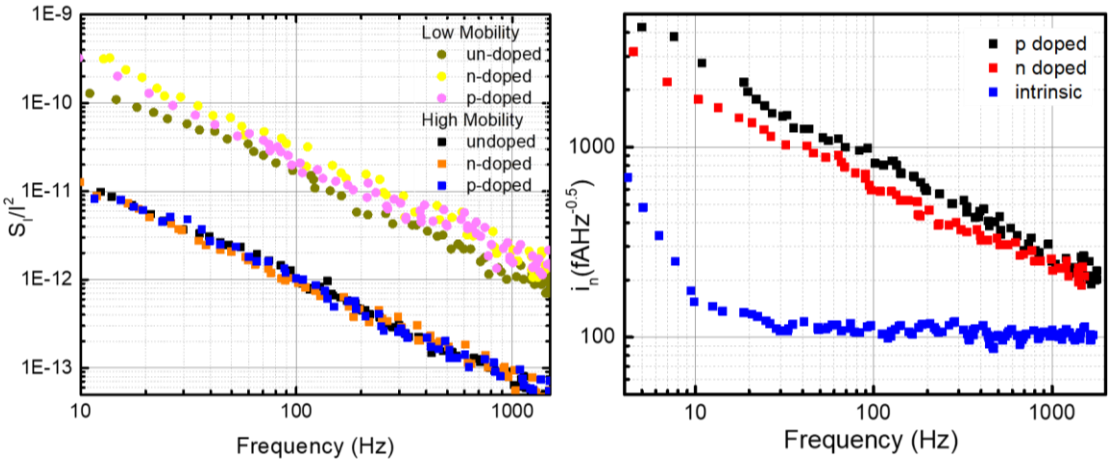

Figure 6-13. Noise spectra. (a) 1/f noise of HgTe/hybrid and low mobility HgTe/EDT measured at room temperature. (b) Measured rms current noise in a 1Hz bandwidth of p-doped, n-doped and intrinsic HgTe/hybrid film at 80K. This figure is adapted from Ref 27.

The benefit of the increased mobility is easily understood if the noise is due to the shot noise of the dark current. In this case, $i_n \sim \sqrt{\mu}$, and since the photocurrent scales as μ, the detectivity scales as $\sqrt{\mu}$. This is the observed scaling at low temperatures, where the devices are indeed shot noise limited. However, at higher temperatures, 1/f noise dominates, as is typical for colloidal metal or quantum dots sensors and photodetectors.[39] In that case, the scaling of the detectivity with mobility is not so obvious. In CQD detector films, 1/f noise can be dominant until rather high frequencies[40] and a modified Hooge equation was shown empirically to allow comparisons of the 1/f noise between different nanocrystals solid.[41] The modified Hooge expression is $\frac{S_I}{I^2} = \frac{\alpha_H}{N_{nc} f}$ where $S_I = i_n^2$ is the frequency-dependent noise spectral density, f is the frequency, N_{nc} the number of nanocrystals in the conductor, and α_H a unitless Hooge constant. The constant α_H was shown to vary approximately inversely with the conductivity between nanocrystals and to be weakly sensitive to the chemical nature of the materials. An increase in mobility should therefore

reduce α_H, and the 1/f noise is expected to scale as $i_n \sim\sqrt{\alpha_H} I\sim \sqrt{\mu}$ in CQD films of different mobility, if all other components are equal. Since the photocurrent scales as μ , we can expect the detectivity to still scale as $D^*\sim\sqrt{\mu}$. Therefore, the improved mobility is expected to also improve the detectivity of CQD films when the system is 1/f noise limited.

This conjecture was tested by measurements of the 1/f noise. **Fig.6-13a** shows the normalized 1/f noise at room temperature for the two systems and different doping levels. It first shows that the normalized 1/f noise is insensitive to the doping. and this agrees with a previously reported observation, and supports the notion that 1/f noise is driven by mobility fluctuations.[38] To determine α_H , we need to estimate the nanocrystal number with all the films for noise measurement covering an area A=0.048mm^2 with the thickness D~100 nm as measured by AFM, and we get $N_{nc} = 0.7 \times \frac{3}{4\pi r^3} * A * D = 8.7 \times 10^9$. At room temperature, near-intrinsic HgTe/hybrid films are dominated by 1/f noise below 10 kHz and α_{298K}~0.8. At 80K, there is no 1/f noise above 100 Hz, and α_{80K} ~0.05. For HgTe/EDT α_{298K} ~18 and α_{80K} ~1. HgTe/hybrid ligands film has therefore an effective Hooge constant ~ 20 times smaller than HgTe/EDT. Although the Hooge constant is thus not exactly inversely proportional to the mobility, it decreases strongly for increasing mobility. Besides the intrinsic 1/f noise from a granular conductor, 1/f noise can also come from contacts and cracks in the films and it is possible that 1/f noise may be improved with further investigations. The weaker scaling of the 1/f noise with the mobility at room temperature leads to a smaller detectivity advantage than at 80K but the higher mobility still improves the detectivity in both shot noise and 1/f noise regimes.

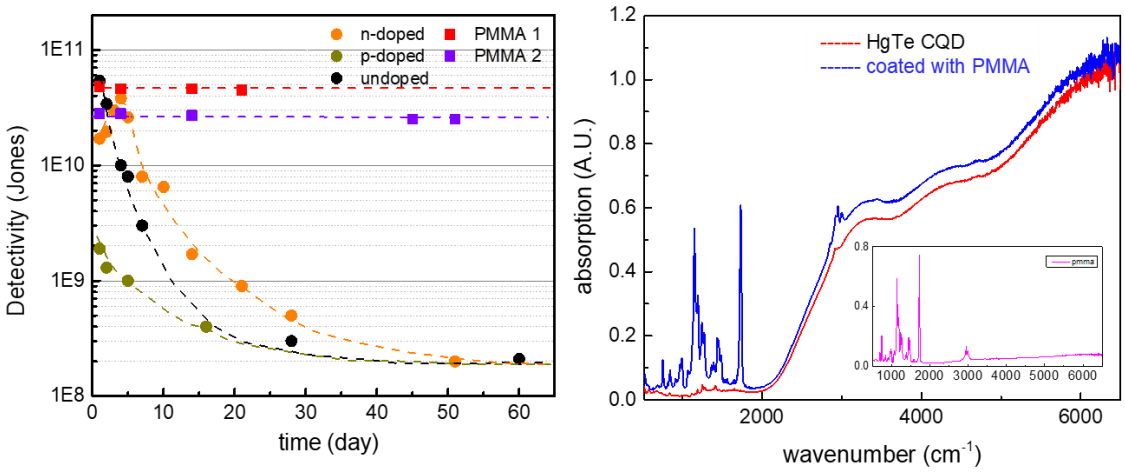

Figure 6-14. Device stability. (a) The detectivity of photoconductive devices using HgTe/hybrid with and without encapsulation. (b) HgTe/hybrid film absorption with and without encapsulation. This figure is adapted from Ref 27.

To evaluate the application potential, we tested the device stability. **Figure 6-14** shows the evolution of the detectivity over several weeks as samples are stored in air between measurements and cooling cycles. Consistent with a gradual oxidation moving the doping towards p-type over several days, the detectivity for the n-type films first increase, then decrease with time, while it monotonously decreases with time for both intrinsic and p type films. A simple solution is to spin coat a thin ~ 100 nm coating layer of poly methyl methacrylate (PMMA). This stabilizes the devices over a period of months without noticeably changing the doping level of the films. Furthermore, since PMMA is quite transparent above the CO stretch at 1730 cm^{-1}, except for the narrow band of the CH-stretch, it is an appropriate encapsulant for 5 microns detectors (**Fig.6-14b**). With 1.5 V bias, the PMMA coated sample has the similar noise level and a responsivity R=0.20 A/W, resulting in a measured $D^* = 4.5 \times 10^{10}\, Jones$. With the PMMA coating, we observed no degradation after several cooling cycles and over at least two months.

6.4 Conclusion

In this chapter, we presented an improved film fabrication process for HgTe CQD photodetectors. We compared films made by a new polar-phase-transfer-ligand-exchange, HgTe/hybrid, with films made by the previous solid-state-ligand-exchange, HgTe/EDT. Electrochemical gating and FET measurement confirmed that the polar-phase-transfer leads to ~100-fold larger mobility compared to the solid-state ligand exchange. We then made intrinsic films by tuning the doping, and investigated the effect of carrier mobility on the photoconductive properties of HgTe CQDs. The best detector using HgTe/hybrid ligands showed $D^*= 5.4 \times 10^{10}$ at 80 K and 500 Hz, and 5 microns cut-off wavelength. Normalizing for differences in film thickness, this is a 10-fold detectivity improvement over HgTe/EDT. This arises in part from ~ 100-fold responsivity increase, in agreement with the expectation that the photocurrent should scale like the mobility if the carrier lifetime is unchanged. This chapter also investigated the noise and found that it scales like the square root of the mobility in the short noise regime, as expected, and slightly less in the $1/f$ noise regime. This explains the ~10-fold improved detectivity. Therefore, improving ambipolar mobility, while preserving the good optical properties of the materials, is demonstrated to be a successful route for improving CQD photodetectors. With mobility already in the 1 cm^2/Vs range, future notable improvements will likely come from other directions, including sharpening the absorption edge by improving the synthetic protocol, and increasing the low photoluminescence efficiency.

6.5 Methods

CQD preparation: HgTe CQDs are prepared following reference.[24,25] For high mobility sample, the oleylamine-capped HgTe QDs (HgTe 0.4 mM) in hexane are mixed with 5mL DMF with 0.025mM $HgCl_2$, 140µL 2-Mercaptoethanol, 400 µL butylamine, and 55mg butylammonium chloride in a glovebox.[26] Following anti-solvent precipitation process with toluene, the final precipitate is re-dispersed in a small amount of DMF. The $HgCl_2$ amount is adjusted to control the final n-, p- or intrinsic doping. For low mobility sample, the devices are directly prepared from films of oleylamine-capped HgTe QDs in a non-polar solvent, followed by the solid ligand exchange with 2% HCl and 1,2-Ethanedithiol/ Isopropyl alcohol (v/v). To prepare p-type HgTe/EDT sample, the film is exposed to a H_2S atmosphere for 10 secs. To prepare n-type HgTe/EDT film, a small amount of dodecanethiol is added on the film. The photoconduction devices are made of 4 pairs of interdigitated evaporated gold fingers of width 20 microns, gap 20 microns, and length 300 microns, and cover an area of 0.3mm x 0.16mm. The substrates are glass microscope slides or heavily doped Si wafer with 300nm thermally grown SiO_2 layer, for FET measurements on the same device. CQD Films are spin coated on the interdigitated electrodes in ambient environment. The CQD films is covered by spin-coating PMMA dissolved in chlorobenzene. **Figure 6-15** shows TEM images of HgTe CQD before and after phase-transfer ligand exchange.

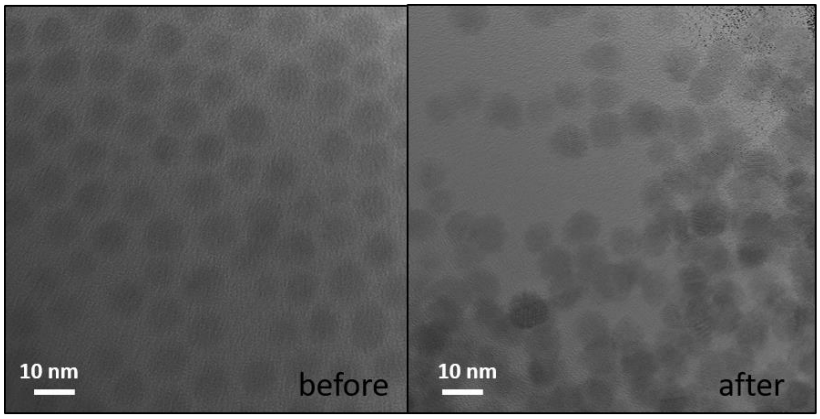

Figure 6 -15. TEM image. TEM image of ~9nm diameter HgTe dots before and after phase transfer.

Electrochemistry: There are four electrodes in the setup: two Pt working electrodes, one Ag/AgCl reference electrode, and one Pt counter electrode. All the electrodes are controlled by a bipotentiostat (DY2300 series Digi-Ivy), following reference[19].

Photocurrent and noise: The devices face the 600 °C blackbody source chopped with a 200 Hz frequency. The bias is applied with a battery, the current across the sample is amplified by a Femto DLPCA-200 current amplifier and a SR570 voltage amplifier. The noise is measured using a SR760 spectrum analyzer.

Photocurrent spectrum: A Nicolet 550 FTIR spectrometer is used to measure the photocurrent spectra. The internal glow bar light source is directed to the outer port and imaged on the sample with a 5 cm focal parabolic mirror. A scanning speed of ~0.9 cm/s is typically used (corresponding to ~0.1 msec for the interferogram peak).

References

[1] Rogalski, A. Recent progress in infrared detector technologies *Infrared Phys. Technol.* **2011**, 54, 136.

[2] Kovalenko, M. V.; Manna, L.; Cabot, A.; Hens, Z.; Talapin, D. V.; Kagan, C. R.; Klimov, V. I.; Rogach, A. L.; Reiss, P.; Milliron, D. J.; Guyot-Sionnnest, P.; Konstantatos, G.; Parak, W. J.; Hyeon, T.; Korgel, B. A.; Murray, C. B.; Heiss, W. Prospects of Nanoscience with Nanocrystals. *ACS Nano* **2015**, 9, 1012-1057.

[3] Leatherdale, C. A. ; Kagan, C. R.; Morgan, N. Y.; Empedocles, S. A.; Kastner, M. A.; Bawendi, M. G. Photoconductivity in CdSe quantum dot solids. *Phys. Rev. B* **2000**, 62, 2669-2680.

[4] Sargent, E. H.; Solar Cells, Photodetectors, and Optical Sources from Infrared Colloidal Quantum Dots *Adv. Mater.* **2008**, 20, 3958-3964.

[5] McDonald,S. A.; Konstantatos, G.; Zhang, S.; Cyr,P. W. ; Klem, E. J.; Levina, L.; Sargent, E. H. Solution-processed PbS quantum dot infrared photodetectors and photovoltaics. *Nat. Mater* **2005**, 4, 138-142.

[6] Konstantatos, G.; Howard, I.; Fischer, A.; Hoogland, S.; Clifford, J.; Klem, E.; Levina, L.; Sargent, E.H. Ultrasensitive solution-cast quantum dot photodetectors. *Nature* **2006**, 442, 180-183.

[7] Tang, J.; Sargent E. H. Infrared Colloidal Quantum Dots for Photovoltaics: Fundamentals and Recent Progress. *Adv. Mater*. **2011**, 23, 12–29.

[8] Keuleyan, S.; Lhuillier, E.; Brajuskovic, V.; Guyot-Sionnest, P. Mid-infrared HgTe colloidal quantum dot photodetectors. *Nat. Photonics* **2011**, *5*, 489-493.

[9] Böberl, M.; Kovalenko, M. V.; Gamerith, S.; List, E. J. W.; Heiss, W. Inkjet-Printed Nanocrystal Photodetectors Operating up to 3 μm Wavelengths. *Adv. Mater.* **2007**, 19 , 3574–3578.

[10] Tang, X.; Ackerman, M. M.; Chen, M.; Guyot-Sionnest, P. Dual-band infrared imaging using stacked colloidal quantum dot photodiodes. *Nat. Photonics* **2019**, 13, 277–282.

[11] Rauch, T.; Boberl, M.; Tedde, S.F.; Furst, J.; Kovalenko, M.V.; Hesser, G.N.; Lemmer, U.; Heiss, W.; Hayden, O. Near-infrared imaging with quantum-dot-sensitized organic photodiodes. *Nat. Photonics* **2009**, 3, 332-336.

[12] Lee, J. W.; Kim, D. Y.; Baek, S.; Yu, H.; So, F. Inorganic UV–Visible–SWIR Broadband Photodetector Based on Monodisperse PbS Nanocrystals. *Small* **2016**,12, 1328–1333.

[13] Saran, R.; Curry, R. J.; Lead sulphide nanocrystal photodetector technologies. *Nat. Photonics* **2016**. 10, 81–92.

[14] Hafiz, S.B., Scimeca, M., Sahu, A.; Ko, D.; Colloidal quantum dots for thermal infrared sensing and imaging. *Nano Convergence* **2019**, 6, 7.

[15] Chen,M,; Yu, H.; Kershaw, S. V.; Xu, H.; Gupta, S.; Hetsch, F.; Rogach, A.L.; Zhao, N. Fast, Air-Stable Infrared Photodetectors based on Spray-Deposited Aqueous HgTe Quantum Dots. *Adv. Funct. Mater.* **2014**, 24, 53-59.

[16] Buurma, C.; Pimpinella, R. E.; Ciani, A. J.; Feldman, J. S.; Grein, C. H.; Guyot-Sionnest, P. MWIR imaging with low cost colloidal quantum dot films. *Proc. Soc. Photo-Opt. Instrum. Eng.* **2016**, 993303-993309.

[17] Zhitomirsky, D.; Voznyy, O.; Levina, L.; Hoogland, S.; Kemp, K. W.; Ip, A. H.; Thon S. M.; Sargent, E. H. Engineering colloidal quantum dot solids within and beyond the mobility-invariant regime. *Nat. Commun.* **2014**, 5, 3803.
[18] Guyot-Sionnest, P. Electrical Transport in Colloidal Quantum Dot Films. *J. Phys. Chem. Lett.* **2012**, 3, 1169-1175.

[19] Chen, M.; Guyot-Sionnest, P. Reversible electrochemistry of mercury chalcogenide colloidal quantum dot films. *ACS Nano* **2017**, 11, 4165-4173.

[20] Lhuillier, E.; Keuleyan, S.; Zolotavin, P.; Guyot-Sionnest, P. Mid-Infrared HgTe/As2S3 Field Effect Transistors and Photodetectors. *Adv. Mater.* **2013**, 25 , 137-141.

[21] Kovalenko, M. V.; Scheele, M.; Talapin D. V.; Colloidal Nanocrystals with Molecular Metal Chalcogenide Surface Ligands. *Science* **2009**, 324, 1417-1420.

[22] Tang, J.; Kemp, K. W.; Hoogland, S.; Jeong, K. S.; Liu, H.; Levina, L.; Furukawa, M.; Wang, X.; Debnath, R.; Cha, D.; Chou, K. W.; Fischer, A.; Amassian, A.; Asbury, J. B.; Sargent, E. H., Colloidal-quantum-dot photovoltaics using atomic-ligand passivation. *Nat. Mater.* **2011**, 10, 765-771.

[23] Nag, A.; Kovalenko, M. V.; Lee, J. S.; Liu, W.; Spokoyny, B.; Talapin, D. V. Metal-free Inorganic Ligands for Colloidal Nanocrystals: S^{2-}, HS^{-}, Se2^{-}, HSe^{-}, Te^{2-}, HTe^{-}, TeS_3^{2-}, OH^{-}, and NH_2^{-} as Surface Ligands. *J. Am. Chem. Soc.* **2011**,133, 10612-10620.

[24] Shen, G.; Chen, M.; Guyot-Sionnest, P. Synthesis of nonaggregating HgTe Colloidal quantum dots and the emergence of air-stable n-doping. *J. Phys. Chem. Lett.* **2017**, *8*, 2224-2228.

[25] Hudson, M. H.; Chen, M.; Kamysbayev, V.; Janke, E. M.; Lan, X.; Allan, G.; Delerue, C.; Lee, B.; Guyot-Sionnest, P.; Talapin D. V. Conduction band fine structure in colloidal HgTe quantum dots. *ACS Nano* **2018**, 12, 9397-9404.

[26] Lan, X.; Chen, M.; Hudson, M. H.; Kamysbayev, V.; Wang, Y.; Guyot-Sionnest, P.; Talapin, D.V. Quantum Dot Solids Showing State-Resolved Bandlike Transport, *Nature Materials* **2020**.

[27] Chen, M.; Lan, X.; Tang, X. ; Wang, Y. ; Hudson, M. H. ; Talapin, D.V. ; Guyot-Sionnest, P. High Carrier Mobility in HgTe Quantum Dot Solids Improves Mid-IR Photodetectors. *ACS Photonics* **2019**, 6, 2358-2365.

(27) Martinez, B.; Ramade, J.; Livache, C.; Goubet, N.; Chu, A.; Gréboval, C.; Qu, J.; Watkins, W. L.; Becerra, L.; Dandeu, E.; Fave, L.J.; Méthivier, C.; Lacaze, E.; Lhuillier, E. HgTe Nanocrystal Inks for Extended Short-Wave Infrared Detection. *Adv. Opt. Mater.* **2019**, 1900348.

[28] Yu, D.; Wang, C. J.; Guyot-Sionnest, P. n-Type Conducting CdSe Nanocrystal Solids. *Science* **2003**, *300*, 1277-1280.

[29] Talapin, D. V.; Murray, C. B. PbSe Nanocrystal Solids for n- and p-Channel Thin Film Field-Effect Transistors. *Science* **2005**, *310*, 86-89.

[30] Jeong, K. S.; Deng, Z.; Keuleyan, S.; Liu, H.; Guyot-Sionnest, P. Air-Stable n-Doped Colloidal HgS Quantum Dots. *J. Phys. Chem. Lett.* **2014**, *5*, 1139-1143.

[31] Reich, K. V.; Chen, T.; Shklovskii, B. I. Theory of a field-effect transistor based on a semiconductor nanocrystal array. *Phys. Rev. B* **2014**, 89, 235303.

[32] Brown, M. A.; Crosser, M. S.; Leyden, M. R.; Qi, R.; Minot, E. D. Measurement of high carrier mobility in graphene in an aqueous electrolyte environment. *Appl. Phys. Lett.* **2016**, *109*, 093104.

[33] Browning, A.; Kumada, N.; Sekine, Y.; Irie, H.; Muraki, K.; Yamamoto, H. Evaluation of disorder introduced by electrolyte gating through transport measurements in graphene. *Appl. Phys. Express* **2016**, *9*, 065102.

[34] Petach, T. A.; Reich, K. V.; Zhang, X.; Watanabe, K.; Taniguchi, T.; Shklovskii, B. I.; Goldhaber-Gordon, D. Disorder from the Bulk Ionic Liquid in Electric Double Layer Transistors. *ACS Nano* **2017**, *11*, 8395-8400.
[35] Tang, X.; Ackerman, M. M.; Guyot-Sionnest, P. Thermal imaging with plasmon resonance enhanced HgTe colloidal quantum dot photovoltaic devices. *ACS Nano* **2018**, *12*, 7362-7370.

[36] Ackerman, M. M.; Tang, X.; Guyot-Sionnest, P. Fast and sensitive colloidal quantum dot mid-wave infrared photodetectors. *ACS Nano* **2018**, *12*, 7264-7271.

[37] Liu, H.; Keuleyan, S.; Guyot-Sionnest, P. N-and p-Type HgTe quantum dot films. *J. Phys. Chem. C* **2011** 116, 1344-1349,

[38] Rosencher, E.; Vinter, B. Optoelectronics, Cambridge University Press, Cambridge, UK **2001** pp. 513-530

[39] Kurdak, C.; Kim, J.; Kuo,A.; Lucido, J. J.; Farina, L. A.; Bai, X.; Rowe, M. P.; Matzger, A. J. 1/f noise in gold nanoparticle chemosensors. *Appl. Phys. Lett.* **2005**, *86*, 073506.

[40] De Iacovo, A. ; Venettacci, C. ; Colace, L. ; Scopa, L.; Foglia, S. Noise performance of PbS colloidal quantum dot photodetectors. *Appl. Phys. Lett.* **2017**, 111, 211104.

[41] Liu, H.; Lhuillier, E.; Guyot-Sionnest, P. 1/*f* noise in semiconductor and metal nanocrystal solids. *J. Appl. Phys.* **2014**, *115*, 154309.

Chapter 7: Conclusions and Perspectives

PGS Lab is one of the early research groups that stepped in the colloidal nanoparticle research. For the past 30 years, the lab investigated colloidal quantum dots with creative and impactful ideas. For example, PGS Lab came up with a core-shell structure to improve nanoparticle sturdiness and first successfully synthesized the CdSe/ZnSe core-shell[1] structure in 1996. The lab also contributed two-photon spectroscopy[2], intraband spectroscopy[3], as well as the study on induced n-doping in quantum dot[4] a few years later.

In 2011, the group successfully synthesized the first mid-IR CQD based on HgTe and applied the material to photodetection[5]. Since then, The HgX(X=S, Se, Te) CQDs have been extensively studied in photodetection devices, evolving from simple photoconductors[6,7] to photodiode[8-12-7] and multispectral photodetectors[13] with a complex design. The spectroelectrochemistry[14-16] and Field effect transistor[17] are good tools to precisely measure the QD energy levels, which are essential inputs into device design as discussed in Chapter 2 and Chapter 4. In these chapters, I characterized the energy levels but also tuned the energies by surface dipoles. The findings of high mobility n-type and p-type QDs[17] could be used for improved photodiode performance after overcoing some fabrication issues.

Besides infrared detection, HgX CQDs could be potential candidates for emitting infrared light. Taking HgSe CQDs as an example, the n-type doping results in the suppressed Auger relaxation which is at least three orders of magnitude slower than for bulk materials of similar gaps[18], and this is a significant motivation to pursue mid-infrared light-emission utilizing intraband transitions.

The HgX CQDs are not only new infrared materials but they also have become a model system to study the transport properties in quantum dots solids[19], and this has been the main thread in my

Ph.D. research. Transport study on the quantum dot is one of the traditional advantages in our lab. The lab members developed the solid state ligand exchange[20] in 2003, improving mobility by ~3 orders of mangitude and changing the traditional opinion that quantum dot films were almost insulating. They first applied electrochemistry[20] to this field in 2003 and used variable range hopping theory[21] to explain the carrier transport in quantum dot solids at low temperature a year later. My research work with co-workers on liquid ligands exchange further improved mobility by 2~3 orders compared with solid state ligand exchange[19] and we found a nice system that exhibits similar Hall and drift mobility with rather high mobility value above 1 cm^2/Vs. However, I remain unclear whether the transport is fully hopping in nature or partially delocalized. It would be nice if one could improve the Hall measurement resolution to see whether Hall and drift mobility also match in the low mobility 10^{-2} cm^2/Vs sample. The Hall effect in the QD system is therefore still worth investigating further.

The effect of magnetic fields on transport goes beyond just measuring the Hall effect, and I carried out these studies to learn more about the nature of transport and to look for possible evidence of delocalization[22]. In Chapter 5, I measured the MR as a function of doping in rather high mobility HgTe QD films (1-10 cm^2/Vs) at different Fermi level with a FET structure, as a function of temperature down to 10K. A positive-quadratic magnetoresistance is observed which can be several 100% at low temperature and scales like x (1- x) where x is the fractional occupation of the $1S_e$ state. It might be attributed to the increased confinement induced by the magnetic field and the increased hopping activation energy, but the explanation fails to capture the temperature dependence behavior. There is also a negative magnetoresistance of 1-20% from 300 K to 10 K which is rather independent of the fractional occupation, and which follows a negative exponential dependence with the magnetic field. These results have not been not fully understood yet.

Using chiral molecules as ligands might be another interesting direction for the transport study. Recent developments[23] based on the chiral-induced spin selectivity effect show that the spin orientation is linked to molecular symmetry and can be controlled. During electron transfer processes in chiral materials, electron backscattering is suppressed because of the coupling between the momentum and the spin direction. For a chiral molecule, one spin is stabilized during electron transfer by the effective magnetic field. While one spin will be stabilized when the electrons move in one direction through a chiral molecule, the opposite spin will be stabilized when electrons move in the opposite direction. Hence, for an electron to be elastically backscattered, it would have to change both its momentum direction and spin direction, which is improbable. This might be beneficial in carrier transfer in the QD system.

Besides my interest in the basic studies on transport, the improved mobility while retaining the clean quantum dot states led me to measure the photoconductive response and I found that it is indeed a very important avenue for improving photodetectors. There is a lot more to do with these latest HgTe CQD systems, and the first should probably be to incorporate them into np photodiodes to achieve record performances with CQD in the mid-infrared. With the intraband HgSe CQDs, the challenges are controlling the precise doping, improving the quantum yield, and reducing the size distribution, just mentionning a few. In Chapter 4, I discussed how the interband and intraband conductivity gap are affected quite differently by size distribution, since $1S_h$ has a small dispersion because of the heavy hole while $1S_e$ and $1P_e$ have a strong dispersion because of the light effective electron mass. The simulation shows that HgSe intraband photodetection could be much improved with better size control control, which would be worth the effort.

Looking forward, it seems likely that there are many reachable improvements of the material synthesis and the interfacial chemistry, and that the prospect for CQD having a valuable role in developing new infrared technologies is quite promising

Reference

[1] MA Hines, P Guyot-Sionnest Synthesis and characterization of strongly luminescing ZnS-capped CdSe nanocrystals. *J. Phys. Chem* **1996** 100, 468-471.

[2] SA Blanton, MA Hines, ME Schmidt, P Guyot-Sionnest Two-photon spectroscopy and microscopy of II–VI semiconductor nanocrystals. *Journal of luminescence* **1996,** 70 , 253-268

[3] P Guyot-Sionnest, MA Hines. Intraband transitions in semiconductor nanocrystals. *Applied Physics Letters*, **1998**, 72, 686-688

[4] M Shim, P Guyot-Sionnest N-type colloidal semiconductor nanocrystals. *Nature* **2000**, 407, 981-983.

[5] S Keuleyan, E Lhuillier, P Guyot-Sionnest Synthesis of colloidal HgTe quantum dots for narrow mid-IR emission and detection. *Journal of the American Chemical Society* 2011, 133, 16422-16424.

[6] Keuleyan, S.; Lhuillier, E.; Brajuskovic, V.; Guyot-Sionnest, P. Mid-Infrared HgTe Colloidal Quantum Dot Photodetectors. *Nat. Photonics* **2011**, *5*, 489-493.

[7] Deng, Z; Jeong, K.S. ; Guyot-Sionnest, P. Colloidal Quantum Dots Intraband Photodetectors. *ACS Nano* **2014**, *8*, 11707–11714.

[8] Guyot-Sionnest, P.; Roberts, J. A. Background Limited Mid-infrared Photodetection with Photovoltaic HgTe Colloidal Quantum Dots. *Appl. Phys. Lett.* **2015**, *107*, 253104.

[9] Ackerman, M. M.; Tang, X.; Guyot-Sionnest, P. Fast and Sensitive Colloidal Quantum Dot Mid-wave Infrared Photodetectors. *ACS nano* **2018**, 12, 7264-7171.

[10] Buurma, C.; Pimpinella, R.E.; Ciani, A. J.; Feldman, J.S.; Grein, C.H.; Guyot-Sionnest, P. MWIR Imaging with Low Cost Colloidal Quantum Dot Films. *SPIE Nanoscience+ Engineering. International Society for Optics and Photonics*, **2016**, 993303-993303-7.

[11] Tang, X.; Ackerman, M. M.; Guyot-Sionnest, P. Thermal Imaging with Plasmon Resonance Enhanced HgTe Colloidal Quantum Dot Photovoltaic Devices. *ACS nano* **2018**, 12, 7362-7370.

[12] Tang, X.; Tang, X.; Lai, K. W. C. Scalable Fabrication of Infrared Detectors with Multispectral Photoresponse Based on Patterned Colloidal Quantum Dot Films. *ACS Photonics* **2016**, *3*, 2396-2404.

[13] Tang, X.; Ackerman, M. M.; Chen, M.; Guyot-Sionnest, P. Dual-band Infrared Imaging using Stacked Colloidal Quantum Dot Photodiodes. *Nature Photonics* **2019**, 13, 277.

[14] Chen, M.; Guyot-Sionnest, P. Reversible electrochemistry of mercury chalcogenide colloidal quantum dot films. *ACS Nano* **2017**, 11, 4165– 4173.

[15] Shen, G.; Chen, M.; Guyot-Sionnest, P. Synthesis of Nonaggregating HgTe Colloidal Quantum Dots and the Emergence of Air-stable N-doping. *J. Phys Chem. Lett.* **2017**, 8, 2224-2228.

[16] Hudson, M. H.; Chen, M.; Kamysbayev, V.; Janke, E. M.; Lan, X.; Allan, G.; Delerue, C.; Lee, B.; Guyot-Sionnest, P.; Talapin, D. V. Conduction band fine structure in colloidal HgTe quantum dots. *ACS Nano* **2018**, 12, 9397– 940

[17] M. Chen, X. Lan, X. Tang, Y. Wang, M. H. Hudson, D. V. Talapin, P. Guyot-Sionnest. High Carrier Mobility in HgTe Quantum Dot Solids Improves Mid-IR Photodetectors. ACS photonics, 6, 2358-2365, 2019

[18] C. Melnychuk, P. Guyot-Sionnest Auger Suppression in n-Type HgSe Colloidal Quantum Dots ACS Nano 2019, 13, 9, 10512-10519

[19] X. Lan, M. Chen, M. H. Hudson, V. Kamysbayev, Y. Wang, P. Guyot-Sionnest, D.V. Talapin. Quantum Dot Solids Showing State-Resolved Bandlike Transport. Nature Materials, 19, 323-329, 2020

[20] D Yu, C Wang, P Guyot-Sionnest n-Type conducting CdSe nanocrystal solids. *Science*, **2003** 300, 1277-1280.

[21] D Yu, C Wang, BL Wehrenberg, P Guyot-Sionnest. Variable range hopping conduction in semiconductor nanocrystal solids. *Physical review letters* **2004**, 92 (21), 216802

[22] M. Chen, X. Lan, M. H. Hudson, G. Shen, P. B. Littlewood, D. V. Talapin, P. Guyot-Sionnest. Magnetoresistance of HgTe Quantum Dot Films (In preparation)

[23] Naaman, R. & Waldeck, D. H. Spintronics and chirality: spin selectivity in electron transport through chiral molecules. Ann. Rev. Phys. Chem. **2015**, 66, 263–281.